UNIVERSITY OF CALIFORNIA

Santa Barbara

Synthesis, Behavior, and Applications of Molecules with Redox-Switchable Properties

A dissertation submitted in partial satisfaction of the

requirements for the degree Doctor of Philosophy

in Chemistry

by

Camden Hunt

Committee in charge:

Professor Gabriel Ménard, Chair

Professor Peter Ford

Professor Steven Buratto

Professor Susannah Scott

December 2019

The dissertation of Camden Hunt is approved.

Peter Ford

Steven Buratto

Susannah Scott

Gabriel Ménard, Committee Chair

December 2019

Synthesis, Behavior, and Applications of Molecules with Redox-Switchable Properties

by

Camden Hunt

ACKNOWLEDGEMENTS

First and foremost, I would like to thank my supervisor, Prof. Gabriel Ménard. Gab, you took a chance on me when you first accepted me into your lab, and I will always appreciate it. Thank you for teaching me, and for giving me freedom to explore my chemistry. I realized writing this that I would likely not be going to Vancouver for my postdoctoral work if you hadn't excitedly sent me an email in the middle of the night about a review in *Nature* on cold fusion, suggesting that I read it. You helped me in a way I can never really pay back, but I hope to one day pay it forward.

Next, I would like to thank the Gab Lab for keeping me sane during my PhD. You all gave countless helpful discussions, encouragement, and just good conversation. I can't wait to see what you all do and discover, and I hope to have you all as colleagues in the future. I would also like to thank the incredible staff and facility managers of the UCSB Chemistry Department, especially Guang Wu and Hongjun Zhou for their expertise and patience.

I am also deeply indebted to Lior Sepunaru, for how helpful he has been to me and our group as a whole. Thank you for everything and I wish you and your group the best. I would also like to thank my committee for their encouragement, guidance, and time.

And finally, I would like to thank my family. Mom, you taught me to think, and to use my thoughts for a good purpose. Anything I accomplish in science will only be because of you. Dad, you showed me the beauty of science that kept me going even when my PhD got tough. And to my brothers, you all are incredible people that shaped me as a person. I'd also like to thank Sarah, who represents something uniquely good in this world, and whom I hope to know for the rest of my life.

VITA OF CAMDEN HUNT
December 2019

EDUCATION

Bachelor of Science in Chemistry, Utah State University, May 2014
Doctor of Philosophy in Chemistry, University of California, Santa Barbara, December 2019 (expected)

PROFESSIONAL EMPLOYMENT

2009-2012: Researcher, USDA Bee Research Lab, Utah State University
2010: NSF REU Summer Internship, University of Missouri
2014-2019: Teaching Assistant, Department of Chemistry, University of California, Santa Barbara

SELECT PUBLICATIONS

Hunt, C.; Peterson, M.; Anderson, C.; Chang, T.; Wu, G.; Scheiner, S.; Ménard, G. *J. Am. Chem. Soc.* **2019**, *141* (6), 2604–2613.

Hunt, C.; Mattejat, M.; Anderson, C.; Sepunaru, L.; Ménard, G. *ACS Appl. Energy Mater.* **2019**.

Hunt, S.; Hunt, C.; Iliadis, C.; Falvo, M. *Nucl. Instruments Methods Phys. Res. Sect. A Accel. Spectrometers, Detect. Assoc. Equip.* **2018**.

Carroll, T. G.; Hunt, C.; Garwick, R.; Wu, G.; Dobrovetsky, R.; Ménard, G. *Chem. Commun.* **2019**, *55* (26), 3761–3764.

Keener, M.; Hunt, C.; Kampel, V.; Dobrovetsky, R.; Hayton, T. W.; Ménard, G. *Nature.* **2019.** "Redox-Switchable Chelation for Uranium Capture and Release" Accepted 10/1/2019.

PATENTS

U.S. Provisional Patent Application No. 62,742,715: *Redox-Active Material for Application in Symmetric Redox Flow Batteries*

FIELDS OF STUDY

Major Field: Inorganic Chemistry

Minor Field: Electrochemistry

ABSTRACT

Synthesis, Behavior, and Applications of Molecules with Redox-Switchable Properties

by

Camden Hunt

Molecules with reversible, redox-switchable properties have potential application in many fields, including catalysis, electronics, waste remediation, and energy storage. To further this field, a detailed understanding of the relationship between chemical structure and electronic properties must be developed for different systems. Here, we first examine this relationship for phthalocyanines, a well-studied class of macrocyclic ligand. We first discuss generalized synthesis and characterization of a library of soluble, metal phthalocyanine species, and then proceed to investigate the electronic character of this macrocyclic ligand in extreme detail with modern experimental and computational methods, and discuss a fundamental discovery regarding a terminal manganese nitride phthalocyanine (^{EtO}PcMnN) that is the first reported molecular species capable of reversibly switching between aromatic, non-aromatic, and anti-aromatic states. We then discuss possible reasons for the extreme stability of ^{EtO}PcMnN, and discuss more generalized conclusions pertaining to the electronic character of other phthalocyanines and related aromatic macrocycles.

Further studies leverage the unusual stability of ^{EtO}PcMnN for energy storage applications, revealing a potential use as a symmetric redox-flow battery charge carrier. Electrochemical kinetics and battery measurements are performed, revealing that ^{EtO}PcMnN can function as a

2-electron symmetric charge carrier capable of functioning as both anolyte and catholyte in a redox flow battery. A new architecture for redox-flow batteries is also developed, in which a redox-active “sediment” is utilized in lieu of a traditional solution-state charge carrier, and represents a possible strategy for increasing charge carrier loading beyond the solubility limit while preventing the high viscosity typically associated with slurry-based systems. Finally, the redox-switchable properties of another class of ligand, carboranes, are examined for application as reversible chelating agents. It is demonstrated with a carborane phosphine species that redox events can be accessed to induce a C-C bond scission which results in a structural distortion of the carborane that can be utilized as a “molecular switch” capable of changing the bond angle of the phosphine ligands, resulting in a convenient electrochemical switch for the capture and release of metal ions. We demonstrate a proof-of-concept system in which uranyl can be electrochemically captured and released from biphasic systems in a reversible manner, and discuss the application of such systems for new nuclear waste remediation strategies.

TABLE OF CONTENTS

LIST OF FIGURES

LIST OF SCHEMES

LIST OF TABLES

LIST OF SYMBOLS AND ABBREVIATIONS

A	amp
Å	angstrom
Abs coeff	absorption coefficient
AEM	anion exchange membrane
Anal. Calc.	analytical calculated
atm	atmosphere
B3LYP/def2-SVP	DFT functional
Bu_4N	tetrabutylammonium
C_6D_6	deuterated benzene
CD_2Cl_2	deuterated dichloromethane
Cp	cyclopentadienyl
Cp^*	pentamethylcyclopentadienyl
CPCM	conductor-like polarizable continuum model
CV	cyclic voltammetry
d	day
DCE	1,2-dichloroethane
DCM	dichloromethane
DCM-d_2	deuterated dichloromethane
DFT	density functional theory
DMF	dimethylformamide
EPR	electron paramagnetic resonance
equiv	equivalent
Et	ethyl

^{EtO}Pc	1,4,8,11,15,18,22,25-Octaethoxyphthalocyanine
Fc	ferrocene
FEP	fluorinated ethylene propylene
g	gram
GBE	galvanostatic bulk electrolysis
h	hour
HOMO	highest occupied molecular orbital
Hz	hertz
I	current
I	isoindolic planes
J	joule
J	scalar coupling constant
K	degrees Kelvin
Kryptofix-222	2.2.2.-Cryptand
L	Liter
LMCT	ligand-to-metal charge transfer
LUMO	lowest unoccupied molecular orbital
m	meter
M	molar
M06-2X	DFT functional
MALDI	matrix-assisted laser desorption/ionization
Me	methyl
MeCN-d_3	deuterated acetonitrile

min	minute
mol	mole
MS	mass spectrometry
*n*BuLi	n-butyl lithium
NICS	nucleus-independent chemical shift
NMR	nuclear magnetic resonance
OAc	acetate
^{o}C	degrees Celsius
OLEX^{2}	crystallography software
Pc	phthalocyanine
PC	propylene carbonate
Ph	phenyl
POV-Ray	crystallography software
ppb	parts per billion
ppm	parts per million
PUREX	plutonium and uranium reduction extraction
PV	photovoltaic
r.t.	room temperature
RVC	reticulated vitreous carbon
SHELXTL	crystallography software
SOC	state of charge
T	temperature
t	time
T_1	relaxation time

THF	tetrahydrofuran
THF-d_8	deuterated tetrahydrofuran
TOF	time-of-flight
TPO	triphenylphosphine oxide
UV-Vis	ultraviolet-visible
V	volume
W	watt
XRD	x-ray diffraction
α	angle
β	angle
γ	angle
δ	chemical shift
ΔG	free energy
ΔH	enthalpy
ΔS	entropy
λ	wavelength
ν	frequency
π	pi orbital
σ	sigma orbital

Chapter 1

Introduction

1.1 Renewable Energy and Grid-Scale Energy Storage

1.1.1 Overview

Renewable energy production is rapidly expanding as humanity attempts to shift away from fossil fuel as an energy source in an effort to mitigate the effects of climate change, which is unarguably the most critical issue facing our species, and is occurring faster than initial models predicted.[1] As of 2018, there is an estimated 33.1 Gt of anthropogenic CO_2 in the atmosphere, and we continue to emit it at an accelerated rate.[2] Atmospheric CO_2 concentrations reside at 407.4 ppm as of 2018, an unsettling value given that pre-industrial era CO_2 levels resided between 180 and 280 ppm.[2] The unanimous consensus in the scientific community is that we must make efforts to reduce our dependency on fossil fuel, as the results of an unmitigated rise in global temperatures will be calamitous to the species in a short period of time.[3] There are many urgently needed technological and socioeconomic shifts that must occur in order to reduce our dependency on fossil fuel and petroleum-based products, but arguably the most urgent task is to shift energy production from non-renewable to renewable sources, as fossil fuel combustion accounts for 76% of all anthropogenic CO_2 emitted.[4]

Fortunately, photovoltaic (PV) technologies have been nothing short of a success story and have seen a price reduction of two orders of magnitude in a 40-year period.[5] The current cost of PV power production in the U.S. currently around $0.05/kWh[5], and expected to drop to as a low as $0.03/kWh[6], which would be directly competitive with fossil steam. Additionally, PV is an inherently modular technology with the added benefit of almost arbitrary scalability, unlike fossil steam which requires greater initial capital investment for the plant development. The current installed capacity of PV power production is 500 GW, with an additional 500 GW expected by 2022-2023.[7]

Recently, it was proposed that TW-scale photovoltaic energy production may be possible, with targets of 3 to 10 TW of PV by 2030, and 30 to 70 TW by 2050.[7] While ambitious, this is not an impossible task, especially if new PV technologies continue to lower the cost of production. However, for this timetable to be realized monumental improvements in grid-scale energy storage will need to be developed in tandem with the aim of developing a network of generation, storage, and distribution that can overcome the inherent intermittency of PV power production and allow for comprehensive renewable energy-based electrical grid.[8]

Most modern electrical grids have virtually no storage capacity, with the United States (U.S.) grid only capable of storing ~2.5% of the electrical energy generated[9], and the majority of that (94%) coming from pumped-storage hydroelectricity.[10] Any viable method for storing and releasing energy at grid-scale must do so at a cost comparable with fossil steam power production for meaningful, widespread implementation. Given the previously mentioned low cost of power production by fossil fuel combustion, this is a demanding challenge. Of the potential methods of storage that could meet this challenge (physical[11,12], thermal[13], chemical[14], electrochemical[15], etc.), electrochemical energy storage is an obvious choice that will likely play a major role due to the scalability, versatility, and well-established manufacturing methodologies. However, the vast majority of electrochemical cell architectures are specifically designed for device applications, where the primary considerations are cost, cycle life, and energy density, with the chemistries and cell design reflecting a careful balance of this triad. In contrast, this balance is tilted for grid-scale energy storage: there is more emphasis placed on cost and cycle life, and less placed on energy density, necessitating alternative strategies that would traditionally not be considered for device applications due to a lower energy density. This need is growing an

underexplored regime of electrochemical research, resulting in novel battery chemistries and cell designs intended for low-cost, mass production to meet the colossal storage demand of a renewable-centric electrical grid.[8,16]

1.1.2 Redox Flow Batteries

Of the aforementioned new battery architectures, redox flow batteries (RFBs) have been identified as promising candidates capable of meeting the near-term U.S. Department of Energy (DOE) economic targets for grid-scale energy storage systems ($250/kWh with a system efficiency of ~80% and a cycle life of 3,900 cycles).[17] RFBs utilize dissolved or suspended electroactive material that is pumped past inert flow field electrodes, with the electrodes mediating charge/discharge processes of the electroactive material, and a thin separator allowing the selective transport of supporting electrolyte ions (Figure 1.1) to maintain charge balance on charge/discharge.[16] This is in contrast with non-flow battery systems where the electrodes themselves are the electroactive material.

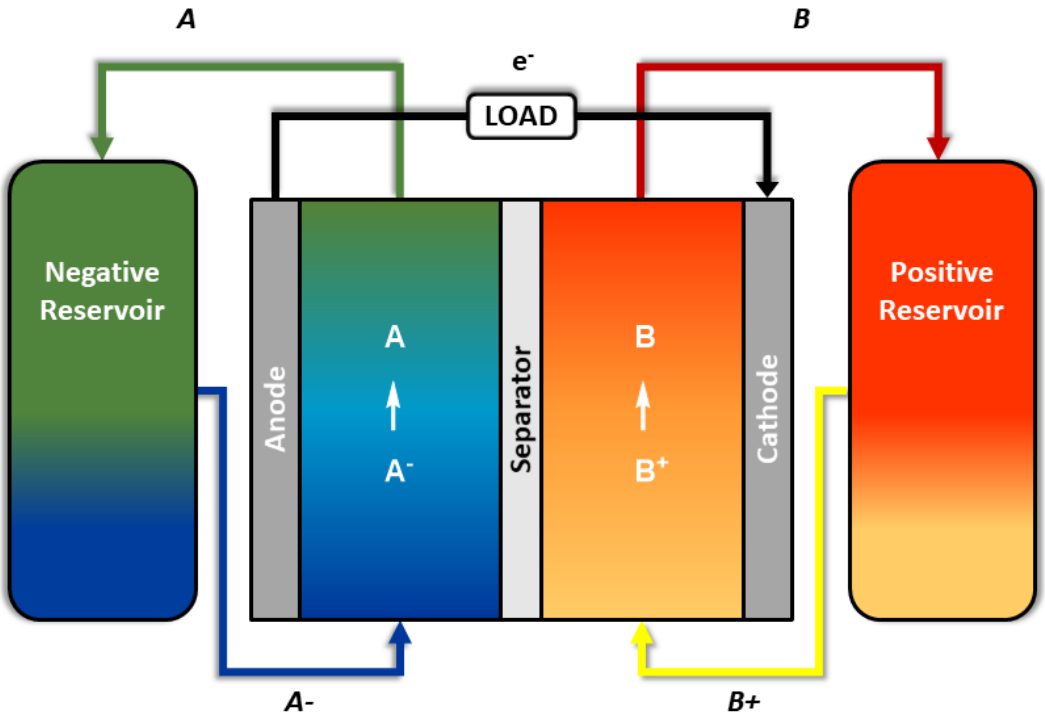

Figure 1.1. General operating principles of an asymmetric RFB.

The principal advantage of RFBs is that total energy and power densities are decoupled, meaning the charge/discharge rates of the cell can be varied to match the power flux of the grid by control of electrode surface area, while the energy capacity can be adjusted by control of the reservoir sizes.[18] Despite advantageous design characteristics, widespread commercialization of systems such as RFBs is hindered by an inadequate balance of performance and cost, rendering the cost uncompetitive with conventional Li-ion batteries ($80-$150/kWh).[8,19]

A significant portion of initial capital cost (up to ~20%) of RFBs and notable obstacle to widespread commercialization is the membrane which separates the catholyte and anolyte

compartments containing the negatively and positively charged redox-active components, respectively.[20] It serves to prevent self-discharge and allow migration of supporting electrolyte ions, while also preventing the mixing of catholyte and anolyte solutions, a commonly observed problem which leads to cumulative capacity fade and eventual cell degradation. While much research is currently focused on improving membrane performance[21], an alternative strategy of increasing cycle life and lowering cost involves the use of a symmetric electrolyte where the catholyte and anolyte contain the same redox-active components (Figure 1.2).[22–27]

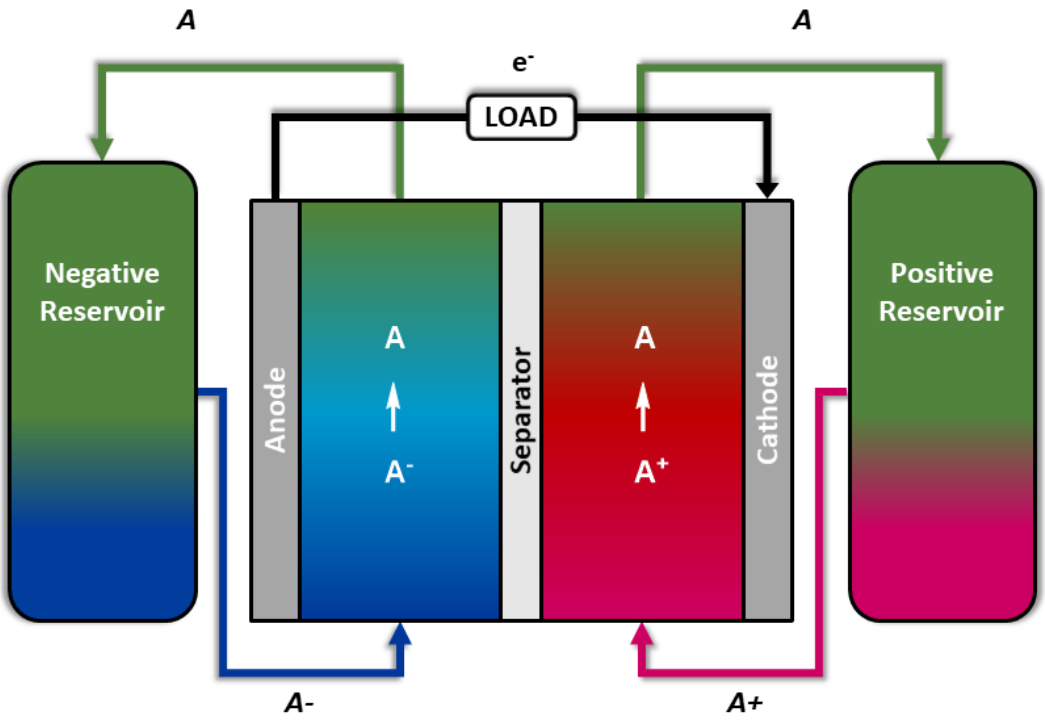

Figure 1.2. General operating principles of a symmetric RFB.

This both increases the cycle life by eliminating capacity fade due to membrane crossover of electroactive species and reduces the cost by substituting ion-exchange membranes with inexpensive porous membranes.[22] This is especially attractive for non-aqueous systems, as the majority of commercially available ion-exchange membranes are designed and optimized for use with aqueous systems, and suffer from poor conductivity in non-aqueous solvents.[21] Additionally, most non-aqueous RFBs operate at high potentials with charged carrier states potentially incompatible with ion-exchange membranes. Utilizing a chemically-inert, porous separator of known composition and morphology has the potential to eliminate membrane/charge carrier degradation pathways, and typically gives low resistance in non-aqueous solvents.[21,28] Despite these advantages, there are still only a few examples of symmetric charge carriers used for RFB applications, primarily due to the difficulty of developing complexes with that can be both reversibly oxidized and reduced in a stable manner and that are also economically-feasible.

1.2 Nuclear Power Production and Nuclear Waste Remediation

1.2.1 Overview

As discussed previously, a major limitation of renewable energy power production is the inherent intermittency of renewable energy sources, necessitating the need for grid-scale energy storage or an alternative method of producing consistent, base-load power.[29] One attractive base-load power source to supplement renewables is nuclear power.[30] Nuclear power currently accounts for ~20% of all electrical power produced in the U.S.[31], but widespread proliferation has been historically limited for a variety of concerns, including disposal of fissile byproducts, potential catastrophic failure of plants, and the national security danger associated with producing and using enriched fissile uranium.[32] Despite

these concerns, nuclear power is capable of providing large quantities of clean electrical energy as there is no combustion process to produce CO_2. It is widely recognized that increasing nuclear power development is a likely necessity to supplement renewable energy in an effort to reduce fossil fuel dependence. Indeed, despite hesitation by the U.S. to fully commit to expanding nuclear power, France has demonstrated that is feasible to safely provide a tremendous quantity of electrical energy in a safe manner, as currently 87% of French electricity is derived from fission.[33] Additionally, the design of smaller, modular reactors is currently underway, which is predicted to substantially streamline production of nuclear power plants and lower initial capital cost while simultaneously providing a much safer system than existing nuclear power plants.[34] As this reactor technology becomes available nuclear power is likely to experience a rapid growth in developed nations, but the concern of fissile waste disposal remains.[35]

1.2.2 Nuclear Waste Chelation and the PUREX Process

Despite the potential benefits of expanding nuclear power and a technological effort to design smaller/safer reactors, waste disposal remains a principle cause of nations that are refraining from producing new nuclear power plants.[35] One method of mitigating this concern is through nuclear waste reprocessing, in which uranium and plutonium are selectively extracted from spent fissile material and purified for further use.[36] This reduces the amount of nuclear waste produced, reducing disposal costs, and provides more fissile material for further use. Currently, reprocessing of spent nuclear fuel is performed through the industrial Plutonium and Uranium Reduction EXtraction (PUREX) process, which utilizes tributylphosphate in an organic phase to extract UO_2^{2+} and Pu^{IV} from a highly acidic aqueous phase.[36,37] While possible, this decades-old process is difficult and expensive.

Developing alternative methods of reprocessing could prove invaluable in advancing the proliferation of nuclear power and could prove of great importance to the long-term viability and safety of the nuclear energy sector.

1.3 Scope of Thesis

As will be described in this thesis, the primary objective of my graduate research was to examine 3d metal phthalocyanines as potential charge carrier candidates for symmetric redox flow batteries, and to better understand their electrochemical behavior (Chapter 2). In doing so, we made a fundamental discovery regarding the behavior and nature of phthalocyanine aromatic circuits through the synthesis and characterization of the first crystallographically-isolated phthalocyanine terminal nitride, a complex with extraordinary electrochemical stability and a highly unusual lack of reactivity for a nitride. This complex was demonstrated to be the first characterized example of a molecular species that can switch between aromatic, non-aromatic, and antiaromatic states without forming or breaking covalent bonds (Chapter 3). We proceed to demonstrate that this complex is capable as functioning as a charge carrier in a sediment-based symmetric redox flow battery, and discuss the electrochemical kinetics and stability in depth (Chapter 4). Finally, we leverage the knowledge and expertise developed during the flow battery project to design an elegant method for the reversible electrochemical capture and release of UO_2^{2+} ions from a biphasic system utilizing a novel carborane-based bidentate chelator, with the intent of further developing the system for nuclear waste remediation.

In Chapter 2, all compounds except **2.4**, **2.5**, and **2.8** were prepared and characterized by the author. **2.4** was prepared by Shannon Heinrich, **2.5** was prepared by Zongheng Wang, and **2.8** was prepared by both the author and Madeline Peterson. Matrix-assisted laser

desorption/ionization time-of-flight mass spectrometry (MALDI-TOF) was performed by Madeline Peterson for all compounds discussed. With the exception of elemental analyses and X-ray experiments, all synthetic, electrochemical, and characterization work in Chapter 3 and Chapter 4 were performed by the author. Computational analyses in Chapter 3 was performed by Prof. Steven Scheiner at Utah State University. The structure of compound **3.2**$^{2+}$ was collected by Tieyang Chang at ChemMatCARS at the University of Chicago. In chapter 5, the vast majority of the synthesis and characterization was performed by Megan Keener and Tim Carroll, and the electrochemistry was performed by the author and Megan Keener.

I would like to acknowledge that Chapter 2 is collaborative effort, for which I am incredibly grateful to Madeline Peterson, Zongheng Wang, and Shannon Heinrich for their expertise and efforts.

I would like to acknowledge that the work in Chapter 5 was started of Megan Keener, who was incredibly creative in developing this system. My role in this project was to take what I had learned about electrochemistry while working on flow batteries to aid in developing an electrochemical system in which we could demonstrate reversible capture and release of UO_2^{2+}, both in a monophasic and biphasic system. I would like to thank Megan and Gab for the opportunity to contribute to this work, and also to Tim Carroll, who was invaluable in finishing the synthetic portion of this project, and who really pioneered the development of the biphasic system.

At the time of this writing, portions of Chapter 2 are currently being prepared as a manuscript. Portions of Chapter 3 and Chapter 4 have been published. Portions of Chapter 5 have been accepted.

Chapter 2: Manuscript in preparation.

Chapter 3: Hunt, C.; Peterson, M.; Anderson, C.; Chang, T.; Wu, G.; Scheiner, S.; Ménard, G. *J. Am. Chem. Soc.* **2019**, *141* (6), 2604–2613.

Chapter 4: Hunt, C.; Mattejat, M.; Anderson, C.; Sepunaru, L.; Ménard, G. *ACS Appl. Energy Mater.* **2019**.

Chapter 5: Keener, M.; Hunt, C.; Kampel, V.; Dobrovetsky, R.; Hayton, T. W.; Ménard, G. Nature. **2019**. "Redox-Switchable Chelation for Uranium Capture and Release" *Accepted 10/1/2019.*

1.4 References

(1) Harvey, L. D. D. *Global warming*; Routledge: Abingdon, **2018**.

(2) *Global Energy and CO2 Status Report*; International Energy Agenecy, **2018**.

(3) Kellogg, W. W. *Climate change and society: consequences of increasing atmospheric carbon dioxide*; RoutledgeL Abingdon, **2019**.

(4) *Inventory of U.S. Greenhouse Gas Emissions and Sinks: 1990-2017, Executive Summary*; U.S. Environmental Protection Agency, **2019**.

(5) Haegel, N. M.; Margolis, R.; Buonassisi, T.; Feldman, D.; Froitzheim, A.; Garabedian, R.; Green, M.; Glunz, S.; Henning, H.-M.; Holder, B. *Science (80-.).* **2017**, *356* (6334), 141–143.

(6) Jones-Albertus, R.; Feldman, D.; Fu, R.; Horowitz, K.; Woodhouse, M. *Prog. Photovoltaics Res. Appl.* **2016**, *24* (9), 1272–1283.

(7) Haegel, N. M.; Atwater, H.; Barnes, T.; Breyer, C.; Burrell, A.; Chiang, Y.-M.; De Wolf, S.; Dimmler, B.; Feldman, D.; Glunz, S. *Science (80-.).* **2019**, *364* (6443), 836–838.

(8) Dunn, B.; Kamath, H.; Tarascon, J.-M. *Science (80-.).* **2011**, *334* (6058), 928–935.

(9) *Handbook of Energy Storage for Transmission and Distribution Applications*; Electric Power Research Institute & U.S. Department of Energy, **2003**.

(10) *Global Energy Storage Database Projects*; U.S. Department of Energy, **2019**.

(11) Lund, H.; Salgi, G. *Energy Convers. Manag.* **2009**, *50* (5), 1172–1179.

(12) Bolund, B.; Bernhoff, H.; Leijon, M. *Renew. Sustain. Energy Rev.* **2007**, *11* (2), 235–258.

(13) Sharma, A.; Tyagi, V. V.; Chen, C. R.; Buddhi, D. *Renew. Sustain. energy Rev.* **2009**, *13* (2), 318–345.

(14) Aho, A.; Antonietti, M.; Arndt, S.; Behrens, M.; Bill, E.; Brandner, A.; Centi, G.; Claus, P.; Cox, N.; DeBeer, S. *Chemical energy storage*; Walter de Gruyter, **2012**.

(15) Lawder, M. T.; Suthar, B.; Northrop, P. W. C.; De, S.; Hoff, C. M.; Leitermann, O.; Crow, M. L.; Santhanagopalan, S.; Subramanian, V. R. *Proc. IEEE* **2014**, *102* (6), 1014–1030.

(16) Alotto, P.; Guarnieri, M.; Moro, F. *Renew. Sustain. energy Rev.* **2014**, *29*, 325–335.

(17) Yang, Z.; Zhang, J.; Kintner-Meyer, M. C. W.; Lu, X.; Choi, D.; Lemmon, J. P.; Liu, J. *Chem. Rev.* **2011**, *111* (5), 3577–3613.

(18) Weber, A. Z.; Mench, M. M.; Meyers, J. P.; Ross, P. N.; Gostick, J. T.; Liu, Q. *J. Appl. Electrochem.* **2011**, *41* (10), 1137.

(19) Yoshio, M.; Brodd, R. J.; Kozawa, A. *Lithium-ion batteries*; Springer, **2009**; Vol. 1.

(20) Prifti, H.; Parasuraman, A.; Winardi, S.; Lim, T. M.; Skyllas-Kazacos, M. *Membranes* . **2012**.

(21) Shin, S.-H.; Yun, S.-H.; Moon, S.-H. *RSC Adv.* **2013**, *3* (24), 9095–9116.

(22) Potash, R. A.; McKone, J. R.; Conte, S.; Abruña, H. D. *J. Electrochem. Soc.* **2016**,

163 (3), A338–A344.

(23) Cabrera, P. J.; Yang, X.; Suttil, J. A.; Hawthorne, K. L.; Brooner, R. E. M.; Sanford, M. S.; Thompson, L. T. *J. Phys. Chem. C* **2015**, *119* (28), 15882–15889.

(24) Winsberg, J.; Stolze, C.; Muench, S.; Liedl, F.; Hager, M. D.; Schubert, U. S. *ACS Energy Lett.* **2016**, *1* (5), 976–980.

(25) Hagemann, T.; Winsberg, J.; Haupler, B.; Janoschka, T.; Gruber, J. J.; Wild, A.; Schubert, U. S. *NPG Asia Mater*. The Author(s) January 13, **2017**, p e340.

(26) VanGelder, L. E.; Kosswattaarachchi, A. [space]M.; Forrestel, P. L.; Cook, T. R.; Matson, E. M. *Chem. Sci.* **2018**, *9* (6), 1692–1699.

(27) Ma, T.; Pan, Z.; Miao, L.; Chen, C.; Han, M.; Shang, Z.; Chen, J. *Angew. Chemie Int. Ed.* **2018**, *57* (12), 3158–3162.

(28) Hendriks, K. H.; Robinson, S. G.; Braten, M. N.; Sevov, C. S.; Helms, B. A.; Sigman, M. S.; Minteer, S. D.; Sanford, M. S. *ACS Cent. Sci.* **2018**, *4* (2), 189–196.

(29) Barton, J. P.; Infield, D. G. *IEEE Trans. energy Convers.* **2004**, *19* (2), 441–448.

(30) Jenkins, J. D.; Zhou, Z.; Ponciroli, R.; Vilim, R. B.; Ganda, F.; De Sisternes, F.; Botterud, A. *Appl. Energy* **2018**, *222*, 872–884.

(31) Morgan, M. G.; Abdulla, A.; Ford, M. J.; Rath, M. *Proc. Natl. Acad. Sci.* **2018**, *115* (28), 7184–7189.

(32) Campbell, J. L. *Collapse of an industry: Nuclear power and the contradictions of US policy*; Cornell University Press, **2019**.

(33) Cany, C.; Mansilla, C.; Mathonnière, G.; Da Costa, P. *Energy* **2018**, *151*, 289–296.

(34) Abu-Khader, M. M. *Prog. Nucl. Energy* **2009**, *51* (2), 225–235.

(35) Pasqualetti, M. J. *Nuclear power: Assessing and managing hazardous technology*; Routledge, **2019**.

(36) Herbst, R. S.; Baron, P.; Nilsson, M. In *Advanced separation techniques for nuclear fuel reprocessing and radioactive waste treatment*; Elsevier, **2011**; pp 141–175.

(37) Paiva, A. P.; Malik, P. *J. Radioanal. Nucl. Chem.* **2004**, *261* (2), 485–496.

Chapter 2

Synthesis, Characterization, and Electrochemistry of a Series of Phthalocyanines

2.1 Introduction

Phthalocyanines (Pcs) are a well-studied class of easily-prepared macrocycle that exhibit excellent stability, rich electrochemistry, and useful optoelectronic properties.[1–3] Pcs share a structural similarity with porphyrins (Figure 2.1) including similar delocalized π-bonding networks, chemical behavior, and material properties.[4–6]

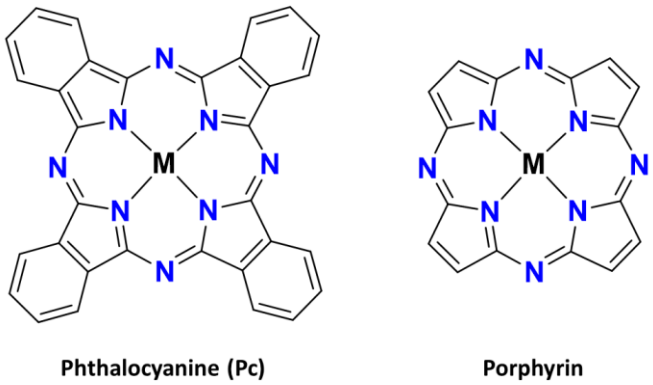

Figure 2.1. General structure of phthalocyanines (left) and porphyrins (right).

Pcs have found use in a variety of technologies for both their physical and chemical properties, including semiconductors[7–9], sensors[10–13], dyes/sensitizers[14–16], catalysts[17,18], and energy storage.[19–21] Despite their utility, design principles for how ligand substituent and choice of metal center affect the optoelectronic properties are still being developed. The role of ligand substitution is fairly well understood, and trends for how substitution on the aromatic periphery influences the optoelectronic properties have been developed through comparative series comprised of Pc rings with varying substitution patterns.[22–24] However, a direct analysis of the role of the metal center is often difficult due to the extremely diverse number of substituted Pcs in the literature, as a comparative analysis of a metal Pc series

with different substituents is inconclusive at best, misleading at worst. Developing a large, isostructural comparative series would aid in treating the metal center as a meaningful parameter space, and help understand the role of metal choice in the spatial and energetic position of the frontier orbitals, both important metrics to understand for virtually all optical, electronic, catalytic, and energy storage applications.[25,26] As our group has demonstrated in previous work[27], the key for drawing reliable conclusions from such a comparative series is the isolation of material that is of demonstratable high purity (i.e isolation of single crystals), followed by extensive experimental and computational characterization.

Here, we report an isostructural Pc 3d transition metal series containing VO, Cr, Fe, Co, Ni, and Cu as the central motif. We explore the structural properties through a combination of single crystal X-ray diffraction (XRD), UV-Vis, and cyclic voltammetry. The series is discussed within the context of a previously performed 3d phthalocyanine series computational analysis[28], and the electrochemistry reveals that many members of the series do not exhibit clean reversible redox events, whereas other members of the series do. As part of this study, we believe we have identified a key pattern: Phthalocyanines with non-labile terminal substituents appear to exhibit more reversible, well-defined electrochemistry when compared with their axially-bare counterparts, and also do not appear to exhibit non-diffusional electrochemical plating responses. This pattern may provide an important design principle for the development of Pc species with reversible electrochemistry, whether for optical, electronic, catalytic, or energy storage applications.

Below, we will discuss the general synthetic routes and routine characterization of each ^{EtO}PcM (^{EtO}Pc = 1,4,8,11,15,18,22,25-octaethoxy-Pc; M = HLi, H_2, VO, Cr, Fe, Co, Ni, Cu) species discussed, followed by an in-depth discussion of the structural and electrochemical properties of each species.

2.2 Results and Discussion

*2.2.1 Synthesis and Characterization of ^{EtO}PcHLi (**2.1**)*

The symmetrically substituted mono-lithiated Pc, Lithium 1,4,8,11,15,18,22,25-Octaethoxyphthalocyanine (**2.1**), was prepared by previously reported methods[27] with minor optimization (see Experimental). The monomeric precursor 3,6-diethoxyphthalonitrile is readily prepared by alkylation of 2,3-dicyanohydroquinone with ethyl iodide by a Williamson ether synthesis, and subsequent treatment of 3,6-diethoxyphthalonitrle in refluxing EtOH with excess Li^0 under an argon atmosphere resulted in a dark blue solution that was left at reflux for 5 days (Scheme 2.1, path i).

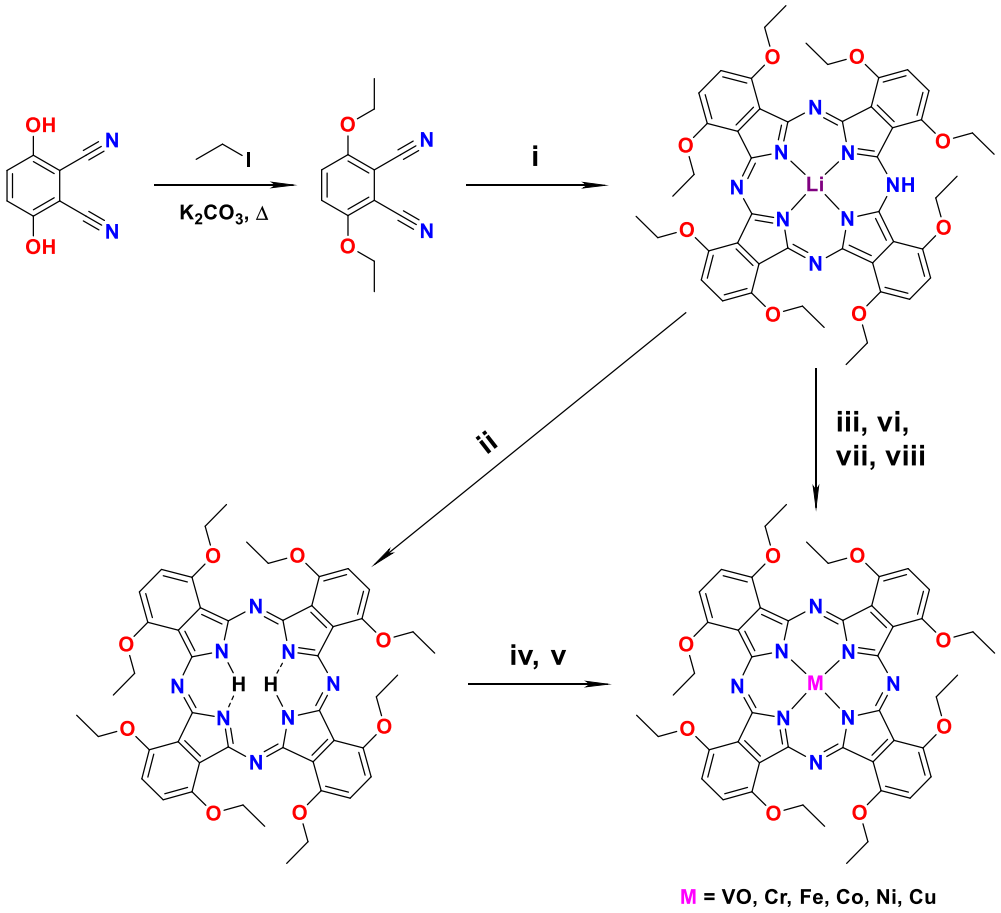

Scheme 2.1. Synthesis of all ^{EtO}PcM species discussed (M = HLi, H_2, VO, Cr, Fe, Co, Ni, Cu). i) Li^0, EtOH, reflux, 5 days; ii) HCl, H_2O, r.t., 2 days; iii) $VOSO_4(H_2O)_5$, $NaHCO_3$, DMF, 145 ^oC, 4 h; iv) $CrCl_2$, $NaHCO_3$, DMF, 100 ^oC, 5 h; v) $Fe(OAc)_2$, $C_6H_5CH_3$, reflux, 1 d; vi) $CoCl_2$, $NaHCO_3$, DMF, 145 ^oC, 4 h; vii) $NiCl_2$, $NaHCO_3$, DMF, 145 ^oC, 4 h; viii) $CuCl_2$, $NaHCO_3$, DMF, reflux, 20 h

Exposure of this solution to oxygen resulted in an immediate color change from dark blue to dark green. The blue coloration is presumably the mono-anion of **2.1**, produced by reduction from the excess Li^0. The generated macrocyclic **2.1** is a dark green solid with moderate solubility in CH_2Cl_2, and exhibits 2 strong absorbance bands in the red (Figure 2.1, λ_{max} = 723 nm; λ_{max} = 783 nm). Comparable splitting of spectral bands in porphyrin-based systems has been attributed to dimerization/aggregation[29–31], although here we cannot exclude the possible of reduced symmetry as the root cause of the splitting[32], which has been demonstrated with other porphyrinoids to split the e_g set of Gouterman's D_{4h}-derived four orbital model.[33] Given the ^{EtO}HLi is essentially pseudo-C_{2v} with a C_2-axis bisecting the site of protonation, it is not unreasonable to assume that the e_g set is split into the non-degenerate a_2 and b_1 set, similar to corroles, another C_{2v} porphyrinoid.

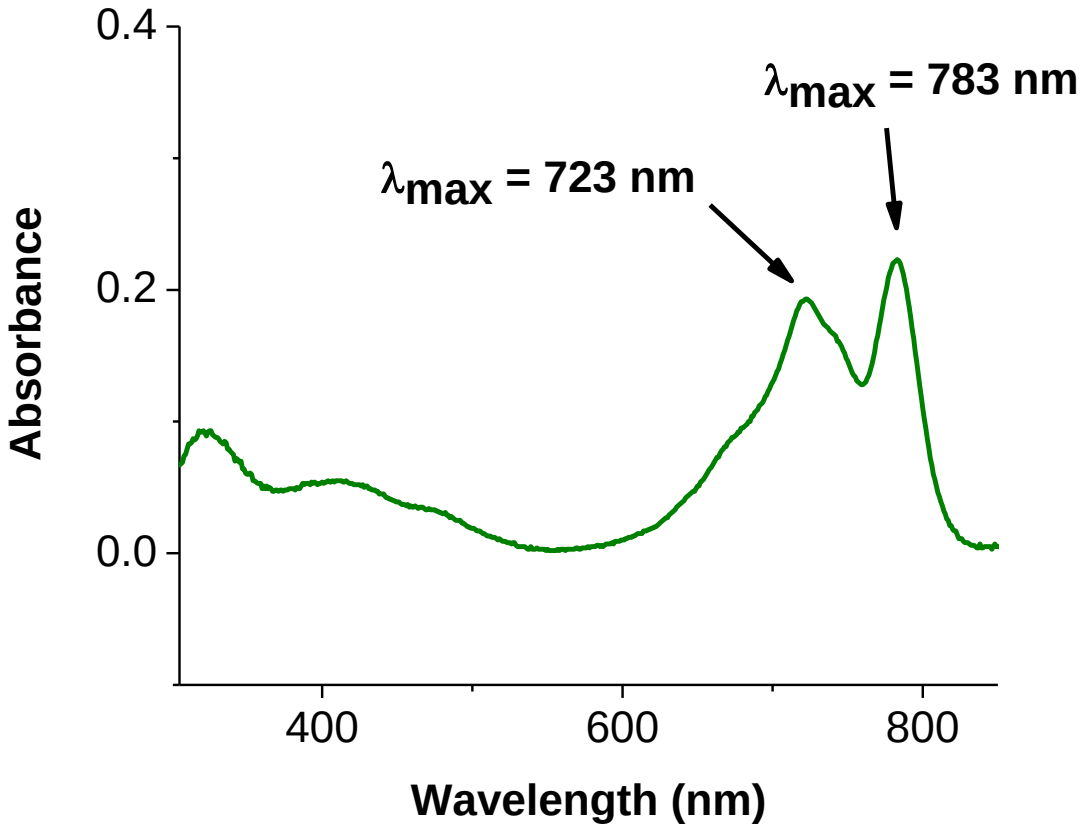

Figure 2.2. UV-Vis spectrum of **2.1** taken in CH_2Cl_2 (2.9 μM).

Trapezoidal single crystals of **2.1** suitable for XRD studies were grown by vapor diffusion of diethyl ether into a saturated solution of CH_2Cl_2, confirming the presence of Li in the central cavity (Figure 2.2).

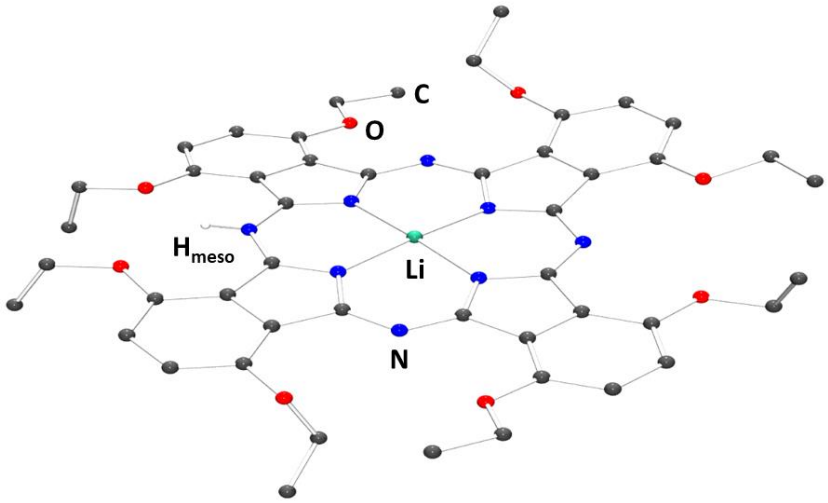

Figure 2.3. Solid-state molecular structure of **2.1**. Hydrogen atoms (excluding H_{meso}) and co-crystallized solvent are omitted for clarity.

Bond metrics of **2.1** are comparable (Table 2.9) to other reported metallophthalocyanine species with the same octa-ethoxy substitution pattern.[27,34] The diamagnetic species exhibits reduced symmetry in the ^{1}H NMR, and a far downfield singlet at 14.75 ppm, both of which suggests protonation of a meso/bridging nitrogen, illustrating the capacity of the mono-protonated Pc framework to act as a mono-anionic, L_3X-type macrocyclic ligand.

*2.2.2 Synthesis and Characterization of $^{EtO}PcH_2$ (**2.2**)*

2.2 could be obtained in high yield by treatment of an aqueous suspension of **2.1** with concentrated HCl over the course of several days (Scheme 2.1, path ii), which was tracked by ^{1}H NMR, gradually resolving the low-symmetry aromatic, methylene, and methyl signals of **2.1** into a well-defined singlet, quartet, and triplet (respectively) over 48 h (Figure 2.4).

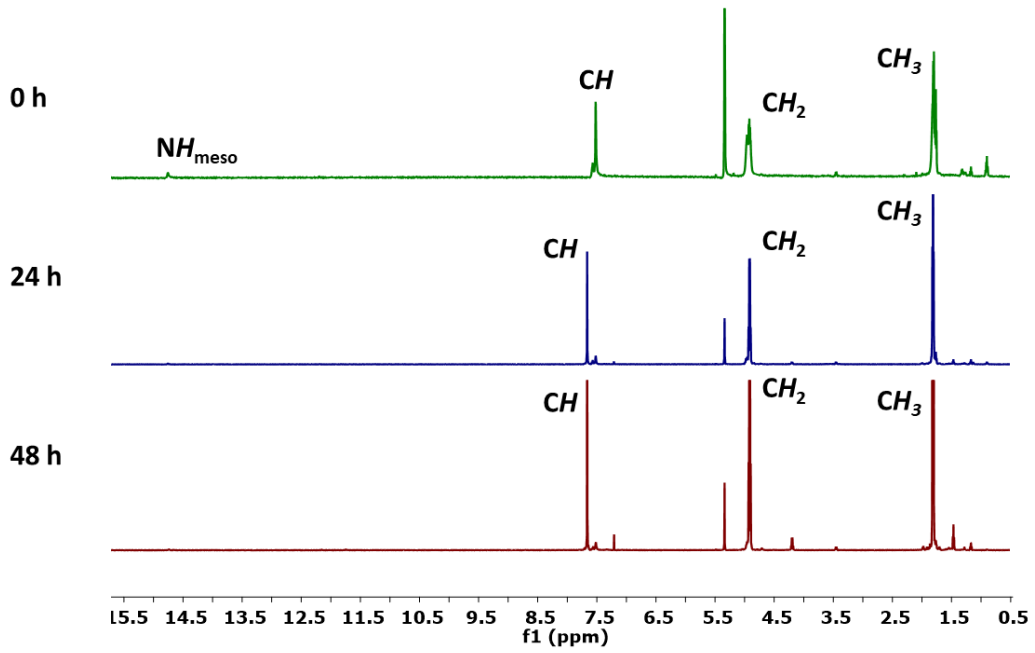

Figure 2.4. ^{1}H NMR spectra illustrating the HCl-induced conversion of **2.1** to **2.2** over 48 h, taken in CD_2Cl_2.

Square single crystals of **2.2** were grown in a similar manner as for **2.1**, by vapor diffusion of diethyl ether into a saturated solution of CH_2Cl_2, confirming the absence of any metal center (Figure 2.5).

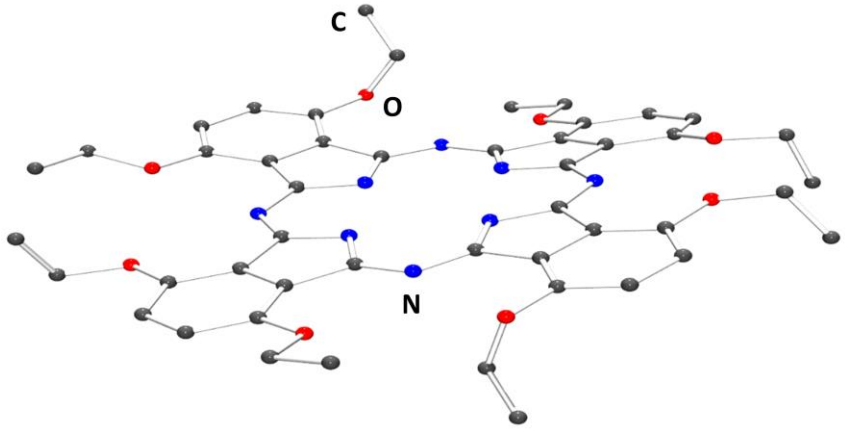

Figure 2.5. Solid-state molecular structure of **2.2**. Hydrogen atoms and co-crystallized solvent are omitted for clarity.

The dark green solid material has moderate solubility in CH_2Cl_2 with a slightly shifted absorbance relative to **2.1**, (Figure 2.6, λ_{max} = 770 nm).

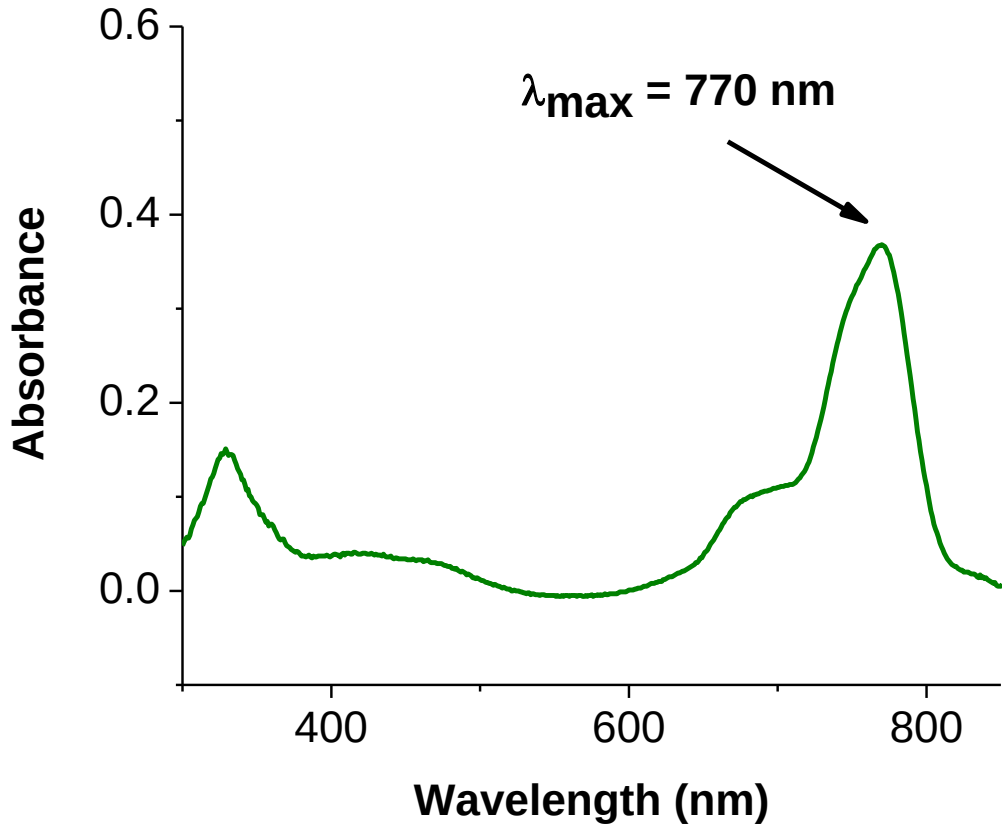

Figure 2.6. UV-Vis spectrum of **2.2** taken in CH_2Cl_2 (3.6 μM).

*2.2.3 Synthesis and Characterization of ^{EtO}PcVO (**2.3**)*

2.3 was prepared by previously reported methods[34] with minor optimization (see Experimental). A mixture of **2.1**, $VO(SO_4)*5H_2O$, and $NaHCO_3$ was heated to 145 °C in DMF for 4 h yielded a dark green product (Figure 2.7, λ_{max} = 786 nm) after purification (Scheme 2.1, path iii).

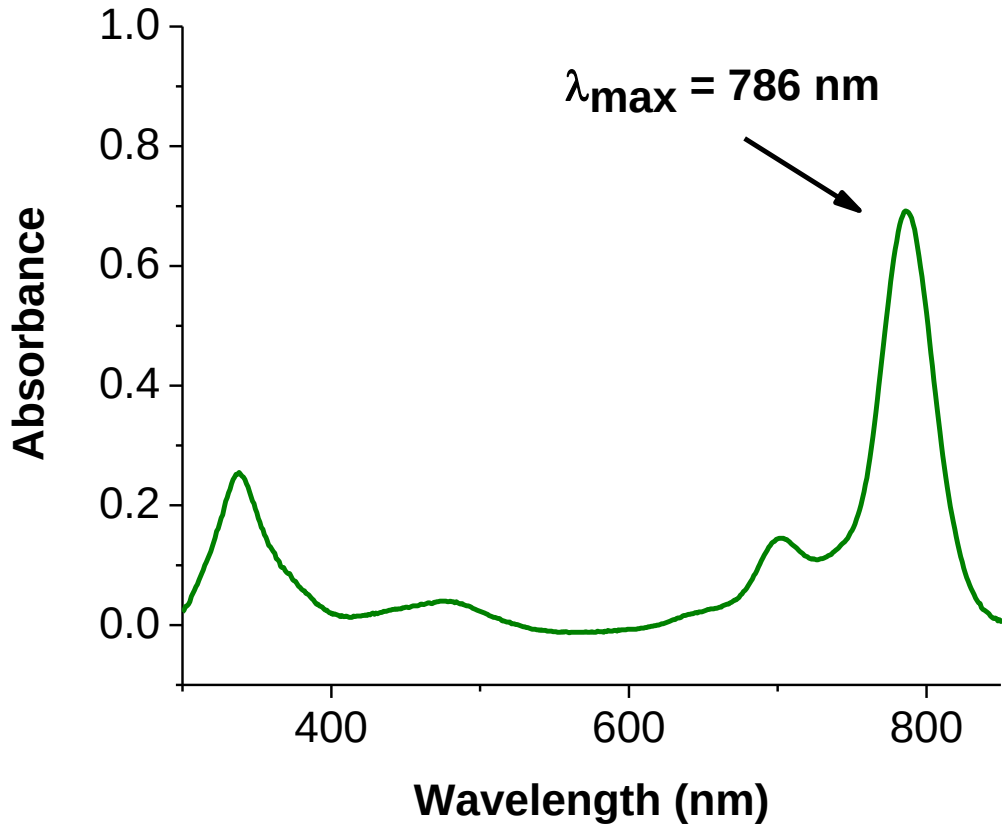

Figure 2.7. UV-Vis spectrum of **2.3** taken in CH_2Cl_2 (4.3 μM).

Single crystals suitable for XRD studies were grown by vapor diffusion of ether into a saturated solution of CH_2Cl_2, confirming the presence of the VO moiety in the central cavity of the Pc ring (Figure 2.8). The V=O bond in **2.3** is 1.593 Å, similar to other V=O bonds in comparable symmetry and oxidation state. Bond metrics of the central phthalocyanine ring were comparable to other Pc species described here (Table 2.11), although the ring is slightly bent out of plane (Figure 2.8). The central V(IV) atom is slightly puckered out of the ring plane by 0.545 Å, a common occurrence for vanadyl macrocyclic species.[35,36]

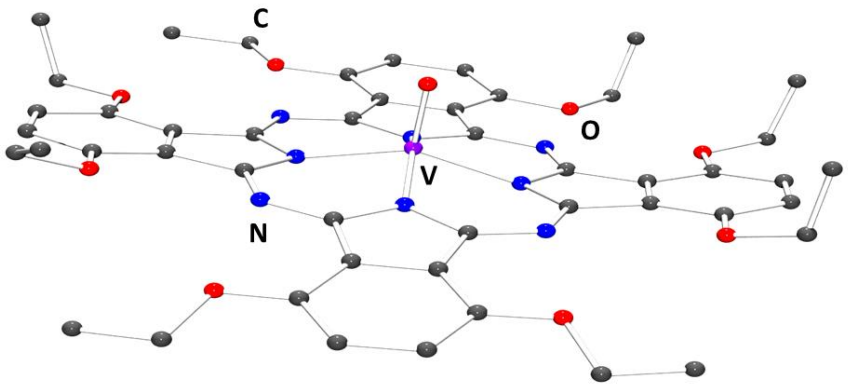

Figure 2.8. Solid-state molecular structure of **2.3**. Hydrogen atoms and co-crystallized solvent are omitted for clarity.

X-band EPR was performed on **2.3** in a frozen CH_2Cl_2 at 100 K, revealing an axial 8-line signal indicative of a d^1-system localized on V (Figure 2.9).

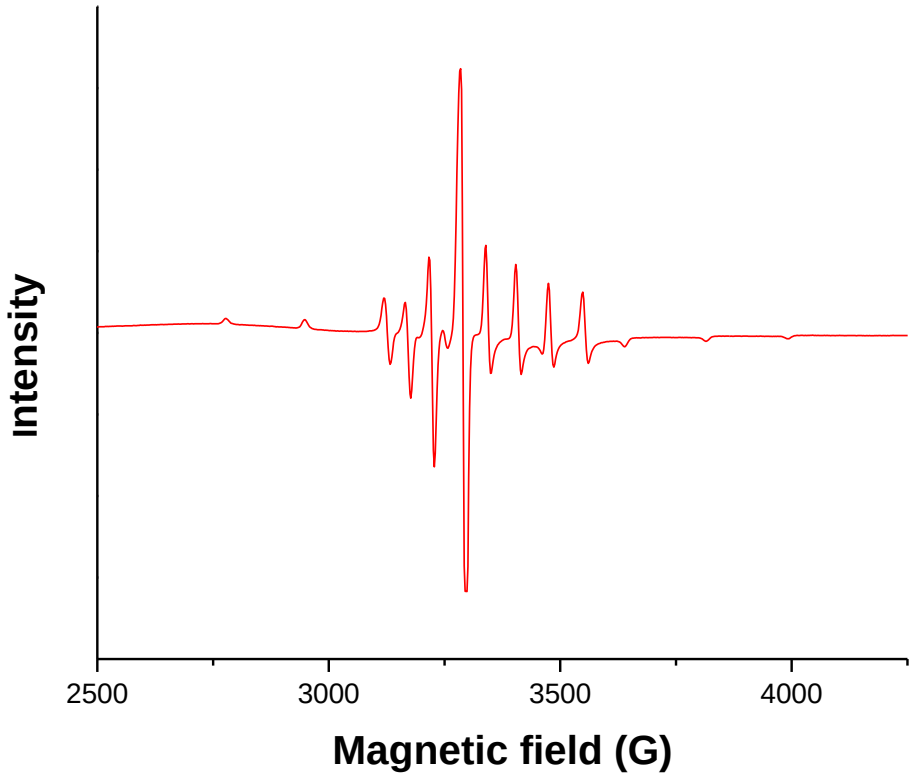

Figure 2.9. X-band EPR spectrum of **2.3** taken in CH_2Cl_2 at 100K.

Localization of the unpaired electron on the V center is also supported by the ^1H NMR spectrum in CD_2Cl_2 (Figure 2.10), which show weakly paramagnetically-broadened signals for the aromatic, methylene, and methyl peaks, but not silent as has been reported for delocalized Pc radicals reported in this ligand framework.[27]

*2.2.4 Synthesis and Characterization of ^{EtO}PcCr (**2.4**)*

2.4 was prepared under inert atmosphere using a similar methodology as for other metallophthalocyanine species. A mixture of **2.1**, $CrCl_2$, and $NaHCO_3$ was slurried with

DMF in a pressure vessel, sealed, and heated to 100 °C for 5 h, resulting in a dark blue-green product (Figure 2.11, λ_{max} = 771 nm) after purification (Scheme 2.1, path iv).

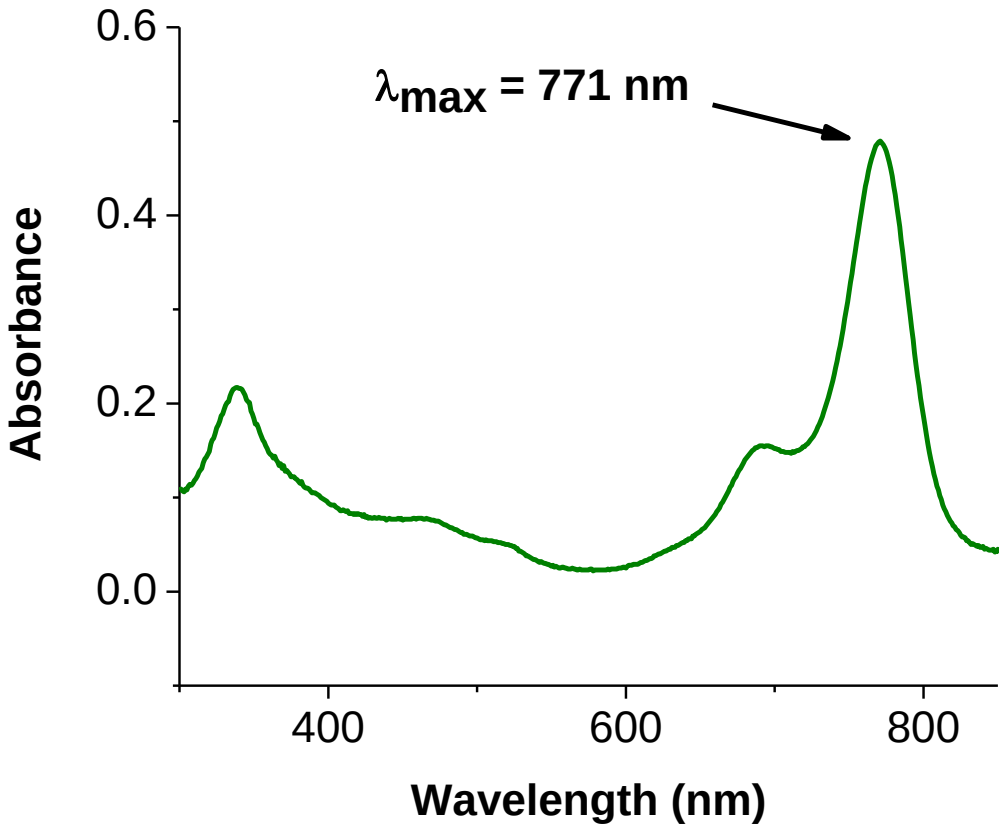

Figure 2.10. UV-Vis spectrum of **2.4** taken in CH_2Cl_2 (5.2 μM).

Single crystals suitable for XRD studies were grown by vapor diffusion of 2,2,4,4-methylpentane into a saturated solution of THF, revealing the presence of Cr with two axially coordinated THF molecules, with a Cr-O^{THF} distance of 2.062 Å (Figure 2.12).

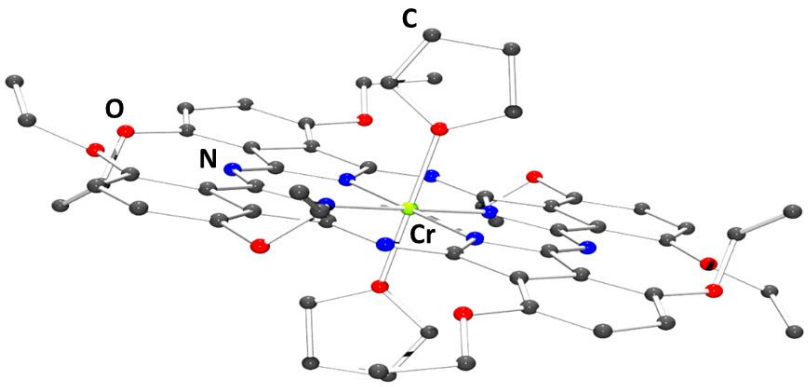

Figure 2.11. Solid-state molecular structure of **2.4**. Hydrogen atoms and co-crystallized solvent are omitted for clarity.

The dried, isolated crystals of **2.4** displayed a paramagnetically-broadened ^{1}H NMR signal, suggesting an intermediate or high spin d^4 system (Figure 2.13).

*2.2.5 Synthesis and Characterization of ^{EtO}PcFe (**2.5**)*

2.5 was prepared under inert atmosphere using a similar methodology as for other metallophthalocyanine species. A mixture of **2.2** and $Fe(OAc)_2$ was heated to reflux in toulene for 24 h yielded a dark green powder (Figure 2.14, λ_{max} = 765 nm) after purification (Scheme 2.1, path v).

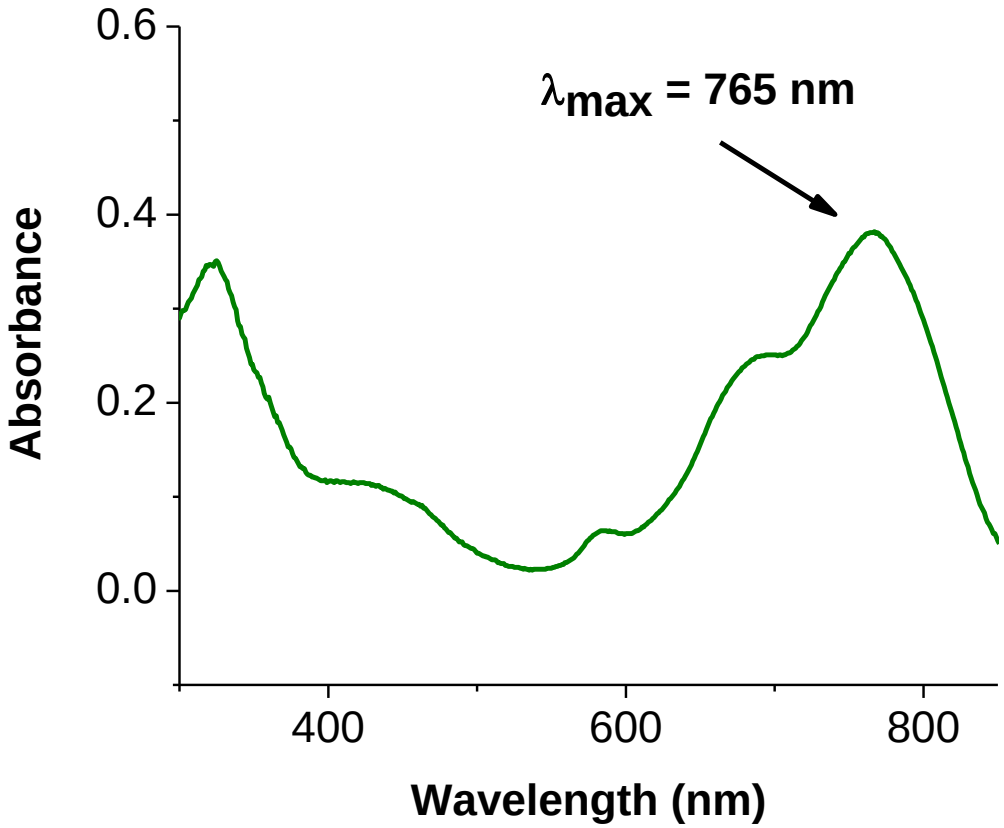

Figure 2.12. UV-Vis spectrum of **2.5** taken in CH_2Cl_2 (9.1 μM).

Single crystals suitable for XRD studies were grown by vapor diffusion of diethyl ether into a saturated solution of CH_2Cl_2, revealing the presence of Fe in the central cavity with no axial substituents (Figure 2.15).

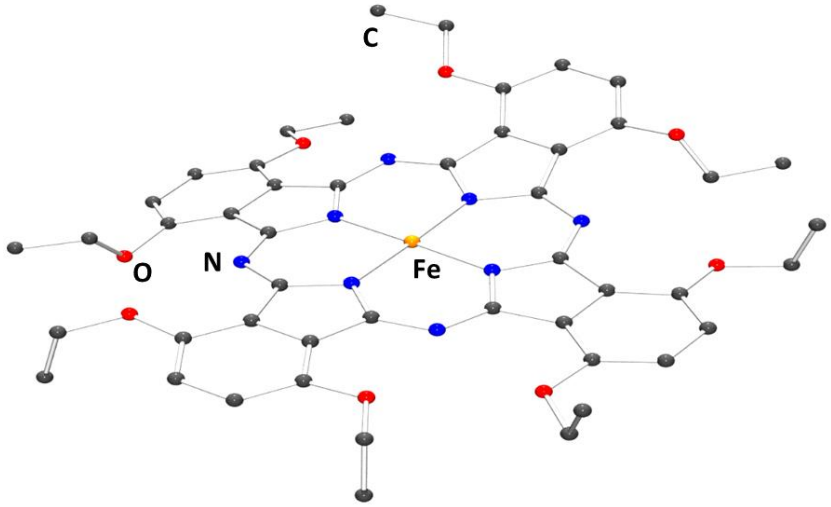

Figure 2.13. Solid-state molecular structure of **2.5**. Hydrogen atoms and co-crystallized solvent are omitted for clarity.

The isolated crystals of **2.5** displayed a paramagnetically-shifted ^{1}H NMR spectrum, with an aromatic singlet at 3.44 ppm, a methylene triplet at 4.32 ppm, and a methyl quartet at 9.90 ppm. The unusual position of the aromatic and methyl resonances is consistent with a paramagnetically-shifted spectrum (Figure 2.16), suggesting an intermediate or high spin d^6 Fe center. These atypical ^{1}H NMR assignments are supported by both ^{1}H-^{1}H Correlation Spectroscopy (COSY; Figure 2.17), although it is unclear why the signals are well resolved and residing within a traditional diamagnetic window.

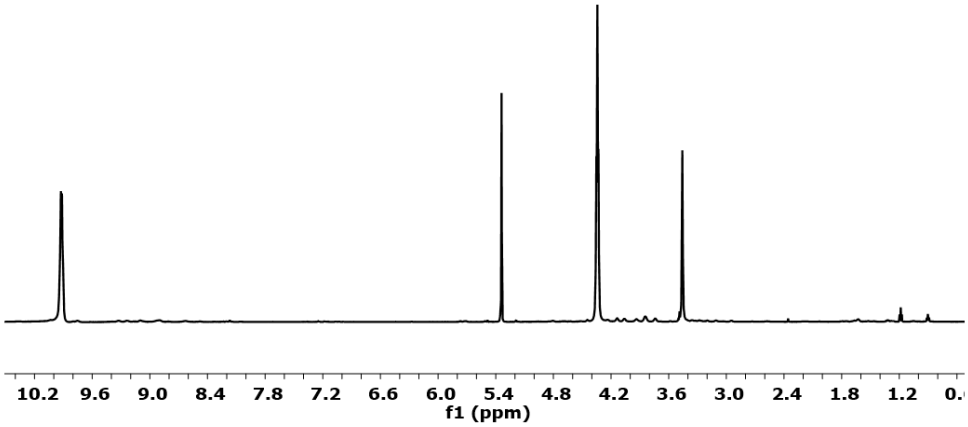

Figure 2.14. ^{1}H NMR spectrum of **2.5**, taken in CD_2Cl_2.

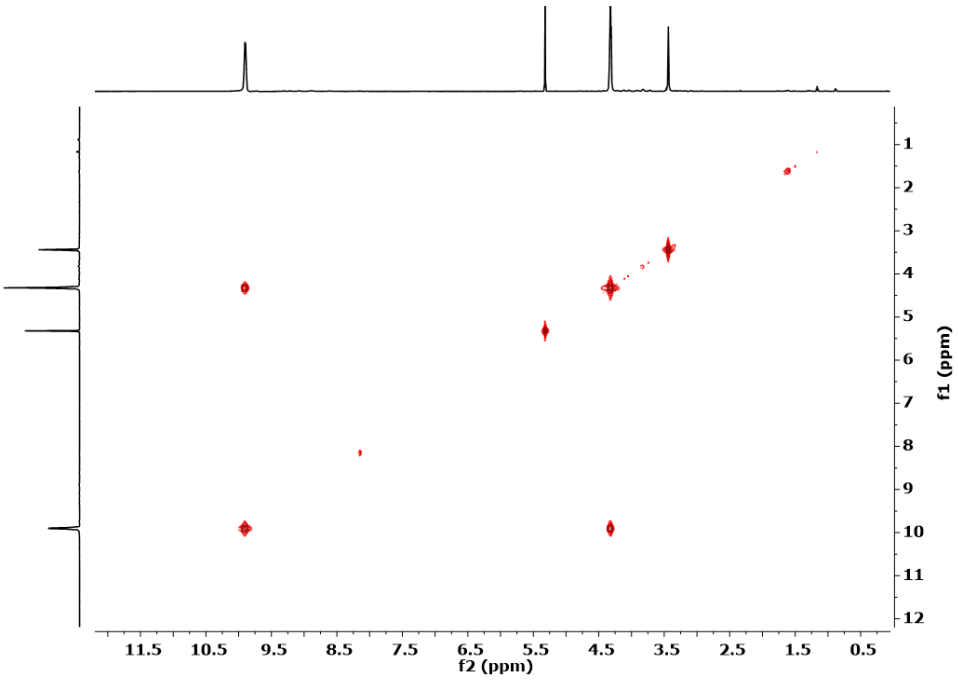

Figure 2.15. COSY NMR spectrum of **2.5**, taken in CD_2Cl_2.

Zero-field ^{57}Fe Mössbauer spectroscopic measurements revealed a quadrupole doublet with an isomer shift value at δ = 0.33 mm*s^{-1} with a quadrupole splitting value of 1.37 mm*s^{-1}. The isomer shift is intermediate between a low-spin and high-spin Fe(II), consistent with the spin assignment of unsubstituted Fe(II) phthalocyanines (Figure 2.18).[37]

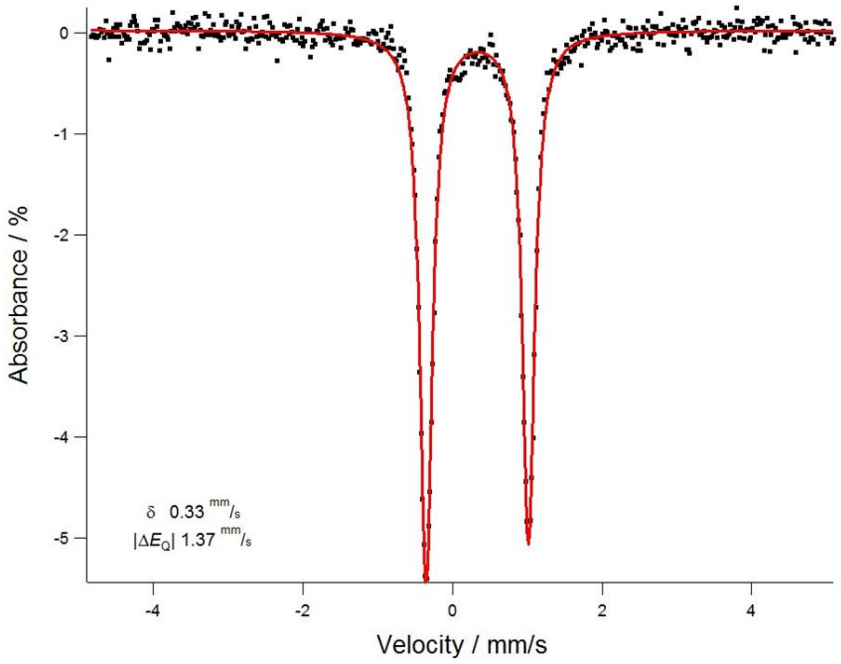

Figure 2.16. Mössbauer spectrum of **2.5**, with isomer shift and quadrupole splitting values (lower left). Taken at 100 K.

*2.2.6 Synthesis and Characterization of ^{EtO}PcCo (**2.6**)*

2.6 was prepared under an inert atmosphere using a similar methodology as for other metallophthalocyanine species. A mixture of **2.1**, $CoCl_2$, and $NaHCO_3$ was heated to reflux in DMF for 4 h yielded a dark blue-green product (Figure 2.19, λ_{max} = 738 nm) after purification (Scheme 2.1, path vi).

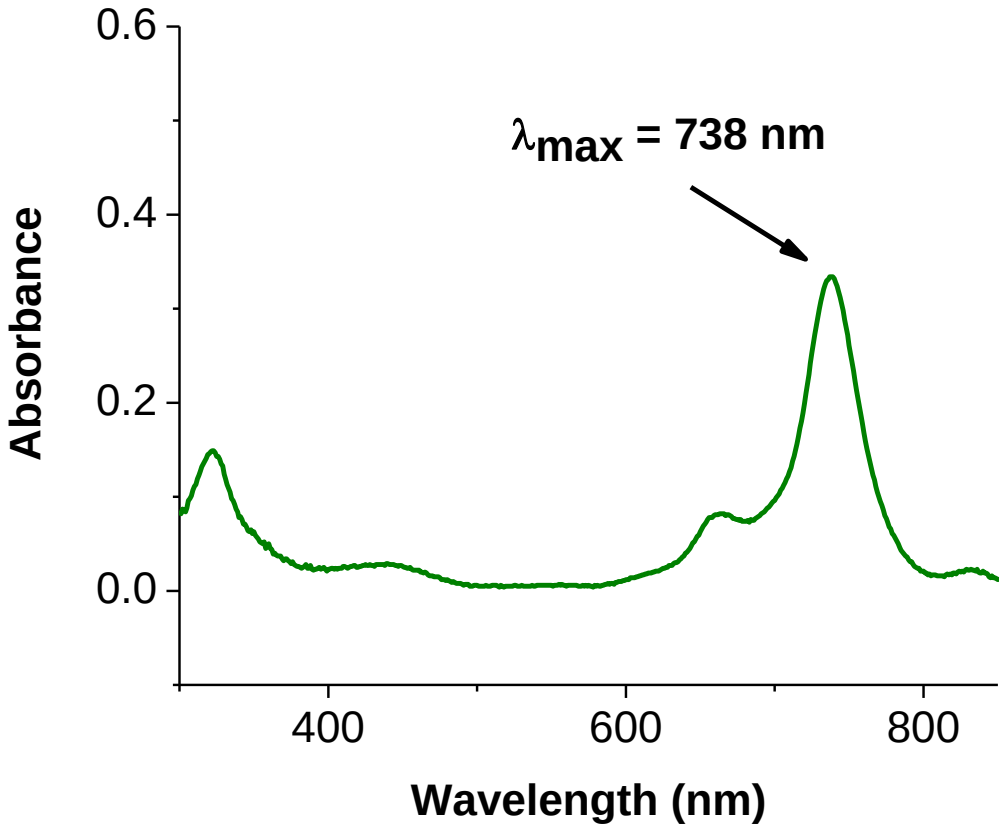

Figure 2.17. UV-Vis spectrum of **2.6** taken in CH_2Cl_2 (11.6 μM).

Single crystals suitable for XRD studies were grown by vapor diffusion of diethyl ether into a saturated solution of CH_2Cl_2, revealing the presence of Co in the central cavity with no axial substituents (Figure 2.20).

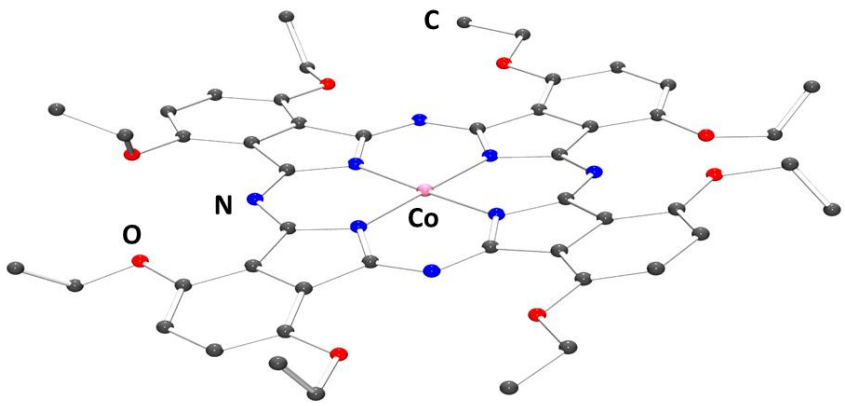

Figure 2.18. Solid-state molecular structure of **2.6**. Hydrogen atoms and co-crystallized solvent are omitted for clarity.

The isolated crystals of **2.6** exhibited a surprising sharp reduction in solubility in CH_2Cl_2 in comparison to the powder product, prohibiting collection of the ^1H NMR in CD_2Cl_2. However, the crystalline product was sparingly soluble in THF-d_8, and displayed a paramagnetically-broadened ^1H NMR signal (Figure 2.21).

*2.2.7 Synthesis and Characterization of ^{EtO}PcNi (**2.7**)*

2.7 was prepared using a similar method as previously reported. A mixture of **2.1**, $NiCl_2$, and $NaHCO_3$ in heated to 145 ^oC in DMF for 4 h yielded a dark green product (Figure 2.22, λ_{max} = 742 nm) after purification (Scheme 2.1, path vii).

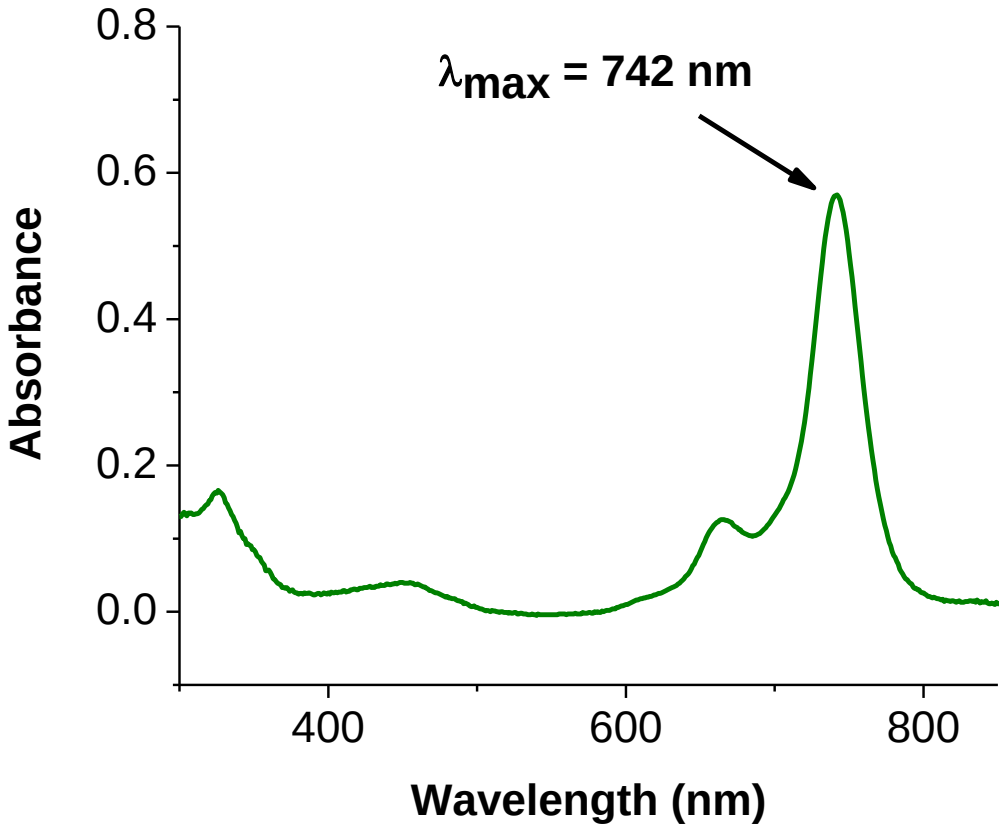

Figure 2.19. UV-Vis spectrum of **2.7** taken in CH_2Cl_2 (4.7 μM).

Single crystals suitable for XRD studies were grown by vapor diffusion of ether into a saturated solution of CH_2Cl_2, confirming the presence of Ni metal in the central cavity of the Pc ring (Figure 2.23). Bond metrics of the central phthalocyanine ring were comparable to other Pc species described here.

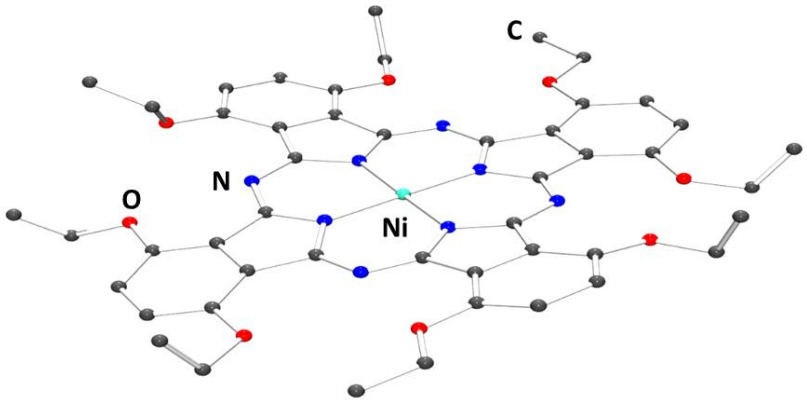

Figure 2.20. Solid-state molecular structure of **2.7**. Hydrogen atoms and co-crystallized solvent are omitted for clarity.

The ^{1}H NMR taken CD_2Cl_2 reveals three broad signals in the diamagnetic region, suggesting either an intermediate or high spin system localized on the Ni center (Figure 2.24), similar to **2.3**.

*2.2.8 Synthesis and Characterization of ^{EtO}PcCu (**2.8**)*

2.8 was prepared in similar manner to previously reported methods. A mixture of **2.1**, $CuCl_2$, and $NaHCO_3$ in heated to 145 ^{o}C in DMF for 4 h yielded a dark green product (Figure 2.25, λ_{max} = 750 nm) after purification (Scheme 2.1, path viii).

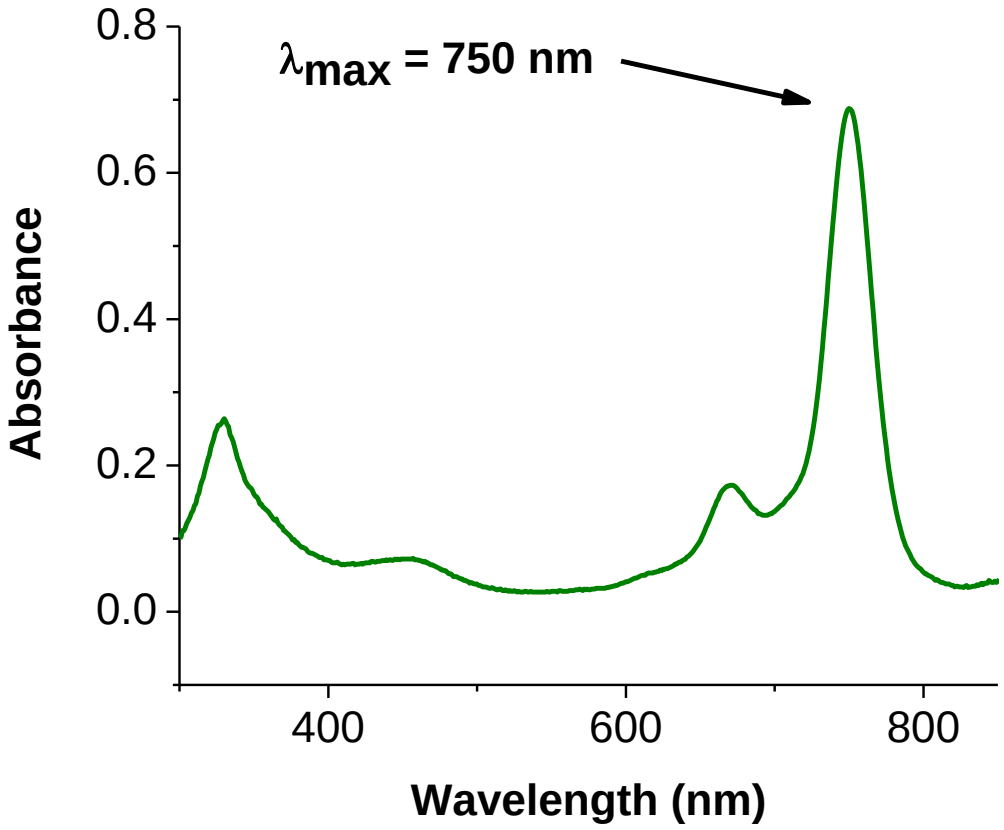

Figure 2.21. UV-Vis spectrum of **2.8** taken in CH_2Cl_2 (9.5 μM).

The ^1H NMR taken CD_2Cl_2 reveals three broad signals in the diamagnetic region, suggesting an intermediate or high spin system localized on the Cu center (Figure 2.26), similar to **2.3**. X-band EPR was performed on **2.8** in a frozen CH_2Cl_2 at 100 K, revealing a rhombic 8-line signal indicative of a d^1-system localized on V (Figure 2.27).

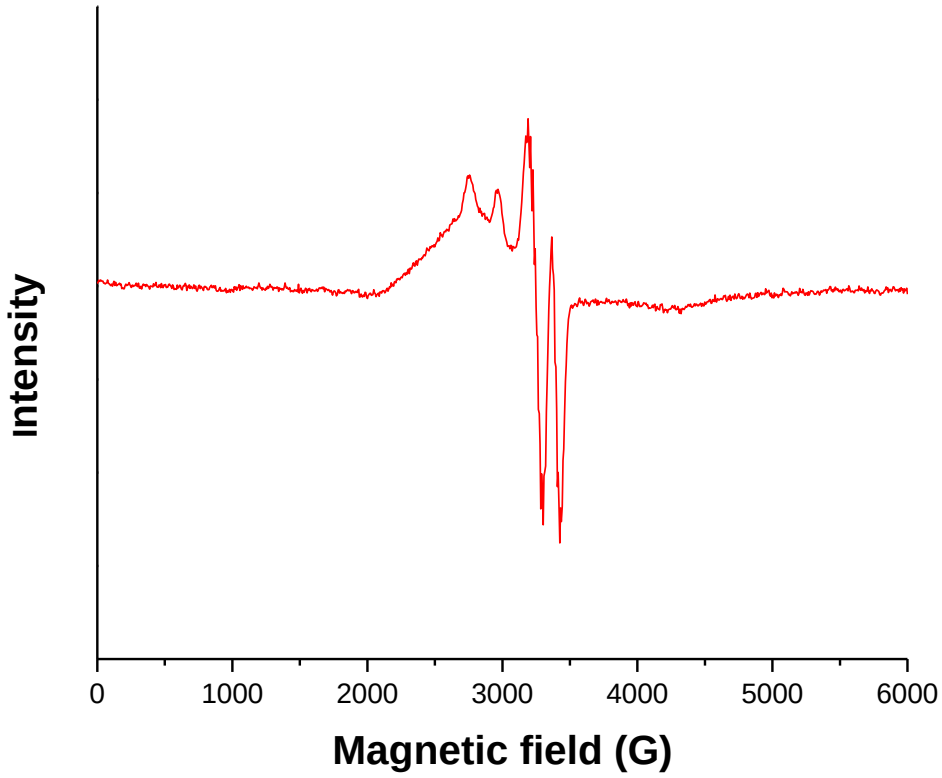

Figure 2.22. X-band EPR spectrum of **2.8** taken in CH_2Cl_2 at 100K.

2.2.9 Electrochemistry

The electrochemistry of all isolated ^{EtO}PcM (M = HLi, H_2, VO, Cr, Fe, Co, Ni, Cu) species was investigated to gain an understanding of the effect of the central metal atom on the electrochemical profile. As will be seen in the following chapter, we have demonstrated the electrochemical properties of this particular ligand framework with ^{EtO}PcMnN (**3.2**), in which a central Mn(V)≡N acted as a inert motif that allowed isolation of all available redox states of the ring, spanning Pc(0)-Pc(4-).[27] Previous computational reports seem to suggest that the HOMO-LUMO position will shift from metal-centered for early 3d metals to ring centered for late 3d metals.[28] The electrochemistry of phthalocyanines has been explored in

depth,[38,39] but doing so with a crystallography-isolated metal series of demonstratable purity with identical ring substitution patterns for all metals is critical to begin drawing meaningful conclusions regarding the role of the metal center on the electrochemical profile.

First, cyclic voltammetry (CV) was performed on **2.1** and **2.2** to examine the behavior in the absence of a redox-active metal and in the absence of any metal, respectively. All CVs discussed were performed under inert atmosphere and reference versus an internal Fc/Fc^{+} couple (See Experimental for full conditions), and $E_p(X)$ denotes the peak potential of the event at a scan rate of X V/s. The CV of **2.1** in CH_2Cl_2 revealed one quasi-reversible reduction centered at $E_p(0.5)$ = -1.54 V and two quasi-reversible oxidations at $E_p(0.5)$ = -0.13 V and $E_p(0.5)$ = 0.27 V (Figure 2.28)

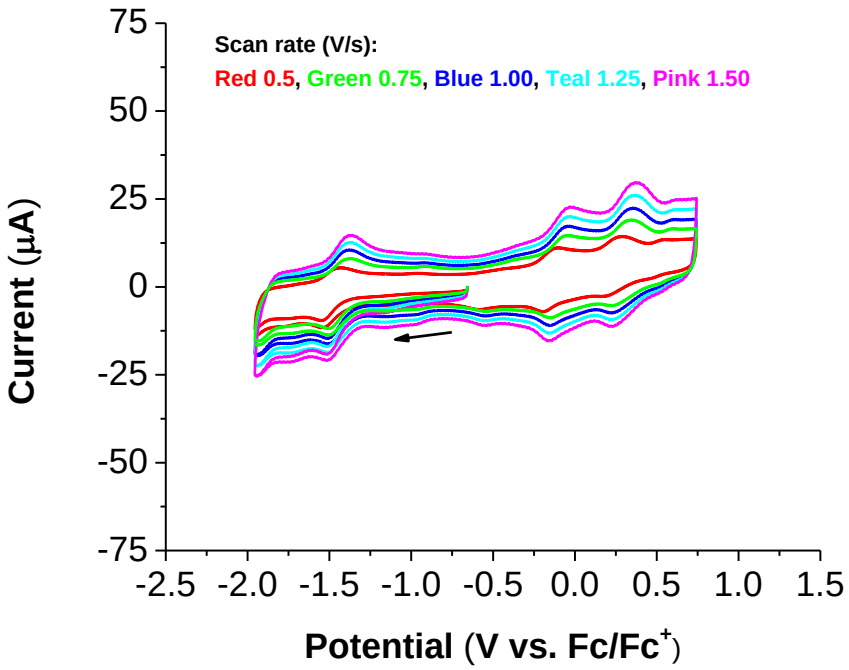

Figure 2.23. CVs of **2.1** at varying scan rates (inset). Experimental conditions: Taken in CH_2Cl_2 with 0.53 mM of **2.1**, 0.1 M of $[Bu_4N][PF_6]$, 3 mm diameter glassy carbon working

electrode, Pt wire counter electrode, and Pt wire pseudo-reference electrode. Internally referenced to Fc/Fc^{+}.

Further negative expansion of the window revealed a large irreversible current response. The lack a second quasi-reversible event is not unexpected, as there is a proton that can reasonably be expected to undergo reduction in a similar potential regime. It should be noted that the current response is fairly low for the concentration, possible due to dimerization or aggregation effects previously suggested to be responsible for the spectral band-splitting observed in the UV-Vis (Figure 2.1). As will be discussed below, aggregation effects are a suspected cause of the reduced electrochemical reversibility observed in ^{EtO}PcM species lacking non-labile axial substituents.

The CV of **2.2** also displays a series of quasi-reversible reductions and oxidations (Figure 2.29). The first reduction occurs at $E_p(0.5)$ = -1.49 V, and unlike **2.1** there is a second observable quasi-reduction at $E_p(0.5)$ = -1.83 V. We postulate that the protons in **2.2** primarily reside with the central cavity of the Pc ring, and it has been previously suggested that these interior protons are shared between multiple basic sites as a fast-switching tautomer.[40] Within this context, we propose that the pkA of the protic H atoms in **2.2** is increased due to the stabilizing effect of being located in the central cavity[41] and having bonding interactions with multiple N atoms, resulting in proton reduction occurring beyond the second reduction event, in contrast with **2.1** where the protic H atom resides outside the central cavity.

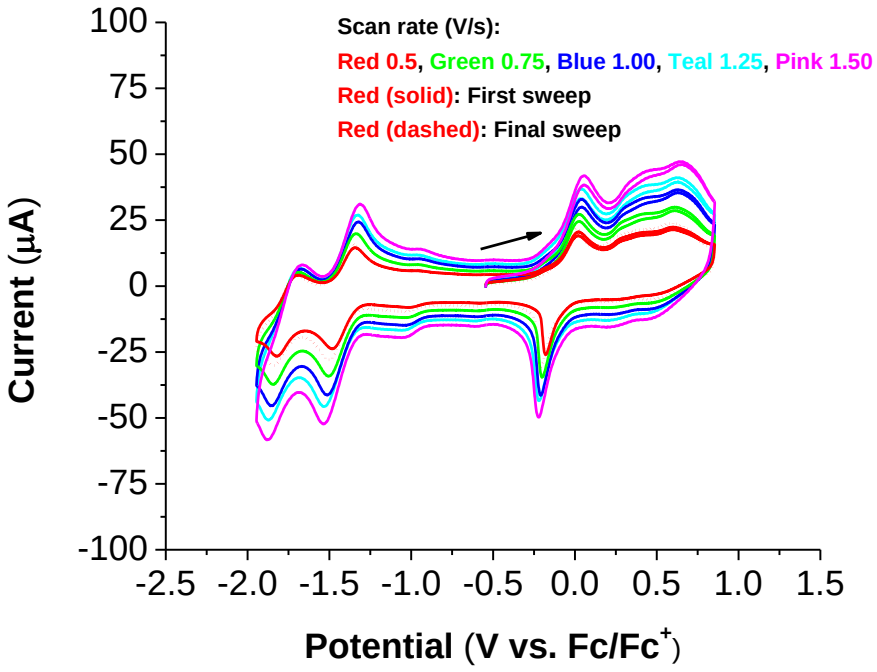

Figure 2.24. CVs of **2.2** at varying scan rates (inset). Experimental conditions: Taken in CH_2Cl_2 with 0.53 mM of **2.2**, 0.1 M of $[Bu_4N][PF_6]$, 3 mm diameter glassy carbon working electrode, Pt wire counter electrode, and Pt wire pseudo-reference electrode. Internally referenced to Fc/Fc^+.

The oxidative side of **2.2** exhibits a broad quasi-reversible oxidation at $E_p(0.5)$ = 0.52 V, followed by an exceedingly broad oxidation response that is unassigned. The return sweep of the oxidative profile gives what appears to be a non-diffusional response at $E_p(0.5)$ = -0.18 V, possibly indicating that the broad feature evident on the oxidative sweep is some form of deposition event (Figure 2.29). This non-diffusional return sweep does not grow in response with multiple scans, indicating if the broad oxidative feature is film deposition, it is readily removed on the return sweep.

While the ^{EtO}Pc framework does not exhibit highly reversible with a redox-innocent metal (**2.1**) or no metal (**2.2**), it does exhibit highly reversible electrochemistry with **2.3**, displaying two quasi-reversible reductions with $E_p(0.5)$ = -1.29 V and $E_p(0.5)$ = -1.65 V, and two quasi-reversible oxidations at $E_p(0.5)$ = 0.12 V and $E_p(0.5)$ = 0.55 V. Interestingly, this electrochemical response (Figure 2.30) is almost identical to that of ^{EtO}PcMnN, for which it was demonstrated that all reduction and oxidation events were ring-centered.[27] As previously mentioned, it has been suggested that dimerization/aggregation is a major factor in reducing the reversibility of redox events for phthalocyanines, and we suspect the non-labile terminal substituent of both **2.3** and ^{EtO}PcMnN coupled with the stable metal oxidation state play a major role in the reversibility of their electrochemical profile.

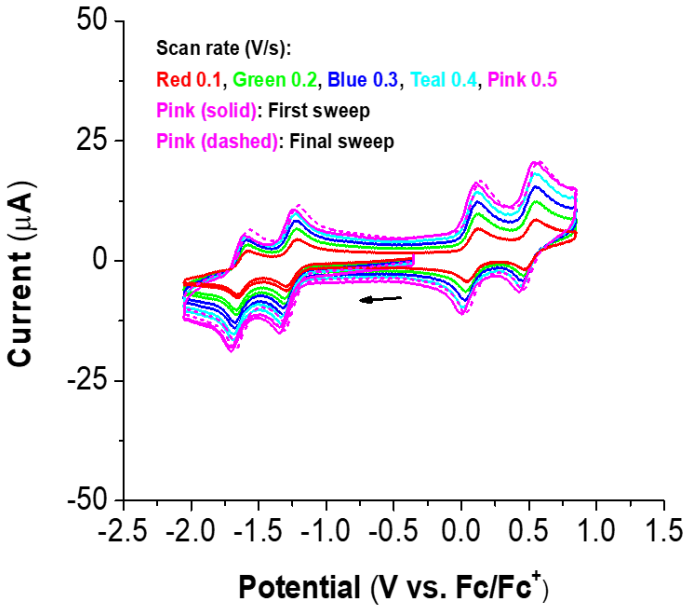

Figure 2.25. CVs of **2.3** at varying scan rates (inset). Experimental conditions: Taken in CH_2Cl_2 with 0.45 mM of **2.3**, 0.1 M of $[Bu_4N][PF_6]$, 3 mm diameter glassy carbon working electrode, Pt wire counter electrode, and Pt wire pseudo-reference electrode. Internally referenced to Fc/Fc^+.

Similar to **2.1**, isolated **2.4** exhibits a series of quasi-reversible events (Figure 2.31), all of which exhibit a fairly low current response, with a number of poorly defined and/or overlapping reductive events. Assignment of accurate E_p values for these redox features is made difficult due to the low current response and overlapping nature of the events. Additionally, the events cannot be definitely assigned as either ring- or metal-centered, due to the presence of a redox-active Fe center and the non-innocent Pc ligand.

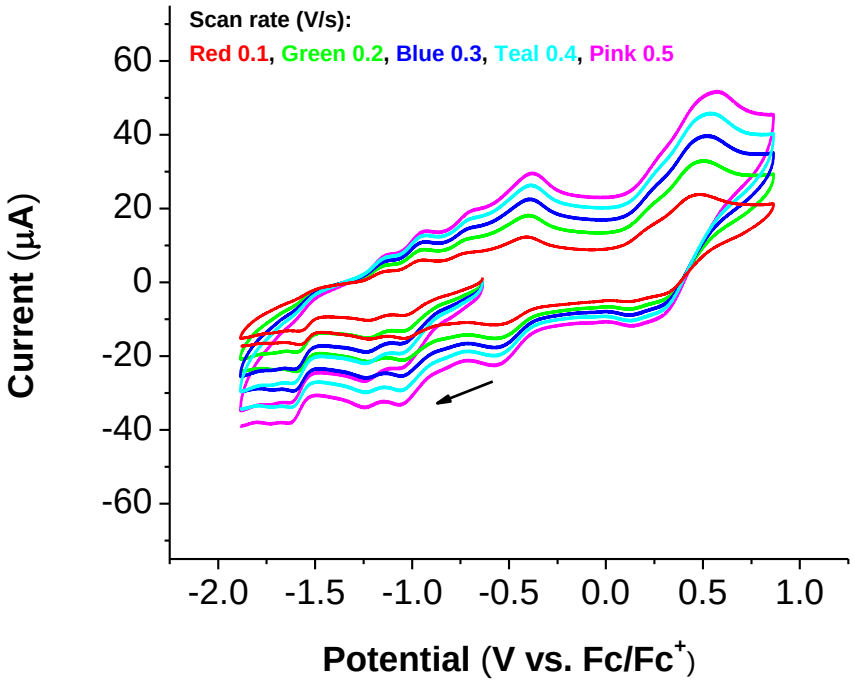

Figure 2.26. CVs of **2.4** at varying scan rates (inset). Experimental conditions: Taken in CH_2Cl_2 with 0.59 mM of **2.4**, 0.1 M of $[Bu_4N][PF_6]$, 3 mm diameter glassy carbon working electrode, Pt wire counter electrode, and Pt wire pseudo-reference electrode. Internally referenced to Fc/Fc^+.

Similar to both **2.1** and **2.4**, **2.5** exhibits a series of quasi-reversible events (Figure 2.32). As with **2.4**, definitive assignment of these reduction events as ring- or metal-centered is not possible due to the presence of a redox-active metal and non-innocent ligand. There are two clear reductive events occurring at $E_p(0.1)$ = -1.60 V and $E_p(0.1)$ = -2.25 V, and three overlapping oxidative events at $E_p(0.1)$ = -0.09 V, $E_p(0.1)$ = 0.42 V, and $E_p(0.1)$ = 0.78 V. Given the similarity in potential with **2.3** and ^{EtO}PcMnN, it is possible that both reductions are dominantly ring-centered and that two of the oxidations are also ring-centered, with the third representing the Fe(II)/Fe(III) couple, but more definitive evidence would be needed to make this assertion.

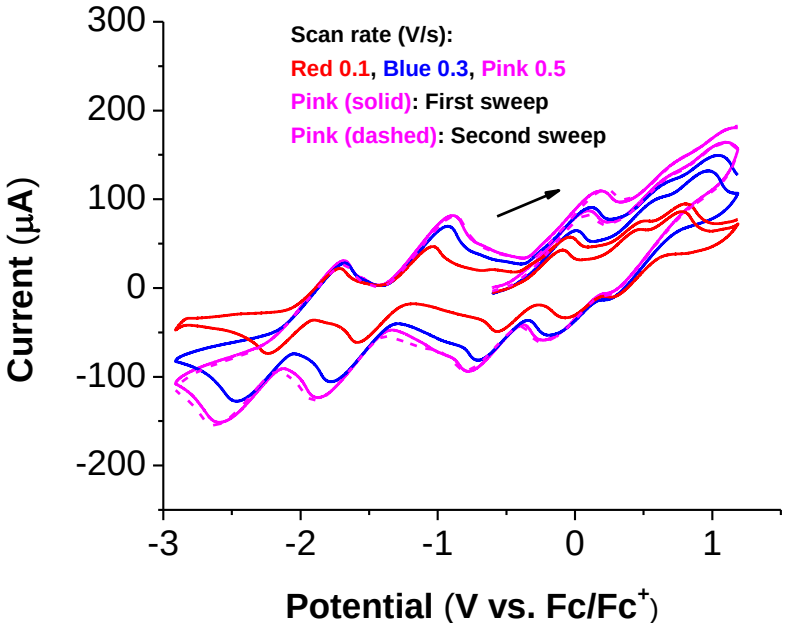

Figure 2.27. CVs of **2.5** at varying scan rates (inset). Experimental conditions: Taken in THF with 0.50 mM of **2.5**, 0.1 M of $[Bu_4N][PF_6]$, 3 mm diameter glassy carbon working electrode, Pt wire counter electrode, and Pt wire pseudo-reference electrode. Internally referenced to Fc/Fc^+.

For **2.6**, the recrystallized product exhibits a drastic drop in solubility after isolation of crystalline material from diethyl ether and CH_2Cl_2, making acquisition of a suitably concentrated CV on high purity material difficult (Figure 2.33). Other solvents screened (MeOH, EtOH, THF, DMF, CH_3CN), also showed limited capacity to dissolve isolate **2.6**.

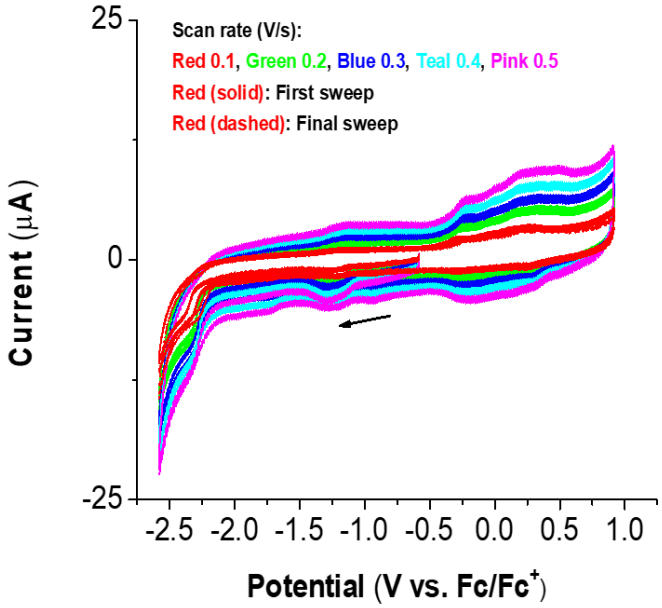

Figure 2.28. CVs of **2.6** at varying scan rates (inset). Experimental conditions: Taken in CH_2Cl_2/THF (95:5 by volume) with 0.48 mM* of **2.6**, 0.1 M of $[Bu_4N][PF_6]$, 3 mm diameter glassy carbon working electrode, Pt wire counter electrode, and Pt wire pseudo-reference electrode. Internally referenced to Fc/Fc^+. *Material appeared suspended and poorly soluble.

The CV of **2.7** shows two quasi-reversible reductions at $E_p(0.5)$ = -1.65 V and $E_p(0.5)$ = -2.03 V, and two broad, irreversible oxidation events at $E_p(0.5)$ = 0.01 V and $E_p(0.5)$ = 0.66 V (Figure 2.34). The return sweep of these oxidation events gives an initial irreversible response ~ $E_p(0.5)$ = 0.51 V followed by a clean, non-diffusional response at $E_p(0.5)$ = -0.24 V, suggesting that film deposition occurred. Additionally, unlike **2.1**, repeated sweeps

within the window causes an increase in the current response, suggesting that irreversible deposition is occurring at the electrode surface during oxidation, with cathodic stripping occurring on the return reductive sweep.[42]

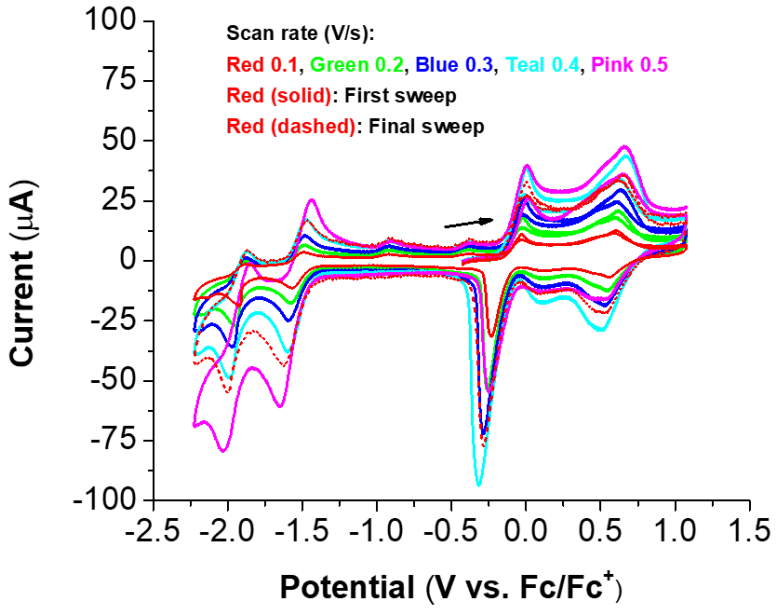

Figure 2.29. CVs of **2.7** at varying scan rates (inset). Experimental conditions: Taken in CH_2Cl_2 with 0.48 mM of **2.7**, 0.1 M of $[Bu_4N][PF_6]$, 3 mm diameter glassy carbon working electrode, Pt wire counter electrode, and Pt wire pseudo-reference electrode. Internally referenced to Fc/Fc^+.

Similar to **2.1**, the CV of **2.8** shows two quasi-reversible oxidation events at $E_p(0.5)$ = -0.11 V and $E_p(0.5)$ = 0.30 V. Additionally, there are a series of quasi-reversible and irreversible reduction events, similar to **2.4** (Figure 2.35). The final redox event at $E_p(0.5)$ = -2.37 V gives a sharp response characteristic of film deposition, although the lack of reversibility suggests it may be reduction of Cu(II) to Cu^0 with concurrent metal deposition.

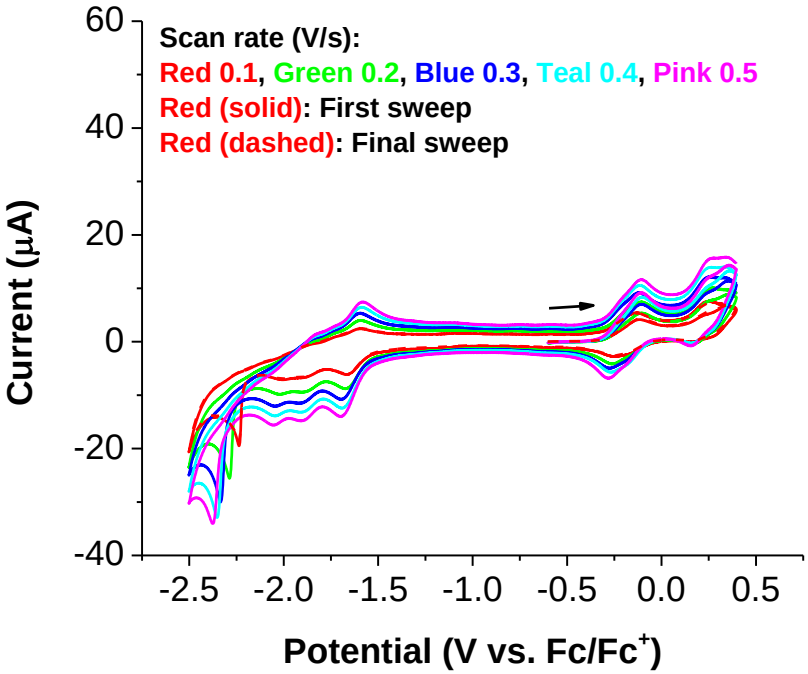

Figure 2.30. CVs of **2.8** at varying scan rates (inset). Experimental conditions: Taken in CH_2Cl_2 with 0.60 mM of **2.8**, 0.1 M of $[Bu_4N][PF_6]$, 3 mm diameter glassy carbon working electrode, Pt wire counter electrode, and Pt wire pseudo-reference electrode. Internally referenced to Fc/Fc^+.

2.3 Summary

We describe the synthesis, characterization, and electrochemistry of a series of substituted ^{EtO}PcM series, where M = HLi, H_2, Vo, Cr, Fe, Co, Ni, Cu. It is demonstrated in the initial ring synthesis that ^{EtO}Pc ligand is capable of acting as a L_3X-type ligand with single proton occupying the N_{meso} position (Figure 2.2). For all Pc complexes discussed, there is minor change in the absorption properties of each as a function of the metal center. The electrochemistry reveals that the species lacking non-labile axial substituents give low current responses and redox events with a lower degree of reversibility in CH_2Cl_2 and/or

THF, whereas those with non-labile axial substituents show well-defined, quasi-reversible features. It is postulated that the low current response and poorly defined features of the pseudo-D_{4h} species is caused by aggregation, and that the presence of a non-labile axial substituent inhibits this aggregation in solution. Ultimately, this needs to be tested by synthesizing a larger library of Pc species with axial substituents, both with and without redox-active metal centers, and studying their electrochemistry. An additional method of testing the aggregation hypothesis would be to performe variable temperature CV: If aggregation is indeed the cause of the low current response and poorly reversible features, increasing the temperature would reasonably be expected to reduce aggregation and cause significant change to the electrochemical profile. These experiments are currently underway in the Ménard Group.

2.4 Experimental

2.4.1 Considerations

Techniques and Reagents. All air-free manipulations were performed under an atmosphere of dry, oxygen-free N_2 within an MBraun glovebox (MBRAUN UNIlab Pro SP Eco equipped with a -40 ^oC freezer), or by standard Schlenk techniques. C_5H_{12}, C_6H_6, Et_2O, CH_2Cl_2, and THF (inhibitor-free) were dried and degassed on an MBraun Solvent Purification System and stored over activated 4 Å molecular sieves. All other solvents were degassed by freeze-pump-thaw and stored on activated 4 Å molecular sieves prior to use. Celite® and 4 Å molecular sieves were dried at 250 ^oC under dynamic vacuum (<0.1 Torr) for 24 h prior to use. Elemental analyses were recorded at the University of California, Berkeley using a Perkin Elmer 2400 Series II combustion analyzer. Metal salts were purchased from Strem Chemicals, Li metal, 2,3-dicyanohydroquinone from Acros Organics,

and ethyl iodide from Alfa Aesar and all were used without further purification. All other reagents were obtained from Sigma-Aldrich, Fisher Scientific, or VWR and used without further purification.

Spectroscopic Measurements. NMR spectra were obtained on an Agilent Technologies 400 MHz spectrometer, or a Varian 600 MHz spectrometer, and referenced to residual solvent. Chemical shifts (δ) are recorded in ppm and the coupling constants are in Hz. J-Young air-tight adaptors were used for air- and water-sensitive compounds. Perpendicular-mode X-band EPR spectra were collected on a Bruker EMX EPR Spectrometer equipped with an Oxford ESR 900 liquid helium cryostat. All EPR samples contained ~ 1 mg of material and data acquisition collected at 100K in frozen CH_2Cl_2 or THF. It should be noted that a small residual free radical signal is often observed in phthalocyanines, and has been attributed to sample grinding-induced defects.[43] UV-Vis spectra were collected on a Shimadzu UV-2401PC spectrophotometer. All measurements were performed on recrystallized product. All stock solutions and dilutions were prepared by mass. ^{57}Fe Mössbauer spectroscopy was performed using a SEE Co Model W304 resonant gamma-ray spectrometer (activity = 50 mCi +/- 10%), ^{57}Co/Rh source (manufactured by Ritverc) equipped with a Janis Research Model SVT-400 cryostat system. The source linewidth is <0.12 mm/s for the outermost lines of a 25 micron alpha-Fe foil standard. Isomer shifts are referenced to alpha-Fe foil at room temperature. All ^{57}Fe Mossbauer samples were prepared using ~30 mg powdered material and measured at 100 K unless otherwise noted. Data was fitted using a custom Igor Pro (Wavemetrics) macro package developed by the Betley group at Harvard University.

X-ray Crystallography. Data was collected on a Bruker KAPPA APEX II diffractometer equipped with an APEX II CCD detector using a TRIUMPH monochromator with a Mo Kα X-ray source (α = 0.71073 Å). The crystals were mounted on a cryoloop under Paratone-N

oil, and all data were collected at 100 K using an Oxford nitrogen gas cryostream system. A hemisphere of data was collected using ω scans with 0.5° frame widths. Data collection and cell parameter determination were conducted using the SMART program. Integration of the data frames and final cell parameter refinement were performed using SAINT software. Absorption correction of the data was carried out using SADABS. Structure determination was done using direct or Patterson methods and difference Fourier techniques. All hydrogen atom positions were idealized and rode on the atom of attachment. Structure solution, refinement, graphics, and creation of publication materials were performed using SHELXTL or OLEX[2].

Electrochemical Measurements. CV was performed on a CH Instruments 630E Electrochemical Analysis Potentiostat. Unless otherwise noted, the working electrode was a 1.5 mm radius glassy carbon (CH Instruments) and was cleaned prior to each experiment by sequentially polishing with a gradient of 1.0 μm, 0.3 μm, and 0.05 μm alumina (CH Instruments) on a cloth pad, followed by rinsing with distilled water and acetone. The Pt wire pseudo-reference and counter electrodes were rinsed with distilled water and acetone and heated white-hot with a butane torch. All measurements were performed on recrystallized product and referenced to the Fc/Fc^+ redox couple unless otherwise stated.

2.4.2 Syntheses

3,6-Diethoxyphthalonitrile. 3,6-Diethoxyphthalonitrile was synthesized using a modified procedure previously reported by Rauchfuss[34] and Ménard.[27] A mixture of 5.20 g (32.5 mmol, 1 equiv) of 2,3-dicyanohydroquinone and 5.00 g (36 mmol, 1.1 equiv) of K_2CO_3 in 125 mL of wet acetone was heated to reflux and sparged with Ar for 30 mins. Ethyl iodide (13 mL, 162 mmol, 5 equiv) was then added dropwise to the mixture. The yellow slurry was

stirred under reflux for 48 h. After cooling, the yellow solid was filtered off onto a glass frit, and subsequently transferred to a glass mortar and pestle, where it was ground into a powder. The powder was reintroduced to the glass frit, where it was washed successively with ~500 mL H_2O, ~150 mL EtOH, and ~150 mL of Et_2O. The product was collected and dried under reduced pressure for 24 h, affording a white powder. Additional product could be recovered from the effluent after the wash, and was similarly washed with H_2O, EtOH, and Et_2O. Yield: 5.154 g (73.4%). ^{1}H NMR (600 MHz, CD_2Cl_2): δ 7.21 (s, 2H, C_6H_2.), 4.16 (q, J = 7.0 Hz, 4H, OCH_2CH_3), 1.48 (t, J = 3.0 Hz, 6H, OCH_2CH_3).

Lithium 1,4,8,11,15,18,22,25-Octaethoxyphthalocyanine (2.1). **2.1** was synthesized using a procedure previously reported by Ménard.[27] High purity product could be recrystallized from CH_2Cl_2/Et_2O by vapor diffusion. ^{1}H NMR (600 MHz, CD_2Cl_2): δ 14.75 (s, 1H, N*H*), 7.57-7.52 (m, 8H, C_6H_2), 4.97-4.89 (m, 16H, OCH_2CH_3), 1.82-1.75 (m, 24H, OCH_2CH_3). $\lambda_{max}(Q_I\text{-peak})$ = 723 nm; $\lambda_{max}(Q_{II}\text{-peak})$ = 783 nm. MS (MALDI-TOF) Anal. Calc. $C_{48}H_{49}LiN_8O_8^+$: 872.38 (M+). Found: 873.40.

1,4,8,11,15,18,22,25-Octaethoxyphthalocyanine (2.2). **2.2** was synthesized using a modified procedure reported by Rauchfuss[34] and Ménard.[27] **2.1** (1.00 g, 0.98 mmol, 1 equiv) was slurried in 50 mL of H_2O in a flask. ~5 mL HCl (12.1 M, excess) was added dropwise over the course of 5 mins, changing the green slurry to a purple solution. The progress of the reaction was monitored by ^{1}H NMR every 24 h, with a small aliquot of solution removed and neutralized with excess bicarbonate, before filtering over a plug Celite®/glass wool, leaving a dark green pad that was washed with excess water and then extracted with CH_2Cl_2, resulting in a forest green effluent that was reduced to dryness and subsequently dissolved in CD_2Cl_2 for analysis. >95% conversion as realized after 48 h (Figure 2.4). After >95% conversion, the product was neutralized with $NaHCO_3$ (20.000 g, 238 mmol, excess),

collected by filtration, and washed with ~500 mL H_2O, ~250 mL EtOH, and ~150 mL of Et_2O, resulting a dark green powder that was dried under reduced pressure. High purity product could be recrystallized from CH_2Cl_2/Et_2O by vapor diffusion. Yield: 0.857 g (86.0%). ^{1}H NMR (600 MHz, CD_2Cl_2): δ 7.66 (s, 2H, C_6H_2), 4.92 (q, *J* = 7.0 Hz, 4H, OCH_2CH_3), 1.81 (t, *J* = 7.0 Hz, 6H, OCH_2CH_3), 0.23 (s, 2H, N*H*). λ_{max}(Q-peak) = 770 nm. MS (MALDI-TOF) Anal. Calc. $C_{48}H_{50}N_8O_8^+$: 866.38 (M+). Found: 867.44.

1,4,8,11,15,18,22,25-Octaethoxyphthalocyanine (2.3). **2.3** was synthesized using a modified procedure previously reported by Rauchfuss.[34] Under open atmosphere, 0.200 g (0.23 mmol, 1 equiv) of **2.1**, 0.200 g of $VOSO_4$*$5H_2O$ (excess), and 0.200 g (excess) of $NaHCO_3$ were combined in a RB flask with 15 mL of DMF, and the resulting mixture was heated to 145 ^{o}C for 4 h. After, 100 mL of H_2O was added and the solution was stirred for 15 min, and subsequently filtered through a glass frit, leaving a dark green solid. The solid was washed successively with ~150 mL of water, 50 mL EtOH, and 50 mL of Et_2O and subsequently collected and dried under reduced pressure. High purity product could be recrystallized from CH_2Cl_2/Et_2O by vapor diffusion. Yield: 0.090 g (42.15%). ^{1}H NMR (600 MHz, CD_2Cl_2): δ 8.53 (bs), 5.03 (bs), 1.86 (bs). λ_{max}(Q-peak) = 786 nm. MS (MALDI-TOF) Anal. Calc. $C_{48}H_{48}VN_8O_9^+$: 931.30 (M+). Found: 932.40.

1,4,8,11,15,18,22,25-Octaethoxyphthalocyanine (2.4).

A mixture of 0.50 g (0.58 mmol, 1.0 equiv) of **2.2**, 0.80 g (0.63 mmol, 1.1 equiv) of $CrCl_2$, and 0.242 g (11.5 mmol, 5 equiv) of $NaHCO_3$ was slurried in 30 mL DMF in a pressure vessel and heated to 100 ^{o}C for 5 h, resulting in a blue solution. Under inert atmosphere, the solution was filtered and extracted with THF. The filtrate was collected and dried under vacuum at 100 ^{o}C. High purity product could be recrystallized from THF/2,2,4,4-methylpentane by vapor diffusion at room temperature. Yield: 0.260 g (49.0%). ^{1}H NMR

(600 MHz, THF-d_8): Silent. λ_{max}(Q-peak) = 771 nm. MS (MALDI-TOF) Anal. Calc. $C_{48}H_{48}CrN_8O_8^+$: 916.30 (M+). Found: 917.39.

1,4,8,11,15,18,22,25-Octaethoxyphthalocyanine (2.5). A mixture of 1.00 g (1.15 mmol, 1 eq.) of **2.2** and 0.24 g (1.2 eq) of $Fe(OAc)_2$ was slurried in 15 mL Toluene under nitrogen and heated to reflux for 1 day, resulting in a dark green solution. After cooling, all volatile was removed under reduced pressure, yielding a dark green powder. The crude mixture was washed with 25 mL of pentane and 25 mL of EtO_2 over a glass frit. The resulting dark green filtride was extracted with 50 ml CH_2Cl_2 and solution was reduced to ~10 mL under reduced pressure, and then layered with pentane. Single crystals suitable for XRD studies were obtained by vapor diffusion with EtO_2 over a saturated CH_2Cl_2 solution at -35°C. Yield: 0.840 g (75.77%). ^{1}H NMR (600 MHz, CD_2Cl_2): δ 9.90 (q, *J* = X.X Hz, 16H, OC*H*$_2$CH$_3$), 4.32 (t, *J* = X.X Hz, 24H, OCH$_2$C*H*$_3$), 3.44 (s, *J* = X.X Hz, 8H, C$_6$*H*$_2$). Anal. Calc. for $C_{48}H_{48}FeN_8O_8$: C, 62.61; H, 5.25; N, 10.77. Found: C, 61.76; H, 4.98; N, 12.08. λ_{max}(Q-peak) = 765 nm. MS (MALDI-TOF) Anal. Calc. $C_{48}H_{48}NiN_8O_8^+$: 922.29 (M+). Found: 920.40.

1,4,8,11,15,18,22,25-Octaethoxyphthalocyanine (2.6). Under open atmosphere, 0.200 g (0.23 mmol, 1 equiv) of **2.1**, 0.200 g of $CoCl_2$*$6H_2O$ (excess), and 0.200 g (excess) of $NaHCO_3$ were combined in a RB flask with 15 mL of DMF, and the resulting mixture was heated to 145 ^{o}C for 4 h. After, 100 mL of H_2O was added and the solution was stirred for 15 min, and subsequently filtered through a glass frit, leaving a dark green solid. The solid was washed successively with ~150 mL of water, 10 mL EtOH, and 25 mL of Et_2O and subsequently collected and dried under reduced pressure. High purity product could be recrystallized from CH_2Cl_2/pentane by vapor diffusion, or by slow evaporation from EtOH. Note: The dry recrystallized product has exceedingly low solubility in CH_2Cl_2, necessitating

the use of THF-d_8 for acquisition of the ^{1}H NMR spectrum. Yield: 0.204 g (96.38%). ^{1}H NMR (600 MHz, THF-d_8): δ 10.92 (bs), δ 9.07 (bs), δ 7.35 (bs), δ 6.54-6.44 (bm), δ 3.90 (bs), δ 3.86 (bs), δ 3.65 (bs), δ 2.73 (bs). λ_{max}(Q-peak) = 738 nm. MS (MALDI-TOF) Anal. Calc. $C_{48}H_{48}CoN_8O_8^+$: 923.89 (M+). Found: 923.41.

1,4,8,11,15,18,22,25-Octaethoxyphthalocyanine (2.7). **2.7** was synthesized using a modified procedure previously reported by Rauchfuss.[34] Under open atmosphere, 0.208 g (0.24 mmol, 1 equiv) of **2.1**, 0.200 g of $NiCl_2$*$6H_2O$ (excess), and 0.200 g (excess) of $NaHCO_3$ were combined in a RB flask with 15 mL of DMF, and the resulting mixture was heated to 145 ^{o}C for 4 h. After, 100 mL of H_2O was added and the solution was stirred for 15 min, and subsequently filtered through a glass frit, leaving a dark green solid. The solid was washed successively with ~150 mL of water, 50 mL EtOH, and 50 mL of Et_2O and subsequently collected and dried under reduced pressure. High purity product could be recrystallized from CH_2Cl_2/Et_2O by vapor diffusion. Yield: 0.230 g (>100% (excluding co-crystallized CH_2Cl_2); 88.24% (including co-crystallized CH_2Cl_2)). ^{1}H NMR (600 MHz, CD_2Cl_2): δ 7.56 (bs, 8H, C_6H_2), 4.85 (bs, 16H, OCH_2CH_3), 1.77 (bs, 24H, OCH_2CH_3). λ_{max}(Q-peak) = 742 nm. MS (MALDI-TOF) Anal. Calc. $C_{48}H_{48}NiN_8O_8^+$: 922.29 (M+). Found: 923.40.

1,4,8,11,15,18,22,25-Octaethoxyphthalocyanine (2.8).

2.8 was synthesized using a modified procedure previously reported by Rauchfuss.[34] Under inert atmosphere, 0.207 g (0.24 mmol, 1 equiv) of **2.1**, 0.161 g of $CuCl_2$ (1.20 mmol, 5 equiv), and 0.107 g (1.27 mmol, 5.3 equiv) of $NaHCO_3$ were combined in a RB flask with 10 mL of DMF, and the resulting mixture was heated to 175 ^{o}C for 20 h.

After, 80 mL of H_2O was added and the solution was stirred for 30 min, and subsequently filtered through a glass frit, leaving a dark green solid. The solid was washed successively

with 100 mL of water and 20 mL EtOH and subsequently collected and dried under reduced pressure. High purity product could be recrystallized from CH_2Cl_2/hexanes by vapor diffusion, or by slow evaporation from EtOH. Yield: 0.091 g (41.4%). ^{1}H NMR (600 MHz, CD_2Cl_2): δ 4.58 (bs, 2H), δ 1.61 (bs, 3H). λ_{max}(Q-peak) = 750 nm. MS (MALDI-TOF) Anal. Calc. $C_{48}H_{48}CuN_8O_8^+$: 928.29 (M+). $C_{48}H_{48}CuN_8O_8^+$: 927.29 (M+). Found: 927.40 (M+).

2.5 Crystallographic Tables

2.5.1 Selected Crystallographic Data

Table 2.1 – Selected crystallographic data for **2.1**.

Formula	$C_{48}H_{49}LiN_8O_8$
Formula wt.	872.91
Crystal system	Monoclinic
Space group	P 1 21/c 1
a(Å)	15.182(3)
b(Å)	20.962(4)
c(Å)	13.078(3)
α(deg)	90
β(deg)	92.720(13)
γ(deg)	90
V(Å^3)	4157.4(15)
Z	4
T (K)	100(2)
d(calc) g/cm^3	1.3945
Abs coeff, μ, mm^{-1}	0.096
Data collected	8500
R_{int}	0.0741
Data used	3734
Parameters	593
R (>2σ)	0.2038
wR_2	0.1746
GOF	0.9833

Table 2.2 – Selected crystallographic data for **2.2**.

Formula	$C_{48}H_{50}N_8O_8$
Formula wt.	866.98
Crystal system	Monoclinic
Space group	P 1 21/c 1
a(Å)	15.1518(16)
b(Å)	20.927(2)
c(Å)	13.0887(13)
α(deg)	90
β(deg)	92.599(7)
γ(deg)	90
V(Å^3)	4146.0(7)
Z	4
T (K)	100(2)
d(calc) g/cm^3	1.3872
Abs coeff, μ, mm^{-1}	0.096
Data collected	10713
R_{int}	0.0630
Data used	3113
Parameters	585
R (>2σ)	0.2488
wR_2	0.1652
GOF	0.7685

Table 2.3 – Selected crystallographic data for **2.3**.

Formula	$C_{53}H_{60}Cl_2VN_8O_{10}$
Formula wt.	1090.95
Crystal system	Orthorhombic
Space group	P 2ac 2ab
a(Å)	17.122(3)
b(Å)	21.527(4)
c(Å)	27.625(5)
α(deg)	90
β(deg)	90
γ(deg)	90
V(Å^3)	10182(3)
Z	8
T (K)	102.81
d(calc) g/cm^3	1.3339
Abs coeff, μ, mm^{-1}	0.365
Data collected	10482
R_{int}	0.1330
Data used	8385
Parameters	721
R (>2σ)	0.1640
wR_2	0.3913
GOF	2.1451

Table 2.4 – Selected crystallographic data for **2.4**.

Formula	$C_{70}H_{95.75}CrN_8O_{13}$
Formula wt.	1309.29
Crystal system	Monoclinic
Space group	C 2/c
a(Å)	32.759(2)
b(Å)	24.050(3)
c(Å)	22.8653(15)
α(deg)	90
β(deg)	134.27
γ(deg)	90
V(Å^3)	12900.4(19)
Z	8
T (K)	120(2)
d(calc) g/cm^3	1.348
Abs coeff, μ, mm^{-1}	0.250
Data collected	9675
R_{int}	0.0949
Data used	6131
Parameters	617
R (>2σ)	0.1399
wR_2	0.3086
GOF	1.075

Table 2.5 – Selected crystallographic data for **2.5**.

Formula	$C_{54}H_{54}FeN_8O_8$
Formula wt.	998.90
Crystal system	Monoclinic
Space group	C 2/c
a(Å)	21.508(3)
b(Å)	24.769(4)
c(Å)	9.0646(14)
α(deg)	90
β(deg)	110.690(9)
γ(deg)	90
V(Å^3)	4517.5(12)
Z	4
T (K)	110(2)
d(calc) g/cm^3	1.469
Abs coeff, μ, mm^{-1}	0.404
Data collected	3649
R_{int}	0.0539
Data used	2546
Parameters	323
R (>2σ)	0.0887
wR_2	0.1458
GOF	1.040

Table 2.6 – Selected crystallographic data for **2.6**.

Formula	$C_{50}H_{52}Cl_4CoN_8O_8$
Formula wt.	1093.72
Crystal system	Monoclinic
Space group	P 21/c
a(Å)	15.072(8)
b(Å)	19.377(8)
c(Å)	16.392(5)
α(deg)	90
β(deg)	97.374(14)
γ(deg)	90
V(Å^3)	4748(3)
Z	4
T (K)	120(2)
d(calc) g/cm^3	1.530
Abs coeff, μ, mm^{-1}	0.653
Data collected	8250
R_{int}	0.0612
Data used	4578
Parameters	648
R (>2σ)	0.1416
wR_2	0.1386
GOF	0.968

Table 2.7 – Selected crystallographic data for **2.7**.

Formula	$C_{50}H_{52}Cl_4NiN_8O_9$
Formula wt.	1093.50
Crystal system	Monoclinic
Space group	P 21/c
a(Å)	15.0873(9)
b(Å)	19.2617(11)
c(Å)	16.4895(9)
α(deg)	90
β(deg)	97.573(3)
γ(deg)	90
V(Å^3)	4750.2(5)
Z	4
T (K)	100(2)
d(calc) g/cm^3	1.529
Abs coeff, μ, mm^{-1}	0.699
Data collected	10758
R_{int}	0.0414
Data used	7974
Parameters	644
R (>2σ)	0.0673
wR_2	0.1053
GOF	0.900

Table 2.8 – Selected crystallographic data for **2.8**.

Formula	$C_{50}H_{52}Cl_4CuN_8O_8$
Formula wt.	1098.33
Crystal system	Monoclinic
Space group	P 21/c
a(Å)	15.080(4)
b(Å)	19.284(6)
c(Å)	16.581(5)
α(deg)	90
β(deg)	97.719(18)
γ(deg)	90
V(Å^3)	4778(2)
Z	4
T (K)	126(2)
d(calc) g/cm^3	1.527
Abs coeff, μ, mm^{-1}	0.746
Data collected	9801
R_{int}	0.0625
Data used	6072
Parameters	653
R (>2σ)	0.1193
wR_2	0.1821
GOF	0.927

2.5.2 Bond Length Tables

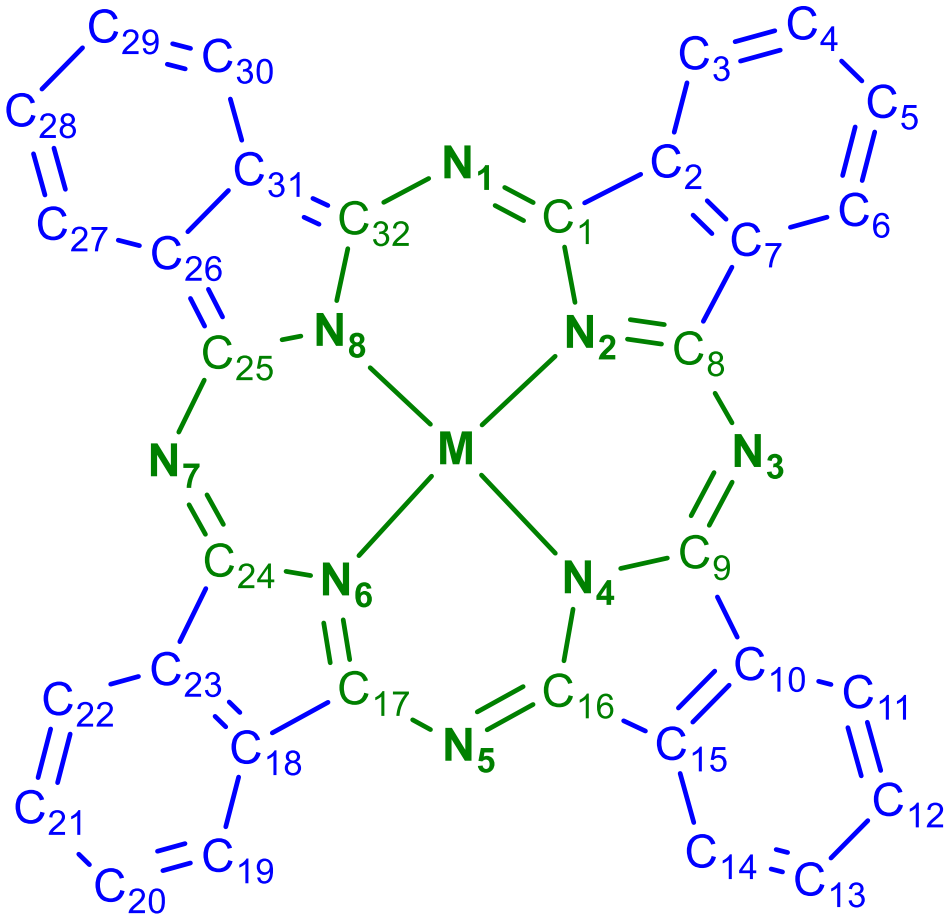

Figure 2.31. Atom denotations for ^{EtO}PcM (M =VO, Cr, Fe, Co, Ni, Cu), used to construct the bond length metrics in Tables 2.9-2.16. Atomic labels do not correspond with CIF atomic labels, but rather an arbitrarily designated orientation. Bond lengths were measured from the CIF in Olex2. For unit cells containing multiple ^{EtO}PcM molecules, one was chosen as a representative molecule.

Table 2.9. Bond length metrics for **2.1**.

Core Bond Lengths (CW from N1; Å)	
N1-C1	1.366(5)
C1-N2	1.342(5)
N2-C8	1.374(5)
C8-N3	1.327(5)
N3-C9	1.343(5)
C9-N4	1.357(5)
N4-C16	1.371(5)
C16-N5	1.328(5)
N5-C17	1.339(5)
C17-N6	1.369(5)
N6-C24	1.349(5)
C24-N7	1.357(5)
N7-C25	1.327(5)
C25-N8	1.379(5)
N8-C32	1.325(5)
C32-N1	1.357(5)

Periphery Bond Lengths (CW from C1; Å)			
C1-C2	1.439(6)	**C17-C18**	1.469(6)
C2-C3	1.408(6)	**C18-C19**	1.404(6)
C2-C7	1.403(5)	**C18-C23**	1.406(5)
C3-C4	1.383(6)	**C19-C20**	1.397(6)
C4-C5	1.395(6)	**C20-C21**	1.391(6)
C5-C6	1.394(6)	**C21-C22**	1.380(6)
C6-C7	1.388(6)	**C22-C23**	1.398(6)
C7-C8	1.474(6)	**C23-C24**	1.459(6)
C9-C10	1.472(6)	**C25-C26**	1.471(6)
C10-C11	1.396(6)	**C26-C27**	1.404(6)
C10-C15	1.404(6)	**C26-C31**	1.399(6)
C11-C12	1.390(6)	**C27-C28**	1.395(6)
C12-C13	1.388(6)	**C28-C29**	1.392(6)
C13-C14	1.378(6)	**C29-C30**	1.390(6)
C14-C15	1.402(6)	**C30-C31**	1.396(6)
C15-C16	1.481(6)	**C31-C32**	1.442(6)

Table 2.10. Bond length metrics for **2.2**.

Core Bond Lengths (CW from N1; Å)	
N1-C1	1.323(5)
C1-N2	1.391(5)
N2-C8	1.374(5)
C8-N3	1.326(5)
N3-C9	1.338(4)
C9-N4	1.358(4)
N4-C16	1.363(4)
C16-N5	1.336(4)
N5-C17	1.319(5)
C17-N6	1.368(5)
N6-C24	1.377(5)
C24-N7	1.307(5
N7-C25	1.355(4)
C25-N8	1.348(4)
N8-C32	1.368(4)
C32-N1	1.29(4)

Periphery Bond Lengths (CW from C1; Å)			
C1-C2	1.451(5)	**C17-C18**	1.454(5)
C2-C3	1.414(5)	**C18-C19**	1.407(5)
C2-C7	1.410(5)	**C18-C23**	1.415(5)
C3-C4	1.372(5)	**C19-C20**	1.369(5)
C4-C5	1.393(6)	**C20-C21**	1.398(6)
C5-C6	1.382(5)	**C21-C22**	1.384(5)
C6-C7	1.399(5)	**C22-C23**	1.405(5)
C7-C8	1.460(5)	**C23-C24**	1.460(5)
C9-C10	1.470(5)	**C25-C26**	1.461(5)
C10-C11	1.392(5)	**C26-C27**	1.386(5)
C10-C15	1.404(5)	**C26-C31**	1.400(5)
C11-C12	1.385(5)	**C27-C28**	1.384(5)
C12-C13	1.391(5)	**C28-C29**	1.385(5)
C13-C14	1.378(5)	**C29-C30**	1.378(5)
C14-C15	1.410(5)	**C30-C31**	1.407(5)
C15-C16	1.459(5)	**C31-C32**	1.457(5)

Table 2.11. Bond length metrics for **2.3**.

Core Bond Lengths (CW from N1; Å)	
N1-C1	1.322(9)
C1-N2	1.382(9)
N2-C8	1.375(9)
C8-N3	1.334(9)
N3-C9	1.334(9)
C9-N4	1.379(8)
N4-C16	1.378(9)
C16-N5	1.323(9)
N5-C17	1.326(9)
C17-N6	1.369(9)
N6-C24	1.380(9)
C24-N7	1.328(9)
N7-C25	1.335(9)
C25-N8	1.368(9)
N8-C32	1.385(9)
C32-N1	1.323(9)

Periphery Bond Lengths (CW from C1; Å)			
C1-C2	1.447(9)	**C17-C18**	1.463(9)
C2-C3	1.403(10)	**C18-C19**	1.401(10)
C2-C7	1.407(10)	**C18-C23**	1.398(10)
C3-C4	1.390(11)	**C19-C20**	1.401(10)
C4-C5	1.402(11)	**C20-C21**	1.385(11)
C5-C6	1.402(11)	**C21-C22**	1.401(10)
C6-C7	1.402(10)	**C22-C23**	1.403(10)
C7-C8	1.462(9)	**C23-C24**	1.461(9)
C9-C10	1.466(10)	**C25-C26**	1.457(9)
C10-C11	1.403(10)	**C26-C27**	1.400(10)
C10-C15	1.401(10)	**C26-C31**	1.410(10)
C11-C12	1.388(11)	**C27-C28**	1.390(10)
C12-C13	1.393(11)	**C28-C29**	1.404(11)
C13-C14	1.395(10)	**C29-C30**	1.396(10)
C14-C15	1.403(10)	**C30-C31**	1.416(10)
C15-C16	1.451(9)	**C31-C32**	1.446(9)

Table 2.12. Bond length metrics for **2.4**.

Core Bond Lengths (CW from N1; Å)	
N1-C1	1.324(8)
C1-N2	1.397
N2-C8	1.383(8)
C8-N3	1.328(9)
N3-C9	1.330(8)
C9-N4	1.370(8)
N4-C16	1.379(8)
C16-N5	1.345(8)
N5-C17	1.324(8)
C17-N6	1.397
N6-C24	1.383(8)
C24-N7	1.328(9)
N7-C25	1.330(8)
C25-N8	1.370(8)
N8-C32	1.379(8)
C32-N1	1.345(8)

Periphery Bond Lengths (CW from C1; Å)			
C1-C2	1.439(9)	**C17-C18**	1.439(9)
C2-C3	1.393(9)	**C18-C19**	1.393(9)
C2-C7	1.414(10)	**C18-C23**	1.414(10)
C3-C4	1.386(10)	**C19-C20**	1.386(10)
C4-C5	1.371(11)	**C20-C21**	1.371(11)
C5-C6	1.401(10)	**C21-C22**	1.401(10)
C6-C7	1.407(9)	**C22-C23**	1.407(9)
C7-C8	1.452	**C23-C24**	1.452
C9-C10	1.463(10)	**C25-C26**	1.463(10)
C10-C11	1.392(10)	**C26-C27**	1.392(10)
C10-C15	1.421(9)	**C26-C31**	1.421(9)
C11-C12	1.383(11)	**C27-C28**	1.383(11)
C12-C13	1.423(12)	**C28-C29**	1.423(12)
C13-C14	1.380(10)	**C29-C30**	1.380(10)
C14-C15	1.411(10)	**C30-C31**	1.411(10)
C15-C16	1.432(9)	**C31-C32**	1.432(9)

Table 2.13. Bond length metrics for **2.5**.

Core Bond Lengths (CW from N1; Å)	
N1-C1	1.322(4)
C1-N2	1.366(5)
N2-C8	1.396(4)
C8-N3	1.319(4)
N3-C9	1.329(4)
C9-N4	1.387(4)
N4-C16	1.364(5)
C16-N5	1.329(4)
N5-C17	1.329(4)
C17-N6	1.364(5)
N6-C24	1.387(4)
C24-N7	1.329(4)
N7-C25	1.319(4)
C25-N8	1.396(4)
N8-C32	1.366(5)
C32-N1	1.322(4)

Periphery Bond Lengths (CW from C1; Å)			
C1-C2	1.454(5)	**C17-C18**	1.435(5)
C2-C3	1.406(5)	**C18-C19**	1.398(5)
C2-C7	1.395(5)	**C18-C23**	1.377(5)
C3-C4	1.381(5)	**C19-C20**	1.383(5)
C4-C5	1.373(5)	**C20-C21**	1.382(5)
C5-C6	1.378(5)	**C21-C22**	1.402(5)
C6-C7	1.396(5)	**C22-C23**	1.398(5)
C7-C8	1.452(5)	**C23-C24**	1.447(5)
C9-C10	1.447(5)	**C25-C26**	1.452(5)
C10-C11	1.398(5)	**C26-C27**	1.396(5)
C10-C15	1.402(5)	**C26-C31**	1.378(5)
C11-C12	1.382(5)	**C27-C28**	1.373(5)
C12-C13	1.383(5)	**C28-C29**	1.381(5)
C13-C14	1.377(5)	**C29-C30**	1.395(5)
C14-C15	1.398(5)	**C30-C31**	1.406(5)
C15-C16	1.435(5)	**C31-C32**	1.454(5)

Table 2.14. Bond length metrics for **2.6**.

Core Bond Lengths (CW from N1; Å)	
N1-C1	1.320(6)
C1-N2	1.377(6)
N2-C8	1.383(6)
C8-N3	1.322(6)
N3-C9	1.327(6)
C9-N4	1.382(6)
N4-C16	1.383(6)
C16-N5	1.320(6)
N5-C17	1.307(6)
C17-N6	1.385(6)
N6-C24	1.377(6)
C24-N7	1.325(6)
N7-C25	1.322(6)
C25-N8	1.381(6)
N8-C32	1.379(6)
C32-N1	1.321(6)

Periphery Bond Lengths (CW from C1; Å)			
C1-C2	1.450(7)	**C17-C18**	1.448(7)
C2-C3	1.404(7)	**C18-C19**	1.405(7)
C2-C7	1.396(7)	**C18-C23**	1.388(7)
C3-C4	1.389(7)	**C19-C20**	1.374(7)
C4-C5	1.380(7)	**C20-C21**	1.381(7)
C5-C6	1.403(7)	**C21-C22**	1.392(7)
C6-C7	1.394(7)	**C22-C23**	1.409(7)
C7-C8	1.472(7)	**C23-C24**	1.457(7)
C9-C10	1.457(7)	**C25-C26**	1.460(7)
C10-C11	1.402(7)	**C26-C27**	1.406(7)
C10-C15	1.407(7)	**C26-C31**	1.399(7)
C11-C12	1.387(7)	**C27-C28**	1.386(7)
C12-C13	1.389(7)	**C28-C29**	1.392(7)
C13-C14	1.378(7)	**C29-C30**	1.376(7)
C14-C15	1.413(7)	**C30-C31**	1.408(7)
C15-C16	1.444(7)	**C31-C32**	1.434(7)

Table 2.15. Bond length metrics for **2.7**.

Core Bond Lengths (CW from N1; Å)	
N1-C1	1.313(3)
C1-N2	1.376(3)
N2-C8	1.383(3)
C8-N3	1.321(3)
N3-C9	1.320(3)
C9-N4	1.385(3)
N4-C16	1.378(3)
C16-N5	1.313(3)
N5-C17	1.318(3)
C17-N6	1.374(3)
N6-C24	1.386(3)
C24-N7	1.323(3)
N7-C25	1.324(3)
C25-N8	1.383(3)
N8-C32	1.370(3)
C32-N1	1.319(3)

Periphery Bond Lengths (CW from C1; Å)			
C1-C2	1.453(3)	**C17-C18**	1.450(3)
C2-C3	1.403(3)	**C18-C19**	1.399(4)
C2-C7	1.399(3)	**C18-C23**	1.396(3)
C3-C4	1.384(4)	**C19-C20**	1.393(4)
C4-C5	1.391(4)	**C20-C21**	1.392(4)
C5-C6	1.393(4)	**C21-C22**	1.384(4)
C6-C7	1.410(3)	**C22-C23**	1.410(3)
C7-C8	1.466(3)	**C23-C24**	1.460(3)
C9-C10	1.464(3)	**C25-C26**	1.464(3)
C10-C11	1.407(3)	**C26-C27**	1.410(3)
C10-C15	1.397(3)	**C26-C31**	1.395(3)
C11-C12	1.392(3)	**C27-C28**	1.392(4)
C12-C13	1.394(4)	**C28-C29**	1.393(4)
C13-C14	1.384(3)	**C29-C30**	1.383(3)
C14-C15	1.408(3)	**C30-C31**	1.404(3)
C15-C16	1.453(3)	**C31-C32**	1.451(3)

Table 2.16. Bond length metrics for **2.8**.

Core Bond Lengths (CW from N1; Å)	
N1-C1	1.317(6)
C1-N2	1.377(6)
N2-C8	1.374(6)
C8-N3	1.322(6)
N3-C9	1.323(6)
C9-N4	1.385(6)
N4-C16	1.372(6)
C16-N5	1.323(6)
N5-C17	1.318(6)
C17-N6	1.375(6)
N6-C24	1.371(6)
C24-N7	1.330(6)
N7-C25	1.342(6)
C25-N8	1.374(5)
N8-C32	1.381(5)
C32-N1	1.322(6)

Periphery Bond Lengths (CW from C1; Å)			
C1-C2	1.452(6)	**C17-C18**	1.448(6)
C2-C3	1.401(7)	**C18-C19**	1.406(7)
C2-C7	1.398(7)	**C18-C23**	1.399(7)
C3-C4	1.383(7)	**C19-C20**	1.376(7)
C4-C5	1.376(8)	**C20-C21**	1.379(7)
C5-C6	1.393(7)	**C21-C22**	1.412(7)
C6-C7	1.409(6)	**C22-C23**	1.405(6)
C7-C8	1.463(6)	**C23-C24**	1.472(6)
C9-C10	1.471(6)	**C25-C26**	1.465(6)
C10-C11	1.412(6)	**C26-C27**	1.399(6)
C10-C15	1.385(6)	**C26-C31**	1.395(6)
C11-C12	1.390(7)	**C27-C28**	1.402(7)
C12-C13	1.378(7)	**C28-C29**	1.389(7)
C13-C14	1.385(7)	**C29-C30**	1.374(7)
C14-C15	1.410(6)	**C30-C31**	1.431(6)
C15-C16	1.455(6)	**C31-C32**	1.447(6)

2.6 References

(1) Dahlen, M. A. *Ind. Eng. Chem.* **1939**, *31* (7), 839–847.

(2) McKeown, N. B. *Phthalocyanine materials: synthesis, structure and function*; Cambridge University Press, 1998.

(3) Laurs, H.; Heiland, G. *Thin Solid Films* **1987**, *149* (2), 129–142.

(4) Armstrong, N. R. *J. Porphyr. Phthalocyanines* **2012**.

(5) Walter, M. G.; Rudine, A. B.; Wamser, C. C. *J. Porphyr. Phthalocyanines* **2010**, *14* (09), 759–792.

(6) Okura, I. *Photosensitization of porphyrins and phthalocyanines*; CRC Press, 2017.

(7) Eley, D. D. *Nature* **1948**, *162* (4125), 819.

(8) Turek, P.; Petit, P.; Andre, J. J.; Simon, J.; Even, R.; Boudjema, B.; Guillaud, G.; Maitrot, M. *J. Am. Chem. Soc.* **1987**, *109* (17), 5119–5122.

(9) Vartanyan, A. T. *Semiconductor properties of organic dyes. 1. Phthalocyanines*; FOREIGN TECHNOLOGY DIV WRIGHT-PATTERSON AFB OH, 1990.

(10) Bouvet, M. *Anal. Bioanal. Chem.* **2006**, *384* (2), 366–373.

(11) Öztürk, Z. Z.; Kılınç, N.; Atilla, D.; Gürek, A. G.; Ahsen, V. *J. Porphyr. Phthalocyanines* **2009**, *13* (11), 1179–1187.

(12) Zhou, R.; Josse, F.; Göpel, W.; Öztürk, Z. Z.; Bekaroğlu, Ö. *Appl. Organomet. Chem.* **1996**, *10* (8), 557–577.

(13) Janata, J. *Anal. Chem.* **1992**, *64* (12), 196–219.

(14) Grätzel, M. *J. Photochem. Photobiol. C Photochem. Rev.* **2003**, *4* (2), 145–153.

(15) Ragoussi, M.; Ince, M.; Torres, T. *European J. Org. Chem.* **2013**, *2013* (29), 6475–6489.

(16) Rosenthal, I. *Photochem. Photobiol.* **1991**, *53* (6), 859–870.

(17) Zagal, J. H.; Griveau, S.; Silva, J. F.; Nyokong, T.; Bedioui, F. *Coord. Chem. Rev.* **2010**, *254* (23), 2755–2791.

(18) Sorokin, A. B. *Chem. Rev.* **2013**, *113* (10), 8152–8191.

(19) Hunt, C.; Mattejat, M.; Anderson, C.; Sepunaru, L.; Ménard, G. *ACS Appl. Energy Mater.* **2019**.

(20) Oni, J.; Ozoemena, K. I. *J. Porphyr. Phthalocyanines* **2012**, *16* (07n08), 754–760.

(21) Yamaki, J.; Yamaji, A. *J. Electrochem. Soc.* **1982**, *129* (1), 5–9.

(22) Kobayashi, N.; Ogata, H.; Nonaka, N.; Luk'yanets, E. A. *Chem. – A Eur. J.* **2003**, *9* (20), 5123–5134.

(23) Kobayashi, N.; Sasaki, N.; Higashi, Y.; Osa, T. *Inorg. Chem.* **1995**, *34* (7), 1636–1637.

(24) Nyokong, T. *Coord. Chem. Rev.* **2007**, *251* (13–14), 1707–1722.

(25) Schlettwein, D.; Armstrong, N. R. *J. Phys. Chem.* **1994**, *98* (45), 11771–11779.

(26) Usol'tseva, N. V; Smirnova, A. I.; Kazak, A. V; Giricheva, N. I.; Galanin, N. E.; Shaposhnikov, G. P.; Bodnarchuk, V. V; Yablonskii, S. V. *Opto-Electronics Rev.* **2017**, *25* (2), 127–136.

(27) Hunt, C.; Peterson, M.; Anderson, C.; Chang, T.; Wu, G.; Scheiner, S.; Ménard, G. *J. Am. Chem. Soc.* **2019**, *141* (6), 2604–2613.

(28) Liao, M.-S.; Scheiner, S. *J. Chem. Phys.* **2001**, *114* (22), 9780–9791.

(29) El-Khoury, P. Z.; Honkala, K.; Hess, W. P. *J. Phys. Chem. A* **2014**, *118* (37), 8115–8123.

(30) Prieto, I.; Pedrosa, J. M.; Martín-Romero, M. T.; Möbius, D.; Camacho, L. *J. Phys. Chem. B* **2000**, *104* (43), 9966–9972.

(31) Rubires, R.; Crusats, J.; El-Hachemi, Z.; Jaramillo, T.; López, M.; Valls, E.; Farrera,

J.-A.; Ribó, J. M. *New J. Chem.* **1999**, *23* (2), 189–198.

(32) Yüksel, F.; Gül Gürek, A.; Lebrun, C.; Ahsen, V. *New J. Chem.* **2005**, *29* (5), 726–732.

(33) Ceulemans, A.; Oldenhof, W.; Gorller-Walrand, C.; Vanquickenborne, L. G. *J. Am. Chem. Soc.* **1986**, *108* (6), 1155–1163.

(34) Contakes, S. M.; Beatty, S. T.; Dailey, K. K.; Rauchfuss, T. B.; Fenske, D. *Organometallics* **2000**, *19* (23), 4767–4774.

(35) Ziolo, R. F.; Griffiths, C. H.; Troup, J. M. *J. Chem. Soc. Dalt. Trans.* **1980**, No. 11, 2300–2302.

(36) Dar, T. A.; Tomar, R.; Mian, R. M.; Sankar, M.; Maurya, M. R. *RSC Adv.* **2019**, *9* (18), 10405–10413.

(37) Bell, N. A.; Brooks, J. S.; Robinson, J. K.; Thorpe, S. C. *J. Chem. Soc. Faraday Trans.* **1998**, *94* (20), 3155–3159.

(38) Sakamoto, K. In *Voltammetry*; IntechOpen, 2018.

(39) Milaeva, E. R.; Speier, G.; Lever, A. B. *The redox chemistry of metallophthalocyanines in solution*; YORK UNIV NORTH YORK (ONTARIO) DEPT OF CHEMISTRY, 1992.

(40) Wehrle, B.; Limbach, H. *Chem. Phys.* **1989**, *136* (2), 223–247.

(41) Lüning, U. Bethell, D. B. T.-A. in P. O. C., Ed.; Academic Press, 1995; Vol. 30, pp 63–116.

(42) Bard, A. J.; Faulkner, L. R.; Leddy, J.; Zoski, C. G. *Electrochemical methods: fundamentals and applications*; wiley New York, 1980; Vol. 2.

(43) More, K. M.; Eaton, G. R.; Eaton, S. S. *J. Magn. Reson.* **1980**, *37* (2), 217–222.

Chapter 3

Switchable Aromaticity in an Isostructural Mn Phthalocyanine Series Isolated in Five Separate Redox States

3.1 Introduction

Hückel's $(4n + 2)\pi$ e^- rule is conventionally used to predict the aromatic character of cyclic, planar, π-conjugated compounds. However, in extended aromatic systems this rule often gives unsatisfactory predictions of in/stability and deviations from the tenets of Hückel's rule, such as the requirement for planarity, become more common.[1-3] In concert with this, macrocyclic platforms often adopt localized internal π circuits within the extended π manifold as exemplified by Vogel's [18]annulene/18 π e^- model applied to porphyrins[4-5] and related phthalocyanines (Pc) (Figure 3.1a-b).[6] An alternative but less common model involving the dianionic $([16]annulene)^{2-}$ substructure has also been proposed as the primary aromatic circuit, particularly for metalloporphyrins (Figure 3.1c).[5, 7] While the annulene model aids in understanding the complexity of aromaticity in large macrocyclic systems, it is not a complete description, particularly regarding correlations between local and macrocyclic ring currents, both demonstrated to be important considerations when describing total aromaticity.[2, 8-10]

The inherent interplay of resonance circuits and electronic properties has resulted in the development of several structure/function relationships between aromaticity and electronic behavior in large, conjugated systems.[11] Notably, the correlation between aromaticity and conductance has been well described by many and may have important implications for the development of next generation organic electronic devices.[12-15] In contrast, "switchable" aromatic character may be used to design single-molecule transistors and other molecular-scale electronic gates. A molecular macrocyclic platform spanning separate aromatic states – and correlated structural perturbations – may guide the development of such materials and their properties. While redox-switchable aromaticity in macrocyclic platforms, such as porphyrinoids, has been studied,[1] with several isolated discreet anti-aromatic or non-

aromatic species reported,[16-26] to the best of our knowledge, there are no known examples of a single stable, isostructural complex – either porphyrin or Pc-based, or other – isolated in multiple separate redox states, including radical states, and spanning the aromatic, non-aromatic, and anti-aromatic triad. Previous work has created a backbone of information regarding the electronic character of Pc complexes in various oxidation states, and extensive effort has been focused on determining the loci of redox events and how they relate to the aromaticity of a given system, producing a large body of useful knowledge for the field.[18, 20, 27-31] However, while many Pc complexes have been studied in each of the states separately, it can be difficult to make direct comparisons due to the many different substituents and redox-active metal centers used across publications. It is therefore of interest to use an isostructural Pc redox series with a redox-inactive metal core in order to ensure that all comparisons are due primarily to the change in oxidation state while minimizing the effect of ring substitution or choice of metal.

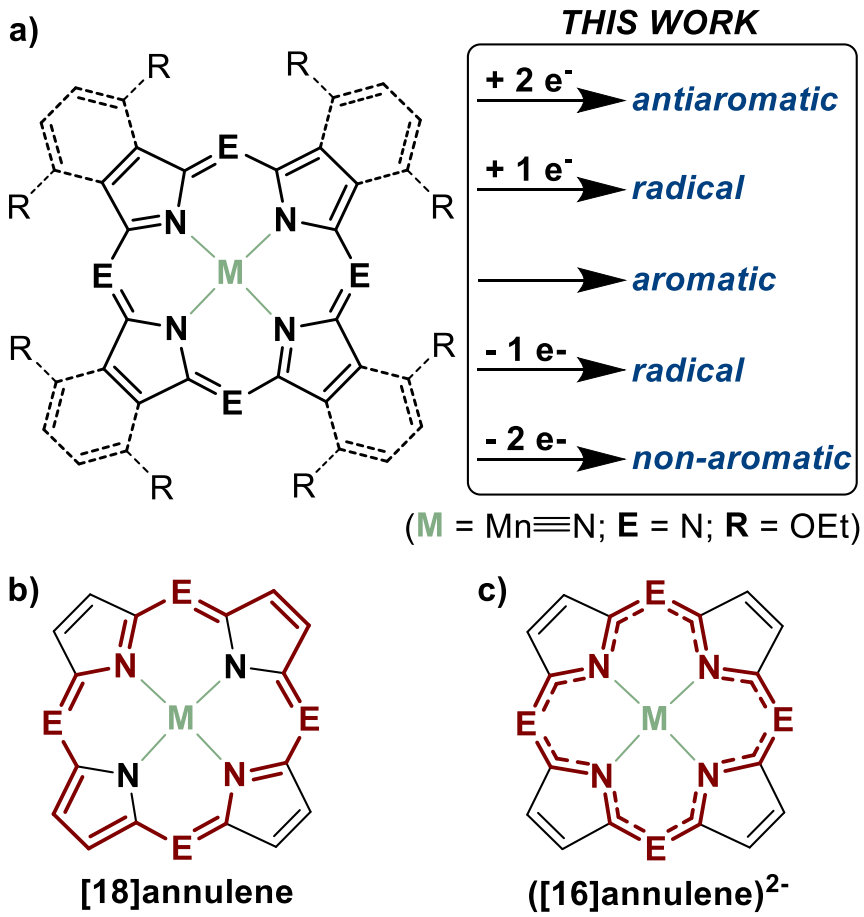

Figure 3.1. a) Depiction of porphine (solid lines), the parent molecule to porphyrins, and the related phthalocyanine (solid + dashed lines) coordinated to a generic metal (M). b) The [18]annulene/18 π e^- circuit, in bold. c) The dianionic $([16][annulene])^{2-}$/18 π e^- circuit in bold.

Herein, we demonstrate what we credit as the first such clearly characterized example of a macrocyclic Pc complex that can readily access aromatic (neutral), anti-aromatic (di-reduced), and non-aromatic (di-oxidized) states, in addition to the singly oxidized or reduced states. This was accomplished using the new Mn-nitride, (^{OEt}Pc)MnN (**3.2**, ^{OEt}Pc = 1,4,8,11,15,18,22,25-octaethoxy-Pc), by chemical oxidation or reduction. The redox behavior and electronic structure were probed through a suite of structural, spectroscopic,

electrochemical, and computational methods and revealed ligand-borne redox events with the Pc ligand spanning from Pc(0) to Pc(4-) formal oxidation states. Additionally, compelling evidence for the operative local and macrocyclic resonance circuits are provided. We consider this complex a rare class of resonance circuit model compound due to the capability of accessing all three principal states of aromatic behavior in a stable and isolable manner, and apparent changing of resonance circuit pathways as a function of redox state. This study may provide valuable information on the interplay of redox state and aromatic character in Pc and related macrocycles, and may serve as an excellent platform in which to study molecular material applications pertaining to tunable aromaticity.

3.2 Results and Discussion

3.2.1 Synthesis and Characterization.

The symmetrically substituted pro-ligand, $^{EtO}PcH_2$, was prepared by previously reported methods.[32-33] Metallation of $^{EtO}PcH_2$ with $MnCl_2$ under aerobic conditions in refluxing dimethyl formamide (DMF) for 5 h yielded a dark red product (λ_{max} = 825 nm) after purification (Note: all λ_{max} values reported correspond to the Q peaks) (Scheme 3.1, path i).[34] Single crystals suitable for XRD studies were grown by layering benzene over a saturated fluorobenzene solution and confirmed the structure as the Mn(III) species, ^{EtO}PcMnCl (**3.1**) (Figure 3.2). Bond metrics are similar to other Mn(III)Cl macrocyclic species, such as a similar porphyrin derivative.[35] The high-spin, S = 2 state at Mn was confirmed by solution magnetic moment determination using the Evans method,[36] and resulted in paramagnetically broadened resonances in the ^{1}H NMR spectrum.

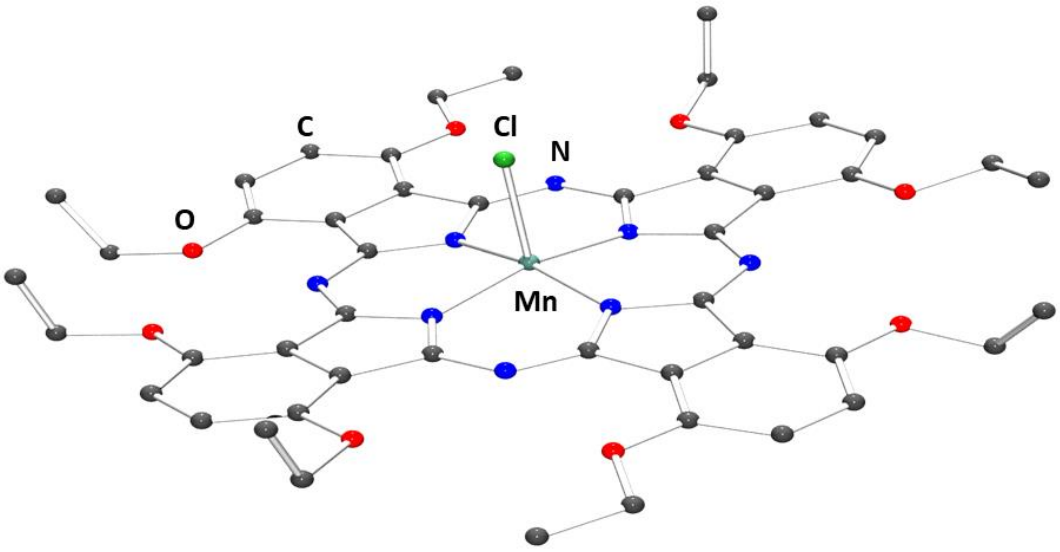

Figure 3.2. Solid-state molecular structure of **3.1**. Hydrogen atoms, ethoxy carbon atoms, and co-crystallized solvent are omitted for clarity.

Our interest in generating a terminal Mn-nitride stemmed from our previous work.[37] The nitride, ^{EtO}PcMnN (**3.2**), was readily generated from **3.1** under oxidative conditions using NaOCl and aqueous NH_3 in methanol (Scheme 3.1, path ii).[37-39]

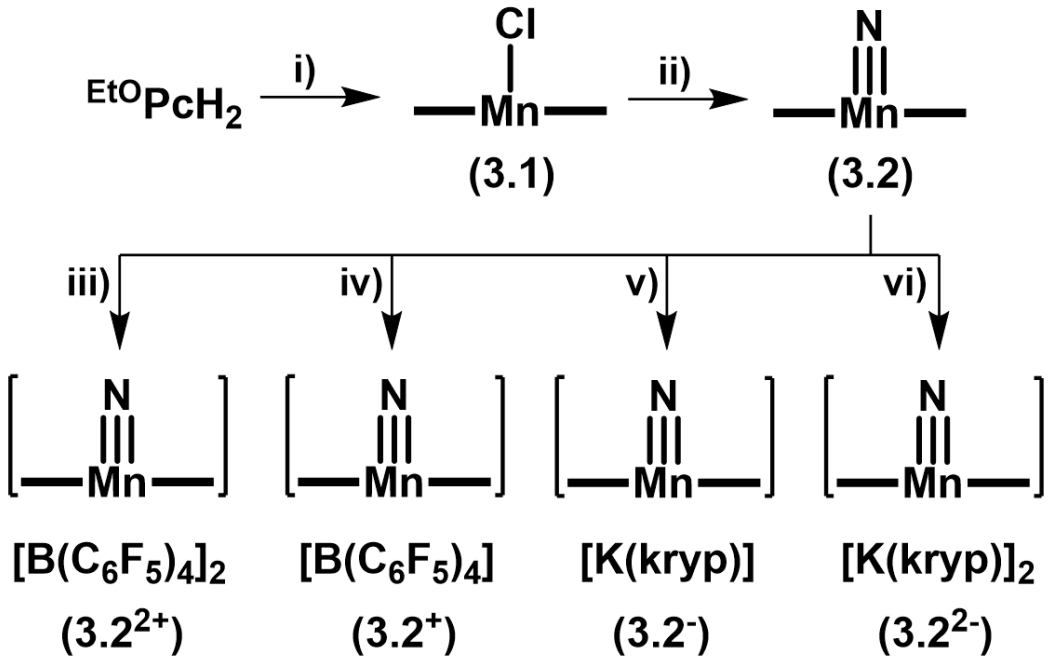

Scheme 3.1. Synthesis of reported complexes following the general conditions: i) $MnCl_2$, DMF, 100 °C, 5 h, O_2; ii) NH_4OH/NaOCl, MeOH, r.t., 15 mins; iii) [(4-$BrC_6H_4)_3N$][$B(C_6F_5)_4$] (2 eq.), DCM, r.t., 5 mins; iv) [(4-$BrC_6H_4)_3N$][$B(C_6F_5)_4$] (1 eq.), DCM, r.t., 5 mins; v) KC_8 (1 eq.), kryp (1 eq.), THF, r.t., 10 mins; vi) KC_8 (5 eq.), kryp (2 eq.), THF, r.t., 10 mins.

The dark green, diamagnetic complex (λ_{max} = 767 nm) was isolated in high yield (~89%) and was structurally characterized by XRD studies (Figure 3.3). While several Pc metal nitrides have been reported,[40-41] including with Mn,[42-45] **3.2** represents the first crystallographically characterized terminal Pc-metal nitride complex, according to the Cambridge Structural Database. The Mn≡N in **3.2** is 1.555(9) Å, similar to other Mn≡N bonds in comparable symmetry and oxidation state.[39, 46-47] A more detailed structural analysis is provided in the following section. The low-spin, diamagnetic nature of **3.2** is

further consistent with other triply bonded Mn(V) nitrides, as is the Mn≡N stretching frequency located at 1030 cm^{-1}, identified by comparison with the isotopologue, **3.2-^{15}N**.[37, 48]

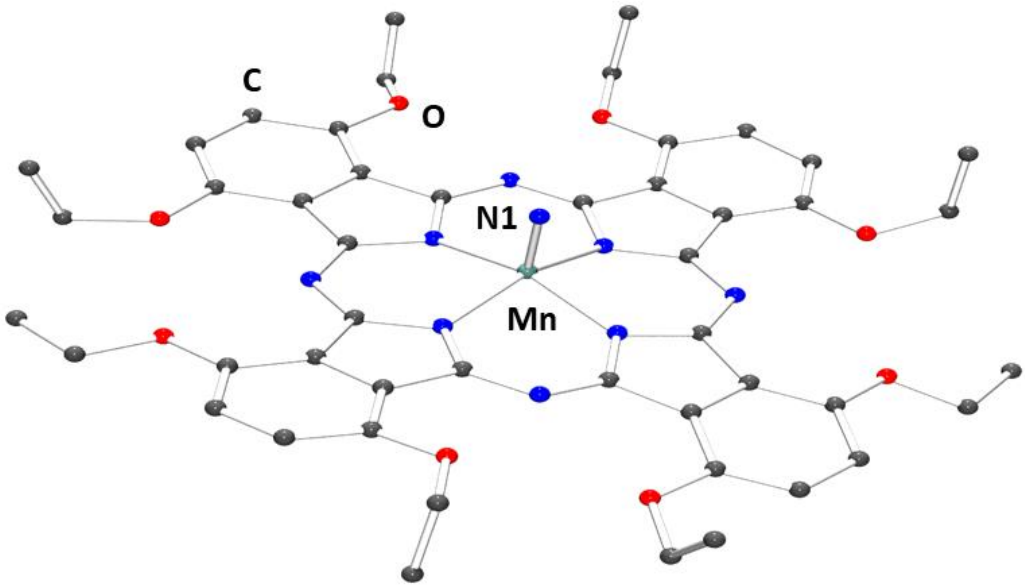

Figure 3.3. Solid state molecular structure of **3.2**. H atoms and co-crystallized solvent have been omitted for clarity.

Phthalocyanines are well-known redox-active ligands capable of spanning multiple oxidation states from Pc(0) to Pc(6-).[34] In conjunction with a highly redox-active metal center (Mn), we next proceeded to evaluate the redox behavior of **3.2**. Electrochemical analysis of **3.2** by cyclic voltammetry (CV) in dichloromethane (CH_2Cl_2) revealed a total of 4 reversible redox events (Figure 3.4): 2 separate oxidation events at $E_{1/2}$ = 0.02 V and $E_{1/2}$ = 0.45 V, and 2 reduction events at $E_{1/2}$ = -1.38 V and $E_{1/2}$ = -1.75 V referenced to the ferrocene/ferrocenium (Fc/Fc^+) redox couple.

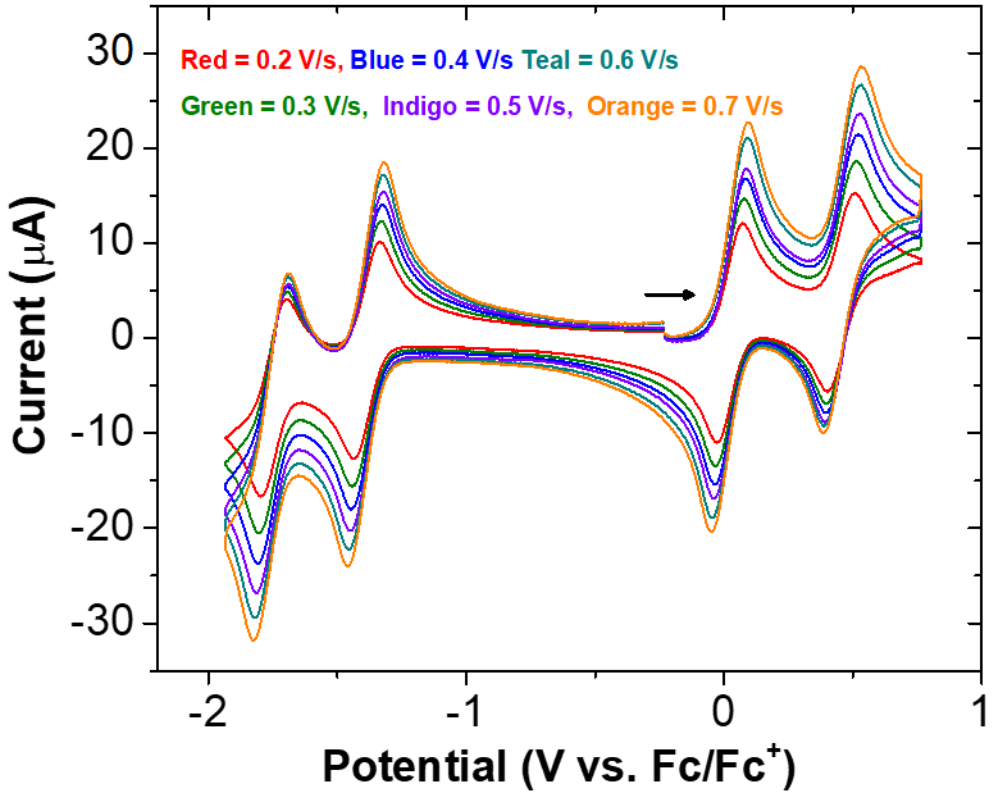

Figure 3.4. CV of **3.2** at varying scan rates (inset). Experimental conditions: Taken in CH_2Cl_2 with 0.29 mM of **3.2**, 0.1 M of $[Bu_4N][PF_6]$, 3 mm diameter glassy carbon working electrode, Pt wire counter electrode, and Pt wire pseudo-reference electrode.

Given the aromatic nature of **3.2**, as well as the relative scarcity of crystallographically-characterized PcM complexes in varying oxidation states,[18, 20-21, 49-53] we next proceeded to isolate each redox state to gain an understanding of the changing aromaticity and concomitant structural changes. Certainly, similar work has been done with other systems. Leznoff has published a non-isostructural CrPc series that was characterized across five oxidation states.[53] The comparison is interesting given the redox activity of the Cr center coupled with the redox non-innocence of the Pc ring. However, there are two distinct differences between the Leznoff work and the work presented here. First the CrPc series is

non-isostructural. Second, as will be described below, the Mn(V) does not appear to participate in the reported redox events which is not true of the CrPc series. Here, the Mn(V) core (perhaps surprisingly) appears to be electronically inert, with the nitride functioning as a non-reactive "cap", rather than a reactive motif, allowing the redox behavior of the Pc ring to be studied in isolation.

The oxidized complexes were targeted using the tris(4-bromophenyl)ammoniumyl tetrakis(pentafluorophenyl)borate "magic blue" oxidant, $[(4\text{-}BrC_6H_4)_3N][B(C_6F_5)_4]$ ($E_{1/2}$ = 0.70 V vs. Fc/Fc^+).[37, 54-55] To isolate the mono-oxidized product, a dark green diamagnetic solution of **3.2** in CH_2Cl_2 was treated to 1 equivalent of $[(4\text{-}BrC_6H_4)_3N][B(C_6F_5)_4]$ resulting in a dark red (λ_{max} = 820 nm) solution with a paramagnetically-broadened ^1H NMR (Scheme 3.1, path iv). Single crystals suitable for XRD studies of the product were grown by layering benzene over a saturated fluorobenzene solution. The solid-state structure confirmed the composition of the new product as $[^{EtO}PcMnN][B(C_6F_5)_4]$ (**3.2**$^+$) (Figure 3.5).

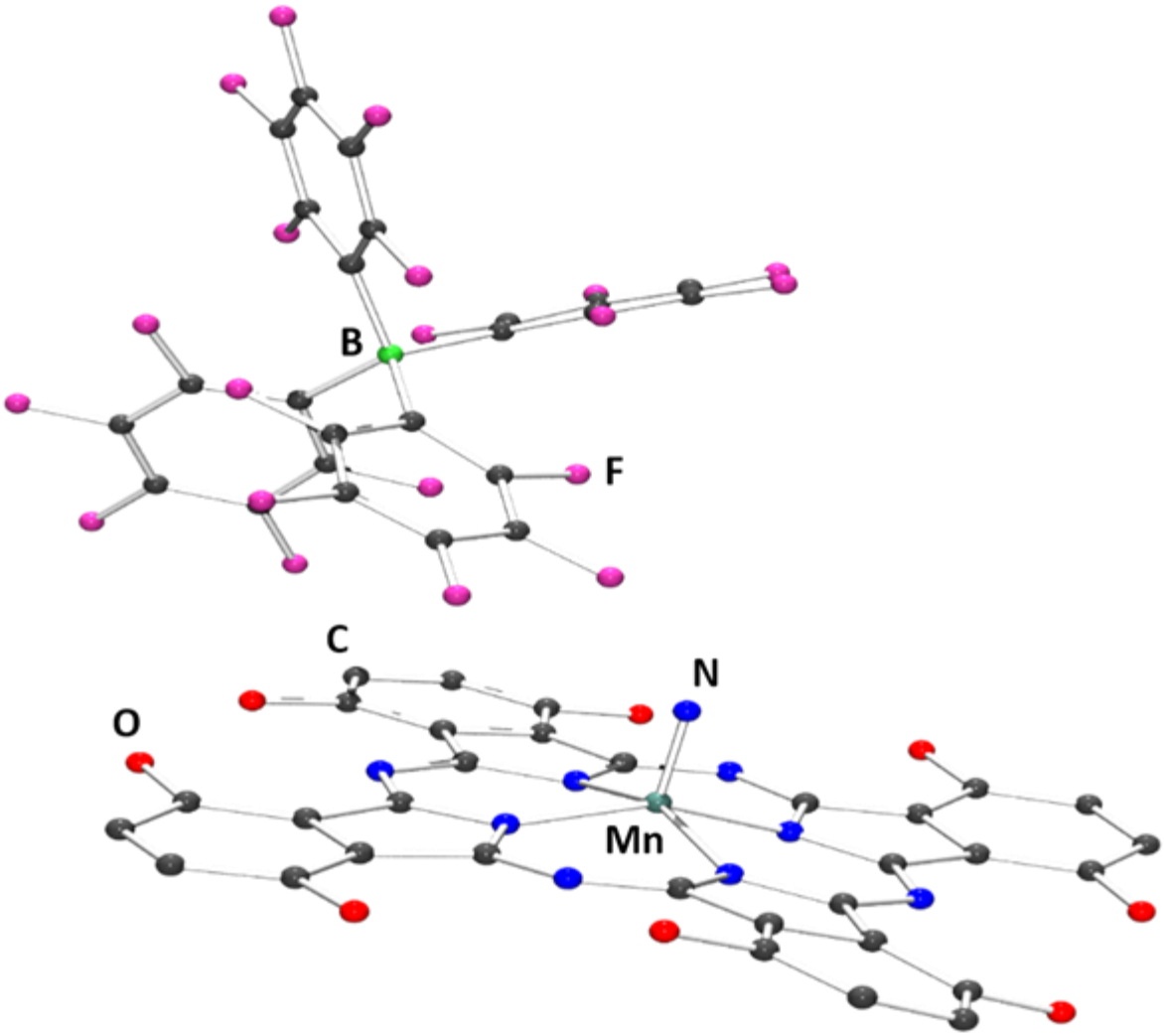

Figure 3.5. Solid-state molecular structure of **3.2**$^{+}$. Hydrogen atoms, ethoxy carbon atoms, and co-crystallized solvent are omitted for clarity.

To probe the locus of oxidation in **3.2**$^{+}$, single crystals were dissolved in CH_2Cl_2 and analyzed by X-band EPR spectroscopy at 100 K. An intense isotropic signal centered at g = 1.995 indicative of an organic radical species is observed, consistent with a 1 e^- oxidation of the ligand π system.

In contrast, treatment of **3.2** with 2 equivalents of $[(4\text{-}BrC_6H_4)_3N][B(C_6F_5)_4]$ resulted in a deep fuchsia (λ_{max} = 832 nm) solution which, after workup, displayed an upfield shifted

diamagnetic ^{1}H NMR spectrum relative to **3.2** (*vide infra*) (Scheme 3.1, path iii). Single crystals suitable for XRD studies were isolated by layering a concentrated solution of product in fluorobenzene with benzene at room temperature. The identity of the product was confirmed as the di-cation, $[^{EtO}PcMnN][B(C_6F_5)_4]_2$ (**3.2**$^{2+}$) (Figure 3.6). Structural characteristics for both **3.2**$^{+}$ and **3.2**$^{2+}$ are described in more detail in the following section.

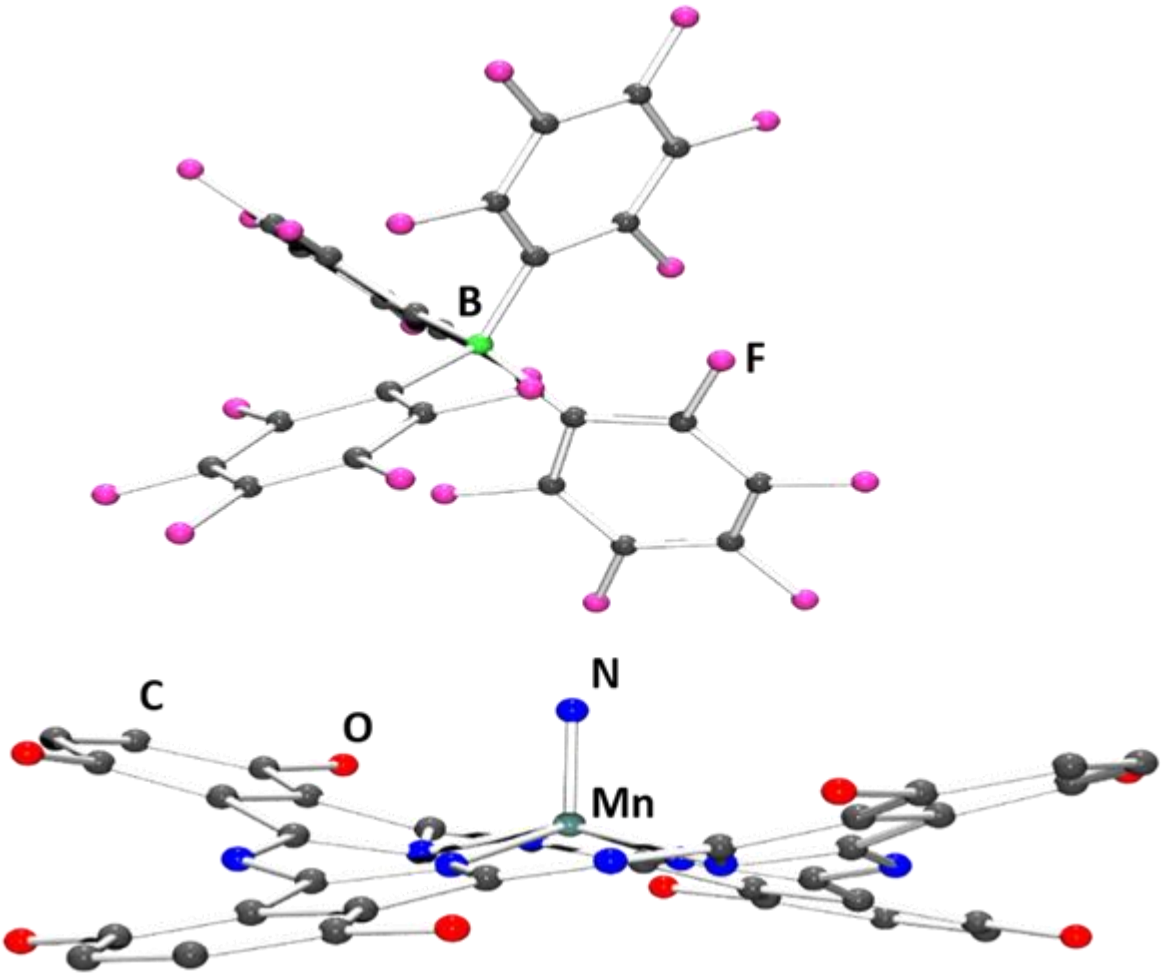

Figure 3.6. Solid-state molecular structure of **3.2**$^{2+}$. Hydrogen atoms, ethoxy carbon atoms, and co-crystallized solvent are omitted for clarity. The unit cell consists of a half-fragment of **3.2**$^{2+}$ and a full $[B(C_6F_5)_4]^{-}$ fragment. The former is grown for clarity.

For the anionic states of **3.2**, potassium graphite (KC_8) was used as the reductant of choice.[56] Chemical reduction of **3.2** with 1 equivalent of KC_8 in the presence of the cryptand, 4,7,13,16,21,24-hexaoxa-1,10-diazabicyclo[8.8.8]hexacosane (Kryptofix-222 = kryp), resulted in a dark teal, ^{1}H NMR silent solution (λ_{max} = 767 nm). Single crystals suitable for XRD studies were grown from tetrahydrofuran (THF)/isooctane by vapor diffusion and the solid-state structure confirmed the composition as the mono-anion, [K(kryp)][^{EtO}PcMnN] (**3.2**$^-$) (Figure 3.7, Scheme 3.1, path v).

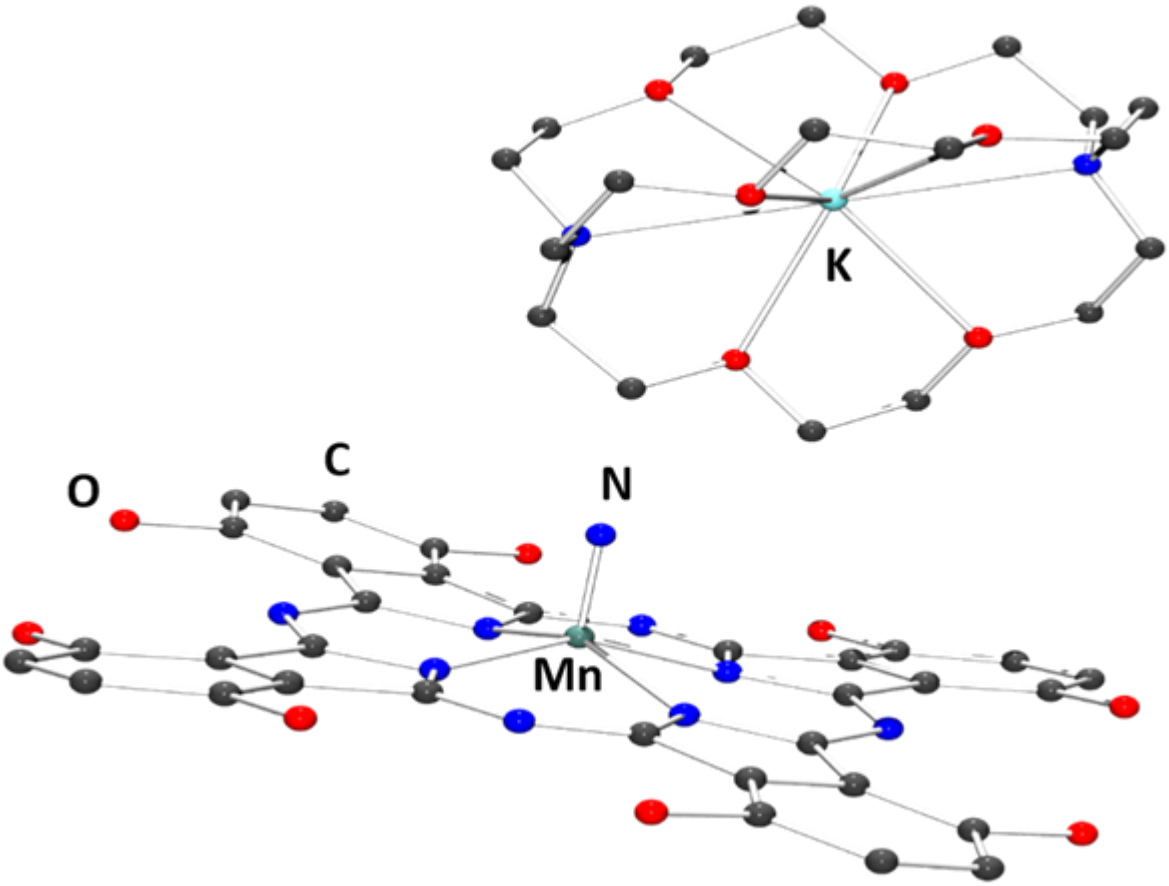

Figure 3.7. Solid-state molecular structure of **3.2**$^-$. Hydrogen atoms, ethoxy carbon atoms, and co-crystallized solvent are omitted for clarity.

Similar to **3.2**$^{+}$, the EPR spectrum of **3.2**$^{-}$ dissolved in THF revealed an intense, isotropic signal centered at g = 1.996 consistent with a ligand-borne reduction event.

Similarly, treatment of **3.2** with excess KC_8 in the presence of Kryptofix-222 yielded a dark blue, diamagnetic complex which, similar to **3.2**$^{2+}$, displays an upfield shifted ^{1}H NMR spectrum relative to **3.2** (*vide infra*) (λ_{max} = 767 nm). Single crystals suitable for XRD studies were grown from benzene/isooctane by vapor diffusion and the solid-state structure confirmed the composition as the di-anion, [K(kryp)]$_2$[^{EtO}PcMnN] (**3.2**$^{2-}$) (Figure 3.8, Scheme 3.1, path vi). Structural characteristics for both **3.2**$^{-}$ and **3.2**$^{2-}$ are described in more detail in the following section.

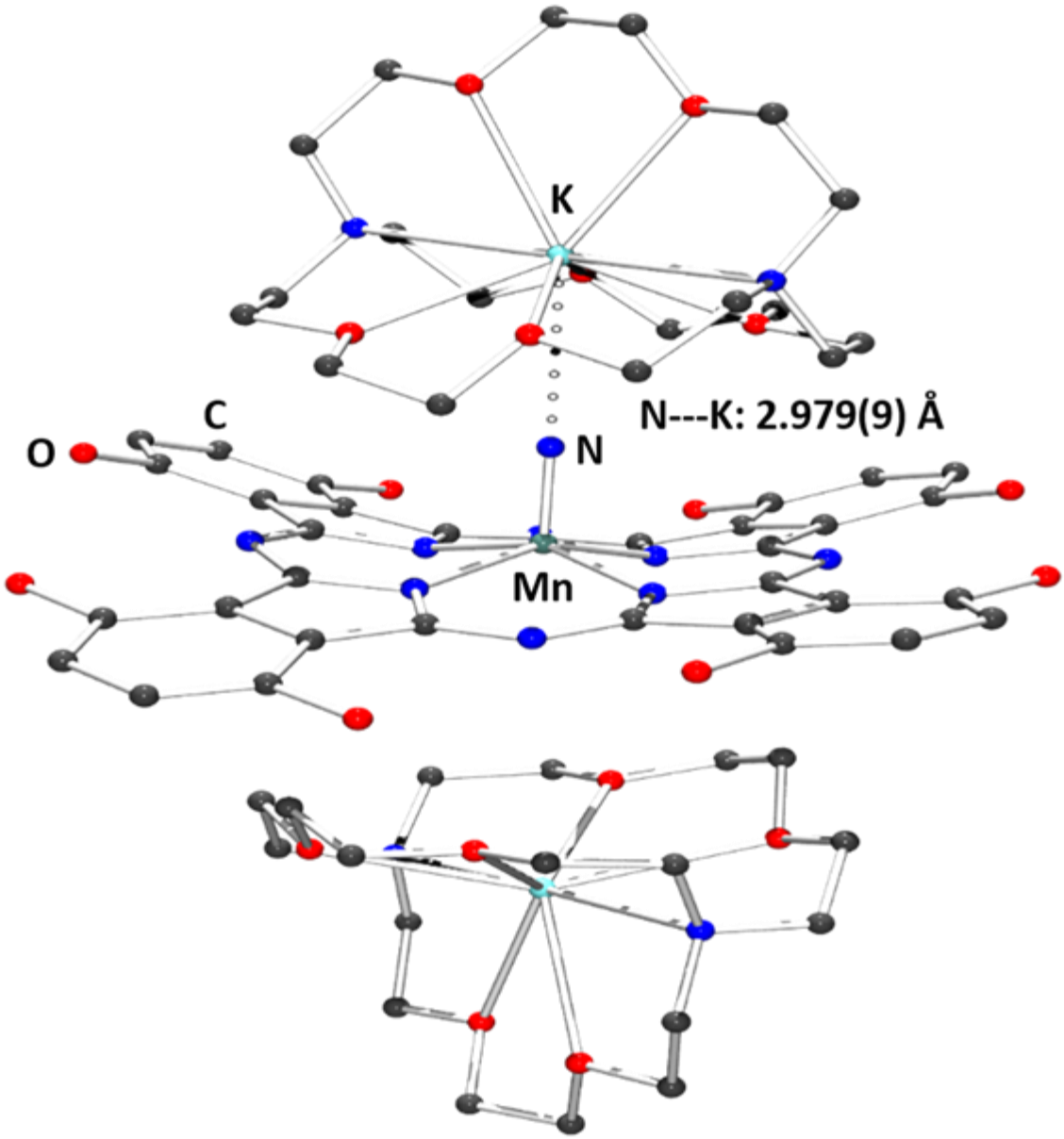

Figure 3.8. Solid-state molecular structure of **3.2**$^{2-}$. Hydrogen atoms, ethoxy carbon atoms, and co-crystallized solvent are omitted for clarity.

We note that **3.2**$^{2-}$ likely contains trace **3.2**$^{-}$ in solution as observed by a resonance in the EPR spectrum similar to **3.2**$^{-}$. This is a known issue with compounds containing the highly reduced Pc(4-) ligand[21] and likely accounts for a small amount of contamination in solution.

3.2.2 Structural Properties.

While both metal and/or ligand-based redox events are possible in this system, a closer look at the Mn≡N bond lengths for **3.2**$^{2+}$→**3.2**$^{2-}$ (Figure 3.9) suggests little to no participation of the Mn center in the observed redox processes, consistent with the EPR spectroscopic results above.

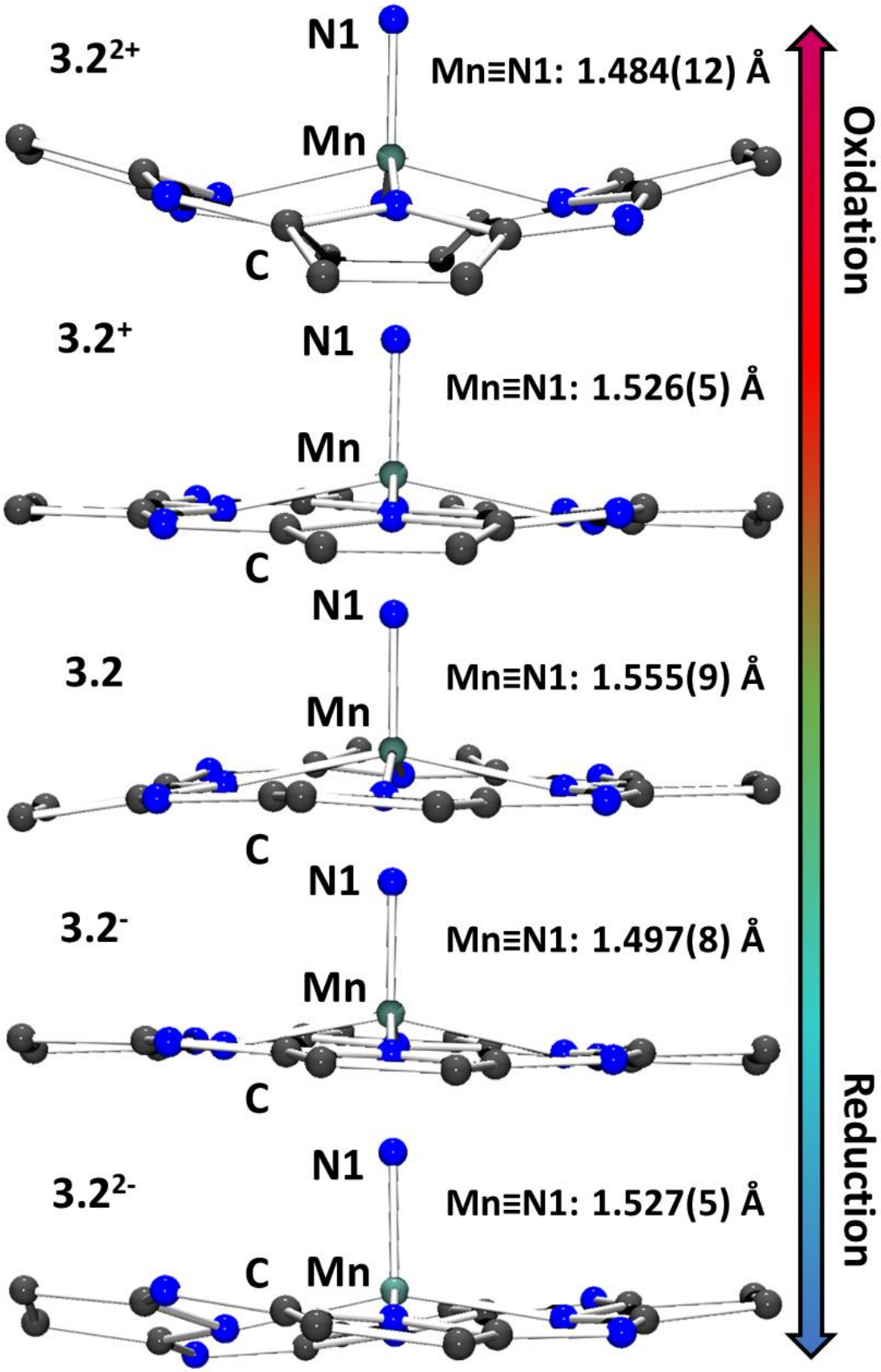
3.2²⁺
N1
Mn≡N1: 1.484(12) Å
Mn
C
3.2⁺
N1
Mn≡N1: 1.526(5) Å
Mn
C
N1
3.2
Mn≡N1: 1.555(9) Å
Mn
C
N1
3.2⁻
Mn≡N1: 1.497(8) Å
Mn
C
N1
3.2²⁻
Mn≡N1: 1.527(5) Å
C
Mn
Oxidation
Reduction

Figure 3.9. Solid-state structures of **3.2**$^{2+}$, **3.2**$^{+}$, **3.2**, **3.2**$^{-}$, and **3.2**$^{2-}$ illustrating Mn≡N bond lengths and core structural distortions. Hydrogen atoms, peripheral substituted benzene groups, and co-crystallized solvent molecules are omitted for clarity.

Such participation would be expected to either render the Mn≡N bond reactive[37, 57] and/or alter its bond length. In contrast, the observed bond lengths are all similar to other Mn(V)≡N bonds in comparable symmetry and oxidation states.[37, 39, 46-48]. It should be noted that while M≡N bond length is a useful metric for determining the oxidation state of the metal in nitride complexes, it cannot reliably serve as a standalone measure for determining metal oxidation state. The only notable change is with **3.2**$^{2-}$ where nitride coordination to a K^+ (from $[K(kryp)]^+$) occurs (Figure 3.8). However, this appears to have no impact on the Mn≡N bond length (Figure 3.9) or the resulting diamagnetism of the compound.[58]

Perhaps the most striking differences between all structures are the pronounced Pc ring distortions. While PcM complexes generally adopt planar geometries,[16, 18, 34, 49, 59] axial metal bonding (ex. M-Cl, M=O)[20, 49, 51-52, 60] and/or heavy element bonding in the pocket[61-62] typically yields domed structures. In contrast, *ortho* group incorporation in the isoindole rings[63-66] can result in saddling of the Pc ring with adjacent isoindole rings pointing in opposite directions relative to the N_4 plane (N_4 = N2-N4-N6-N8, Figure 3.10a).[65] The degree of doming or saddling is reported with respect to the dihedral angles formed between the N_4 and isoindole planes or between opposing isoindole planes (ex. I_1 vs. I_3, Figure 3.10a), respectively.[20-21, 63-66]

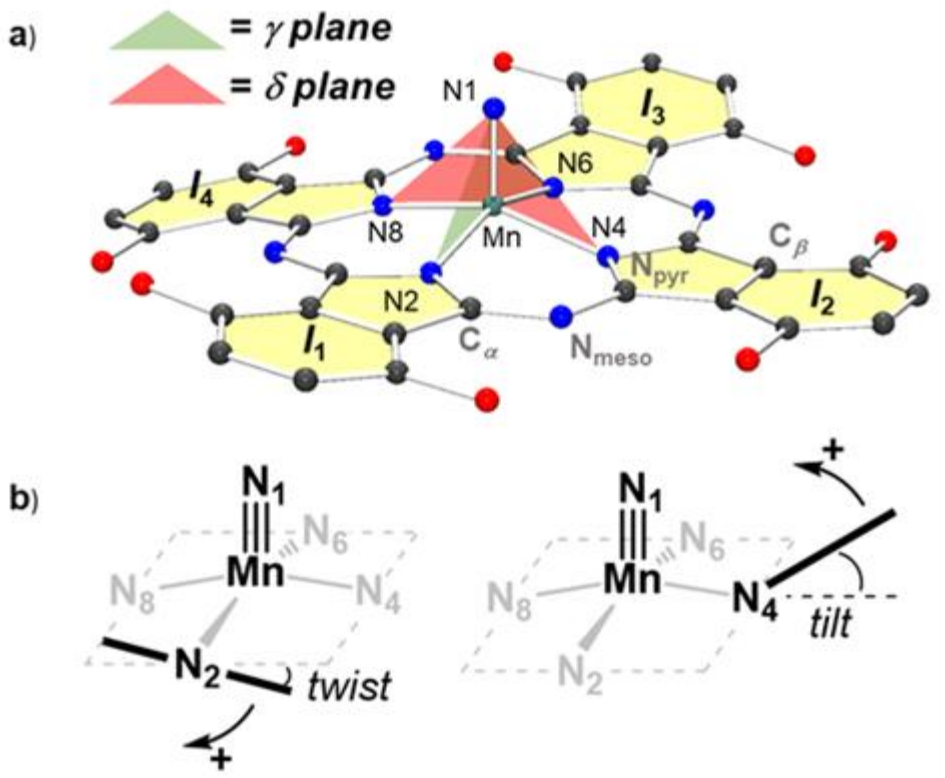

Figure 3.10. a) Depictions of the γ, *δ*, and isoindolic (*I*$_1$-*I*$_4$) planes, as well as relevant atom labels. b) Twist and tilt notation used in this report where clockwise twist and upward tilt are given positive values.

While the Mn≡N bond vector sits atop the N_4 planes in our complexes (Figure 3.9) with Mn–N_4 distances ranging from 0.40-0.48 Å (Table 3.1), none of the structures are domed. Only **3.2**$^{2+}$ is saddled and contains dihedral angles of 27.7° and 36.9° (average 32.3°) for the *I*$_1$-*I*$_3$ and *I*$_2$-*I*$_4$ planes, respectively (Figure 3.10a), comparable to very saddled structures.[63] In contrast, **3.2**$^{+}$, **3.2**, **3.2**$^{-}$, and **3.2**$^{2-}$ are best described as adopting mixed non-planar conformations.[49] As such, we find that a description of each structure's distortions applying the domed/saddled dihedral convention is insufficient as each isoindole ring can be twisted and/or tilted relative to the N_4 plane. Therefore, we define secondary γ and *δ* planes

Table 3.1. Tilt and twist dihedral angles for 3.2^{2+}, 3.2^{+}, 3.2, 3.2^{-}, and 3.2^{2-}.[a]

	Mn⋯N_4 (Å)	twist(°)					tilt(°)					Σ twist-tilt
		I_1-δ	I_2-γ	I_3-δ	I_4-γ	|avg.|	I_1-γ	I_2-δ	I_3-γ	I_4-δ	|avg.|	
3.2^{2+}	0.48	-1.8	-4.6	-1.8	-4.6	**3.2**	-18.4	13.1	-18.4	13.1	**15.8**	**19.0**
3.2^{+}	0.42	9.7	-4.6	-0.3	0.1	**3.7**	-2.7	4.0	0.1	-5.8	**3.2**	**6.9**
3.2 [b]	0.40 (0.41)	3.2 (1.1)	3.0 (1.0)	-3.8 (-5.6)	0.4 (-0.2)	**2.3**	5.2 (2.6)	1.4 (1.9)	5.7 (4.6)	-11.7 (-8.7)	**5.2**	**7.5**
3.2^{-} [b]	0.41 (0.45)	-6.0 (6.9)	-4.1 (1.7)	-6.0 (6.9)	-4.1 (1.7)	**4.7**	-2.1 (-13.1)	-2.6 (0.9)	-2.1 (-13.1)	-2.6 (0.9)	**4.7**	**9.4**
3.2^{2-}	0.45	11.8	-5.0	8.2	-11.2	**9.0**	-11.4	-5.0	11.3	-10.8	**9.6**	**18.6**

[a] calculated from the normal of an isoindole plane (I_i) relative to the γ or δ plane where a clockwise twist or an upward tilt are given as positive (Figure 3.10b).

[b] values in parentheses are from a second molecule in the asymmetric unit of the solid-state structure. Averages are taken of all values.

encompassing the Mn-N1-N4-N8 and Mn-N1-N2-N6 planes, respectively. The twist/tilt angles are then calculated from the normal of an isoindole plane (I_i) relative to a given γ or δ plane (Table 3.1) with a clockwise twist or an upward tilt given as positive (Figure 3.10b). Using this approach provides a more detailed look at Pc ring distortions, while also capturing traditional saddled dihedral angles, such as for **3.2^{2+}**, by instead summing the I_1-I_3 and I_2-I_4 tilt angles (Table 3.1). As an overall metric of distortion, we have summed the average twist and tilt values and have found a clear trend in structural distortions wherein both **3.2^{2+}** and **3.2^{2-}** are heavily distorted – 19.0° and 18.6°, respectively – relative to **3.2^{+}** (6.9°), **3.2** (7.5°), and **3.2^{-}** (9.4°) (Table 3.1).

A closer look at the bond lengths within the ^{EtO}Pc structures may provide insight as to the nature of the distortions. While the Pc(2-) ligand is overall aromatic, this aromaticity is often ascribed to localized internal neutral [18]annulene or dianionic ([16]annulene)$^{2-}$ 18 π e^{-} circuits encircling the central pocket, as described above (Figure 3.1b-c).[5, 7, 18, 20-21]

Assuming average C–N single and double bond lengths of 1.47 Å and 1.27 Å,[67] respectively, a closer look at the bond lengths in **3.2** suggests a [16]annulene circuit is at play (Figures 3.1c, Table 3.7). Specifically, the average C–N bond length of the [16]annulene (C_8N_8) circuit between pyrrolic nitrogen (N_{pyr}) and C_α, as well as between meso nitrogen (N_{meso}) and C_α (Figure 3.10a) is 1.351 Å (range: 1.307-1.408 Å). In contrast, the average C_α–C_β bond length is 1.459 Å (range: 1.436-1.473 Å), suggesting a disconnection between the central C_8N_8, 18 π e^- circuit from each of the outer 6 π phenyl aromatic systems (Figure 3.3). Furthermore, the C_8N_8 ring is nearly perfectly planar with an average atom-to-plane displacement of only 0.032 Å (range: 0.002-0.095 Å). Together, this is consistent with a $([16]annulene)^{2-}$, 18 π e^- model in **3.2** (Figure 3.1c).[5, 7]

Similar to **3.2**, the average C_α–C_β bonds in $\mathbf{3.2^{2+}}$ are elongated (Table 3.9, average: 1.444 Å; range: 1.434-1.454 Å) relative to the C–N bonds of the C_8N_8 core (average: 1.344 Å; range: 1.294-1.380 Å). This again suggests disconnected 6 π phenyl aromatic fragments tethered to a 16 π *non*-aromatic C_8N_8 core (*vide infra*). In contrast to **3.2**, the change to a non-aromatic system in $\mathbf{3.2^{2+}}$ is evidenced by the significant distortions from planarity observed in the C_8N_8 core where the average atom-to-plane displacement is now 0.145 Å (range: 0.006-0.296 Å). Such reported 16 π non-aromatic porphyrinoid cores show similar degrees of distortions from planarity.[22]

A similarly distorted C_8N_8 core is observed in $\mathbf{3.2^{2-}}$ where the average atom-to-plane displacement is slightly higher than $\mathbf{3.2^{2+}}$ at 0.159 Å (range: 0.007-0.322 Å). However, in contrast to **3.2** and $\mathbf{3.2^{2+}}$, the N_{meso}-C_α bonds (Figure 3.10a) display a distinct short/long pattern with mean short and long bonds of 1.298 Å (range: 1.295-1.301 Å) and 1.374 Å (range: 1.370-1.377 Å), respectively (Table 3.11). Furthermore, this short/long pattern propagates along a single axis containing two trans-disposed isoindole units, connected to

the C_8N_8 core by shortened C_α–C_β bonds (mean: 1.412 Å; range: 1.397-1.426 Å) relative to the perpendicular C_α–C_β set (mean: 1.467 Å; range: 1.460-1.474 Å), the latter being similar to those in **3.2** and **3.2**$^{2+}$. Together, this data suggests a 20 π e^-, dianionic ([18]annulene)$^{2-}$ *anti*-aromatic framework (Figure 3.1b). The bond length patterns are also similar to previously observed anti-aromatic Pc(4-) systems.[18, 20-21]

In contrast to the redox extrema in **3.2**$^{2+}$ and **3.2**$^{2-}$, **3.2**$^{+}$ and **3.2**$^{-}$ show minimal net distortions relative to **3.2** (Table 3.1), consistent with a delocalized radical state. The average C_α–C_β bond length for **3.2**$^{+}$ and **3.2**$^{-}$ do not vary significantly from the values of **3.2** (Table 3.9, Table 3.10). Additionally, the M≡N bond length in both **3.2**$^{+}$ (1.526(5) Å) and **3.2**$^{-}$ (1.497(8) Å) relative to **3.2** (1.555(9) Å) seem to suggest little electronic participation of the metal or apical nitrogen towards these events, corroborating the solution-state spectra that suggest a highly delocalized radical residing on the ring, a common state for mono-oxidized and mono-reduced macrocyclic systems.[16, 35, 50-52]

3.2.3 Spectroscopic Properties.

NMR spectroscopy is one of the most direct experimental methods for distinguishing diatropic from paratropic ring currents commonly associated with classic Hückel aromatic (4n + 2)π and anti-aromatic (4n)π systems, respectively.[1, 68-70] Diatropic π electron ring currents result in typical downfield shifted outer ring protons (ex. benzene), whereas an opposite paratropic current emerges in anti-aromatic systems resulting in an opposite upfield shift of outer ring protons.[17-19, 71-72] The ^{1}H NMR resonances of **3.2** appear at 7.63 (CH), 4.97 (CH_2), and 1.85 (CH_3) ppm in CD_2Cl_2 (Figure 3.11a). The corresponding resonances for **3.2**$^{2+}$ in the same solvent are only slightly upfield shifted (7.51, 4.60, and 1.60 ppm) and not indicative of any major paratropic ring current supporting a localized inner, non-

aromatic [16]annulene ring (Figure 3.11b). The ^{1}H NMR resonances of **3.2**$^{2+}$ and **3.2**$^{2-}$ both exhibit C_4 symmetry in solution, likely a result of rapid interchange of orthogonal tautomers consistent with other similar annulene structures.[73] In contrast, the resonances of **3.2**$^{2-}$ are significantly upfield shifted (4.53, 2.53, 0.64 ppm) and indicative of a strong, inner paratropic current. In addition, the resonances attributed to the Kryptofix-222 protons are broadened and significantly *downfield* shifted at (6.30, 5.79, 4.29 ppm) relative to published values (Figure 3.11c).[74-76] This may be the result of equilibrium coordination to the terminal nitride forcing the [K(kryp)]$^{+}$ cations to reside above the plane of the paratropic current, as observed in the solid state structure (Figure 3.8), and resulting in a downfield shift similar to previous reports.[17-19] We note that the spectrum of **3.2**$^{2-}$ was collected in C_6D_6 for stability reasons, and then directly compared to **3.2**, also collected in C_6D_6, and reveals that the shift is not merely from solvent effects.

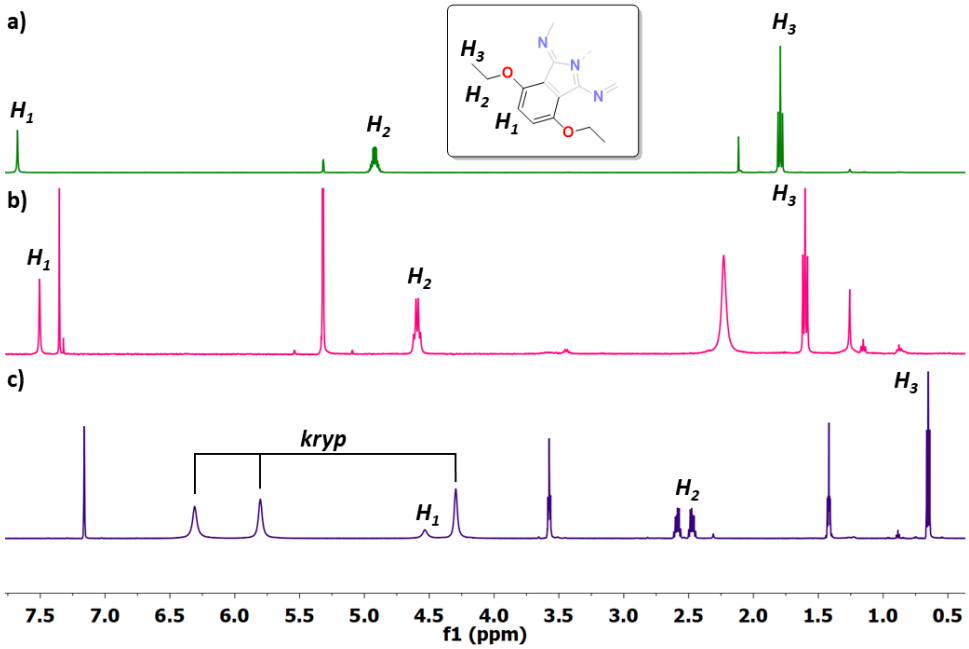

Figure 3.11. ^{1}H NMR spectra of a) **3.2** in CD_2Cl_2; b) **3.2**$^{2+}$ in CD_2Cl_2; c) **3.2**$^{2-}$ in C_6D_6, illustrating the shift in phenyl (H_1), methylene (H_2), and methyl (H_3) resonances as a

function of oxidation state and associated aromatic character. Kryptofix-222 (kryp) resonances are also shown in c). Other peaks in a-c correspond to residual solvents.

The UV-Vis spectra of all five isolated redox states in the series were measured. The Q-band for **3.2** occurs at 767 nm and becomes progressively red-shifted and broadened upon oxidation (**3.2**$^{+}$: 820 nm, **3.2**$^{2+}$ 832 nm). These results do not follow predictive models proposed by Gouterman and Lever for the correlation between oxidation state and Q-band position in metallophthalocyanines.[77] However, the apparent switching from an aromatic core (**3.2**) to non-aromatic (**3.2**$^{2+}$), and the high degree of structural distortion adds complexity that is not necessarily represented in the above predictive models. It should be noted that the UV-Vis spectrum of **3.2**$^{2+}$ still displays strikingly low energy transitions for our non-aromatic assignment, differing from analogous 16 π e^{-} porphyrin-based systems. However, non-aromatic Pc-derivatives have been demonstrated to display such UV-Vis spectra, and may be the result of intra-macrocycle charge transfer transitions.[78] Due to the surprisingly small shift in the observed Q-band, we also performed time-dependent UV-Vis experiments to verify that **3.2**$^{2+}$ did not decompose within the timescale of data collection, and verified that it is stable (Figure 3.12).

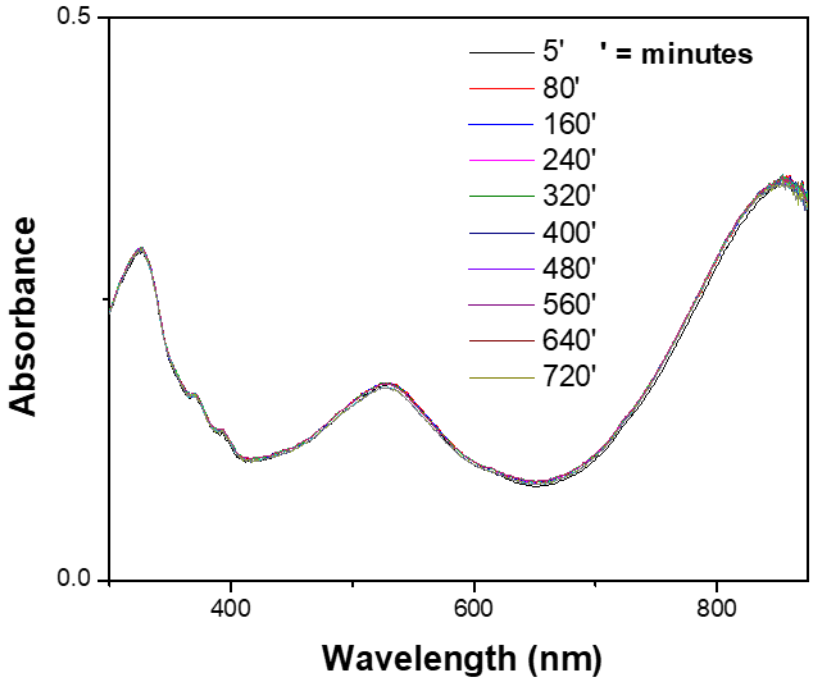

Figure 3.12. Time-dependent UV-Vis spectrum of **3.2**$^{2+}$ taken in CH_2Cl_2 (5.6 μM).

In contrast to the oxidation series, the reduction products are quite air- and moisture-sensitive. This coupled with the necessarily low concentration for collection led to increased difficulty in data collection. Indeed, time-dependent UV-Vis spectral acquisition of putative **3.2**$^{2-}$ indicates decomposition (Figure 3.13), with two initial weak blue-shifted absorption peaks, at 577nm and 624nm, in the expected regime for Pc(4-) complexes decomposing into two new red-shifted bands, at 673nm and 752nm, similar to the peaks of **3.2**.[79-81] Lastly, attempted acquisition of the spectrum for **3.2**$^{-}$ reveal two bands similar to **3.2**, again indicating likely decomposition. Given the above considerations, the UV-Vis of the reductive products remain unassigned.

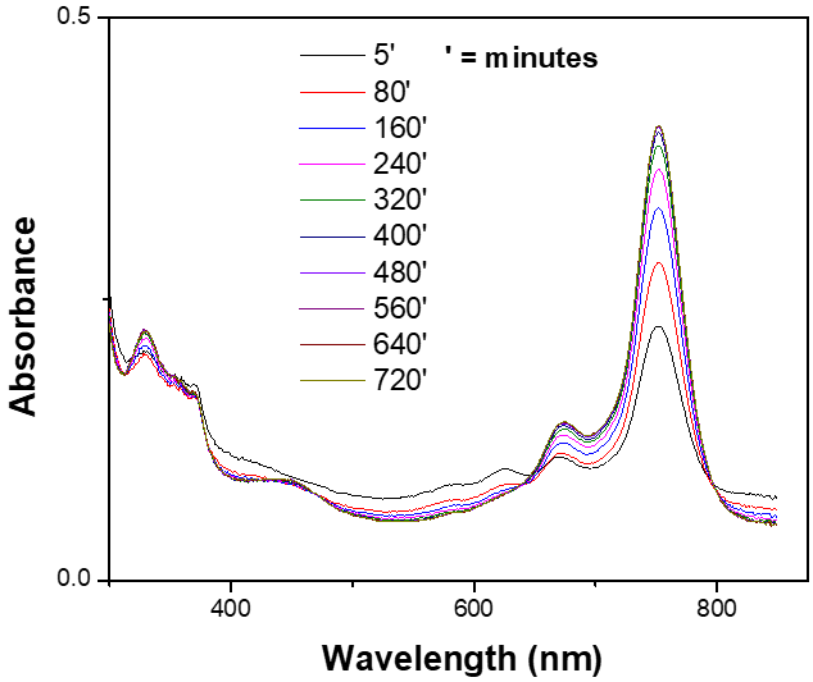

Figure 3.13. Time-dependent UV-Vis spectrum of **3.2**$^{2-}$ taken in THF (4.0 μM).

3.2.4 Computational Results.

To correlate our NMR data, we performed Nucleus-Independent Chemical Shift (NICS) calculations on **3.2**, **3.2**$^{2+}$, and **3.2**$^{2-}$ (Figure 3.14 a-c). Developed by Schleyer,[82] this technique has been highly effective in distinguishing diatropic (aromatic) from paratropic (anti-aromatic) ring currents in macrocyclic compounds, such as porphyrinoids and Pc.[2, 9, 17-18, 25, 68, 83] The NICS calculations were performed at a point in space 1 Å above the plane of each sub-ring following the normal (see Figure 6a blue dots which indicate the centers of each sub-ring). For **3.2**, negative NICS values are observed throughout the entire ring system (Figure 3.14a), consistent with diatropic (aromatic) current. In contrast, a substantial reduction in diatropic current is observed in **3.2**$^{2+}$, particularly in the central [16]annulene core and adjacent pyrrole sub-rings, indicating a significant decrease in aromaticity (Figure

3.14b). The outer phenyl fragments, however, are significantly less affected by this loss in diatropic current, supporting a localized aromaticity switch from aromatic (**3.2**) to non-aromatic (**3.2**$^{2+}$) at the [16]annulene core. These NICS data are also consistent with the observed modest upfield shift of the ^{1}H NMR resonances for **3.2**$^{2+}$ relative to **3.2** (Figure 3.11a-b). Together, we propose that the switch from aromatic (**3.2**) to non-aromatic (**3.2**$^{2+}$) π systems *is likely the root cause of the significant structural distortions observed in **3.2**$^{2+}$ relative to **3.2*** (Figure 3.9, Table 3.1), with the former adopting a central [16]annulene 16 π e^{-} core. Indeed, structural parameters, such as atom-to-plane displacement patterns (*vide supra*, Figure 3.9), largely mimic those reported for the solid state structure of authentic [16]annulene.[84]

More drastic changes are observed in the high positive NICS values of **2**$^{2-}$ relative to **3.2**, consistent with a strong paratropic ring current extending along a dianionic ([18]annulene)$^{2-}$ 20 π e^{-} antiaromatic core (Figure 6c). These NICS data are consistent with the large upfield shifts observed for peripheral Pc protons, and downfield shifts observed for Kryptofix-222 protons sitting atop the paratropic ring current (*vide supra*, Figure 3.14c). This paratropic circuit, spanning a single [18]annulene axis, is also supported by the structural data indicating short vs. long C_{α}–C_{β} bond lengths in orthogonal isoindole units (*vide supra* and Figure 3.14c). As in **3.2**$^{2+}$, we believe that the aromaticity switch between **3.2** (aromatic) and **3.2**$^{2-}$ (antiaromatic) is mostly responsible for the significant structural distortions observed (*vide supra*, Figure 3.9, Table 3.1), similar to those observed from planar [18]annulene[85] to the distorted ([18]annulene)$^{2-}$ dianion.[86]

DFT studies at the M06-2X level of theory with the 6-31+G** basis set were also performed on the entire isostructural series **3.2**$^{2+}$, **3.2**$^{+}$, **3.2**, **3.2**$^{-}$, and **3.2**$^{2-}$, utilizing the XRD coordinates as starting geometries (see Experimental Considerations for full computational

details). The highest occupied molecular orbitals (HOMOs) for **3.2**, **3.2**$^{2+}$, and **3.2**$^{2-}$ are shown in Figures 3.14d, 3.14e, and 3.14f, respectively.

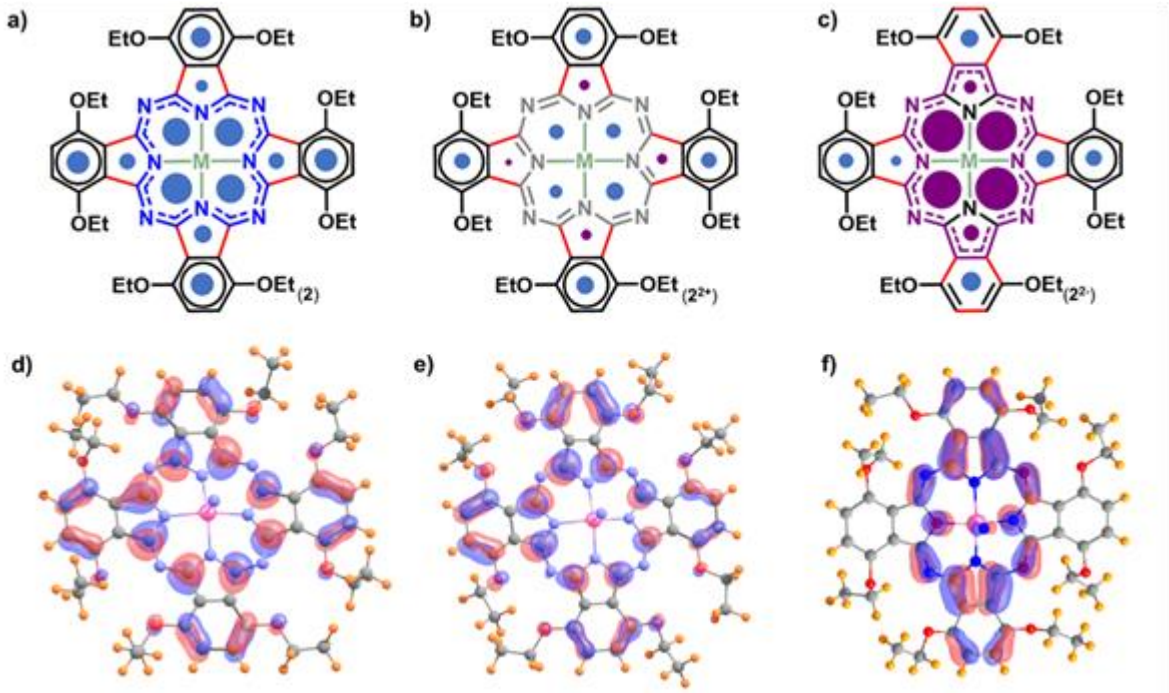

Figure 3.14. (a-c) Proposed aromatic (blue), non-aromatic (gray), and anti-aromatic (purple) circuits, as well as elongated single bonds (red) for **3.2** (a), **3.2**$^{2+}$ (b), **3.2**$^{2-}$ (c). Circles represent NICS values, with the area of each circle directly proportional to the NICS value (blue=negative, purple=positive), at 1 Å above the respective sub-ring geometric center and normalized against the highest absolute value (see Experimental Considerations for full computational details). (d-f) Corresponding HOMOs for **3.2** (d), **3.2**$^{2+}$ (e), **3.2**$^{2-}$ (f).

For **3.2** and **3.2**$^{2+}$, a central orbital density contribution encompassing the proposed [16]annulene core, encircled by a circular node, is observed and is flanked by orbital densities on the outer benzene fragments (Figures 3.14a-b,d-e). Interestingly, the HOMO of **3.2**$^{2-}$ also reflects the structural data and model proposed for the anti-aromatic [18]annulene model (Figures 3.14c,f). The orbital density shown also corresponds to the short bonds

described above. Together, the frontier orbitals of all complexes are consistent with exclusively ligand-borne redox events with little to no contribution from the Mn center (Figure 3.14). The only exception is in **3.2**$^{2-}$ where the HOMO displays a small fraction of orbital density at the nitride, consistent with its coordination to [K(kryp)]$^{+}$ (Figures 3.14f, 3.8).

3.3 Summary

In conclusion, we have outlined the synthesis and characterization of a novel manganese nitride phthalocyanine (**3.2**), which is the first clearly characterized example of a large macrocyclic system that can access the triad of aromatic, non-aromatic, and antiaromatic states through a series of reversible redox events. Combined structural, spectroscopic, and computational studies reveal that all redox events are ligand-borne centering on specific annulene-like internal circuits. Altering the degree of aromaticity and pathway of these circuits is proposed to be the root cause of the observed structural distortions. Perhaps surprisingly, the frontier orbitals are demonstrated to have minimal contribution from the Mn(V) center or the apical nitrogen, with the Mn≡N motif functioning more as an inert "cap" than an electronic participant. The synthetic accessibility, stability, isolable nature, and scope of aromatic behavior make this complex an attractive platform for studying switchable aromaticity in broader contexts, such as in organic electronic devices. Our current interests are in studying these stable complexes as charge carriers for energy storage applications.

3.4 Experimental

3.4.1 Considerations

Techniques and Reagents. All manipulations were performed under an atmosphere of dry, oxygen-free N_2 within an MBraun glovebox (MBRAUN UNIlab Pro SP Eco equipped with a -40 ^oC freezer), or by standard Schlenk techniques. Pentane, Et_2O, CH_2Cl_2 and THF (inhibitor-free) were dried and degassed on an MBraun Solvent Purification System and stored over activated 4 Å molecular sieves. All other solvents were degassed by freeze-pump-thaw and stored on activated 4 Å molecular sieves prior to use. Celite® and 4 Å molecular sieves were dried at 250 ^oC under dynamic vacuum (<0.1 Torr) for 24 h prior to use. Elemental analyses were recorded at the University of California, Berkeley using a Perkin Elmer 2400 Series II combustion analyzer. $MnCl_2$ and NH_4OH were purchased from Fisher Scientific, Li metal, 2,3-dicyanohydroquinone from Acros Organics, and ethyl iodide from Alfa Aesar and all were used without further purification. $[(4\text{-}BrC_6H_4)_3N][B(C_6F_5)_4]$[37] and KC_8[56] were prepared following previous reports. All other reagents were obtained from Sigma-Aldrich, Fisher Scientific, or VWR and used without further purification.

Spectroscopic Measurements. NMR spectra were obtained on an Agilent Technologies 400 MHz spectrometer, or a Varian 600 MHz spectrometer, and referenced to residual solvent. Chemical shifts (δ) are recorded in ppm and the coupling constants are in Hz. J-Young air-tight adaptors were used for air- and water-sensitive compounds. Perpendicular-mode X-band EPR spectra were collected on a Bruker EMX EPR Spectrometer equipped with an Oxford ESR 900 liquid helium cryostat. All EPR samples contained ~ 1 mg of material and data acquisition collected at 100K in frozen CH_2Cl_2 or THF for $\mathbf{3.2}^+$ or $\mathbf{3.2}^-$, respectively. It should be noted that a small residual free radical signal is often observed in phthalocyanines, and has been attributed to sample grinding-induced defects.[87] UV-Vis spectra were collected on a Shimadzu UV-2401PC spectrophotometer. All measurements were performed on recrystallized product. All stock solutions and dilutions were prepared by mass. ATR FT-IR

spectra were collected on a Bruker Alpha Platinum with an ATR Quicksnap® Sampling Module. All measurements were performed on recrystallized product.

Magnetic Measurements. Solution magnetic moment measurements were performed by the Evans method[36] utilizing fluorobenzene residual solvent in combination with ^{19}F NMR spectroscopy. All moments were measured in triplicate with averages reported.

X-ray Crystallography. Data was collected on a Bruker KAPPA APEX II diffractometer equipped with an APEX II CCD detector using a TRIUMPH monochromator with a Mo Kα X-ray source (α = 0.71073 Å). The crystals were mounted on a cryoloop under Paratone-N oil, and all data were collected at 100 K using an Oxford nitrogen gas cryostream system. A hemisphere of data was collected using ω scans with 0.5° frame widths. Data collection and cell parameter determination were conducted using the SMART program. Integration of the data frames and final cell parameter refinement were performed using SAINT software. Absorption correction of the data was carried out using SADABS. Structure determination was done using direct or Patterson methods and difference Fourier techniques. All hydrogen atom positions were idealized and rode on the atom of attachment. Structure solution, refinement, graphics, and creation of publication materials were performed using SHELXTL or OLEX^2. Data collection for **3.2**$^{2+}$ was performed at The Center for Advanced Radiation Sources (CARS) utilizing the Advanced Photon Source (APS), a high-brilliance synchrotron X-ray source at Argonne National Lab.

Electrochemical Measurements. CV was performed on a CH Instruments 630E Electrochemical Analysis Potentiostat. The working electrode was a 1.5 mm radius glassy carbon (CH Instruments) and was cleaned prior to each experiment by sequentially polishing with a gradient of 1.0 μm, 0.3 μm, and 0.05 μm alumina (CH Instruments) on a cloth pad, followed by rinsing with distilled water and acetone. The Pt wire pseudo-reference and

counter electrodes were rinsed with distilled water and acetone and heated white-hot with a butane torch. All measurements were performed on recrystallized product and referenced to the Fc/Fc^+ redox couple unless otherwise stated.

DFT computations. Quantum calculations were carried out using the Gaussian-09 suite of programs.[88] The 6-31+G** basis set was used in conjunction with the M06-2X DFT functional.[89] Geometries were obtained using the X-ray coordinates and optimizing the positions of all H atoms. NICS data was calculated 1 Å above the geometric center of each sub-ring, using X-ray coordinates.

3.4.2 Syntheses

3,6-Diethoxyphthalonitrile. 3,6-Diethoxyphthalonitrile was synthesized using a modified procedure previously reported by Rauchfuss.[33] A mixture of 10.00 g (0.062 mol, 1 eq.) of 2,3-dicyanohydroquinone and 17.26 g (0.124 mol, 2 eq.) of K_2CO_3 in 125 mL of wet acetone was heated to reflux and sparged with N_2 for 10 mins. Ethyl iodide (29.02 g, 0.186 mol, 3 eq.) was then added dropwise to the mixture. The yellow slurry was stirred under reflux for 24 h. After cooling, the yellow solid was filtered off and washed with 500 mL of water, 150 mL of Et_2O, collected, and then dried under vacuum to afford an off-white powder. Yield: 6.78 g (50.2%). ^{1}H NMR (400 MHz, $CDCl_3$): δ 7.14 (s, 2H, C_6H_2.), 4.13 (q, J = 7.0 Hz, 4H, OCH_2CH_3), 1.47 (t, J = 7.0 Hz, 6H, OCH_2CH_3).

Lithium 1,4,8,11,15,18,22,25-Octaethoxyphthalocyanine (^{EtO}PcHLi). This precursor was synthesized using a modified procedure previously reported by Rauchfuss.[33] A mixture of 6.00 g (0.028 mol, 1 eq.) of 3-6-diethoxyphthalonitrile in 75 mL of wet EtOH was heated to reflux and sparged with N_2 for 10 mins. Li pellets (2.43 g, 0.347 mol, 12.5 eq.) were added over the course of 10 mins, resulting in a large quantity of white gas evolving as the mixture

turned dark green. After addition of the Li pellets, another 75 mL of wet EtOH was added. The mixture was refluxed for 5 days. After cooling, 100 mL of EtOH and 100 mL of H_2O was added and the green solid was filtered off and washed with 100 mL of H_2O, 100 mL of EtOH, and 100 mL of Et_2O. The resulting green powder was dried under dynamic vacuum for 24 h. Yield: 4.64 g (76.6%). ^{1}H NMR (400 MHz, $CDCl_3$): δ 14.74 (s, 1H, N*H*), 7.52-7.42 (m, 8H, C_6H_2), 4.95 (m, 16H, OCH_2CH_3), 1.82 (m, 24H, OCH_2CH_3). ^{7}Li NMR ($CDCl_3$): Silent.

1,4,8,11,15,18,22,25-Octaethoxyphthalocyanine ($^{EtO}PcH_2$). ^{EtO}PcHLi (4.00 g, 4.56 mmol, 1 eq.) was slurried in 100 mL of H_2O in a flask and heated to 60 °C. HCl (12.1 M, 4 mL, 10 eq.) was added dropwise over the course of 15 mins, changing the green slurry to a purple solution. After 72 h of stirring, 19 g (0.1368 mol, 30 eq.) of K_2CO_3 was carefully added over the course of 15 mins, returning the purple solution to a green slurry. The slurry was filtered, and washed with 100 mL of H_2O, and 100 mL of Et_2O. The resulting green powder was dried under vacuum. Yield: 2.81 g (71 %). ^{1}H NMR (400 MHz, $CDCl_3$): δ 7.61 (s, 8H, C_6H_2), 4.95 (q, *J* = 7.0 Hz, 16H, OCH_2CH_3), 1.84 (t, *J* = 7.0 Hz, 24H, OCH_2CH_3), 0.21 (s, 2H, N*H*).

^{EtO}PcMnCl (3.1). A mixture of 2.00 g (2.3 mmol, 1 eq.) of $^{EtO}PcH_2$, 2.00 g (excess) of $MnCl_2$, and 0.969 g (11.5 mmol, 5 eq.) of $NaHCO_3$ was slurried in 20 mL DMF in open air and heated to 100 °C for 5 h, resulting in a red/purple solution. After cooling, 150 mL of water was added, and the solution was stirred for 30 mins. The mixture was filtered, and washed with 100 mL of water, followed by 100 mL of Et_2O. The resulting red powder was dried under vacuum. Single crystals suitable for XRD studies were obtained by layering benzene over a saturated fluorobenzene solution of **3.1** at room temperature. Yield: 1.35 g (61.4%). ^{1}H NMR (400 MHz, CD_2Cl_2): δ 6.69 (bs), 1.74 (bs), -5.82 (bs). Anal. Calc. for

$C_{48}H_{48}ClMnN_8O_8 \bullet CH_2Cl_2$: C, 56.58; H, 4.84; N, 10.77. Found: C, 55.66; H, 4.47; N, 11.73. μ_{eff} (Evans method): 4.64 μ_B (S = 2). λ_{max}(Q-peak) = 825 nm.

^{EtO}PcMnN (3.2). Compound **3.1** (1.05 g, 1.05 mmol, 1 eq.) was added to 100 mL of MeOH, resulting in a purple/red solution. Concentrated NH_4OH (1.05 mL, 14.7 mmol, 15 eq.) was added dropwise over the course of 5 mins followed by 9.5 mL (~6 eq.) Clorox® bleach over the course of 15 mins, resulting in the production of a white gas and a green solution. The solution was stirred for an additional 5 mins and then placed into an ice bath for 10 mins. While cooling, 75 mL of CH_2Cl_2 was slowly added, followed by 50 mL of H_2O, and subsequently transferred to a separatory funnel. The organic layer was washed 3 times with 50 mL of H_2O and then reduced to dryness under vacuum at 60 ^oC, yielding a dark green powder which was then dissolved in CH_2Cl_2 and recrystallized by layering with Et_2O, yielding dark green plate-like crystals. Yield: 0.908 g (88.5 %). ^1H NMR (400 MHz, CD_2Cl_2): δ 7.63 (s, 8H, C_6H_2), 4.97 (m, 16H, OCH_2CH_3), 1.85 (t, J = 7.0 Hz, 24H, OCH_2CH_3). $^{13}C\{^1H\}$ NMR: δ 150.9, 148.3, 127.2, 117.6, 67.0, 15.44. Anal. Calc. for $C_{48}H_{48}MnN_9O_8$: C, 61.73; H, 5.18; N, 13.50. Found: C, 61.59; H, 5.00; N, 13.45. λ_{max}(Q-peak) = 767 nm.

[^{EtO}PcMnN][B(C_6F_5)$_4$] (3.2$^+$). In a glovebox, 0.020 g (0.0214 mmol) of **3.2** was dissolved in ~7.5 mL of CH_2Cl_2. [(4-BrC_6H_4)$_3$N][B(C_6F_5)$_4$] (24.9 mg, 0.0214 mmol, 1 eq.) was dissolved in ~2.5 mL of CH_2Cl_2, which was added dropwise to the green CH_2Cl_2 solution of **3.2** under stirring, turning the solution wine red. The solution was stirred for 5 mins, then reduced to dryness under reduced pressure. Benzene (15 mL) was added, and the solution was stirred for an additional 10 mins. The slurry was filtered through a glass wool Celite® plug resulting in a light green/yellow effluent and dark powder on the plug. The powder was extracted with CH_2Cl_2, resulting in a wine-red solution. The solution was pumped to

dryness, resulting in a dark red powder that was stored at -40 °C. Recrystallizations were performed by layering in fluorobenzene with benzene at room temperature, resulting in small trapezoidal red crystals. Yield: 0.031 g (90.9%). ^{1}H NMR (400 MHz, CD_2Cl_2): Silent. $^{11}B\{^{1}H\}$ NMR: δ -14.7 (s). $^{19}F\{^{1}H\}$ NMR: δ 131.2 (bs), 161.8 (t), 165.6 (bs). Anal. Calc. for $C_{72}H_{48}BF_{20}MnN_9O_8$: C, 53.62; H, 3.00; N, 7.82. Found: C, 53.46; H, 2.67; N, 7.38. λ_{max}(Q-peak) = 820 nm.

[^{EtO}PcMnN][B(C_6F_5)$_4$]$_2$ (3.2^{2+}). In a glovebox, 0.020 g (0.0214 mmol) of **3.2** was dissolved in ~7.5 mL of CH_2Cl_2. [(4-BrC_6H_4)$_3$N][B(C_6F_5)$_4$] (49.7 mg, 0.0428 mmol, 2 eq.) was dissolved in ~2.5 mL of CH_2Cl_2, which was added dropwise to the green CH_2Cl_2 solution of **3.2** under stirring, turning the solution deep fuchsia. The solution was stirred for 5 mins, then reduced to dryness under reduced pressure. Benzene (15 mL) was added, and the solution was stirred for an additional 10 mins. The slurry was filtered through a glass wool Celite® plug resulting in a light blue effluent and dark powder on the plug. The powder was extracted with CH_2Cl_2, resulting in a deep fuchsia solution. The solution was pumped to dryness, resulting in dark purple microcrystals that were stored at -40 °C. Recrystallizations were performed by layering in fluorobenzene with benzene at room temperature, resulting in rectangular purple crystals. Yield: 0.031 g (64.0%). ^{1}H NMR (400 MHz, CD_2Cl_2): δ 7.51 (s, 8H, C_6H_2), 4.60 (q, *J* = 7.0 Hz, 16H, OCH_2CH$_3$), 1.60 (t, *J* = 7.0 Hz, 24H, OCH$_2$CH_3). $^{13}C\{^{1}H\}$ NMR (low signal/noise): δ 149.7, 147.2, 137.8, 135.5, 130.4, 128.7, 115.5, 67.3, 15.1. $^{11}B\{^{1}H\}$ NMR: δ -16.7 (s). $^{19}F\{^{1}H\}$ NMR: δ 133.2 (bs), 163.6 (t), 167.5 (bs). Anal. Calc. for $C_{96}H_{48}B_2F_{40}MnN_9O_8$: C, 50.31; H, 2.11; N, 5.50. Found: C, 50.70; H, 1.91; N, 5.24. λ_{max}(Q-peak) = 832 nm.

[K(kryp)][^{EtO}PcMnN] (3.2^{-}). In a glovebox, 0.050 g (0.0535 mmol) of **3.2** was dissolved in ~7.5 mL of THF with 0.022 g (0.0588 mmol, 1.1 eq.) of Kryptofix® 222. KC_8 (0.0072 g,

0.0533 mmol, 1 eq.) was slurried in THF and added dropwise to the green solution of **3.2** under stirring, turning the solution deep teal. The solution was stirred for 10 mins, then reduced to dryness under vacuum. Benzene (10 mL) was added, and the solution stirred for 15 mins, resulting in a dark green/teal solution that was filtered through a glass wool Celite® plug resulting in a deep green/teal effluent and dark powder on the plug. The product was extracted with THF, resulting in a dark teal effluent which was then reduced to dryness to yield the microcrystalline product. Recrystallizations were performed by layering in THF with isooctane at -30 °C, resulting in small, trapezoidal purple/blue crystals. Yield 0.010 g (13.9%). ^{1}H NMR (400 MHz, d_8-THF): Silent with the exception of trace signals of **3.2**$^{2-}$ present. Anal. Calc. for $C_{66}H_{84}KMnN_{11}O_{14}$: C, 58.74; H, 6.27; N, 11.42. Found: C, 58.87; H, 6.37; N, 11.33.

[K(kryp)]$_2$[^{EtO}PcMnN] (3.2^{2-}). In a glovebox, 0.020 g (0.0214 mmol) of **3.2** was dissolved in ~7.5 mL of THF with 0.017 g (0.0454 mol, 2.1 eq.) of Kryptofix® 222. KC_8 (0.0145 g, 0.107 mol, 5 eq.) was slurried in THF and added dropwise to the green solution of **3.2** under stirring, turning the solution deep blue. The solution was stirred for 10 mins, then reduced to dryness under vacuum. Hexane (10 mL) was added, and the solution stirred for 15 mins, resulting in a dark blue suspension that was filtered through a glass wool, Celite® plug, resulting in a clear effluent and dark microcrystalline product on the plug. The product was extracted with THF, resulting in a dark blue effluent which was then reduced to dryness to yield the microcrystalline product. Recrystallizations were performed by layering a concentrated THF solution with isooctane at -30 °C resulting in large, sawtooth purple/blue crystals. Yield 0.016 g (42.3%). ^{1}H NMR (600 MHz, C_6D_6): δ 6.30 (bs, 24H, kryp), 5.79 (bs, 24H, kryp), 4.53 (s, 8H, C_6H_2), 4.29 (bs, 24H, kryp), 2.53 (ddq, J = 69.0, 10.6, 7.0 Hz,

16H, OC*H*$_2$CH$_3$), 0.64 (t, *J* = 7.0 Hz, 24H, OCH$_2$C*H*$_3$). Anal. Calc. for $C_{84}H_{120}K_2MnN_{13}O_{20}$: C, 57.16; H, 6.85; N, 10.32. Found: C, 56.95; H, 6.73; N, 10.06.

3.5 Crystallographic Tables

3.5.1 Selected Crystallographic Data

Table 3.2 – Selected crystallographic data for **3.1**.

Formula	$C_{52}H_{56}ClMnN_8O_9$
Formula wt.	1027.44
Crystal system	Monoclinic
Space group	P 21/c
a(Å)	14.330(5)
b(Å)	22.086(7)
c(Å)	16.661(5)
α(deg)	90
β(deg)	112.147(6)
γ(deg)	90
V(Å^3)	4884(3)
Z	4
T (K)	100(2)
d(calc) g/cm^3	1.395
Abs coeff, μ, mm^{-1}	0.391
Data collected	8246
R_{int}	0.0979
Data used	2961
Parameters	617
R (>2σ)	0.2904
wR_2	0.2592
GOF	0.974

Table 3.3 – Selected crystallographic data for **3.2**.

Formula	$C_{50}H_{48.5}Cl_4MnN_9O_8$
Formula wt.	1100.22
Crystal system	Tetragonal
Space group	I 41
a(Å)	37.0495(15)
b(Å)	37.0495(15)
c(Å)	14.6013(6)
α(deg)	90
β(deg)	90
γ(deg)	90
V(Å^3)	20042.7(18)
Z	16
T (K)	100(2)
d(calc) g/cm^3	1.458
Abs coeff, μ, mm^{-1}	0.541
Data collected	16914
R_{int}	0.0826
Data used	13140
Parameters	1276
R (>2σ)	0.1112
wR_2	0.2268
GOF	1.020

Table 3.4 – Selected crystallographic data for **3.2**$^{+}$.

Formula	$C_{80.5}H_{54}BF_{21.5}MnN_9O_8$
Formula wt.	1749.57
Crystal system	Triclinic
Space group	P -1
a(Å)	12.448(6)
b(Å)	16.428(8)
c(Å)	19.623(10)
α(deg)	72.870
β(deg)	78.954
γ(deg)	70.115(9)
V(Å^3)	3588(3)
Z	2
T (K)	100(2)
d(calc) g/cm^3	1.620
Abs coeff, μ, mm^{-1}	0.308
Data collected	13203
R_{int}	0.0723
Data used	4970
Parameters	1076
R (>2σ)	0.2466
wR_2	0.1437
GOF	0.930

Table 3.5 – Selected crystallographic data for **3.2**$^{2+}$.

Formula	$C_{138}H_{90}B_2F_{40}MnN_9O_8$
Formula wt.	2838.74
Crystal system	Tetragonal
Space group	I 41 c d
a(Å)	45.776(4)
b(Å)	45.776(4)
c(Å)	14.4580(12)
α(deg)	90
β(deg)	90
γ(deg)	90
V(Å^3)	30296(6)
Z	8
T (K)	100(2)
d(calc) g/cm^3	1.245
Abs coeff, μ, mm^{-1}	0.057
Data collected	8795
R_{int}	0.0677
Data used	8237
Parameters	892
R (>2σ)	0.0734
wR_2	0.1981
GOF	0.955

Table 3.6 – Selected crystallographic data for **3.2**$^{-}$.

Formula	$C_{79}H_{92}KMnN_{11}O_{15}$
Formula wt.	1421.58
Crystal system	Triclinic
Space group	P -1
a(Å)	14.123(4)
b(Å)	15.530(5)
c(Å)	16.283(5)
α(deg)	78.073(7)
β(deg)	80.064(6)
γ(deg)	89.083(7)
V(Å^3)	3441.0(18)
Z	2
T (K)	102(2)
d(calc) g/cm^3	1.323
Abs coeff, μ, mm^{-1}	0.299
Data collected	17131
R_{int}	0.0818
Data used	8457
Parameters	903
R (>2σ)	0.2102
wR_2	0.2593
GOF	0.940

Table 3.7 – Selected crystallographic data for **3.2**$^{2-}$.

Formula	$C_{96}H_{132}K_2MnN_{13}O_{20}$
Formula wt.	1921.28
Crystal system	Triclinic
Space group	P -1
a(Å)	14.626(3)
b(Å)	17.578(4)
c(Å)	19.915(4)
α(deg)	87.379(7)
β(deg)	70.556(5)
γ(deg)	89.075(6)
V(Å^3)	4823.2(16)
Z	2
T (K)	100(2)
d(calc) g/cm^3	1.323
Abs coeff, μ, mm^{-1}	0.299
Data collected	17131
R_{int}	0.0758
Data used	8457
Parameters	1193
R (>2σ)	0.1757
wR_2	0.2103
GOF	0.998

3.5.2 Bond Length Tables

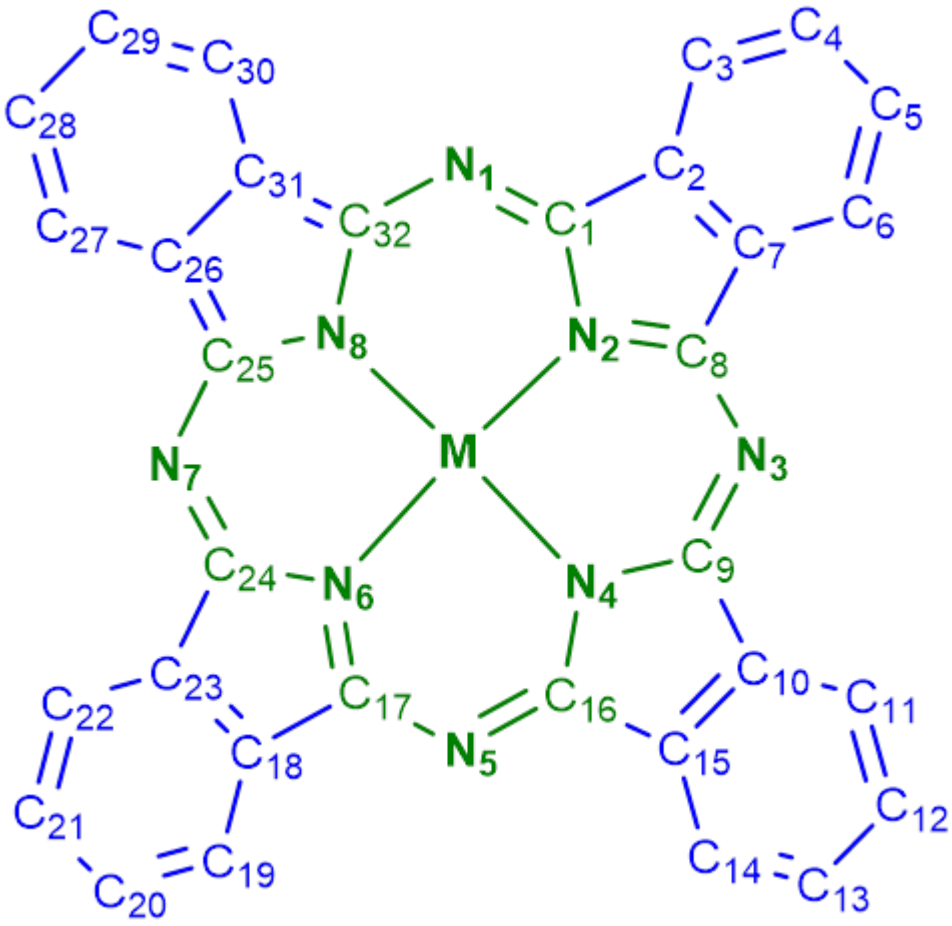

Figure 3.15. Atom denotations for **3.2**, **3.2**$^{+}$, **3.2**$^{2+}$, **3.2**$^{-}$, **3.2**$^{2-}$, used to construct the bond length metrics in Tables 3.X-3.X. Atomic labels do not correspond with CIF atomic labels, but rather an arbitrarily designated orientation. Bond lengths were measured from the CIF in Olex2. For unit cells containing multiple ^{EtO}PcM molecules, one was chosen as a representative molecule.

Table 3.8. Bond length metrics for **3.2**.

Core Bond Lengths (CW from N1; Å)	
N1-C1	1.321(1)
C1-N2	1.378(1)
N2-C8	1.368(1)
C8-N3	1.319(1)
N3-C9	1.322(1)
C9-N4	1.372(1)
N4-C16	1.362(1)
C16-N5	1.330(1)
N5-C17	1.316(1)
C17-N6	1.386(1)
N6-C24	1.376(1)
C24-N7	1.336(1)
N7-C25	1.320(1)
C25-N8	1.374(1)
N8-C32	1.390(1)
C32-N1	1.326(1)

Periphery Bond Lengths (CW from C1; Å)			
C1-C2	1.451(1)	**C17-C18**	1.466(2)
C2-C3	1.410(2)	**C18-C19**	1.412(2)
C2-C7	1.396(2)	**C18-C23**	1.386(2)
C3-C4	1.408(2)	**C19-C20**	1.377(2)
C4-C5	1.384(2)	**C20-C21**	1.354(2)
C5-C6	1.412(2)	**C21-C22**	1.416(2)
C6-C7	1.412(2)	**C22-C23**	1.380(2)
C7-C8	1.441(2)	**C23-C24**	1.469(1)
C9-C10	1.465(2)	**C25-C26**	1.473(2)
C10-C11	1.409(1)	**C26-C27**	1.393(2)
C10-C15	1.409(2)	**C26-C31**	1.399(1)
C11-C12	1.404(2)	**C27-C28**	1.400(2)
C12-C13	1.357(2)	**C28-C29**	1.365(2)
C13-C14	1.360(2)	**C29-C30**	1.391(2)
C14-C15	1.408(2)	**C30-C31**	1.425(2)
C15-C16	1.471(1)	**C31-C32**	1.448(2)

Table 3.9. Bond length metrics for **3.2**$^{+}$.

Core Bond Lengths (CW from N1; Å)			
N1-C1	1.324(9)		
C1-N2	1.378(8)		
N2-C8	1.377(9)		
C8-N3	1.336(8)		
N3-C9	1.353(7)		
C9-N4	1.967(5)		
N4-C16	1.373(7)		
C16-N5	1.337(8)		
N5-C17	1.318(8)		
C17-N6	1.402(8)		
N6-C24	1.372(8)		
C24-N7	1.333(8)		
N7-C25	1.330(7)		
C25-N8	1.371(8)		
N8-C32	1.372(7)		
C32-N1	1.320(8)		
Periphery Bond Lengths (CW from C1; Å)			
C1-C2	1.456(9)	**C17-C18**	1.431(9)
C2-C3	1.413(8)	**C18-C19**	1.416(8)
C2-C7	1.390(9)	**C18-C23**	1.401(9)
C3-C4	1.398(9)	**C19-C20**	1.402(9)
C4-C5	1.366(9)	**C20-C21**	1.396(9)
C5-C6	1.405(8)	**C21-C22**	1.394(8)
C6-C7	1.395(9)	**C22-C23**	1.382(9)
C7-C8	1.465(8)	**C23-C24**	1.469(8)
C9-C10	1.446(9)	**C25-C26**	1.461(9)
C10-C11	1.386(9)	**C26-C27**	1.385(9)
C10-C15	1.404(8)	**C26-C31**	1.426(8)
C11-C12	1.409(8)	**C27-C28**	1.411(8)
C12-C13	1.373(8)	**C28-C29**	1.392(8)
C13-C14	1.397(9)	**C29-C30**	1.363(9)
C14-C15	1.407(9)	**C30-C31**	1.379(9)
C15-C16	1.445(9)	**C31-C32**	1.451(10)

Table 3.10. Bond length metrics for **3.2**$^{2+}$.

Core Bond Lengths (CW from N1; Å)			
N1-C1	1.315(9)		
C1-N2	1.384(9)		
N2-C8	1.366(9)		
C8-N3	1.330(9)		
N3-C9	1.324(9)		
C9-N4	1.372		
N4-C16	1.387(9)		
C16-N5	1.334(9)		
N5-C17	1.315(9)		
C17-N6	1.366(9)		
N6-C24	1.384(9)		
C24-N7	1.330(9)		
N7-C25	1.324(9)		
C25-N8	1.372		
N8-C32	1.387(9)		
C32-N1	1.334(9)		
Periphery Bond Lengths (CW from C1; Å)			
C1-C2	1.479(10)	**C17-C18**	1.479(10)
C2-C3	1.400(10)	**C18-C19**	1.400(10)
C2-C7	1.395(10)	**C18-C23**	1.395(10)
C3-C4	1.416(10)	**C19-C20**	1.416(10)
C4-C5	1.359(10)	**C20-C21**	1.359(10)
C5-C6	1.408(10)	**C21-C22**	1.408(10)
C6-C7	1.386(10)	**C22-C23**	1.386(10)
C7-C8	1.454(10)	**C23-C24**	1.454(10)
C9-C10	1.440(10)	**C25-C26**	1.440(10)
C10-C11	1.386(10)	**C26-C27**	1.386(10)
C10-C15	1.413(10)	**C26-C31**	1.413(10)
C11-C12	1.448(10)	**C27-C28**	1.448(10)
C12-C13	1.357(10)	**C28-C29**	1.357(10)
C13-C14	1.433(10)	**C29-C30**	1.433(10)
C14-C15	1.403(10)	**C30-C31**	1.403(10)
C15-C16	1.433	**C31-C32**	1.433

Table 3.11. Bond length metrics for **3.2**$^{-}$.

Core Bond Lengths (CW from N1; Å)	
N1-C1	1.341(7)
C1-N2	1.383(7)
N2-C8	1.383(7)
C8-N3	1.330(7)
N3-C9	1.309(7)
C9-N4	1.388(7)
N4-C16	1.384(7)
C16-N5	1.302(7)
N5-C17	1.341(7)
C17-N6	1.383(7)
N6-C24	1.383(7)
C24-N7	1.330(7)
N7-C25	1.309(7)
C25-N8	1.388(7)
N8-C32	1.384(7)
C32-N1	1.302(7)

Periphery Bond Lengths (CW from C1; Å)			
C1-C2	1.433(8)	**C17-C18**	1.433(8)
C2-C3	1.400(8)	**C18-C19**	1.400(8)
C2-C7	1.400(8)	**C18-C23**	1.400(8)
C3-C4	1.389(9)	**C19-C20**	1.389(9)
C4-C5	1.387(9)	**C20-C21**	1.387(9)
C5-C6	1.379(9)	**C21-C22**	1.379(9)
C6-C7	1.413(8)	**C22-C23**	1.413(8)
C7-C8	1.435(8)	**C23-C24**	1.435(8)
C9-C10	1.468(7)	**C25-C26**	1.468(7)
C10-C11	1.394(8)	**C26-C27**	1.394(8)
C10-C15	1.393(8)	**C26-C31**	1.393(8)
C11-C12	1.387(8)	**C27-C28**	1.387(8)
C12-C13	1.385(8)	**C28-C29**	1.385(8)
C13-C14	1.382(8)	**C29-C30**	1.382(8)
C14-C15	1.403(8)	**C30-C31**	1.403(8)
C15-C16	1.480(8)	**C31-C32**	1.480(8)

Table 3.12. Bond length metrics for **3.2**$^{2-}$.

Core Bond Lengths (CW from N1; Å)			
N1-C1	1.297(6)		
C1-N2	1.396(6)		
N2-C8	1.401(6)		
C8-N3	1.300(6)		
N3-C9	1.380(6)		
C9-N4	1.380(6)		
N4-C16	1.384(6)		
C16-N5	1.375(6)		
N5-C17	1.302(6)		
C17-N6	1.392(6)		
N6-C24	1.392(6)		
C24-N7	1.301(6)		
N7-C25	1.378(6)		
C25-N8	1.377(6)		
N8-C32	1.379(6)		
C32-N1	1.363(6)		
Periphery Bond Lengths (CW from C1; Å)			
C1-C2	1.458(7)	**C17-C18**	1.472(6)
C2-C3	1.411(7)	**C18-C19**	1.400(7)
C2-C7	1.385(7)	**C18-C23**	1.401(7)
C3-C4	1.384(7)	**C19-C20**	1.386(7)
C4-C5	1.378(7)	**C20-C21**	1.386(8)
C5-C6	1.392(7)	**C21-C22**	1.388(7)
C6-C7	1.399(7)	**C22-C23**	1.391(7)
C7-C8	1.476(7)	**C23-C24**	1.461(7)
C9-C10	1.428(7)	**C25-C26**	1.411(7)
C10-C11	1.410(7)	**C26-C27**	1.414(7)
C10-C15	1.420(7)	**C26-C31**	1.424(7)
C11-C12	1.364(7)	**C27-C28**	1.362(7)
C12-C13	1.429(7)	**C28-C29**	1.427(7)
C13-C14	1.361(8)	**C29-C30**	1.351(7)
C14-C15	1.423(7)	**C30-C31**	1.430(7)
C15-C16	1.399(7)	**C31-C32**	1.417(7)

3.5 References

1. Pawlicki, M.; Latos-Grażyński, L. Aromaticity Switching in Porphyrinoids. *Chemistry – An Asian Journal* **2015,** *10*, 1438-1451.

2. Wu, J. I.; Fernández, I.; Schleyer, P. v. R. Description of Aromaticity in Porphyrinoids. *J. Am. Chem. Soc.* **2013,** *135*, 315-321.

3. Herges, R. Topology in Chemistry: Designing Möbius Molecules. *Chem. Rev.* **2006,** *106*, 4820-4842.

4. Vogel, E., The porphyrins from the 'annulene chemist's' perspective. In *Pure and Applied Chemistry*, 1993; Vol. 65, p 143.

5. Lash, T. D. Origin of aromatic character in porphyrinoid systems. *J. Porphyrins Phthalocyanines* **2011,** *15*, 1093-1115.

6. Sondheimer, F.; Wolovsky, R.; Amiel, Y. Unsaturated Macrocyclic Compounds. XXIII.1 The Synthesis of the Fully Conjugated Macrocyclic Polyenes Cycloöctadecanonaene ([18]Annulene),2 Cyclotetracosadodecaene ([24]Annulene), and Cyclotriacontapentadecaene ([30]Annulene). *J. Am. Chem. Soc.* **1962,** *84*, 274-284.

7. Webb, L. E.; Fleischer, E. B. The Structure of Porphine1. *J. Am. Chem. Soc.* **1965,** *87*, 667-669.

8. Janson, T. R.; Kane, A. R.; Sullivan, J. F.; Knox, K.; Kenney, M. E. Ring-current effect of the phthalocyanine ring. *J. Am. Chem. Soc.* **1969,** *91*, 5210-5214.

9. Jusélius, J.; Sundholm, D. The Aromatic Character of Magnesium Porphyrins. *J. Org. Chem.* **2000,** *65*, 5233-5237.

10. Jusélius, J.; Sundholm, D. The aromatic pathways of porphins, chlorins and bacteriochlorins. *Phys. Chem. Chem. Phys.* **2000,** *2*, 2145-2151.

11. Roncali, J. Molecular Engineering of the Band Gap of π-Conjugated Systems: Facing Technological Applications. *Macromolecular Rapid Communications* **2007,** *28*, 1761-1775.

12. Ronald, B.; Frank, W. F., Jr. Charge transport in nanoscale aromatic and antiaromatic systems. *Journal of Physics: Condensed Matter* **2008,** *20*, 374104.

13. Breslow, R.; Murayama, D. R.; Murahashi, S.; Grubbs, R. Quantitative assessment of the antiaromatic city of cyclobutadiene by electrochemical studies on quinone derivatives. *J. Am. Chem. Soc.* **1973,** *95*, 6688-6699.

14. Chen, W.; Li, H.; Widawsky, J. R.; Appayee, C.; Venkataraman, L.; Breslow, R. Aromaticity Decreases Single-Molecule Junction Conductance. *J. Am. Chem. Soc.* **2014,** *136*, 918-920.

15. Fujii, S.; Marqués-González, S.; Shin, J.-Y.; Shinokubo, H.; Masuda, T.; Nishino, T.; Arasu, N. P.; Vázquez, H.; Kiguchi, M. Highly-conducting molecular circuits based on antiaromaticity. *Nat. Commun.* **2017,** *8*, 15984.

16. Gardberg, A. S.; Doan, P. E.; Hoffman, B. M.; Ibers, J. A. Singly and Doubly Oxidized Phthalocyanine (pc) Rings: [Cu(pc)(ReO4)] and [Cu(pc)(ReO4)2]. *Angew. Chem. Int. Ed.* **2001,** *40*, 244-246.

17. Cissell, J. A.; Vaid, T. P.; Rheingold, A. L. An Antiaromatic Porphyrin Complex: Tetraphenylporphyrinato(silicon)(L)2 (L = THF or Pyridine). *J. Am. Chem. Soc.* **2005,** *127*, 12212-12213.

18. Cissell, J. A.; Vaid, T. P.; DiPasquale, A. G.; Rheingold, A. L. Germanium Phthalocyanine, GePc, and the Reduced Complexes SiPc(pyridine)2 and GePc(pyridine)2 Containing Antiaromatic π-Electron Circuits. *Inorg. Chem.* **2007,** *46*, 7713-7715.

19. Cissell, J. A.; Vaid, T. P.; Yap, G. P. A. Reversible Oxidation State Change in Germanium(tetraphenylporphyrin) Induced by a Dative Ligand: Aromatic GeII(TPP) and Antiaromatic GeIV(TPP)(pyridine)2. *J. Am. Chem. Soc.* **2007,** *129*, 7841-7847.

20. Wong, E. W. Y.; Walsby, C. J.; Storr, T.; Leznoff, D. B. Phthalocyanine as a Chemically Inert, Redox-Active Ligand: Structural and Electronic Properties of a Nb(IV)-Oxo Complex Incorporating a Highly Reduced Phthalocyanine(4−) Anion. *Inorg. Chem.* **2010,** *49*, 3343-3350.

21. Zhou, W.; Platel, R. H.; Teixeira Tasso, T.; Furuyama, T.; Kobayashi, N.; Leznoff, D. B. Reducing zirconium(iv) phthalocyanines and the structure of a Pc4-Zr complex. *Dalton Trans.* **2015,** *44*, 13955-13961.

22. Yamamoto, Y.; Yamamoto, A.; Furuta, S.-y.; Horie, M.; Kodama, M.; Sato, W.; Akiba, K.-y.; Tsuzuki, S.; Uchimaru, T.; Hashizume, D.; Iwasaki, F.

Synthesis and Structure of 16 π Octaalkyltetraphenylporphyrins. *J. Am. Chem. Soc.* **2005,** *127*, 14540-14541.

23. Yamamoto, Y.; Hirata, Y.; Kodama, M.; Yamaguchi, T.; Matsukawa, S.; Akiba, K.-y.; Hashizume, D.; Iwasaki, F.; Muranaka, A.; Uchiyama, M.; Chen, P.; Kadish, K. M.; Kobayashi, N. Synthesis, Reactions, and Electronic Properties of 16 π-Electron Octaisobutyltetraphenylporphyrin. *J. Am. Chem. Soc.* **2010,** *132*, 12627-12638.

24. Sugawara, S.; Hirata, Y.; Kojima, S.; Yamamoto, Y.; Miyazaki, E.; Takimiya, K.; Matsukawa, S.; Hashizume, D.; Mack, J.; Kobayashi, N.; Fu, Z.; Kadish, K. M.; Sung, Y. M.; Kim, K. S.; Kim, D. Synthesis, Characterization, and Spectroscopic Analysis of Antiaromatic Benzofused Metalloporphyrins. *Chem. Eur. J.* **2012,** *18*, 3566-3581.

25. Cissell, J. A.; Vaid, T. P.; Yap, G. P. A. The Doubly Oxidized, Antiaromatic Tetraphenylporphyrin Complex [Li(TPP)][BF4]. *Org. Lett.* **2006,** *8*, 2401-2404.

26. Xie, D.; Liu, Y.; Rao, Y.; Kim, G.; Zhou, M.; Yu, D.; Xu, L.; Yin, B.; Liu, S.; Tanaka, T.; Aratani, N.; Osuka, A.; Liu, Q.; Kim, D.; Song, J. meso-Triaryl-Substituted Smaragdyrins: Facile Aromaticity Switching. *J. Am. Chem. Soc.* **2018,** *140*, 16553-16559.

27. Konarev, D. V.; Kuzmin, A. V.; Faraonov, M. A.; Ishikawa, M.; Khasanov, S. S.; Nakano, Y.; Otsuka, A.; Yamochi, H.; Saito, G.; Lyubovskaya, R. N.

Synthesis, Structures, and Properties of Crystalline Salts with Radical Anions of Metal-Containing and Metal-Free Phthalocyanines. *Chem. Eur. J.* **2015,** *21*, 1014-1028.

28. Konarev, D. V.; Kuzmin, A. V.; Khasanov, S. S.; Otsuka, A.; Yamochi, H.; Saito, G.; Lyubovskaya, R. N. Bis(N-methylimidazole)-Substituted Neutral Phthalocyanines {MIII(MeIm)2(Pc)·3–}0 (M = Al, Ga) Containing Radical Trianionic Phthalocyanine Macrocycles. *Eur. J. Inorg. Chem.* **2016,** *2016*, 4099-4103.

29. Konarev, D. V.; Kuzmin, A. V.; Khasanov, S. S.; Batov, M. S.; Otsuka, A.; Yamochi, H.; Kitagawa, H.; Lyubovskaya, R. N. Salts with titanyl and vanadyl phthalocyanine radical anions. Molecular design and effect of cations on the structure and magnetic and optical properties. *CrystEngComm* **2018,** *20*, 385-401.

30. Myers, J. F.; Canham, G. W. R.; Lever, A. B. P. Higher oxidation level phthalocyanine complexes of chromium, iron, cobalt and zinc. Phthalocyanine radical species. *Inorg. Chem.* **1975,** *14*, 461-468.

31. Kobayashi, N.; Shirai, H.; Hojo, N. Iron(III) phthalocyanines: oxidation and spin states of iron in iron phthalocyanines with carboxyl groups. *J. Chem. Soc. Dalton Trans.* **1984**, 2107-2110.

32. Cook, M. J.; Dunn, A. J.; Howe, S. D.; Thomson, A. J.; Harrison, K. J. Octa-alkoxy phthalocyanine and naphthalocyanine derivatives: dyes with Q-

band absorption in the far red or near infrared. *J. Chem. Soc. Perkin Trans. 1* **1988**, 2453-2458.

33. Contakes, S. M.; Beatty, S. T.; Dailey, K. K.; Rauchfuss, T. B.; Fenske, D. π-Complexes of Phthalocyanines and Metallophthalocyanines. *Organometallics* **2000,** *19*, 4767-4774.

34. Leznoff, C. C.; Lever, A. B. P., *Phthalocyanines: Properties and Applications*. Wiley VCH: New York, NY, 1989.

35. Wang, H.-H.; Yuan, H.-Q.; Mahmood, M. H. R.; Jiang, Y.-Y.; Cheng, F.; Shi, L.; Liu, H.-Y. Crystal structure, magnetic and catalytic oxidation properties of manganese(iii) tetrakis(ethoxycarbonyl)porphyrin. *RSC Advances* **2015,** *5*, 97391-97399.

36. Evans, D. F. 400. The determination of the paramagnetic susceptibility of substances in solution by nuclear magnetic resonance. *J. Chem. Soc.* **1959**, 2003-2005.

37. Keener, M.; Peterson, M.; Hernández Sánchez, R.; Oswald, V. F.; Wu, G.; Ménard, G. Towards Catalytic Ammonia Oxidation to Dinitrogen: A Synthetic Cycle by Using a Simple Manganese Complex. *Chem. Eur. J.* **2017,** *23*, 11479-11484.

38. Du Bois, J.; Tomooka, C. S.; Hong, J.; Carreira, E. M. Nitridomanganese(V) Complexes: Design, Preparation, and Use as Nitrogen Atom-Transfer Reagents. *Acc. Chem. Res.* **1997,** *30*, 364-372.

39. Du Bois, J.; Hong, J.; Carreira, E. M.; Day, M. W. Nitrogen Transfer from a Nitridomanganese(V) Complex: Amination of Silyl Enol Ethers. *J. Am. Chem. Soc.* **1996,** *118,* 915-916.

40. Frick, K.; Verma, S.; Sundermeyer, J.; Hanack, M. Novel Nitrido- and Oxo(phthalocyaninato) Complexes of Molybdenum, Tungsten and Rhenium. *Eur. J. Inorg. Chem.* **2000,** *2000,* 1025-1030.

41. Goedkent, V. L.; Ercolani, C. Nitrido-bridged iron phthalocyanine dimers: synthesis and characterization. *J. Chem. Soc., Chem. Commun.* **1984**, 378-379.

42. Kudrik, E. V.; Afanasiev, P.; Sorokin, A. B. Synthesis and Properties of FeIII-N=MnIV Heterometallic Complex with Tetra-tert-butylphthalocyanine Ligands. *Macroheterocycles* **2010,** *3,* 19-22.

43. Donzello, M. P.; Ercolani, C.; Russo, U.; Chiesi-Villa, A.; Rizzoli, C. Metal- and Ligand-Centered Monoelectronic Oxidation of μ-Nitrido[((tetraphenylporphyrinato)manganese)(phthalocyaninatoiron)], [(TPP)Mn−N−FePc]. X-ray Crystal Structure of the Fe(IV)-Containing Species [(THF)(TPP)Mn−N−FePc(H2O)](I5)·2THF. *Inorg. Chem.* **2001,** *40,* 2963-2967.

44. Grunewald, H.; Homborg, H. Preparation and Spectroscopical Characterization of Nitridophthalocyaninatomanganese(V). *Z. Naturforsch., B* **1990,** *45b,* 483-489.

45. Grunewald, H.; Homborg, H. Darstellung und Charakterisierung von Chrom(V)- und Mangan(V)- nitridophthalocyaninen(1-) und -(2-): [MNPc(1-)]+; und [MNPc(2-)] (M=Cr, Mn). *Z. Anorg. Allg. Chem.* **1992,** *608*, 81-87.

46. Shields, M. R.; Guzei, I. A.; Goll, J. G. Crystal structure of nitrido[5,10,15,20-tetrakis(4-methylphenyl)porphyrinato]manganese(V). *Acta Cryatallogr. E* **2014,** *70*, 242-245.

47. Ho, C.-M.; Lau, T.-C.; Kwong, H.-L.; Wong, W.-T. Activation of manganese nitrido complexes by Bronsted and Lewis acids. Crystal structure and asymmetric alkene aziridination of a chiral salen manganese nitrido complex. *J. Chem. Soc. Dalton Trans.* **1999**, 2411-2414.

48. Kropp, H.; King, A. E.; Khusniyarov, M. M.; Heinemann, F. W.; Lancaster, K. M.; DeBeer, S.; Bill, E.; Meyer, K. Manganese Nitride Complexes in Oxidation States III, IV, and V: Synthesis and Electronic Structure. *J. Am. Chem. Soc.* **2012,** *134*, 15538-15544.

49. Engel, M. K., 122 - Single-Crystal Structures of Phthalocyanine Complexes and Related Macrocycles A2 - Kadish, Karl M. In *The Porphyrin Handbook*, Smith, K. M.; Guilard, R., Eds. Academic Press: Amsterdam, 2003; pp 1-242.

50. Cissell, J. A.; Vaid, T. P.; Rheingold, A. L. Aluminum Tetraphenylporphyrin and Aluminum Phthalocyanine Neutral Radicals. *Inorg. Chem.* **2006,** *45*, 2367-2369.

51. Wong, E. W. Y.; Leznoff, D. B. Synthesis and structural characterization of a magnesium phthalocyanine(3–) anion. *J. Porphyrins Phthalocyanines* **2012,** *16*, 154-162.

52. Konarev, D. V.; Kuzmin, A. V.; Faraonov, M. A.; Ishikawa, M.; Khasanov, S. S.; Nakano, Y.; Otsuka, A.; Yamochi, H.; Saito, G.; Lyubovskaya, R. N. Synthesis, Structures, and Properties of Crystalline Salts with Radical Anions of Metal-Containing and Metal-Free Phthalocyanines. *Chem. Eur. J.* **2015,** *21*, 1014-1028.

53. Zhou, W.; Thompson, J. R.; Leznoff, C. C.; Leznoff, D. B. The Redox-Active Chromium Phthalocyanine System: Isolation of Five Oxidation States from Pc4−CrI to Pc2−CrIII. *Chem. Eur. J.* **2017,** *23*, 2323-2331.

54. O'Connor, A. R.; Nataro, C.; Golen, J. A.; Rheingold, A. L. Synthesis and reactivity of [N(C6H4Br)3][B(C6F5)4]: the X-ray crystal structure of [Fe(C5H5)2][B(C6F5)4]. *J. Organomet. Chem.* **2004,** *689*, 2411-2414.

55. Connelly, N. G.; Geiger, W. E. Chemical Redox Agents for Organometallic Chemistry. *Chem. Rev.* **1996,** *96*, 877-910.

56. Lalancette, J. M.; Rollin, G.; Dumas, P. Metals Intercalated in Graphite. I. Reduction and Oxidation. *Can. J. Chem.* **1972,** *50*, 3058-3062.

57. Clarke, R. M.; Storr, T. Tuning Electronic Structure To Control Manganese Nitride Activation. *J. Am. Chem. Soc.* **2016,** *138*, 15299-15302.

58. Leeladee, P.; Baglia, R. A.; Prokop, K. A.; Latifi, R.; de Visser, S. P.; Goldberg, D. P. Valence Tautomerism in a High-Valent Manganese–Oxo Porphyrinoid Complex Induced by a Lewis Acid. *J. Am. Chem. Soc.* **2012,** *134*, 10397-10400.

59. Robertson, J. M.; Woodward, I. 37. An X-ray study of the phthalocyanines. Part III. Quantitative structure determination of nickel phthalocyanine. *J. Chem. Soc.* **1937**, 219-230.

60. Ziolo, R. F.; Griffiths, C. H.; Troup, J. M. Crystal structure of vanadyl phthalocyanine, phase II. *J. Chem. Soc. Dalton Trans.* **1980**, 2300-2302.

61. Ukei, K. Lead phthalocyanine. *Acta Crystallogr., Sect. B: Struct. Sci.* **1973,** *29*, 2290-2292.

62. Friedel, M. K.; Hoskins, B. F.; Martin, R. L.; Mason, S. A. A new metal(II) phthalocyanine structure: X-ray and Mossbauer studies of the triclinic tin(II) phthalocyanine. *J. Chem. Soc. D.* **1970**, 400-401.

63. Chambrier, I.; J. Cook, M.; T. Wood, P. Conformationally stressed phthalocyanines: the non-planarity of the 1,4,8,11,15,18,22,25-octaisopentyl derivative. *Chem. Commun.* **2000**, 2133-2134.

64. Kobayashi, N.; Fukuda, T.; Ueno, K.; Ogino, H. Extremely Non-Planar Phthalocyanines with Saddle or Helical Conformation: Synthesis and Structural Characterizations. *J. Am. Chem. Soc.* **2001,** *123*, 10740-10741.

65. Mack, J.; Kobayashi, N. Low Symmetry Phthalocyanines and Their Analogues. *Chem. Rev.* **2011,** *111*, 281-321.

66. Fukuda, T.; Homma, S.; Kobayashi, N. Deformed Phthalocyanines: Synthesis and Characterization of Zinc Phthalocyanines Bearing Phenyl Substituents at the 1-, 4-, 8-, 11-, 15-, 18-, 22-, and/or 25-Positions. *Chem. Eur. J.* **2005,** *11*, 5205-5216.

67. Allen, F. H.; Kennard, O.; Watson, D. G.; Brammer, L.; Orpen, A. G.; Taylor, R. Tables of bond lengths determined by X-ray and neutron diffraction. Part 1. Bond lengths in organic compounds. *J. Chem. Soc., Perkin Trans. 2* **1987**, S1-S19.

68. Gershoni-Poranne, R.; Stanger, A. Magnetic criteria of aromaticity. *Chem. Soc. Rev.* **2015,** *44*, 6597-6615.

69. Mitchell, R. H. Measuring Aromaticity by NMR. *Chem. Rev.* **2001,** *101*, 1301-1316.

70. Gomes, J. A. N. F.; Mallion, R. B. Aromaticity and Ring Currents. *Chem. Rev.* **2001,** *101*, 1349-1384.

71. Pople, J. A.; Untch, K. G. Induced Paramagnetic Ring Currents. *J. Am. Chem. Soc.* **1966,** *88*, 4811-4815.

72. Peeks, M. D.; Claridge, T. D. W.; Anderson, H. L. Aromatic and antiaromatic ring currents in a molecular nanoring. *Nature* **2016,** *541*, 200.

73. Stepien, M.; Latos-Grażyński, L., Porpyrins and Other Cyclic Oligopyrroles. In *Aromaticity in heterocyclic compounds*, Krygowski, T. M.; Cyranski, M. K.; Matos, M. A. R., Eds. Springer Science & Business Media: Berlin, 2009; Vol. 19, pp 87-117.

74. Fieser, M. E.; MacDonald, M. R.; Krull, B. T.; Bates, J. E.; Ziller, J. W.; Furche, F.; Evans, W. J. Structural, Spectroscopic, and Theoretical Comparison of Traditional vs Recently Discovered Ln2+ Ions in the [K(2.2.2-cryptand)][(C5H4SiMe3)3Ln] Complexes: The Variable Nature of Dy2+ and Nd2+. *J. Am. Chem. Soc.* **2015,** *137*, 369-382.

75. Hirakawa, F.; Ichikawa, H.; Ishida, S.; Iwamoto, T. Redox Reactions of a Stable Dialkylphosphinyl Radical. *Organometallics* **2015,** *34*, 2714-2716.

76. Hernández Sánchez, R.; Bartholomew, A. K.; Powers, T. M.; Ménard, G.; Betley, T. A. Maximizing Electron Exchange in a [Fe3] Cluster. *J. Am. Chem. Soc.* **2016,** *138*, 2235-2243.

77. Minor, P. C.; Gouterman, M.; Lever, A. B. P. Electronic spectra of phthalocyanine radical anions and cations. *Inorg. Chem.* **1985,** *24*, 1894-1900.

78. Costa, R.; Schick, A. J.; Paul, N. B.; Durfee, W. S.; Ziegler, C. J. Hydroxybenziphthalocyanines: non-aromatic phthalocyanine analogues that exhibit strong UV-visible absorptions. *New J. Chem.* **2011,** *35*, 794-799.

79. Clack, D. W.; Yandle, J. R. Electronic spectra of the negative ions of some metal phthalocyanines. *Inorg. Chem.* **1972,** *11*, 1738-1742.

80. Gouterman, M., 1 - Optical Spectra and Electronic Structure of Porphyrins and Related Rings. In *The Porphyrins*, Dolphin, D., Ed. Academic Press: New York, 1978; Vol. III, pp 1-165.

81. Mbambisa, G.; Tau, P.; Antunes, E.; Nyokong, T. Synthesis and electrochemical properties of purple manganese(III) and red titanium(IV) phthalocyanine complexes octa-substituted at non-peripheral positions with pentylthio groups. *Polyhedron* **2007,** *26*, 5355-5364.

82. Schleyer, P. v. R.; Maerker, C.; Dransfeld, A.; Jiao, H.; van Eikema Hommes, N. J. R. Nucleus-Independent Chemical Shifts: A Simple and Efficient Aromaticity Probe. *J. Am. Chem. Soc.* **1996,** *118*, 6317-6318.

83. Vaid, T. P. A Porphyrin with a C═C Unit at Its Center. *J. Am. Chem. Soc.* **2011,** *133*, 15838-15841.

84. Johnson, S. M.; Paul, I. C.; King, G. S. D. [16]Annulene: the crystal and molecular structure. *Journal of the Chemical Society B: Physical Organic* **1970**, 643-649.

85. Gorter, S.; Rutten-Keulemans, E.; Krever, M.; Romers, C.; Cruickshank, D. W. J. [18]-Annulene, C18H18, structure, disorder and Huckel's 4n + 2 rule. *Acta Crystallogr., Sect. B: Struct. Sci.* **1995,** *51*, 1036-1045.

86. Oth, J. F. M.; Woo, E. P.; Sondheimer, F. Unsaturated macrocyclic compounds. LXXXIX. Dianion of [18]annulene. *J. Am. Chem. Soc.* **1973,** *95*, 7337-7345.

87. More, K. M.; Eaton, G. R.; Eaton, S. S. Magnetic susceptibility and EPR changes caused by grinding of samples. *J. Magn. Reson.* **1980**, *37* (2), 217–222.

88. *Gaussian 09, Revision B.01*, M. J. Frisch, G. W. Trucks, H. B. Schlegel, G. E. Scuseria, M. A. Robb, J. R. Cheeseman, G. Scalmani, V. Barone, B. Mennucci, G. A. Petersson, H. Nakatsuji, M. Caricato, X. Li, H. P. Hratchian, A. F. Izmaylov, J. Bloino, G. Zheng, J. L. Sonnengerg, M. Hada, M. Ehara, K. Toyota, R. Fukuda, J. Hasegawa, M. Ishida, T. Nakajima, Y. Honda, O. Kitao, H. Nakai, T. Vreven, J. A. Montgomery Jr, J. E. Peralta, F. Ogliaro, M. Bearpark, J. J. Heyd, E. Brothers, K. N. Kudin, V. N. Staroverov, T. Keith, R. Kobayashi, J. Normand, K. Raghavachari, A. Rendell, J. C. Burant, S. S. Iyengar, J. Tomasi, M. Cossi, N. Rega, N. J. Millam, M. Klene, J. E. Knox, J. B. Cross, V. Bakken, C. Adamo, J. Jaramillo, R. Gomperts, R. E. Stratmann, O. Yazyev, A. J. Austin, R. Cammi, C. Pomelli, J. W. Ochterski, R. L. Martin, K. Morokuma, V. G. Zakrzewski, G. A. Voth, P. Salvador, J. J. Dannenberg, S. Dapprich, A. D. Daniels, Ö. Farkas, J. B. Foresman, J. V. Ortiz, J. Cioslowski and D. J. Fox, Gaussian, Inc., Wallingford CT, 2010.

89. Zhao, Y.; Truhlar, D. G. The M06 suite of density functionals for main group thermochemistry, thermochemical kinetics, noncovalent interactions, excited states, and transition elements: Two new functionals and systematic

testing of four M06-class functionals and 12 other function. *Theor. Chem. Acc.* **2008**, *120* (1–3), 215–241.

Chapter 4

Symmetric Phthalocyanine Charge Carrier for Dual Redox Flow Battery/Capacitor Applications

4.1 Introduction

Grid-level energy storage is central to widespread utilization of renewable energy technologies due to their intermittent nature.[1] Electrochemical flow systems, such as redox flow batteries (RFBs) and electrochemical flow capacitors (EFCs), have been identified as promising candidates capable of meeting the near-term U.S. Department of Energy (DOE) economic targets for grid-level energy storage systems ($250/kWh with a system efficiency of ~80% and a cycle life of 3,900 cycles).[2] The principal advantages of flow vs. non-flow systems are that total energy and power densities are decoupled, meaning the charge/discharge rates of the cell can be varied to match the power flux of the grid by control of electrode surface area, while the energy capacity can be adjusted by control of the reservoir sizes (Figure 4.1).[3] Despite advantageous design characteristics, widespread commercialization of both RFBs and EFCs is hindered by an inadequate balance of performance and cost, rendering the cost uncompetitive with conventional Li-ion batteries ($80-$150/kWh), which remain a principal contender for grid-level electrochemical energy storage.[1, 4]

A recurring theme in current RFB research is the perceived requirement of developing charge carriers with both high electrochemical stability and high solubility, addressing long-term cyclability and energy density, respectively.[5-20] However, there is a growing notion that stability and cost may supersede the solubility requirement commonly touted as a central criterion in RFB applications. For instance, research on semi-solid RFBs[21-22] and slurry-based EFCs[23-26] – both adopting similar operational design as conventional solution-state RFBs – highlight how electrochemical flow systems can readily operate under slurry conditions. For RFBs, few reports described the use of slurries which are comprised of a conductive carbon material and a charge carrier material heterogeneously mixed with a

supporting electrolyte solution.[27-29] This strategy allows redox processes to be mediated throughout the mixture by the dynamic behavior of the conductive carbon material, rather than exclusively at the electrode surface. The carbon slurry effectively operates as a conductive percolation network resulting in a system with a higher energy density than an analogous EFC and a higher power density than an analogous RFB. Simplistically, this dual RFB/EFC system can be perceived as utilizing the faster charge/discharge response of an EFC to circumvent the slower charge/discharge response of an RFB, while retaining the higher energy density of the latter.

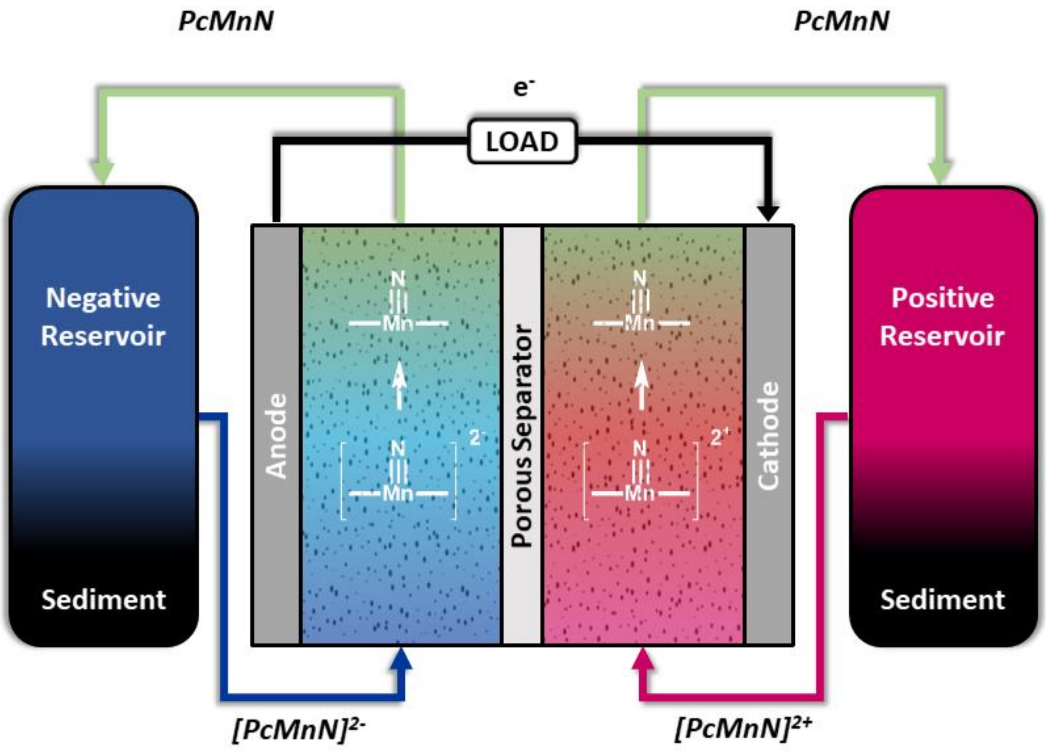

(3.2)

Figure 4.1. General operating principles of a symmetric slurry-based dual RFB/EFC incorporating both faradaic charge carrier (**3.2**) and a conductive percolation network (conductive carbon sediment) components.

4.2 Results and Discussion

4.2.1 Electrochemistry

In Chapter 3, we described the synthesis, isolation, and full characterization of a new phthalocyanine (Pc) Mn-nitride complex, (^{OEt}Pc)MnN (**3.2**; ^{OEt}Pc = 1,4,8,11,15,18,22,25-octaethoxy-Pc; Figure 4.1), as well as its stable, readily accessible oxidized (3.2^{+} and 3.2^{2+}) and reduced (**3.2**$^{-}$, **3.2**$^{2-}$) congeners.[30] Phthalocyanines are chemically-robust aromatic macrocycles produced on a megaton scale by the ink industry from low cost commodity chemicals for as low as $5 USD/kg, and exhibit rich electrochemistry.[31-32] Moreover, such large charge carriers featuring extended, switchable[30] aromatic circuits further benefit from high redox stability due to the extensive π delocalization and low charge density at sites potentially vulnerable to chemical attack.[33] Herein, we describe how **3.2** displays excellent electrochemical stability and how it can be used as both the positive and negative charge carrier for fully symmetric dual RFB/EFC applications. We also describe that while **3.2** displays only modest solubility, integration of it with a commercial conductive carbon additive, Ketjenblack (KB), renders it a viable candidate in a slurry-based dual RFB/EFC system.

As described in Chapter 3, the synthesis and characterization of all five redox states of **3.2** (**3.2**$^{2+}$, **3.2**$^{+}$, **3.2**, **3.2**$^{-}$, **3.2**$^{2-}$) revealed that all redox events are ligand-borne with the terminal Mn≡N motif functioning more as an inert "cap" than an electronic participant.[30] With this detailed understanding in hand, we next proceeded to study this system as a potential

symmetric charge carrier. We first characterized **3.2** by cyclic voltammetry (CV) with a glassy carbon disk working electrode (r = 1.5 mm), Pt wire counter electrode, and Pt wire pseudo-reference electrode. The CV of **3.2** in dichloromethane (DCM) with 0.1 M $[Bu_4N][PF_6]$ as supporting electrolyte at varying scan rates revealed four reversible redox events with half-wave potentials ($E°$) of 0.45 V (**3.2**$^{2+}$/**3.2**$^{+}$), 0.02 V (**3.2**$^{+}$/**3.2**), -1.38 V (**3.2**/**3.2**$^{-}$), and -1.75 V (**3.2**$^{-}$/**3.2**$^{2-}$), versus an internal ferrocene/ferrocenium (Fc/Fc^{+}) reference (Figure 4.2a). Furthermore, the wide voltage gaps of 1.40 V and 2.20 V between the first and second 1 e^{-} redox events, respectively, provides a wide cell potential (V_{cell}), comparable to other non-aqueous RFB systems.[34-35] This system additionally has the added benefit of transferring up to 2 e^{-} (n = 2) per molecule from fully charged to fully discharged, further contributing to the overall energy density of the system. Preliminary evidence of the long-term thermodynamic stability of all charged states towards repeated cycling was supported by comparing the 1st and 500th sweep in the CV demonstrating excellent fidelity between the voltammograms (Figure 4.2b).

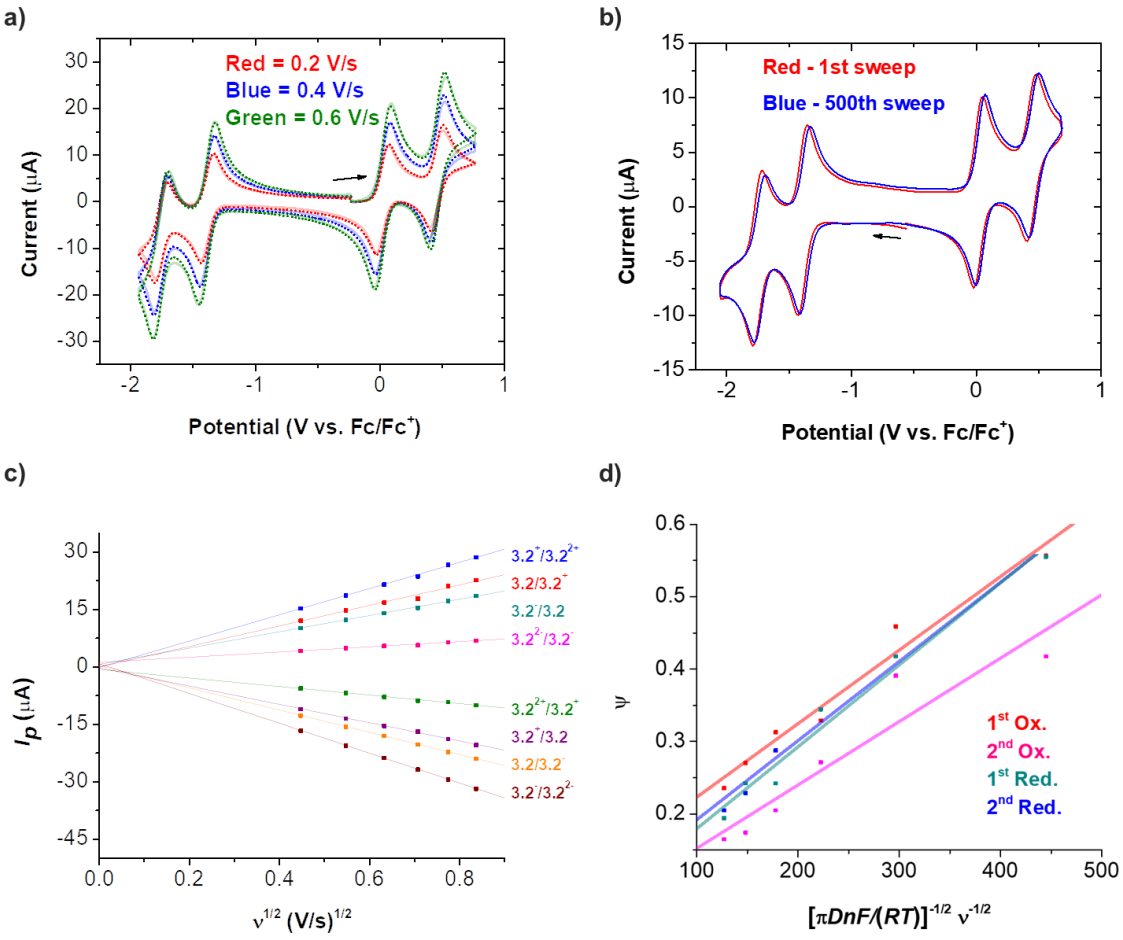

Figure 4.2. (a) Experimental (solid lines) and simulated (dotted lines) varying scan rate CVs of **3.2**. Simulations were performed using DigiSim. Experimental conditions: **3.2** (0.29 mM) in DCM with 0.1 M $[Bu_4N][PF_6]$ supporting electrolyte and using a 3 mm glassy carbon working electrode and Pt wire counter and pseudo-reference electrodes. See supporting information for all scan rates and simulation parameters. (b) Multi-sweep CV of **3.2** (0.24 mM) at 0.5 V/s with all other conditions identical to (a). (c) Randles-Ševčík analysis of **3.2** for each redox event and (d) Nicholson analysis of each redox couple of **3.2**, both calculated using all scan rates. See Figures S2-S5 for full figures and detailed analyses.

We next proceeded to measure key physical parameters, namely the diffusion coefficient (D) and the heterogeneous electron transfer rate constant (k_o) for this system following reported procedures.[18, 29, 34-37] D was initially investigated using the Randles-Ševčík equation (Eq. 4.1) for a reversible event.[38] For a given scan rate (v) and concentration (C), a plot of the peak current values (I_p) as a function of $v^{1/2}$ produced a linear correlation, indicative of a diffusional process. This in turn allowed us to extract D for each event from the slope, assuming n = 1 and given a known electrode surface area (A) (Figure 4.2c).

(4.1) $I_p = 268{,}600n^{3/2}AD^{1/2}Cv^{1/2}$

While D values for all species were obtained (Table 4.1), minor inaccuracies for $\mathbf{3.2^{2+}}$ and $\mathbf{3.2^{2-}}$ were suspected due to a Cotrellian current decay contribution from the $\mathbf{3.2}$/$\mathbf{3.2^{+}}$ and $\mathbf{1}$/$\mathbf{1^{-}}$ couples, respectively, which may manifest in erroneous measured D values. To probe this further, we turned to simulations using the DigiSim software (see Experimental).[39] The simulated values of D (Table 4.1) were in good fit with the experimental results throughout all scan rates (Figure 4.2a). Moreover, the D values of $\mathbf{3.2}$ and $\mathbf{3.2^{+}}$/$\mathbf{3.2^{-}}$ were in close agreement with those obtained from the Randles-Ševčík analyses (Table 4.1). However, the simulated D values of $\mathbf{3.2^{2+}}$ and $\mathbf{3.2^{2-}}$ deviated substantially from their experimentally-derived counterparts (Table 4.1), likely supporting the notion that the observed decrease in D for $\mathbf{3.2^{2+}}$ and $\mathbf{3.2^{2-}}$ is an artifact caused by the close redox potentials of the events. The experimental and simulated values obtained are comparable to charge carriers of similar size.[40]

Table 4.1. Relevant experimental and simulated physical parameters, $E°$, D, and k_o.

Species	$D_{Randles\text{-}Ševčík}$ **(cm^2 s^{-1})**	$D_{simulation}$ **(cm^2 s^{-1})**

3.2^{2+}	4.10*10^{-8}	1.2*10^{-7}	
3.2^{+}	2.88*10^{-7}	2.7*10^{-7}	
3.2	2.58*10^{-7}	3.0*10^{-7}	
3.2^{-}	3.26*10^{-7}	2.7*10^{-7}	
3.2^{2-}	1.52*10^{-8}	1.2*10^{-7}	
Couple	***E*° (V)**	***k*o *-Nicholson*** **(cm s^{-1})**	***k*o *-simulation*** **(cm s^{-1})**
3.2^{+} ⇌ 3.2^{2+} + e^{-}	0.45	0.0009	0.0015
3.2 ⇌ 3.2^{+} + e^{-}	0.02	0.0010	0.0015
3.2 + e^{-} ⇌ 3.2^{-}	-1.38	0.0011	0.0015
3.2^{-} + e^{-} ⇌ 3.2^{2-}	-1.75	0.0011	0.0015

The heterogeneous charge-transfer rate constant (k_o) was next determined by combining the variable scan rate CV data (Figure 4.2) with Nicholson's kinetic parameter[41] (Eq. 4.2):

(4.2) $\Psi = k_o[\pi DnvF/(RT)]^{-1/2}$

With Ψ being determined through Lavagnini's numerical interpretation[42] of Nicholson's working curve (Eq. 4.3) to construct a plot of Ψ vs. $v^{-1/2}$ (Figure 4.2d):

(4.3) $\Psi = (-0.6288 + 0.0021\chi)(1 - 0.017\chi)$

Where χ is the peak-to-peak separation in mV. The slope of such a plot yields k_o. The rates of all four redox events were determined with values ~0.001 cm s^{-1} indicating fast electron

transfer (Table 4.1) acceptable for a charge carrier.[3] These values were further confirmed by simulation and are in excellent agreement (Table 4.1).

4.2.2 Static Cell Measurements.

With the highly symmetric profile, wide voltage gap, and favorable values of D and k_o, we proceeded to determine the viability of **3.2** as a symmetric charge carrier for RFB applications. Static cell measurements were conducted in a two-electrode H-cell separated by a medium porosity glass frit. We note here that a symmetric charge carrier allows for a simple porous separator to be used in lieu of an expensive ion-exchange membrane and, although more resistive than a traditional nanoporous separator, a glass frit was chosen for experimental simplicity.[43] This is especially attractive for non-aqueous systems, as the majority of commercially available ion-exchange membranes are designed and optimized for use with aqueous systems,[44-45] and suffer from poor conductivity in non-aqueous solvents.[46] Additionally, most non-aqueous RFBs operate at high potentials with charged carrier states potentially incompatible with the membranes in use.[45] Thus, using a chemically-inert, porous separator of known composition and morphology has the potential to eliminate membrane/electrolyte degradation pathways, and typically gives low resistance in non-aqueous solvents.[45] Solution-state galvanostatic charge-discharge measurements were performed using a 0.50 mM solution of **3.2** in acetonitrile (CH_3CN) with stirring, using asymmetric charge and discharge currents of 100 and 12.5 μA, respectively, and cycling between ~75-0% state-of-charge (SOC) (Figure 4.4a). The asymmetric charge/discharge was chosen to allow the system to reach a greater depth of discharge (~0%) relative to charge (~75%). Further, the SOC can be visually tracked by a noticeable change in solution color (Figure 4.3).

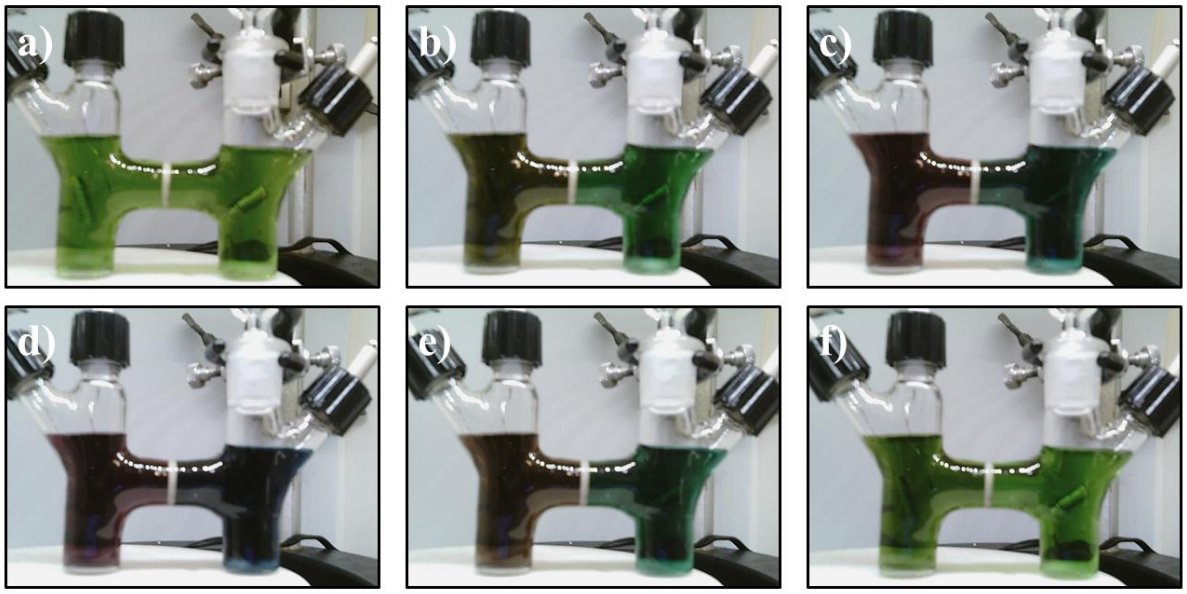

Figure 4.3. One full charge/discharge cycle of **3.2**, in CH_3CN with oxidation and reduction occurring in the left and right compartment on charging, respectively. (a-d) were taking during charging, and (e-f) were taken during discharging. (a) = ~0% state of charge (SOC), (b) = ~25% SOC, (c) = 50% SOC, (d) ~75% SOC, (e) ~35% SOC, (f) = ~0% SOC.

The charge/discharge rates were chosen with the consideration of achieving both a reasonable cycling time and a suitable SOC. The features of charge-discharge follow theoretical models for a five-redox state system,[43] in which there are two well-defined current plateaus corresponding to the $\mathbf{3.2}^{+}/\mathbf{3.2}^{-}$ and $\mathbf{3.2}^{2+}/\mathbf{3.2}^{2-}$ couples (Figure 4.4b). Cycling over 35 cycles reveals excellent fidelity of charge/discharge features, as well as a high faradaic efficiency (*FE*) exceeding 99% per cycle, indicating minimal deleterious side reaction(s) over the course of cycling (~ 5 days) (Figure 4.4c). The voltage efficiency (*VE*) was 75% with a gradual fade to 73% by the 35th cycle. *VE* is largely subject to internal cell resistance and here we attribute the initial *VE* value to cell design, and the 2% fade to cell polarization resistance leading to a new SOC for the given voltage cutoffs, a common

occurrence in charge/discharge experiments.[47] Combining *FE* and *VE*, the system provides an overall energy efficiency (*EE*) of ~75% over 35 cycles (Figure 4.4c). Overall, the faradaic capacity, defined here as the total charge transferred on discharge for a given cycle relative to the initial discharge, decreased by ~0.1% per cycle over 35 cycles.

While solution-state cycling of **3.2** shows promising stability and electron transfer kinetics, the poor solubility of **3.2** (~1 mM in CH_3CN) and associated low energy density (0.02 Wh/L) prohibits its useful application as a charge carrier for conventional solution-state RFB applications. We therefore turned to utilizing a conductive carbon additive, KB, in order to generate a high-surface conductive percolation network for our system.[29] Prior to integrating KB with **3.2**, we first performed a simple control cycling experiment with only KB to better understand the behavior of our conductive carbon additive. Slurry-state galvanostatic charge-discharge measurements were performed with 50 mg of KB in 5 mL of CH_3CN in each compartment with stirring and with asymmetric charge and discharge currents of -500 and 250 μA, respectively, employing the same voltage cutoffs as used for the solution-state cycling of **3.2** (Figure 4.4d). The features of charge-discharge follow those expected for a purely capacitive system, displaying a clear linear relationship between potential and SOC (Figure 4.4e). Cycling over 20 cycles reveals excellent fidelity of charge/discharge features with a high *FE* exceeding 99% per cycle, negligible capacity fade over the course of cycling (~3.5 days), and a low energy density (0.06 Wh/L). The *VE* was 57% with no appreciable fade by the 20th cycle, resulting in an *EE* of ~57% over 20 cycles (Figure 4.4f). Additionally, self-discharge experiments revealed that negligible self-discharge was observed over the course of 24 h.

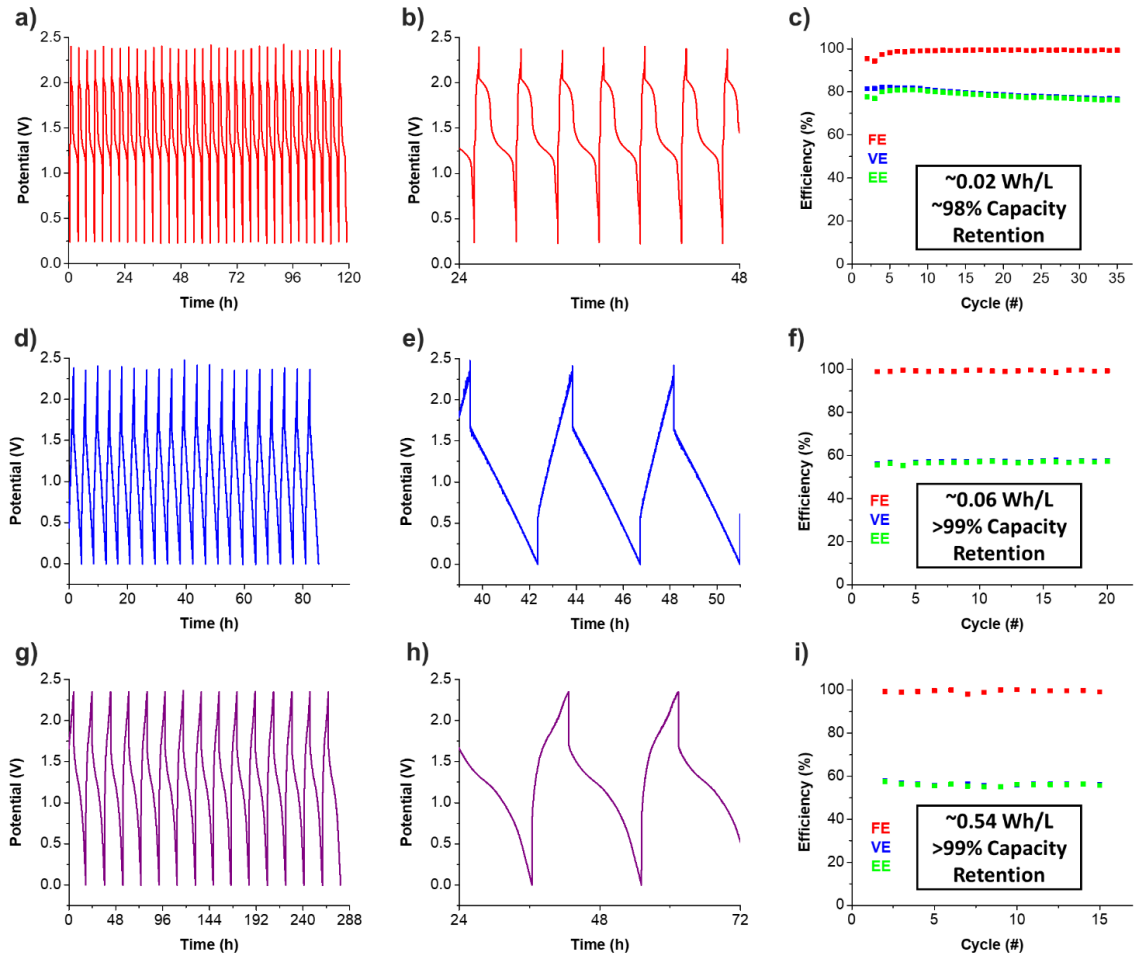

Figure 4.4. (a-b) Solution-state galvanostatic charge-discharge curves and features of **3.2** (-100 μA charge, 12.5 μA discharge) over 35 cycles. (c) Faradaic efficiency (*FE*), voltage efficiency (*VE*), and energy efficiency (*EE*) of **3.2** for solution-state cycling. (d-e) Slurry-state galvanostatic charge-discharge curves and features of KB (-500 μA charge, 250 μA discharge) over 20 cycles. (f) *FE*, *VE*, and *EE* of KB for slurry-state cycling. (g-h) Slurry-state galvanostatic charge-discharge curves and features of **3.2**/KB (-500 μA charge, 250 μA discharge) over 15 cycles. (i) *FE*, *VE*, and *EE* of **3.2**/KB for slurry-state cycling. (c, f, i) Calculated energy densities and capacity retentions are inset. See Experimental for full conditions and calculations.

With a clear basis of charge/discharge behavior for both **3.2** and KB, we proceeded to cycle **3.2** as a slurry with KB functioning as a "conductive extension" to the working electrode. The KB both increases the overall electrochemical capacitance and functions as a direct charge mediator to **3.2**. We would like to briefly mention that a slurry-based dual RFB/EFC system would likely utilize tanks with large quantities of solid-state charge carrier "sediment" and a suspended-state or solution-state supernatant phase that is actively pumped through flow fields, functioning as a conductive extension between the sediment and electrode surface (Figure 4.1).[48-49] As described here, a slurry of **3.2**/KB appears to function in this manner, with a portion of **3.2**/KB actively suspended and a large quantity of sediment residing at the bottom of the cell. Slurry-state galvanostatic charge-discharge measurements were performed in CH_3CN with 65 mg of **3.2** and 105 mg of KB in each compartment under stirring, with asymmetric charge and discharge currents of -500 and 250 μA, respectively, employing the same voltage cutoffs as used for the solution-state cycling of **3.2** (Figure 4.4g). The features of charge-discharge (Figure 4.4h) appear to be intermediate between those of **3.2** (Figure 4.4b) and those of KB (Figure 4.4e), consistent with combined faradaic and capacitive contributions. Cycling over 15 cycles revealed excellent fidelity of charge/discharge features, as well as a high *FE* exceeding 99% per cycle, indicating minimal deleterious side reactions and negligible capacity fade over the course of cycling (~12 days). Furthermore, the system benefited from a substantially increased energy density (0.54 Wh/L) relative to the prior solution-state cycling of **3.2** and slurry-state cycling of KB. The *VE* was 56% with no appreciable fade by the 15th cycle and the corresponding *EE* was ~56% over 15 cycles (Figure 4.4i). Additionally, self-discharge appeared to be negligible over the course of 24 h. It should be noted here that attempts to galvanostatically cycle **3.2** as a slurry in the absence of KB showed egregious capacity fade and ill-defined charge-discharge

features, not unexpected for a kinetically-limited slurry in the absence of a conductive percolation network (Figure 4.6).

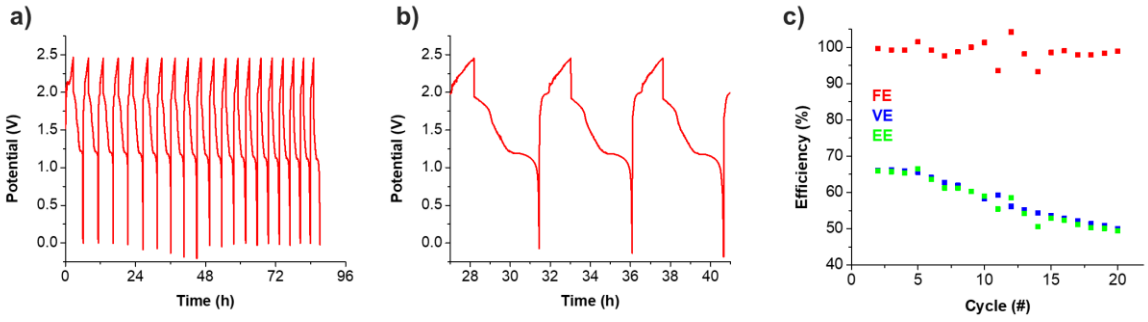

Figure 4.5. (a-b) Slurry-state galvanostatic charge-discharge curves and features of **3.2** as slurry in the absence of KB (-500 µA charge, 250 µA discharge) over 20 cycles. (c) *FE*, *VE*, and *EE* of **3.2** in the absence of KB.

4.3 Summary

Together, these results clearly demonstrate that the KB component is primarily responsible for driving the redox processes of **3.2** throughout the slurry. This also implies that power density is mostly controlled by the capacitive KB component (EFC), and the energy density is primarily controlled by the galvanic component (RFB), suggesting that this dual symmetric RFB/EFC architecture could be adjusted to have an increased power density with higher carbon loading, or an increased energy density with higher charge carrier loading, depending on required applications. Additionally, this system is kinetically limited by the carbon slurry, allowing for effective charge/discharge beyond the solubility limit of the charge carrier. Overall, this study demonstrates that hybrid electrochemical architectures (RFB + EFC) utilizing both galvanic and capacitive components can display higher power densities and energy densities than the individual respective components, and allow for the

use of insoluble species that would otherwise be discounted for use in conventional solution-state systems.

4.4 Experimental

Techniques and Reagents. All manipulations were performed under an atmosphere of dry, oxygen-free N_2 within an MBraun glovebox (MBRAUN UNIlab Pro SP Eco equipped with a -40 ^oC freezer), or under an atmosphere of dry, oxygen-free Ar within a retrofitted VAC glovebox, or by standard Schlenk techniques. Pentane, C_6D_6, Et_2O, DCM and THF (inhibitor-free) were dried and degassed on an MBraun Solvent Purification System and stored over activated 4 Å molecular sieves. All other solvents were degassed by freeze-pump-thaw and stored on activated 4 Å molecular sieves prior to use. Celite® and 4 Å molecular sieves were dried at 250 ^oC under dynamic vacuum (< 0.1 Torr) for 24 h prior to use. Compound **3.2** was prepared by previously reported methods.[30] Ketjenblack® EC-600JD (KB) was purchased from a private supplier. All other reagents were obtained from Sigma-Aldrich, Fisher Scientific, or VWR and used without further purification.

Electrochemical Measurements. Cyclic voltammograms were performed on a CH Instruments 630E Electrochemical Analysis Potentiostat. All working electrodes were of 3.0 mm diameter (CH Instruments) and were cleaned prior to each experiment by sequentially polishing with a gradient of 1.0 μm, 0.3 μm, and 0.05 μm alumina (CH Instruments) on a cloth pad, followed by rinsing with distilled water and acetone. The Pt wire pseudo-reference and counter electrodes were rinsed with distilled water and acetone and heated white-hot with a butane torch. All measurements were performed on recrystallized product and referenced to the Fc/Fc^+ redox couple unless otherwise stated. Static cell cycling experiments were carried out using a Metrohm Autolab PGSTAT128N

potentiostat/galvanostat, utilizing voltage cutoffs. For cycling experiments, two coiled Pt electrodes (Bio-Logic) were used and were cleaned by rinsing with distilled water and acetone and then heating white-hot with a butane torch. All electrodes were transferred into a glovebox and subsequently rinsed with the respective electrolyte solution immediately prior to use. The H-cell was custom-made by the in-house glassblower. All electrochemical measurements were performed under an inert atmosphere. For slurry measurements, solid material was first ground together using a mortar and pestle, and then combined with 5 mL of 0.2 M $[Bu_4N][PF_6]$ in CH_3CN, and sonicated for 1 h prior to addition to the H-cell. For all cycling efficiency metrics, the first cycle was discarded.

Faradaic efficiency (*FE*) was defined by Eq. 4.4:

(4.4) $$FE = (Q_{discharge}/Q_{charge}) \bullet 100\%$$

Where *Q* is charge transferred. Voltage efficiency (*VE*) was defined by Eq. 4.5:

(4.5) $$VE = (V(mean)_{discharge}/V(mean)_{charge}) \bullet 100\%$$

Where $V_{(mean)}$ is the mean voltage. Energy efficiency (*EE*) was defined by Eq. 4.6:

(4.6) $$EE = (FE \bullet VE)/100\%$$

DigiSim simulations. All simulations were performed with the same concentration, starting potential, ending potential, voltage window, experimental $E°$, and scan rate as experimental, and the assumption that T = 298 K, r = 1.5 mm. All events were assumed to have an α/λ

ratio of 0.5, and the diffusion coefficient (D) and the heterogeneous charge transfer constant (k_o) were fitted to all scan rates to produce the closest fits.

Energy density calculations.

The energy density was calculated using the following assumptions:

1) KB provides 2.5 C when 100 mg is used (estimated from experimental charge/discharge curves; Figure 4.4)
2) **3.2** provides 2 e^- per molecule, and has a molecular weight of 934 g/mol
3) Experimental V_{cell}(discharge) values were used for each calculation

Solution-state cycling:

Using the following equation[50]: $\hat{E}_{RFB} = 0.5\ n \bullet V_{cell} \bullet C_{active} \bullet F$

where: $\hat{E}_{RFB}$ = energy density for RFB

n = number of electrons transferred at the electrodes = 2

V_{cell} = cell potential

C_{active} = concentration of the redox active species

F = Faraday's constant = 96,485 C/mol

with: 4.7 mg of **3.2** dissolved in 10 mL

V_{cell} = 1.40 V

then: $\hat{E}_{RFB} = 0.5 \bullet 2 \bullet 1.4\ V \bullet (0.0047\ g/\ 934\ g/mol)(1/0.010\ L) \bullet 96485\ C/mol = 67.9\ J/L \sim 0.02\ Wh/L$

KB cycling:

Using the following equation: $\hat{E}_{RFB} = (q \bullet V_{cell})/(volume)$

where: $\hat{E}_{EFC}$ = energy density for EFC

q = total charge transferred = 2.5 C (using 100 mg KB and following assumption 1 above)

volume = 0.010 L

with: V_{cell} = 0.84 V

then: $\hat{E}_{EFC} = (2.5\ C \bullet 0.84\ V)(1/0.010\ L) = 210\ J/L \sim 0.06\ Wh/L$

Slurry-state cycling:

Using the following equation: $\hat{E}_{total} = \hat{E}_{RFB} + \hat{E}_{EFC}$

with: 130 mg of **3.2**

210 mg of KB

volume = 0.010 L

V_{cell} = 1.04 V

then: $\hat{E}_{EFC} = [0.5 \bullet 2 \bullet 1.04\ V \bullet (0.130\ g)(1/934\ g/mol)(1/0.010\ L) \bullet 96485\ C/mol] + [(210\ mg)(2.5\ C/100\ mg)(1.04\ V)(1/0.010\ L] = 1943\ J/L \sim 0.54\ Wh/L$

4.5 References

1. Dunn, B.; Kamath, H.; Tarascon, J.-M. Electrical Energy Storage for the Grid: A Battery of Choices. *Science* **2011,** *334*, 928-935.

2. Yang, Z.; Zhang, J.; Kintner-Meyer, M. C. W.; Lu, X.; Choi, D.; Lemmon, J. P.; Liu, J. Electrochemical Energy Storage for Green Grid. *Chem. Rev.* **2011,** *111*, 3577-3613.

3. Weber, A. Z.; Mench, M. M.; Meyers, J. P.; Ross, P. N.; Gostick, J. T.; Liu, Q. Redox flow batteries: a review. *J. Appl. Electrochem.* **2011,** *41*, 1137-1164.

4. IEA Energy Storage: Tracking Clean Energy Progress. https://www.iea.org/tcep/energyintegration/energystorage/ (accessed 05/2019).

5. Zhang, C.; Qian, Y.; Ding, Y.; Zhang, L.; Guo, X.; Zhao, Y.; Yu, G. Biredox Eutectic Electrolytes Derived from Organic Redox-Active Molecules: High-Energy Storage Systems. *Angew. Chem. Int. Ed.* **2019,** *58*, 7045-7050.

6. Xing, X.; Liu, Q.; Xu, W.; Liang, W.; Liu, J.; Wang, B.; Lemmon, J. P. All-Liquid Electroactive Materials for High Energy Density Organic Flow Battery. *ACS Applied Energy Materials* **2019,** *2*, 2364-2369.

7. Goulet, M.-A.; Tong, L.; Pollack, D. A.; Tabor, D. P.; Odom, S. A.; Aspuru-Guzik, A.; Kwan, E. E.; Gordon, R. G.; Aziz, M. J. Extending the Lifetime of Organic Flow Batteries via Redox State Management. *J. Am. Chem. Soc.* **2019,** *141*, 8014-8019.

8. Zhang, J.; Jiang, G.; Xu, P.; Ghorbani Kashkooli, A.; Mousavi, M.; Yu, A.; Chen, Z. An all-aqueous redox flow battery with unprecedented energy density. *Energ. Environ. Sci.* **2018,** *11*, 2010-2015.

9. Zhang, C.; Niu, Z.; Ding, Y.; Zhang, L.; Zhou, Y.; Guo, X.; Zhang, X.; Zhao, Y.; Yu, G. Highly Concentrated Phthalimide-Based Anolytes for Organic Redox Flow Batteries with Enhanced Reversibility. *Chem* **2018,** *4*, 2814-2825.

10. Kwabi, D. G.; Lin, K.; Ji, Y.; Kerr, E. F.; Goulet, M.-A.; De Porcellinis, D.; Tabor, D. P.; Pollack, D. A.; Aspuru-Guzik, A.; Gordon, R. G.; Aziz, M. J. Alkaline Quinone Flow Battery with Long Lifetime at pH 12. *Joule* **2018,** *2*, 1894-1906.

11. Hu, B.; Tang, Y.; Luo, J.; Grove, G.; Guo, Y.; Liu, T. L. Improved radical stability of viologen anolytes in aqueous organic redox flow batteries. *Chem. Commun.* **2018,** *54*, 6871-6874.

12. Kowalski, J. A.; Casselman, M. D.; Kaur, A. P.; Milshtein, J. D.; Elliott, C. F.; Modekrutti, S.; Attanayake, N. H.; Zhang, N.; Parkin, S. R.; Risko, C.; Brushett, F. R.; Odom, S. A. A stable two-electron-donating phenothiazine for application in nonaqueous redox flow batteries. *J. Mater. Chem. A* **2017,** *5*, 24371-24379.

13. Beh, E. S.; De Porcellinis, D.; Gracia, R. L.; Xia, K. T.; Gordon, R. G.; Aziz, M. J. A Neutral pH Aqueous Organic–Organometallic Redox Flow Battery with Extremely High Capacity Retention. *ACS Energy Lett.* **2017,** *2*, 639-644.

14. Gong, K.; Xu, F.; Grunewald, J. B.; Ma, X.; Zhao, Y.; Gu, S.; Yan, Y. All-Soluble All-Iron Aqueous Redox-Flow Battery. *ACS Energy Lett.* **2016,** *1*, 89-93.

15. Lin, K.; Chen, Q.; Gerhardt, M. R.; Tong, L.; Kim, S. B.; Eisenach, L.; Valle, A. W.; Hardee, D.; Gordon, R. G.; Aziz, M. J.; Marshak, M. P. Alkaline quinone flow battery. *Science* **2015,** *349*, 1529-1532.

16. Huskinson, B.; Marshak, M. P.; Suh, C.; Er, S.; Gerhardt, M. R.; Galvin, C. J.; Chen, X.; Aspuru-Guzik, A.; Gordon, R. G.; Aziz, M. J. A metal-free organic-inorganic aqueous flow battery. *Nature* **2014,** *505*, 195-198.

17. VanGelder, L. E.; Matson, Ellen M. Heterometal functionalization yields improved energy density for charge carriers in nonaqueous redox flow batteries. *J. Mater. Chem. A* **2018,** *6*, 13874-13882.

18. VanGelder, L. E.; Kosswattaarachchi, A. M.; Forrestel, P. L.; Cook, T. R.; Matson, E. M. Polyoxovanadate-alkoxide clusters as multi-electron charge carriers for symmetric non-aqueous redox flow batteries. *Chem. Sci.* **2018,** *9*, 1692-1699.

19. Sevov, C. S.; Fisher, S. L.; Thompson, L. T.; Sanford, M. S. Mechanism-Based Development of a Low-Potential, Soluble, and Cyclable Multielectron Anolyte for Nonaqueous Redox Flow Batteries. *J. Am. Chem. Soc.* **2016,** *138*, 15378-15384.

20. Sevov, C. S.; Brooner, R. E. M.; Chénard, E.; Assary, R. S.; Moore, J. S.; Rodríguez-López, J.; Sanford, M. S. Evolutionary Design of Low Molecular Weight Organic Anolyte Materials for Applications in Nonaqueous Redox Flow Batteries. *J. Am. Chem. Soc.* **2015,** *137*, 14465-14472.

21. Li, Z.; Smith, K. C.; Dong, Y.; Baram, N.; Fan, F. Y.; Xie, J.; Limthongkul, P.; Carter, W. C.; Chiang, Y.-M. Aqueous semi-solid flow cell: demonstration and analysis. *Phys. Chem. Chem. Phys.* **2013,** *15*, 15833-15839.

22. Duduta, M.; Ho, B.; Wood, V. C.; Limthongkul, P.; Brunini, V. E.; Carter, W. C.; Chiang, Y.-M. Semi-Solid Lithium Rechargeable Flow Battery. *Adv. Energy Mater.* **2011,** *1*, 511-516.

23. Tomai, T.; Saito, H.; Honma, I. High-energy-density electrochemical flow capacitors containing quinone derivatives impregnated in nanoporous carbon beads. *J. Mater. Chem. A* **2017,** *5*, 2188-2194.

24. Yoon, H.; Kim, H.-J.; Yoo, J. J.; Yoo, C.-Y.; Park, J. H.; Lee, Y. A.; Cho, W. K.; Han, Y.-K.; Kim, D. H. Pseudocapacitive slurry electrodes using redox-active quinone for high-performance flow capacitors: an atomic-level understanding of pore texture and capacitance enhancement. *J. Mater. Chem. A* **2015,** *3*, 23323-23332.

25. Boota, M.; Hatzell, K. B.; Kumbur, E. C.; Gogotsi, Y. Towards High-Energy-Density Pseudocapacitive Flowable Electrodes by the Incorporation of Hydroquinone. *ChemSusChem* **2015,** *8*, 835-843.

26. Presser, V.; Dennison, C. R.; Campos, J.; Knehr, K. W.; Kumbur, E. C.; Gogotsi, Y. The Electrochemical Flow Capacitor: A New Concept for Rapid Energy Storage and Recovery. *Adv. Energy Mater.* **2012,** *2*, 895-902.

27. Hatzell, K. B.; Boota, M.; Kumbur, E. C.; Gogotsi, Y. Flowable Conducting Particle Networks in Redox-Active Electrolytes for Grid Energy Storage. *J. Electrochem. Soc.* **2015,** *162*, A5007-A5012.

28. Percin, K.; Rommerskirchen, A.; Sengpiel, R.; Gendel, Y.; Wessling, M. 3D-printed conductive static mixers enable all-vanadium redox flow battery using slurry electrodes. *J. Power Sources* **2018,** *379*, 228-233.

29. Ma, T.; Pan, Z.; Miao, L.; Chen, C.; Han, M.; Shang, Z.; Chen, J. Porphyrin-Based Symmetric Redox-Flow Batteries towards Cold-Climate Energy Storage. *Angew. Chem. Int. Ed.* **2018,** *57*, 3158-3162.

30. Hunt, C.; Peterson, M.; Anderson, C.; Chang, T.; Wu, G.; Scheiner, S.; Ménard, G. Switchable Aromaticity in an Isostructural Mn Phthalocyanine Series Isolated in Five Separate Redox States. *J. Am. Chem. Soc.* **2019,** *141*, 2604-2613.

31. Leznoff, C. C.; Lever, A. B. P., *Phthalocyanines: Properties and Applications*. Wiley VCH: New York, NY, 1989.

32. USITC. Industry & Trade Summary: Synthetic Organic Pigments. https://www.usitc.gov/publications/docs/pubs/industry_trade_summaries/pub3021.pdf (accessed 5/1/2019).

33. Duan, W.; Huang, J.; Kowalski, J. A.; Shkrob, I. A.; Vijayakumar, M.; Walter, E.; Pan, B.; Yang, Z.; Milshtein, J. D.; Li, B.; Liao, C.; Zhang, Z.; Wang, W.; Liu, J.; Moore, J. S.; Brushett, F. R.; Zhang, L.; Wei, X. "Wine-Dark Sea" in an Organic Flow Battery: Storing Negative Charge in 2,1,3-Benzothiadiazole Radicals Leads to Improved Cyclability. *ACS Energy Lett.* **2017,** *2*, 1156-1161.

34. Gong, K.; Fang, Q.; Gu, S.; Li, S. F. Y.; Yan, Y. Nonaqueous redox-flow batteries: organic solvents, supporting electrolytes, and redox pairs. *Energ. Environ. Sci.* **2015,** *8*, 3515-3530.

35. Liu, Q.; Sleightholme, A. E. S.; Shinkle, A. A.; Li, Y.; Thompson, L. T. Non-aqueous vanadium acetylacetonate electrolyte for redox flow batteries. *Electrochem. Commun.* **2009,** *11*, 2312-2315.

36. Hagemann, T.; Winsberg, J.; Häupler, B.; Janoschka, T.; Gruber, J. J.; Wild, A.; Schubert, U. S. A bipolar nitronyl nitroxide small molecule for an all-organic symmetric redox-flow battery. *NPG Asia Mater.* **2017,** *9*, e340.

37. Xie, C.; Duan, Y.; Xu, W.; Zhang, H.; Li, X. A Low-Cost Neutral Zinc–Iron Flow Battery with High Energy Density for Stationary Energy Storage. *Angew. Chem. Int. Ed.* **2017,** *56*, 14953-14957.

38. Zanello, P., *Inorganic Electrochemistry: Theory, Practice and Application*. The Royal Society of Chemistry: Cambridge, UK, 2003.

39. BASi DigiSim® Simulation Software for Cyclic Voltammetry. http://www.basinc.com/products/ec/digisim/ (accessed May, 2019).

40. Hendriks, K. H.; Robinson, S. G.; Braten, M. N.; Sevov, C. S.; Helms, B. A.; Sigman, M. S.; Minteer, S. D.; Sanford, M. S. High-Performance Oligomeric Catholytes for Effective

Macromolecular Separation in Nonaqueous Redox Flow Batteries. *ACS Central Science* **2018,** *4*, 189-196.

41. Nicholson, R. S. Theory and Application of Cyclic Voltammetry for Measurement of Electrode Reaction Kinetics. *Anal. Chem.* **1965,** *37*, 1351-1355.

42. Lavagnini, I.; Antiochia, R.; Magno, F. An Extended Method for the Practical Evaluation of the Standard Rate Constant from Cyclic Voltammetric Data. *Electroanal.* **2004,** *16*, 505-506.

43. Potash, R. A.; McKone, J. R.; Conte, S.; Abruña, H. D. On the Benefits of a Symmetric Redox Flow Battery. *J. Electrochem. Soc.* **2016,** *163*, A338-A344.

44. Prifti, H.; Parasuraman, A.; Winardi, S.; Lim, T. M.; Skyllas-Kazacos, M. Membranes for Redox Flow Battery Applications. *Membranes* **2012,** *2*, 275.

45. Shin, S.-H.; Yun, S.-H.; Moon, S.-H. A review of current developments in non-aqueous redox flow batteries: characterization of their membranes for design perspective. *RSC Advances* **2013,** *3*, 9095-9116.

46. Montoto, E. C.; Nagarjuna, G.; Moore, J. S.; Rodríguez-López, J. Redox Active Polymers for Non-Aqueous Redox Flow Batteries: Validation of the Size-Exclusion Approach. *J. Electrochem. Soc.* **2017,** *164*, A1688-A1694.

47. Goulet, M.-A.; Aziz, M. J. Flow Battery Molecular Reactant Stability Determined by Symmetric Cell Cycling Methods. *J. Electrochem. Soc.* **2018,** *165*, A1466-A1477.

48. Huang, Q.; Li, H.; Grätzel, M.; Wang, Q. Reversible chemical delithiation/lithiation of LiFePO4: towards a redox flow lithium-ion battery. *Phys. Chem. Chem. Phys.* **2013,** *15*, 1793-1797.

49. Pan, F.; Yang, J.; Huang, Q.; Wang, X.; Huang, H.; Wang, Q. Redox Targeting of Anatase TiO2 for Redox Flow Lithium-Ion Batteries. *Adv. Energy Mater.* **2014,** *4*, 1400567.

50. Cabrera, P. J.; Yang, X.; Suttil, J. A.; Hawthorne, K. L.; Brooner, R. E. M.; Sanford, M. S.; Thompson, L. T. Complexes Containing Redox Noninnocent Ligands for Symmetric, Multielectron Transfer Nonaqueous Redox Flow Batteries. *J. Phys. Chem. C* **2015,** *119*, 15882-15889.

Chapter 5

Redox-Switchable Chelation for Uranium Capture and Release

5.1 Introduction

The uranyl ion (UO_2^{2+}; U^{VI} oxidation state) is the most common form of U found in terrestrial and aquatic environments and is a central component in nuclear fuel processing and waste remediation efforts. Nuclear energy is often considered a cleaner energy source than fossil fuels[1]; however, the inadvertent release of radioactive materials to the environment poses potential serious threats to human health[2] and wildlife. Uranyl capture from either seawater or nuclear waste has been well studied and commonly relies on extremely strong chelating/binding affinities to UO_2^{2+} using chelating polymers[3,4], porous inorganic[5-7] or carbon-based[8,9] materials, as well as homogeneous[10,11] compounds. The decades-old industrial Plutonium and Uranium Reduction EXtraction (PUREX) process for nuclear fuel reprocessing relies on the biphasic extraction of UO_2^{2+} and Pu^{IV} from aqueous nitric acid to organic media using hydrophobic tributylphosphate as extractant, followed by stoichiometric reductants for subsequent U and Pu separation.[12] Overall, the release of captured uranyl from either seawater or nuclear fuel reprocessing efforts is typically difficult, expensive, and/or destructive to the initial material[4,13] and its controlled release may be of critical importance to the long-term viability and safety of the nuclear energy sector. Here we show how harnessing the redox-switchable chelating and donating properties of an *ortho*-substituted *closo*-carborane, 1,2-$(Ph_2PO)_2$-1,2-$C_2B_{10}H_{10}$, cluster molecule can lead to the controlled chemical or electrochemical capture and release of UO_2^{2+} in monophasic (organic) or biphasic (organic/aqueous) solvent systems. This controlled redox-switchable chelation/donation of carborane may offer a fundamentally new approach to U management.

5.2 Results and Discussion

Known for over 50 years, carboranes have been extensively studied in coordination chemistry (including with U), catalysis, luminescence, and energy storage applications.[10,14-23] Studies have shown that reduction of substituted *closo*-carboranes to the *nido*-carboranes results in rupture of the C–C bond and cage opening with a simultaneous increase in ligand bite angle, θ (Figure 5.1a; *closo* and *nido* refer to 2n + 2 and 2n + 4 framework bonding electrons, respectively, where n is the number of vertices (in this case = 12); X = alkyl, phenyl, or donating group).[16,22,24-27] We rationalized that by incorporating donating X groups – specifically diphenylphosphine oxide (X = Ph_2PO) – we could tune the chelating properties of the cluster switching from opened to closed conformations by redox-control of the reduced and oxidized states, respectively, and allowing for the chemical and electrochemical capture and release of uranyl in solution (Figure 1b-c).

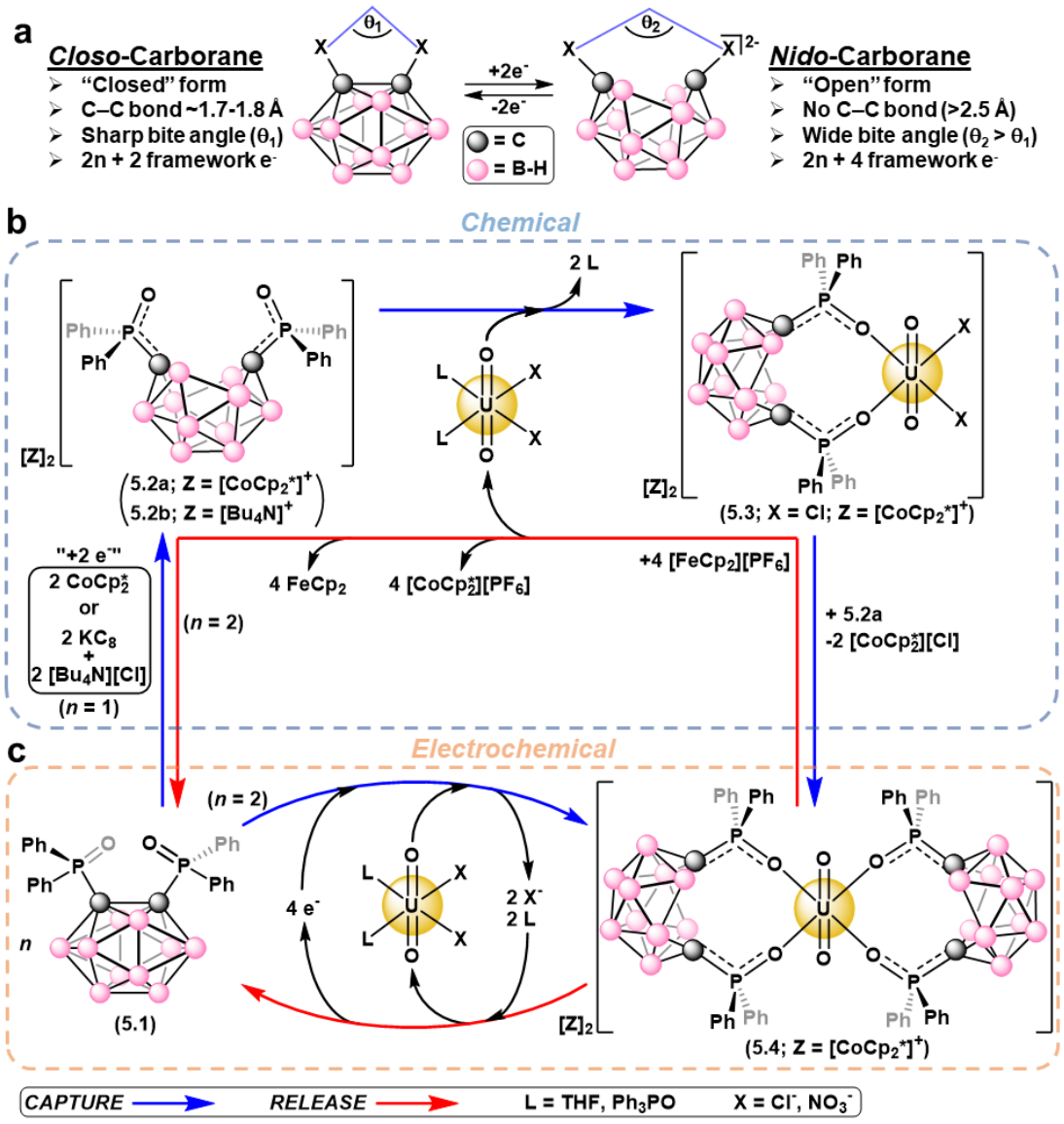

Figure 5.1. a, Depiction of a general cage "closed" *closo*-carborane and reduced cage "open" *nido*-carborane with resulting bite angles, θ (X = alkyl, phenyl, or Ph_2PO). **b,** Monophasic chemical capture and release of uranyl from $UO_2Cl_2L_2$ (L = THF, Ph_3PO (TPO)) using **5.1** under reductive ($CoCp^*_2$) or **5.4** under oxidative ($[FeCp_2][PF_6]$) conditions, respectively. **c,** Mono- or biphasic electrochemical capture and release of $UO_2X_2L_2$ utilizing **5.1** (the product **5.1** is shown for simplicity, but varies depending on the conditions described herein). Experimental details are described in below and in Experimental

Considerations. **b-c**, Blue pathway represents UO_2^{2+} capture; red pathway represents UO_2^{2+} release.

The disubstituted *closo*-carborane, 1,2-$(Ph_2PO)_2$-1,2-$C_2B_{10}H_{10}$ (**5.1**), was synthesized and fully characterized, including by single crystal X-ray diffraction (XRD) studies (Figures 5.1c, 5.2a).[28] The cage C–C bond length (1.688(4) Å) and interatomic P···P distance (3.537 Å) are consistent with similar previously reported compounds.[28,29] We will use these metrics throughout to correlate coordinated and uncoordinated carboranes, both in lieu of, yet proportional to the traditional bite angle, θ (Figure 5.1a). Electrochemical analysis of **5.1** in tetrahydrofuran (THF) revealed two quasi-reversible cathodic waves at -0.93 V and -1.11 V relative to the ferrocene/ferrocenium (Fc/Fc^+) redox couple. Chemical reduction of **5.1** using 2.0 equivalents of decamethylcobaltocene ($CoCp^*_2$) in benzene afforded the direduced *nido*-carborane, $[CoCp^*_2]_2$[(*nido*-1,2-$(Ph_2PO)_2$-1,2-$C_2B_{10}H_{10}$)] (**5.2a**), in 95% isolated yield (Figure 5.1b). The diamagnetic compound revealed four new ^{11}B NMR signals, a downfield shifted ^{31}P resonance, and shifted ^1H resonances, in addition to a new peak at 1.62 ppm for $[CoCp^*_2]^+$, in comparison to **5.1**. Single crystals of **5.2a** suitable for XRD studies were grown by vapor diffusion of diethyl ether into a concentrated solution of **5.2a** in acetonitrile (MeCN) at -38 °C. The solid-state molecular structure revealed an open-cage *nido*-carborane conformation (Figure 5.1a) with a cleaved C–C bond (2.860 Å) and an elongated P···P distance (5.036 Å) relative to **5.1** (Figures 5.1b, 5.2b). We note that an analogous salt, $[Bu_4N]_2$[(*nido*-1,2-$(Ph_2PO)_2$-1,2-$C_2B_{10}H_{10}$)] (**5.2b**) (Figure 5.1b), was also synthesized by initial reduction of **5.1** with K graphite (KC_8), followed by salt metathesis with $[Bu_4N][Cl]$. Compound **5.2b** was fully characterized (with the exception of XRD analysis) and is relevant to the electrochemical experiments described below.

We next investigated the coordination chemistry of **5.1** and **5.2a** to the UO_2^{2+} cation. We found that addition of four equivalents of **5.1** to dimeric $[UO_2Cl_2(THF)_2]_2$ in deuterated dichloromethane (DCM-d_2) resulted in a light-yellow solution from which two new equivalent-intensity, uncoupled ^{31}P resonances appeared at 38.8 and 38.4 ppm in the ^{31}P NMR spectrum downfield shifted from **5.1** (22.8 ppm). The inequivalent P environments suggests that either **5.1** is mono-dentate, or that the two ligands occupy four of five equatorial sites in a pentagonal bipyramidal coordination environment at U, with one chloride occupying the fifth site and the other being outer sphere. While repeated attempts to obtain single crystals suitable for XRD studies failed, the NMR data suggests a 2:1 adduct is formed through displacement of THF to form a complex with a presumed monomeric formulation of UO_2Cl_2(**5.1**)$_2$. In contrast to **5.1**, treatment of two equivalents of **5.2a** to one equivalent of $[UO_2Cl_2(THF)_2]_2$ in MeCN led to the clean formation of a single new resonance at 51.1 ppm in the ^{31}P NMR spectrum, suggesting a bidentate coordination mode for **5.2a** and clean displacement of the THF molecules. Single crystals suitable for XRD studies were grown by vapor diffusion of diethyl ether into a saturated solution of the product in MeCN and confirmed the composition as the salt, $[CoCp^*_2]_2[UO_2Cl_2$(*nido*-1,2-$(Ph_2PO)_2$-1,2-$C_2B_{10}H_{10})]$ (**5.2**) (Figures 5.1b, 5.2c). The structure revealed a chelating *nido*-carborane ligand (from **5.2a**) binding through its O atoms to U, and *trans*-disposed to the Cl atoms in the equatorial plane, resulting in a C_2 rotational axis bisecting the Cl–U–Cl bonds. The C···C (2.855 Å) and P···P distances (4.697 Å) are slightly contracted relative to **5.2a**, and result in a O1–U–O2 bite angle of 86.5(3)° (Figure 5.2c). The bidentate ligand **5.2a** was further capable of displacing the chloride ions at $[UO_2Cl_2(THF)_2]_2$. Addition of four equivalents of **5.2a** to an equivalent of $[UO_2Cl_2(THF)_2]_2$ in MeCN resulted in the isolation of a yellow solid in 80% yield. Monitoring the reaction by ^{31}P NMR spectroscopy revealed

the clean conversion to a new product characterized by a single peak at 52.0 ppm. Single crystals suitable for XRD studies were grown from a concentrated MeCN solution and revealed the composition as the disubstituted complex, $[CoCp^*_2]_2[UO_2(nido\text{-}1,2\text{-}(Ph_2PO)_2\text{-}1,2\text{-}C_2B_{10}H_{10})_2]$ (**5.4**) (Figures 5.1c, 5.2d). The C···C (2.857 Å) and P···P distances (4.806 Å), and resulting O1–U–O2 bite angles of 89.7(17)° are similar to the values observed in **5.3**.

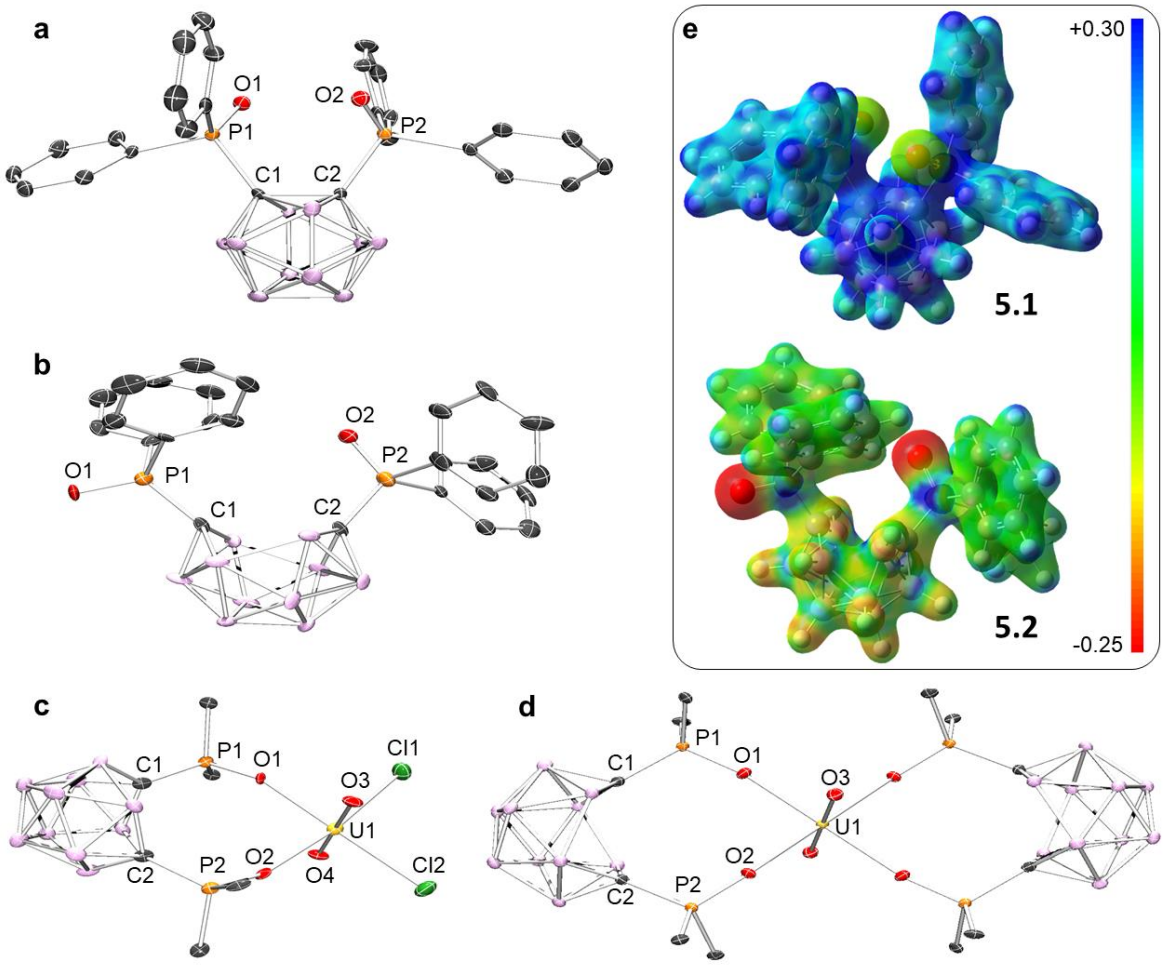

Figure 5.2. a-d, Solid-state molecular structures of **5.1** (**a**), **5.2a** (**b**), **5.3** (**c**), and **5.4** (**d**) obtained from XRD studies. H atoms (**5.1**-**5.4**), $[CoCp^*_2]^+$ counter cations (**5.2a**-**5.4**), phenyl C–H linkages (**5.3**-**5.4**), and all co-crystallized solvent molecules are omitted for clarity. **e,**

Electron density surfaces with colour-coded electrostatic potentials obtained from density functional theory (DFT) calculations using optimized structures of **5.1** and the anion of **5.2a**, labelled **5.2** (red, negative values are indicative of higher electron density).

While both **5.1** and **5.2a** demonstrate an ability to coordinate to UO_2^{2+}, we postulated that a third ligand with a competitive binding affinity to **5.1**, but weaker than **5.2a**, could enable a pathway to UO_2^{2+} release. We devised a series of competition experiments using **5.1**, **5.2a**, and triphenylphosphine oxide (Ph_3PO, TPO) as part of the known complex, $UO_2Cl_2(TPO)_2$.[30] The experiments were monitored by $^{31}P\{^1H\}$ NMR spectroscopy and performed in DCM-d_2. Two equivalents of **5.1** were added to an equivalent of $UO_2Cl_2(TPO)_2$ for a resulting 1:1 molar ratio of **5.1**:TPO. After an equilibration period of 18 hours, the $^{31}P\{^1H\}$ NMR spectrum revealed broadened resonances for $UO_2Cl_2(TPO)_2$ and free TPO, as well as a set of sharp resonances for the proposed complex UO_2Cl_2(**5.1**)$_2$ and free **5.1**. The ratio of UO_2Cl_2(**5.1**)$_2$:**5.1** was determined to be approximately 1:3 suggesting an equilibrium favouring the adduct, $UO_2Cl_2(TPO)_2$, in DCM. The binding affinity of TPO was next compared to **5.2a** by addition of one equivalent of **5.2a** to $UO_2Cl_2(TPO)_2$ in DCM. Rapid precipitation of products was observed. The $^{31}P\{^1H\}$ NMR spectrum of the DCM supernatant revealed clean and full conversion of the starting material, $UO_2Cl_2(TPO)_2$, to the products **5.3** and **5.4**, along with a sharp singlet for TPO, as well as a minor singlet at 47 ppm, the identity of which remains unknown. Analysis of the precipitate dissolved in propylene carbonate (PC) by $^{31}P\{^1H\}$ NMR spectroscopy revealed the clean formation of **5.4**. In contrast to the experiments with **5.1**, these data are consistent with full dissociation of TPO from $UO_2Cl_2(TPO)_2$ in the presence of **5.2a**, with no apparent equilibrium generated (Figure 5.1b-c). The binding affinity of TPO was next tested against PC, a coordinating

solvent which could potentially coordinate to U.[31] An initial $^{31}P\{^{1}H\}$ NMR spectrum of $UO_2Cl_2(TPO)_2$ dissolved in DCM-d_2 revealed two singlets in an approximate 3:1 ratio at 48.09 and 47.97 ppm, respectively, likely arising from the *trans*:*cis* isomerism of this species.[32] While addition of two equivalents of PC to $UO_2Cl_2(TPO)_2$ led to negligible changes as observed by ^{1}H and $^{31}P\{^{1}H\}$ NMR spectroscopy, addition of 20 and 40 equivalents led to broadening of the aromatic peaks in the ^{1}H spectra, as well as broadening of the singlets in the $^{31}P\{^{1}H\}$ spectra. Broadening was measured as the full width at half maximum frequency difference ($\Delta\nu_{FWHM}$) where values of 19 and 43 Hz were respectively observed for the *trans* isomer relative to 2.7 Hz for the starting material, $UO_2Cl_2(TPO)_2$. Together, these data suggest that there is an equilibrium with PC but that it is heavily shifted towards $UO_2Cl_2(TPO)_2$. Lastly, to further support these observations, we enlisted the help of our collaborator, Dr. Roman Dobrovetsky from Tel Aviv University who performed DFT calculations using the B3LYP/def2-SVP level of theory (see Experimental). Electron density surfaces with integrated electrostatic potentials were calculated for **5.1** and **5.2a** and clearly indicate increased electron density at the terminal P=O bonds of **5.2a** upon reduction, accounting for its experimentally observed increased Lewis basicity (Figure 5.2e). This increased basicity is likely complementary to the increased bite angle (Figure 5.1a) in rendering **5.2a** a stronger chelating agent than **5.1**. *In silico* isodesmic reactions of **5.2a**/TPO, TPO/**5.1**, or **5.1**/PC with proton as a model for the uranyl cation were next calculated at the same level of theory in DCM using a conductor-like polarizable continuum model. These results reveal that **5.2a** is several orders of magnitude more basic than TPO, and that **5.1** is several orders of magnitude more basic that PC. In contrast, TPO and **5.1** do not display such large differences, but nonetheless indicate a substantially more basic TPO

than **5.1**. Collectively, the competition reactions and DFT calculations support a relative Lewis basicity trend of: **5.2a** >> TPO > **5.1** >> PC.

With these results in hand, we next investigated the *in situ* chemical capture and release of UO_2^{2+}. To maintain optimal solubility for all compounds (**5.1**-**5.4**), we utilized a 3:1 PC:benzene solvent mixture. An initial 2:4 solution of **5.1**:TPO was prepared and analysed by $^{31}P\{^1H\}$ NMR spectroscopy which revealed the expected two sharp resonances with equivalent integration values. Addition of half an equivalent of $[UO_2Cl_2(THF)_2]_2$ (corresponding to one equivalent of U) resulted in no appreciable change to the resonance for **5.1**, but did result in significant broadening of the resonance for TPO ($\Delta\nu_{FWHM}$ values for TPO are 2.4 Hz and 52 Hz before and after addition, respectively). Interestingly, only trace amounts of $UO_2Cl_2(TPO)_2$ are observed in this spectrum which is likely due to a combination of the rapid exchange with excess free TPO and the large excess (~2000 fold) of PC used relative to U. To initiate chemical capture of UO_2^{2+} with **5.1**, four equivalents of $CoCp^*_2$ were added to the solution. Analysis of the reaction mixture by $^{31}P\{^1H\}$ NMR spectroscopy revealed the rapid and complete conversion of **5.1** to the captured product **5.4** with concomitant release of all TPO, as evidenced by the formation of a sharp singlet at 25.2 ppm that matches the initial integrated value prior to $[UO_2Cl_2(THF)_2]_2$ addition. To initiate the subsequent UO_2^{2+} release by cage-closing of the carborane (Figure 5.1a), we determined the oxidation potential of isolated **5.4** by CV, which revealed a quasi-reversible anodic event at -0.42 V relative to the Fc/Fc^+ redox couple. Thus, we exposed our *in situ* generated solution of **5.4** and TPO to four equivalents of the $[Fc][PF_6]$ oxidant. Analysis of the reaction mixture by $^{31}P\{^1H\}$ NMR spectroscopy revealed the full conversion of **5.4** back to **5.1** along with the re-appearance of a broadened TPO resonance, similar to that of the pre-

reduced solution. Together, these results demonstrate the successful chemical capture and release of UO_2^{2+} in solution.

We next probed cycling the capture and release of UO_2^{2+} electrochemically by galvanostatic bulk electrolysis (GBE). These experiments were conducted using a divided H-cell with two high-surface area coiled Pt electrodes, an anion exchange membrane (AEM) separating the two compartments, and an excess of the Fc/Fc^+ redox couple acting as a Faradaic buffer in the counter compartment (Figure 5.3a). The mixed solvent PC:benzene (3:1) system was again used along with an initial 0.5:5:6 ratio of $[UO_2Cl_2(THF)_2]_2$:**5.1**:TPO reagents and an internal standard for ^{31}P NMR integration. While the use of excess TPO is well reasoned (*vide supra*), the use of excess **5.1** relative to U was found to be necessary for optimal electrochemical performance (see Experimental). An initial $^{31}P\{^1H\}$ NMR spectrum of the solution revealed a sharp signal for **5.1** and a broadened signal for TPO, analogous to those observed for the chemical capture/release experiments (Figure 5.3b, Initial). To initiate the electrochemical capture of UO_2^{2+}, the solution was galvanostatically charged with an applied current of -201.0 μA over 6 hours, achieving a 75% theoretical state of charge (SOC) relative to the UO_2^{2+} concentration (Figure 5.3c, blue). Analysis of the reaction mixture by $^{31}P\{^1H\}$ NMR spectroscopy revealed the conversion of **5.1** to the captured products **5.3** and **5.4** with release of all TPO, as determined by matching its signal intensity with the initial integrated stoichiometry prior to $[UO_2Cl_2(THF)_2]_2$ addition (Figure 5.3b, cycle 1 (blue)). In order to initiate the electrochemical release of UO_2^{2+}, a galvanostatic current of 68.9 μA was applied over 13 hours (Figure 5.3c, red), discharging the cell to a final SOC of 15% (SOC extrema of 0 and 100% were not used in order to allow for reasonably fast charge/discharge rates without potentially shifting into regimes where unwanted secondary electrochemical processes could occur).[33] Analysis of the reaction mixture by $^{31}P\{^1H\}$ NMR spectroscopy

revealed the full conversion of **5.3** and **5.4** back to **5.1**, along with the presence of a broadened TPO resonance (Figure 5.3b, cycle 1 (red)). The electrochemical capture and release by GBE were carried out over the course of another five full cycles (Figure 5.3c), with analyses of the reaction mixtures by $^{31}P\{^{1}H\}$ NMR spectroscopy after each charge and discharge cycle (Figure 5.3b). We observed that repeated cycling resulted in a loss of electrochemically generated **5.3**, which we attribute to chloride migration to the counter compartment over time across the AEM. The gradual appearance of a minor unknown product with a $^{31}P\{^{1}H\}$ resonance at 45 ppm was also observed after each charge cycle. Full integration of all products after each charge cycle revealed little change in excess TPO (average loss of 0.3%/cycle) but slightly higher losses in reduced product **5.4** (average loss of 3.4%/cycle) and in excess ligand **5.1** (average loss of 7.2%/cycle) which may be attributed to electrochemical side reactions.[34,35] Lastly, analysis of measured instrumental charge transferred relative to total charge transferred for UO_2^{2+} capture (determined by $^{31}P\{^{1}H\}$ NMR product integration) reveals a plateauing trend over increasing cycle number with differences in charge attributed to Faradaic losses (Figure 5.3c, top). Together, these results demonstrate the successful monophasic electrochemical capture and release of UO_2^{2+}.

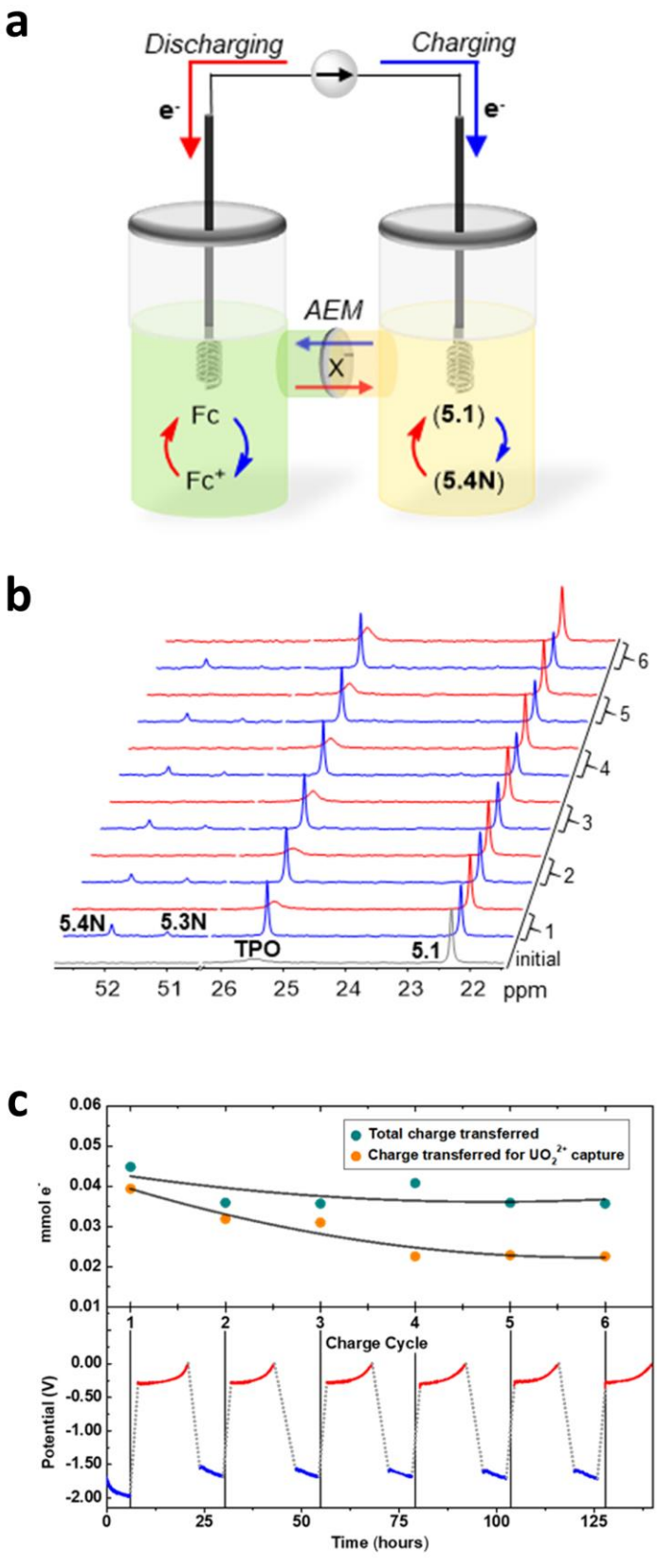
a
Discharging
Charging
e-
e-
AEM
X-
Fc
Fc+
(5.1)
(5.4N)
b
6
5
4
3
2
1
initial
5.4N
5.3N
TPO
5.1
52
51
26
25
24
23
22
ppm
c
Total charge transferred
Charge transferred for UO2 2+ capture
mmol e-
0.06
0.05
0.04
0.03
0.02
0.01
Charge Cycle
Potential (V)
0.00
-0.50
-1.00
-1.50
-2.00
0
25
50
75
100
125
Time (hours)

Figure 5.3. Electrochemical setup and quantification data for the capture (blue) and release (red) of UO_2^{2+} in solution. **a,** Depiction of the H-cell used incorporating excess Fc/Fc^+ as Faradaic buffer (left) and **5.1**, TPO, and $[UO_2Cl_2(THF)_2]_2$ (right) in a 3:1 PC:benzene solvent mixture. Charging the cell (blue) leads to the capture of UO_2^{2+} converting **5.1** to **5.4** (major product) and **5.3** (minor product, not shown). **b,** Quantification of products and reactants by $^{31}P\{^1H\}$ NMR spectroscopy against an inert internal standard, $[Ph_3PNPPh_3][PF_6]$ (not shown). The initial spectrum is shown in grey, while dis/charge cycles are shown in blue (charged spectra) and red (discharged spectra). **c,** Bottom: applied galvanostatic potentials for charge (blue) and discharge (red) cycles. Dashed lines represent wait periods necessary for $^{31}P\{^1H\}$ NMR data acquisition. Each cycle is 24 hours. Top: instrumental measure of delivered charge (teal) versus charge used for reduction of **5.1** measured by quantification of total reduced products, **5.3** and **5.4**, by ^{31}P NMR spectroscopy. Additional experimental details and figures are found in Experimental.

To further demonstrate the potential applicability of our approach, we explored a biphasic extraction scheme involving dissolved UO_2^{2+} (from $UO_2(NO_3)_2(THF)_2$) in the aqueous phase and **5.1** in the organic phase, similar to the PUREX process (Figure 5.4a).[12] Due to the high solubility of PC in water, we switched the organic solvent to 1,2-dichloroethane (DCE). The biphasic capture and release of UO_2^{2+} was simultaneously monitored by $^{31}P\{^1H\}$ NMR spectroscopy for the DCE layer, to monitor the carborane transformations (**5.1**→**5.2b**→**5.3**/**5.4**), and by ultraviolet-visible absorption (UV/Vis) spectroscopy for the aqueous layer, to monitor and quantify the ligand-to-metal charge transfer (LMCT) absorption of UO_2^{2+} centered at 425 nm (Figure 5.4a).[36-38] We note here that this vibronic LMCT absorption is pH-dependent, meaning that the extinction coefficient varies with pH[36];

therefore, we used a buffered solution of UO_2^{2+} below to minimize this potential variability. Due to the incompatibility of DCE with the AEM, we modified our H-cell design for the GBE experiments to instead include a physical glass frit separator coupled with a heterogeneous carbon additive acting as a capacitive buffer, analogous to a previous report.[39] Figure 5.4 outlines the simplified experimental setup displaying only half of the H-cell (see the Experimental for full cell design and methodology). A DCE solution of **5.1** (1.0 equivalent) with $[Bu_4N][PF_6]$ as supporting electrolyte was galvanostatically charged with an applied current of -107.1 μA over 24 hours, achieving a ~ 75% theoretical SOC. Analysis of the solution by $^{31}P\{^1H\}$ NMR spectroscopy revealed the clean conversion of most of **5.1** to **5.2b** (Figure 5.4a). A sodium acetate (NaOAc)-buffered (pH = 5.4) water solution containing 1.25 equivalents of $UO_2(NO_3)_2(THF)_2$ (Figure 5.4a) was next added to the DCE layer with mixing for 2 hours. Approximately 0.9 equivalent of UO_2^{2+} was captured from the aqueous phase as evidenced by comparing the before and after UV/Vis spectra (Figure. 5.4a-4b). Analysis of the DCE solution by $^{31}P\{^1H\}$ NMR spectroscopy revealed the clean formation of a single resonance at 51.5 ppm (Figure 5.4b). Given the similar chemical shifts of isolated complexes **5.3** (51.1 ppm) and **5.4** (52.0 ppm) in DCM, as well as the quantity of UO_2^{2+} captured (0.9 equivalent), we propose that the captured complex is likely a mono-ligated uranyl complex, UO_2X_2(**5.2b**) (termed **5.3N**; X = NO_3^- and/or OAc^-), a derivative of **5.3** (Figure 5.1b); however, we cannot definitively exclude the possibility of a bis-ligated uranyl complex (termed **5.4N**, a derivative of **5.4** (Figure 5.1c)) being formed as well. The aqueous phase was next removed and the cell was galvanostatically discharged to achieve a theoretical final SOC of ~ 0%. Addition of a fresh NaOAc-buffered solution (pH = 5.4) and mixing for 12 hours led to the release of approximately 0.5 equivalent of UO_2^{2+} from the DCE layer to the aqueous layer as confirmed by UV/Vis spectroscopy (Figure 5.4c).

Analysis of the DCE layer by $^{31}P\{^{1}H\}$ NMR spectroscopy revealed the near quantitative conversion to **5.1**, as well as the formation of minor (~20%) unknown byproducts (Figure 5.4c).[40] We propose that the acetate ions likely act as the biphasic ligand analog to the monophasic TPO ligands by competitively binding with **5.1** to UO_2^{2+}. Similarly, control experiments revealed that negligible biphasic capture of UO_2^{2+} from the NaOAc buffered aqueous phase occurred in the presence or absence of **5.1** (see Experimental). Together, these biphasic GBE experiments demonstrate the potential applicability of this redox-switchable capture and release chemistry under real-world conditions.

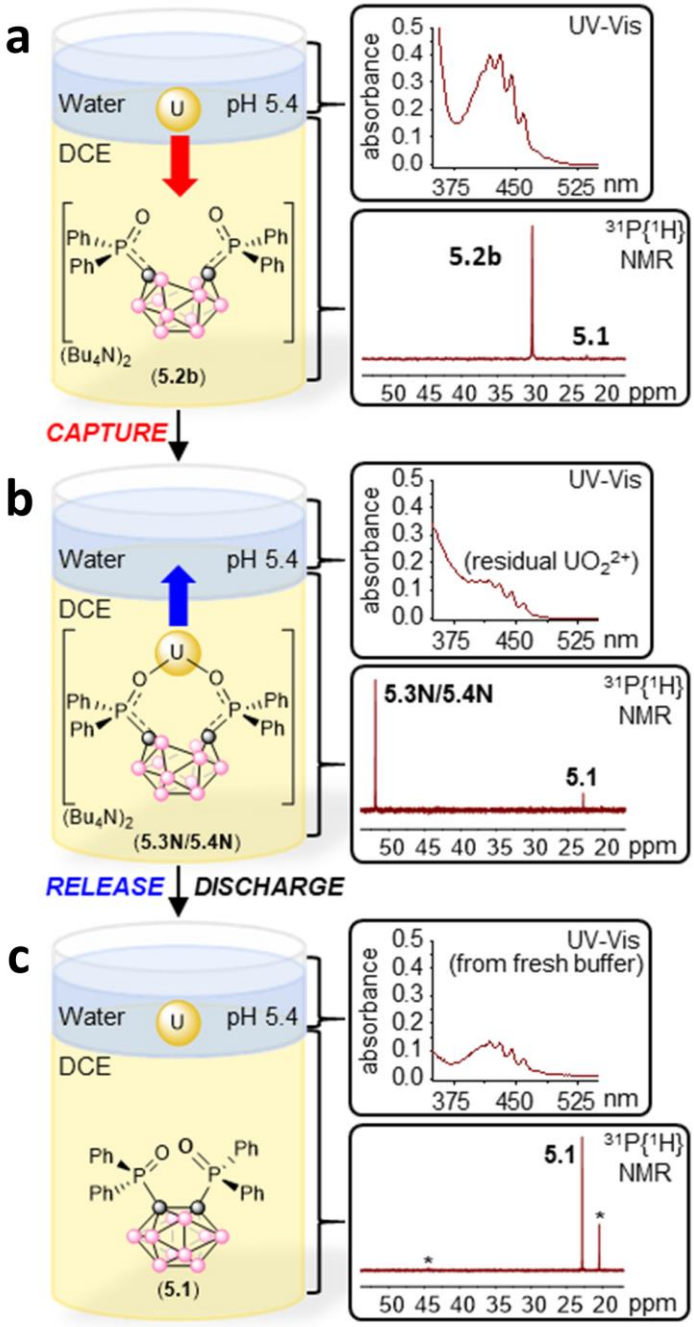

Figure 5.4. Simplified half H-cell depiction of the biphasic electrochemical capture and release of dissolved UO_2X_2 from and to buffered aqueous solutions, respectively, using the initially reduced *nido*-carborane, **5.2b** in DCE. UO_2X_2 is simplified as the yellow sphere "U" and the identity of X may be any combination of OAc^-, NO_3^-, or other depending on the step in the process. **a,** Depiction of the biphasic mixture of UO_2X_2 dissolved in a NaOAc-

buffered aqueous solution (pH = 5.4) and of electrochemically generated **5.2b** from **5.1**. Inset are the aqueous UV/Vis and organic $^{31}P\{^{1}H\}$ NMR spectra after reduction of **5.1** to **5.2b**, but prior to the phases mixing. Residual **5.1** is observed in the latter due to the set SOC. **b,** Depiction of the captured UO_2X_2 in the form of **5.3N** and/or **5.4N**, analogs of **5.3** (with variable X groups) and **5.4**, respectively. Inset top is the aqueous UV/Vis spectrum showing the capture of UO_2X_2 by the **5.2b**/DCE layer. Inset bottom is the corresponding $^{31}P\{^{1}H\}$ NMR spectrum of the DCE layer showing the captured major products (**5.3N/5.4N**), as well as minor residual **5.1**. **c,** Depiction of the biphasic release of UO_2X_2 from the DCE layer to a fresh NaOAc-buffered solution (pH = 5.4) following electrochemical oxidation of **5.3N/5.4N**. Inset are the aqueous UV/Vis and organic $^{31}P\{^{1}H\}$ NMR spectra of free UO_2X_2 and **5.1**, respectively, both consistent with the release of captured UO_2X_2 from the DCE to the aqueous phase. A small amount (~20%) of unknown byproducts (*) is also observed in the $^{31}P\{^{1}H\}$ NMR spectrum.

5.3 Summary

In summary, this report has outlined a new approach to uranyl management involving its capture and, importantly, its release by controlled redox-switchable chelation using a derivatized *ortho*-carborane in monophasic or biphasic (organic/aqueous) environments. We anticipate this fundamentally new direction in cluster carborane chemistry may have a significant impact on nuclear fuel extraction and waste sequestration activities, and may spawn new research directions in related metal capture and release activities.

5.4 Experimental

5.4.1 Considerations

All manipulations were performed under an atmosphere of dry, oxygen-free N_2 or Ar by means of standard Schlenk or glovebox techniques (MBraun (equipped with a -38 °C freezer) or VAC gloveboxes). Hexanes, pentane, dichloromethane (DCM), and benzene were dried on an MBraun solvent purification system. Acetonitrile ($–H_3$ and $–D_3$) was dried over CaH_2 for several days prior to distillation. THF was dried over sodium benzophenone and distilled. Propylene carbonate (PC) was degassed by freeze-pump-thaw and stored on activated 4 Å molecular sieves prior to use. 1,2-Dichloroethane (DCE) was initially distilled followed by drying over CaH_2 for several days prior to a second distillation and subsequent storage on activated 4 Å molecular sieves. $[FeCp_2][PF_6]$, $[Bu_4N][Cl]$, and triphenylphosphine oxide (TPO) were purchased from Fisher Scientific, trimesitylphosphine (Mes_3P) was purchased from VWR International, *n*BuLi (1.6 M in hexanes) was purchased from Aldrich, and all were used without further purification. *Ortho*-carborane was purchased from Boron Specialties and sublimed before use. Ph_2PCl was purchased from Aldrich and vacuumed distilled prior to use. Decamethylcobaltocene ($CoCp^*_2$) was purchased from Aldrich and purified by filtration through Celite using pentane, followed by recrystallization from pentane at -38 °C over several days. $[Bu_4N][PF_6]$ was purchased from Oakwood Chemicals and purified by twice recrystallizing from hot ethanol. The recrystallized product was then washed with cold water, cold ethanol, and pentane prior to drying at 100 °C under vacuum for 24 h. Sodium acetate (NaOAc) buffer was prepared from a stock solution purchased from Aldrich (pH 4.9) and adjusted to pH 5.4 using NaOH. The pH value was confirmed using a pH meter. Ketjenblack® EC-600JD (KB) was purchased from a private supplier. $UO_2Cl_2(TPO)_2$[41], $[UO_2Cl_2(THF)_2]_2$[42], KC_8[43], and bis(triphenyl-phosphoranylidene)ammonium hexafluorophosphate ($[Ph_3PNPPh_3][PF_6]$)[44] were prepared by literature procedures.

NMR spectra were obtained on a Varian Unity Inova 500 MHz or Agilent Technologies 400 MHz spectrometer, and referenced to residual solvent resonances of acetonitrile (MeCN-d_3) or dichloromethane (DCM-d_2), or externally (^{11}B: 85% $(Et_2O)BF_3$, ^{31}P: 85% H_3PO_4,). Chemical shifts (δ) are recorded in ppm. All ^{11}B NMR spectra were processed using MestReNova software in order to reduce background signal with a linewidth of approximately 3000 Hz from the Pyrex NMR tubes. The NMR time-domain data were first left-shifted to discard the first ~0.1 ms. To correct the linear phase change, linear prediction (LP) is used to fill the initial discarded data before Fourier transform or an appropriate linear phase correction is applied to the frequency domain data after Fourier transform. T_1 relaxation values for ^{31}P nuclei were determined using the inversion-recovery method. The delay times after the 180-degree inversion pulse were varied up to the maximum of 5 times of the expected T_1 values. The signal recovery curve was fit with an exponential function to extract the T_1 values. Subsequent 1D spectra were acquired with 5 times the longest T_1 value measured for accurate integrations.

UV/Vis absorption spectra were collected on a Shimadzu UV-2401PC spectrophotometer. The UO_2^{2+} extinction coefficient (ε) was experimentally determined to be 7.715 $L \cdot mol^{-1} \cdot cm^{-1}$ (460 nm) at pH 5.4.

Elemental analyses (C, N, H) were recorded at the University of California, Berkeley using a Perkin Elmer 2400 Series II combustion analyser.

Cyclic Voltammetry was performed on a CH Instruments Electrochemical Analysis potentiostat, equipped with a 3 mm diameter glassy carbon working electrode, a Ag wire pseudo-reference electrode, and a Pt wire counter electrode using a $[Bu_4N][PF_6]$ (0.1 M) solution as supporting electrolyte. CVs were referenced to the ferrocene/ferrocenium (Fc/Fc^+) redox couple.

Galvanostatic Bulk Electrolysis cycling experiments were carried out using a Metrohm Autolab PGSTAT128N potentiostat/galvanostat and carried out inside an Ar glovebox. The full experimental setup for both the mono- and biphasic cycling experiments is described in sections 5.4.4-5.4.5.

X-ray crystallography data was collected on a Bruker KAPPA APEX II diffractometer equipped with an APEX II CCD detector using a TRIUMPH monochromator with a Mo Kα X-ray source (α = 0.71073 Å). The crystals were mounted on a cryoloop under Paratone-N oil, and all data were collected at 100(2) K using an Oxford nitrogen gas cryostream system. A hemisphere of data was collected using ω scans with 0.5° frame widths. Data collection and cell parameter determination were conducted using the SMART program. Integration of the data frames and final cell parameter refinement were performed using SAINT software. Absorption correction of the data was carried out using SADABS. Structure determination was done using direct or Patterson methods and difference Fourier techniques. All hydrogen atom positions were idealized and rode on the atom of attachment. Structure solution, refinement, graphics, and creation of publication materials were performed using SHELXTL or OLEX^2.

5.4.2 Syntheses

Synthesis of *closo*-(1,2-(Ph_2PO)$_2$-1,2-$C_2B_{10}H_{10}$) (5.1):

The synthesis of compound **5.1** was accomplished in two steps by modifications to literature procedures.[45,46]

Step 1:

A solution of *n*BuLi in hexane (1.6 M, 28.2 mL, 45 mmol) was added at -78 °C dropwise to a solution of *ortho*-carborane (3.1 g, 21.5 mmol) in dry diethyl ether (250 mL), resulting in

the formation of a fine colourless precipitate. The reaction was slowly warmed to room temperature, and after stirring for 30 mins at room temperature, the mixture was cooled to 0 ^{o}C and Ph_2PCl (7.7 mL, 41.7 mmol) was added dropwise, resulting in a pale orange solution with a colourless precipitate. The mixture was stirred for 30 mins at 0 ^{o}C. The solution was brought to room temperature and stirred for 30 mins and was subsequently warmed to reflux and stirred for an additional 30 mins. The solution was cooled to 0 °C and water (30 mL) was slowly added to the mixture. The mixture was allowed to stir for 20 mins and was filtered over a glass frit, where the resulting solid was washed with additional water (30 mL) and diethyl ether (20 mL). The solid was dried under vacuum at 100 ^{o}C for 2 h. The product was recrystallized from a mixture of hexane/toluene and was obtained in 81% yield (8.6 g, 16.7 mmol.) ^{1}H NMR (400 MHz, $CDCl_3$): δ 7.06-7.47 (m, 20H); 0.98-2.66 (broad, 10H). ^{11}B NMR (400 MHz, $CDCl_3$): δ -0.40; -9.42. ^{11}B{^{1}H} NMR (400 MHz, $CDCl_3$): δ -0.40; -7.21; -9.42. ^{31}P{^{1}H} NMR (400 MHz, $CDCl_3$): δ 7.88.

Step 2:

A solution of H_2O_2 (30% in water, 1.8 mL, 58.7 mmol) was added dropwise to a solution of [*closo*-(1,2-$(Ph_2P)_2$-1,2-$C_2B_{10}H_{10}$)] (from step 1) (2.1 g, 4.1 mmol) in THF (50 mL). The reaction was stirred for 3 h at room temperature. The reaction was monitored by ^{31}P NMR for formation of an unwanted side-product at 49 ppm. Once this product formed, the reaction was discontinued by addition of chloroform. The mixture was washed with water and brine, the phases separated and the organic layer dried with Na_2SO_4. The solvent was removed, and the solid was slowly recrystallized from acetonitrile to yield a colourless crystalline solid. The solid was dried under vacuum at 80 °C for several hours. (1.4 g, 2.6 mmol, 60% yield). Single crystals suitable for X-ray crystallography were obtained by vapor diffusion of pentane in a saturated THF solution of **5.1**. ^{1}H NMR (400 MHz, MeCN-d_3): δ

7.99 (m, 8H); 7.63 (m, 4H); 7.54 (m, 8H); 2.5 (broad s, 10H). ^{11}B and ^{11}B{^{1}H} NMR (400 MHZ, MeCN-*d*$_3$): δ 0.66; -8.75. ^{31}P{^{1}H} NMR (400 MHz, MeCN-*d*$_3$): δ 22.8. *Anal. Calcd*. for $C_{26}H_{30}B_{10}O_2P_2$: C, 57.35; H, 5.55. Found: C, 57.33; H, 5.66.

Synthesis of UO_2Cl_2(5.1)$_2$:

A 20 mL vial equipped with a magnetic stirbar was charged with **5.1** (54.4 mg, 0.1 mmol) and 2 mL of DCM. In a separate vial, $[UO_2Cl_2(THF)_2]_2$ (24.2 mg, 0.025 mmol) was dissolved in 2 mL of DCM and added to the stirring solution of **5.1**, resulting in the formation of a light-yellow suspension. After 1 h, the reaction mixture became homogeneous. This was stirred for an additional 24 h at room temperature. The solvent was removed, yielding a yellow solid (62.5 mg). Multiple attempts were made to obtain single crystals suitable for XRD studies, but failed. ^{1}H NMR (400 MHz, DCM-*d*$_2$): δ 8.32-6.29 (m, 20H); 2.5 (broad s, 10H). ^{11}B and ^{11}B{^{1}H} NMR (400 MHz, DCM-*d*$_2$): δ 5.84; -8.46. ^{31}P{^{1}H} NMR (400 MHz, DCM-*d*$_2$): δ 38.8 (s); 38.4 (s). *Anal. Calcd*. for $C_{52}H_{60}B_{20}Cl_2O_6P_4U \cdot 1/2CH_2Cl_2$: C, 43.05; H, 4.16. Found: C, 42.76; H, 4.32.

Synthesis of [CoCp$^*_2$]$_2$[(*nido*-1,2-(Ph$_2$PO)$_2$-1,2-C$_2$B$_{10}$H$_{10}$)] (5.2a):

A 20 mL vial equipped with a magnetic stirbar was charged with **5.1** (54.4 mg, 0.1 mmol) and 6 mL of benzene. In a separate vial, $CoCp^*_2$ (69.1 mg, 0.2 mmol, 2.0 equiv) was dissolved in 4 mL of benzene and added dropwise to the stirring solution of **5.1**. Upon addition, a yellow solid immediately precipitated from the reaction mixture and the mixture was stirred for an additional 4 h at room temperature. Stirring was discontinued and the solid was allowed to settle to the bottom of the vial. The supernatant was decanted and filtered on a plug of Celite. The solids were washed with benzene (3 x 6 mL) and each washing was filtered over the same Celite plug. The remaining solids were then dissolved in a minimal amount of MeCN (2 mL) and filtered on the same Celite plug into a new vial. The MeCN

filtrate was collected and the volatiles were removed *in vacuo*, yielding a shiny golden-yellow solid (114.3 mg, 0.95 mmol, 95% yield). Single crystals suitable for X-ray crystallography were obtained by vapor diffusion of Et_2O in a saturated MeCN solution of **5.2a** at -38 °C. ^{1}H NMR (400 MHz, MeCN-d_3): δ 8.05 (broad m, 8H); 7.24 (broad s, 12H); 1.62 (s, 60H). Note: Carborane B–**H** resonances are too broad to be observed. ^{11}B and ^{11}B{^{1}H} NMR (400 MHZ, MeCN-d_3): δ 20.24; -0.62; -18.46; -22.06. ^{31}P{^{1}H} NMR (400 MHz, MeCN-d_3): δ 29.8. *Anal. Calcd*. for $C_{66}H_{90}B_{10}Co_2O_2P_2$: C, 65.88; H, 7.54. Found: C, 65.57; H, 7.67.

Synthesis of [Bu$_4$N]$_2$[(*nido*-1,2-(Ph$_2$PO)$_2$-1,2-C$_2$B$_{10}$H$_{10}$)] (5.2b):

The synthesis of compound **5.2b** was accomplished in two steps.

Step 1:

In the glovebox, a 250 mL round bottom equipped with a magnetic stirbar was charged with **5.1** (272.2 mg, 0.5 mmol), 20 mL of THF, and cooled to -78 °C. In a separate vial, KC_8 (182.4 mg, 1.35 mmol, 2.7 equiv) was suspended in 20 mL of THF and added slowly dropwise to the stirring solution of **5.1**. Upon addition, the KC_8 suspension began to turn grey in colour and was stirred for 30 mins at room temperature. Stirring was discontinued and the mixture was filtered over a pad of Celite on a fine glass frit. The graphite pad was washed additionally with MeCN (3 x 5 mL). The filtrate was collected and the volatiles were removed *in vacuo*, yielding a pale-yellow oil. The oil was redissolved in THF (5 mL) and layered with 5 mL of pentane and was recrystallized at -38 °C, yielding a white solid (234.1 mg, 0.38 mmol, 75% yield). ^{1}H NMR (400 MHz, MeCN-d_3): δ 7.81 (broad m, 8H); 7.28 (broad m, 12H). Note: Carborane B–**H** resonances are too broad to be observed. ^{11}B NMR (400 MHZ, MeCN-d_3): δ 20.24; -0.62; -18.46; -22.06. ^{31}P{^{1}H} NMR (400 MHz,

MeCN-d_3): δ 31.8. *Anal. Calcd*. for $C_{26}H_{30}B_{10}K_2O_2P_2$•THF: C, 51.86; H, 5.51. Found: C, 51.09; H, 5.47.

Step 2:

A 20 mL vial equipped with a magnetic stirbar was charged with $[K]_2$[(*nido*-1,2-$(Ph_2PO)_2$-1,2-$C_2B_{10}H_{10}$)•THF] (655.4 mg, 0.94 mmol) (Step 1), 15 mL of DCM, and was cooled to -78 °C. In a separate vial, $[Bu_4N][Cl]$ (528 mg, 1.88 mmol, 2.0 equiv) was dissolved in 10 mL of DCM and added dropwise to the stirring carborane suspension. Upon addition, the reaction mixture became homogenous and after 1 h, a white precipitate began to crash out. This mixture was stirred for 2 h at room temperature. Stirring was discontinued and all volatiles were removed, yielding a pale yellow solid. A minimal amount of DCM (3 mL) was added and the mixture was filtered on a plug of Celite. The solids were washed with chilled DCM (3 x 2 mL) and each washing was filtered over the same Celite plug. The DCM filtrate was collected and the volatiles were removed *in vacuo*, yielding a pale-yellow residue which was triturated with pentane (10 mL) and dried in vacuo to yield an off-white solid which was recrystallized from DCM and pentane (690.4 mg, 0.67 mmol, 71% yield). ^{1}H NMR (400 MHz, MeCN-d_3): δ 8.03 (m, 8H); 7.25 (broad s, 12H); 3.08 (m, 16H); 1.59 (m, 16H); 1.35 (m, 16H); 0.96 (t, 24H). Note: Carborane B–**H** resonances are too broad to be observed. ^{11}B and ^{11}B{^{1}H} NMR (400 MHZ, MeCN-d_3): δ 20.25; -0.65; -18.42; -22.05. ^{31}P{^{1}H} NMR (400 MHz, MeCN-d_3): δ 30.1. *Anal. Calcd*. for $C_{58}H_{102}B_{10}N_2O_2P_2$: C, 67.67; H, 9.99. Found: C, 66.81; H, 10.29.

Synthesis of $[CoCp^*_2]_2[UO_2Cl_2$(*nido*-1,2-$(Ph_2PO)_2$-1,2-$C_2B_{10}H_{10})]$ (5.3):

A 20 mL vial equipped with a magnetic stirbar was charged with $[UO_2Cl_2(THF)_2]_2$ (16.9 mg, 0.018 mmol) and 4 mL of MeCN. In a separate vial, **5.2a** (42.2 mg, 0.035 mmol) was dissolved in 4 mL of MeCN and then added dropwise to the stirring solution of

$[UO_2Cl_2(THF)_2]_2$, turning dark yellow in colour. After stirring for 5 mins, a yellow solid began to precipitate from the reaction mixture and this was stirred at room temperature for 4 h. Stirring was discontinued and the mixture was passed over a plug of Celite, collecting a yellow solid and a yellow filtrate. The solvent was removed from the yellow filtrate yielding a yellow solid which was washed with THF (3 x 2 mL) and passed over another plug of Celite. The filtrate was collected and the volatiles were removed *in vacuo,* yielding a yellow powder. Residual $[CoCp^*_2][Cl]$ was removed by selectively recrystallizing the mixture from pyridine/Et_2O at -38 °C. The supernatant was transferred and volatiles removed collecting a yellow solid (36.3 mg, 0.024 mmol, 69% yield). Single crystals suitable for XRD studies were grown by vapor diffusion of Et_2O into a saturated MeCN solution of **5.3** at room temperature. ^{1}H NMR (400 MHz, MeCN-d_3): δ 8.13 (m, 10H); 7.35 (m, 10H); 1.66 (s, 60H). Note: Carborane B–**H** resonances are too broad to be observed. ^{11}B and ^{11}B{^{1}H} NMR (400 MHZ, MeCN-d_3): δ 0.27; -16.90; -19.69. ^{31}P{^{1}H} NMR (400 MHz, MeCN-d_3): δ 51.12. *Anal. Calcd.* for $C_{66}H_{90}B_{10}Cl_2Co_2O_4P_2U$•2MeCN: C, 51.70; H, 5.95; N, 1.72. Found: C, 51.91; H, 5.88; N, 1.74.

Synthesis of $[CoCp^*_2]_2[UO_2(nido\text{-}1,2\text{-}(Ph_2PO)_2\text{-}1,2\text{-}C_2B_{10}H_{10})_2]$ (5.4):

A 20 mL vial equipped with a magnetic stirbar was charged with **5.2a** (26.6 mg, 0.022 mmol) and 1.5 mL of MeCN. In a separate vial, $[UO_2Cl_2(THF)_2]_2$ (5.3 mg, 0.0055 mmol) was dissolved in 1.5 mL of MeCN and then added dropwise to the stirring solution of **5.2a**. After stirring for 5 mins, a yellow solid began to precipitate from the reaction mixture and this was stirred at room temperature for 24 h. Stirring was discontinued and the solid was allowed to settle to the bottom of the vial. The supernatant was decanted and filtered on a plug of Celite. The solids were washed with MeCN (3 x 2 mL) and each washing was filtered over the same Celite plug. The remaining solids were then dissolved in a minimal

amount of pyridine and filtered on the same Celite plug into a new vial. The pyridine filtrate was collected and the volatiles removed *in vacuo*, yielding a light-yellow powder (35.5mg, 0.018 mmol, 80% yield). Single crystals suitable for XRD analysis were grown from a small-scale reaction in a J-young NMR tube which was charged with a solution of **5.2a** (12.0 mg, 0.01 mmol) in MeCN-d_3 (0.25 mL). A solution of $[UO_2Cl_2(THF)_2]_2$ (2.4 mg, 0.0025 mmol) in MeCN-d_3 (0.25 mL) was added to this whereupon crystals suitable for XRD analysis slowly formed on the walls of the NMR tube. ^{1}H NMR (400 MHz, MeCN-d_3): δ 8.13 (m, 15H); 7.38 (m, 10H); 7.24 (m, 15H); 1.68 (s, 60H). Note: Carborane B–**H** resonances are too broad to be observed. ^{11}B and ^{11}B{^{1}H} NMR (400 MHZ, MeCN-d_3): δ 0.26; -17.15; -20.66. ^{31}P{^{1}H} NMR (400 MHz, MeCN-d_3): δ 52.0. *Anal. Calcd*. for $C_{92}H_{120}B_{20}Co_2O_6P_4U$: C, 54.76; H, 5.99. Found: C, 55.22; H, 6.36.

5.4.3 Chemical Capture and Release of UO_2^{2+}

Formation of *in-situ* generated [$(UO_2)(TPO)_2Cl_2$]: A 20 mL vial equipped with a magnetic stirbar was charged with **5.1** (2.0 equiv, 5.4 mg, 0.01 mmol), TPO (4.0 equiv, 5.6 mg, 0.02 mmol), and Mes_3P (4.0 equiv, 7.7 mg, 0.02 mmol) and dissolved in a 3:1 PC:benzene (3 mL) solvent system. A 500 μL aliquot was taken from this mixture and placed in an NMR tube equipped with a MeCN-d_3 capillary tube. A ^{31}P{^{1}H} NMR spectrum was collected and the relative integrations recorded. The NMR solution was returned to the vial and $[UO_2Cl_2(THF)_2]_2$ (0.5 equiv, 2.4 mg, 0.0025 mmol) was added. The mixture was stirred vigorously until all the solids were dissolved (~20 mins), resulting in a light-yellow coloured solution. After 1 h, a 500 μL aliquot was taken from the reaction mixture and placed in an NMR tube equipped with a MeCN-d_3 capillary tube. A ^{31}P{^{1}H} NMR spectrum

was obtained. After the spectrum was recorded, the NMR sample was transferred back into the reaction mixture.

Reduction: To the solution generated above, $CoCp^*_2$ (4.0 equiv, 6.6 mg, 0.02 mmol) in 100 μL of benzene was added to the solution dropwise. Upon addition, the solution turned golden in colour and was stirred for 1 h at room temperature. A 500 μL aliquot was then taken from the reaction mixture and placed in an NMR tube equipped with a MeCN-d_3 capillary tube. A $^{31}P\{^1H\}$ NMR spectrum was obtained. After the spectrum was obtained, the NMR solution was transferred back into the reaction mixture.

Oxidation: To the reduced solution above, [Fc][PF_6] (4.0 equiv, 6.6 mg, 0.02 mmol) was added. Upon addition, the solution turned green in colour, and then turned a golden colour. This was stirred for 1 h at room temperature after which a 500 μL aliquot was taken from the reaction mixture and placed in an NMR tube equipped with a MeCN-d_3 capillary tube. A $^{31}P\{^1H\}$ NMR spectrum was obtained. After the spectrum was obtained, the NMR sample was transferred back into the reaction mixture.

5.4.4 Monophasic Electrochemical Capture and Release of UO_2^{2+}

Experimental Conditions: Galvanostatic bulk electrolysis experiments were carried out in a divided glass H-cell (Figure 5.5).

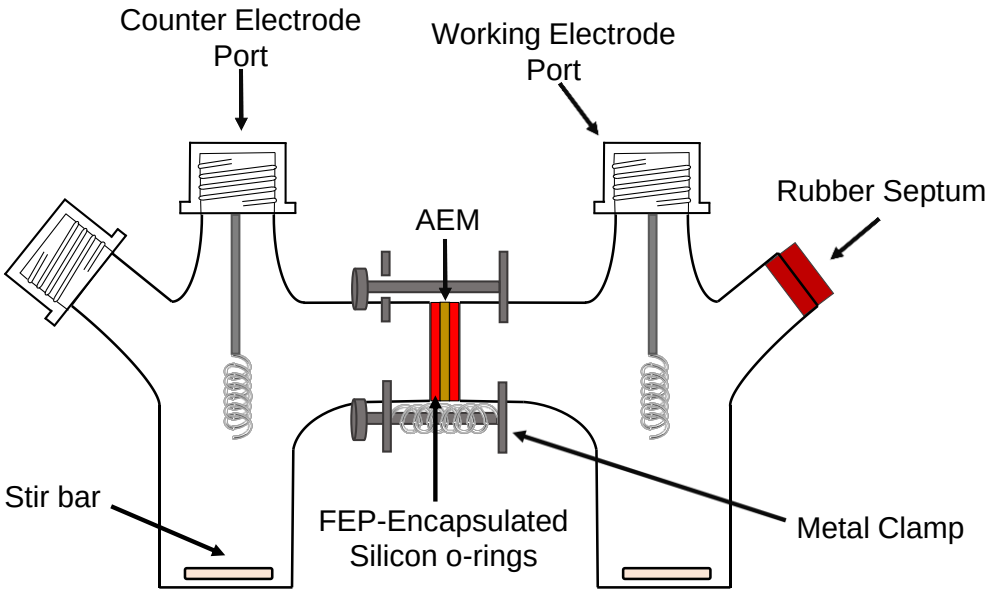

Figure 5.5. Schematic of the divided H-cell used for the monophasic galvanostatic bulk electrolysis cycling experiments with UO_2^{2+}.

The physical barrier between each component of the cell, and the respective two Bio-Logic high-surface coiled Pt electrodes, was an anion exchange membrane (Membranes International, AMI-7001) held in place by two FEP-encapsulated silicon o-rings with a metal clamp. The electrodes were cleaned by rinsing with distilled water and acetone and then heating white-hot with a butane torch prior to use. The anion exchange membrane was soaked in a 0.1 M $[Bu_4N][PF_6]$ solution of PC/benzene (3:1) over 3 Å molecular sieves for 24 hours prior to use. The left compartment, containing the counter electrode, consisted of Fc (41.9 mg, 0.225 mmol) and $[Fc][PF_6]$ (74.5 mg, 0.225 mmol) in 7.0 mL of a 0.1 M $[Bu_4N][PF_6]$ PC:benzene solution. The right compartment, containing the working electrode, contained **5.1** (5 equiv, 40.8 mg, 0.075 mmol), TPO (6 equiv, 25.0 mg, 0.09 mmol), $[UO_2Cl_2(THF)_2]_2$ (0.5 equiv, 7.3 mg, 0.0075 mmol of dimer (1.0 equiv of U monomer)), and

$[Ph_3PNPPh_3][PF_6]$ (1.0 equiv, 10.2 mg, 0.015 mmol) in a 0.1 M $[Bu_4N][PF_6]$ PC:benzene solution (7.0 mL).

Experimental Parameters: The cell was charged/discharged over the course of six cycles. To initiate UO_2^{2+} capture, the first cycle was charged with an applied current of -201.0 μA over the course of 6 h to a 75% state of charge (SOC) relative to the $[UO_2Cl_2(THF)_2]_2$ concentration. After the cell was charged, a wait period of 2 h was incorporated in between charge/discharge cycling (Figure 5.3c, gray dashed). UO_2^{2+} release was achieved by discharging the cell galvanostatically at an applied current of 68.94 μA over the course of 13 h, utilizing voltage cutoffs (0.0 V), to a final SOC of approximately 15% relative to the initial $[UO_2Cl_2(THF)_2]_2$ concentration. After each cell discharge, a wait period ranging between 4–5 h was incorporated (depending on when the voltage cutoffs were applied) in between discharging/charging cycles. Each additional cycle thereafter was charged and discharged galvanostatically at currents of -160.87 μA and 68.94 μA, respectively. This resulted in charging cycles from ~15 to ~75% SOC, and between ~75 to ~15% SOC, respectively. Between each charge/discharge a $^{31}P\{^1H\}$ NMR spectrum was obtained using a 40 s relaxation delay with $[Ph_3PNPPh_3][PF_6]$ as the standard. We note that an excess of **5.1** was used to keep the applied current (I_{app}) below the limiting current at any given time ($I_l(t)$) for the presumed EC mechanism involving reduction of **5.1** followed by uranyl ligation. This allows the use of a galvanostatic charge/discharge procedure operating close to the mass-transfer-controlled plateau (similar to potentiostatic methods) but with the added benefit of not requiring prior knowledge of the optimal applied voltage, which will be a function of both the onset of the reductive process and total cell impedance.[47] Attempts at GBE with stoichiometric equivalents of **5.1**, revealed an earlier than expected onset of $I_{app} > I_l(t)$, clearly indicating that additional and unwanted electrochemical processes were being

accessed, perhaps indicating an initial degradation of **5.1** within the system. Therefore, an initial ratio of 0.5:6:8 for $[UO_2Cl_2(THF)_2]_2$:**5.1**:TPO reagents was utilized.

5.4.5 Biphasic Electrochemical Capture and Release of UO_2^{2+}

Experimental Conditions: A complete, stepwise, half-cell figure of the experiments conducted in this section, along with spectroscopic data is shown in Figure 5.4. Two-electrode galvanostatic bulk electrolysis was performed in an argon glovebox utilizing a two compartment H-cell with a glass frit separator, a stir bar in each compartment, and reticulated vitreous carbon (RVC) foam electrodes for both the working and counter electrodes (Figure 5.6).

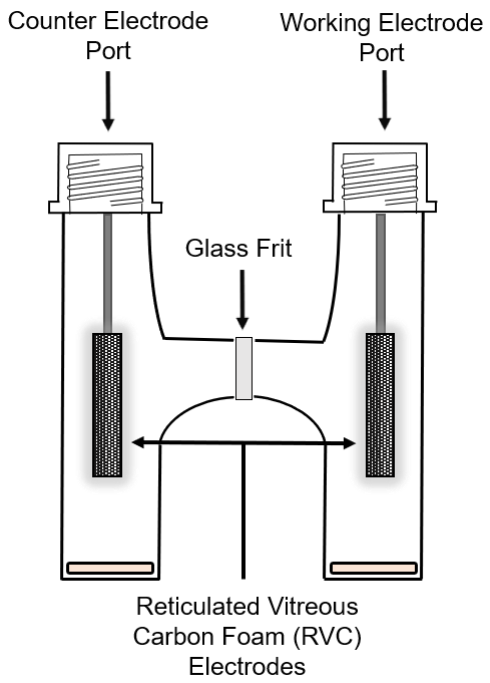

Figure 5.6. Schematic of the two-compartment H-cell used for the biphasic electrochemical capture and release of UO_2^{2+}.

The RVC foam electrodes consisted of a ~5 cm steel rod inserted into 100 PPI Duocel® RVC foam core (length ~2.5 cm; diameter ~3 mm), with a tap bore (length ~5 mm; diameter

~2 mm), which was filled with molten gallium to fuse the steel connector to the RVC foam. Each electrode has an end-to-tip resistance of < 5 Ω. The RVC electrodes were rinsed with methanol and dried under reduced pressure overnight prior to use. The Ketjenblack used was dried for 48 h in a 175 ^{o}C oven and ground in a glass mortar and pestle under inert atmosphere prior to use.

Reduction (charging): The counter compartment consisted of 400 mg of Ketjenblack suspended in 6 mL of a 0.1 M solution of $[Bu_4N][PF_6]$ in DCE. The working compartment consisted of **5.1** (34 mg, 0.0625 mmol, 1.0 equiv) dissolved in 6 mL of a 0.1 M solution of $[Bu_4N][PF_6]$ in DCE. A charging current of -107.1 μA with a -9.25 C charge cutoff was utilized, resulting in a ~ 75% SOC after 24 h assuming 100% columbic efficiency. Upon completion, the working compartment solution was analysed by $^{31}P\{^{1}H\}$ NMR spectroscopy to reveal the formation of **5.2b**. The working compartment solution was then removed from the H-cell and placed in a 20 mL vial for subsequent capture chemistry.

UO_2^{2+} capture: A 5 mL vial was charged with excess $UO_2(NO_3)_2(THF)_2$ (42 mg, 0.078 mmol, 1.25 equiv), and dissolved in 3 mL of a 0.1 M sodium acetate buffer adjusted to pH 5.4 (0.026 M UO_2^{2+}). An aliquot of the resulting pale-yellow solution was used to record an initial UV-Vis spectrum. The aliquot was transferred back to the 5 mL vial and this solution was added slowly dropwise without stirring to the DCE solution containing the electrochemically reduced **5.1** (forming **5.2b**). After addition, the mixture was allowed to stir for 2 hours, resulting in a bright yellow organic phase and a very pale-yellow aqueous phase. Stirring was discontinued and the organic and aqueous phases were separated using a small separatory funnel. An aliquot of the aqueous phase was used to record a UV-Vis spectrum, indicating that 0.022 mmol of UO_2^{2+} remained, which is equivalent to the capture of 0.056 mmol (~0.9 equiv) to the organic phase. A 1 mL aliquot was taken from the pale

yellow dichloroethane layer and transferred to an NMR tube. An unlocked $^{31}P\{^{1}H\}$ NMR spectrum was collected indicating the formation of **5.N/5.4N**. The NMR solution was returned to the 20 mL vial.

Oxidation (discharging): Two-electrode galvanostatic bulk electrolysis (discharging) of the captured DCE solution was performed using the same cell utilized for charging. A discharging current of 107.1 μA was applied until 9.49 C of charge was transferred resulting in a final SOC of ~ 0% (assuming 100% columbic efficiency and no loss of material during the biphasic capture). Upon completion, the working compartment solution was removed and placed in a 20 mL vial for subsequent release chemistry.

UO_2^{2+} release: The 20 mL vial containing the electrochemically oxidized **5.3N/5.4N** yellow DCE solution was equipped with a stirbar and a solution of 0.1 M sodium acetate buffer adjusted to pH 5.4 (3 mL) was added dropwise to it. The mixture was allowed to stir for 12 hours, resulting in a pale-yellow aqueous phase and a colourless organic layer. The organic and aqueous phases were separated using a small separatory funnel, and an aliquot of the aqueous layer was used to take a UV-Vis spectrum indicating the presence of released UO_2^{2+} (0.031 mmol, ~ 0.5 equiv). A 1 mL aliquot was taken from the yellow DCE layer and transferred to an NMR tube. An unlocked $^{31}P\{^{1}H\}$ NMR spectrum was collected indicating the clean formation of **5.1** and a small unknown by-product at 20.1 ppm.

5.4.6 Biphasic Control Experiments

UO_2^{2+} migration from water to DCE in the absence of carborane (5.1 or 5.2a/b): A 5 mL vial was charged with $UO_2(NO_3)_2(THF)_2$ (14.0 mg, 0.026 mmol), and dissolved in 1.5 mL of 0.1 M sodium acetate buffer adjusted to pH 5.4 (0.017 M UO_2^{2+}). An aliquot of the resulting pale-yellow solution was used to record an initial UV-Vis spectrum. The aliquot

was transferred back to the 5 mL vial. A separate 20 mL vial charged with a stirbar, and $[Bu_4N][PF_6]$ (0.2324 g, 0.1 M) dissolved in DCE (6.0 mL). To the clear DCE solution, the pale yellow aqueous solution was added slowly dropwise over the course of two minutes without stirring. After addition, the mixture was allowed to stir for 4 hours and the organic phase remained clear. Stirring was discontinued and the organic and aqueous phases were separated using a small separatory funnel. Small aliquots of the aqueous and organic phases were used to record UV-Vis spectra which together clearly indicated that the UO_2^{2+} had remained in the aqueous phase.

UO_2^{2+} migration from water to DCE in the presence of 5.1: A 5 mL vial was charged with $UO_2(NO_3)_2(THF)_2$ (14.0 mg, 0.026 mmol, 1.0 equiv), and dissolved in 1.5 mL of 0.1 M sodium acetate buffer adjusted to pH 5.4 (0.017 M UO_2^{2+}). An aliquot of the resulting pale-yellow solution was used to record an initial UV-Vis spectrum. The aliquot was transferred back to the 5 mL vial. A separate 20 mL vial was charged with a stirbar, **5.1** (14.1 mg, 0.026 mmol, 1.0 equiv), $[Bu_4N][PF_6]$ (0.2324 g, 0.1 M), and DCE (6.0 mL). To the clear DCE solution, the pale yellow aqueous solution was added slowly dropwise over the course of two minutes without stirring. After addition, the mixture was allowed to stir for 3 hours and the organic phase remained clear. Stirring was discontinued and the organic and aqueous phases were separated using a small separatory funnel. Small aliquots of the aqueous and organic phases were used to record UV-Vis spectra which together clearly indicated negligible transfer of UO_2^{2+} from the aqueous to the organic phase.

5.4.7 DFT Studies

Methods: DFT calculations were performed using Gaussian 09.2.[48] Geometry optimizations for all molecules were performed using the B3LYP/def2-SVP[49,50] level of theory (see S4 for

atom coordinates) in DCM using the conductor-like polarizable continuum model (CPCM) implemented in the Gaussian 09 software.[51-53] Thermal energy corrections were extracted from the results of the frequency analyses performed at the same level of theory. Frequency analyses of all molecules and intermediates contained no imaginary frequency showing that these are energy minima. The equilibrium constants were calculated from Gibbs free energy values for the proton transfer reactions ($K_{eq} = e^{(-\Delta G/RT)}$).

Competition results: To extract the relative basicity of **5.1**, **5.2a**, TPO and PC, DFT calculation were performed on isodesmic reactions of proton transfer between these molecules (NOTE: only the anion of **5.2a** was used in the calculations). Since **5.1** and **5.2a(anion)** have two P=O units, the comparison was made versus two TPO and two PC molecules. The results from the calculations are consistent with the experimental competition experiments wherein **5.2a** is much more basic than 2•TPO with the calculated equilibrium constant (K_{eq}) for the proton transfer from **5.2a**·H^+ to 2•TPO of $1.21 \cdot 10^{-25}$ (Supplementary Scheme 1a). The K_{eq} for the proton transfer from 2•TPO·H^+ to **5.1** is $5.96 \cdot 10^{-5}$, making 2•TPO more basic than 1. Finally, **5.1** is more basic than 2•PC with $K_{eq} = 9.20 \cdot 10^{-12}$ for proton transfer from **5.1**·H^+ to 2•PC. Overall the calculated relative basicities are similar to the experimental ones with **5.2a** >> 2•TPO > **5.1** >> 2•PC.

a **5.2a**•H^+ + 2TPO ⇌ **5.2a** + TPO_2•H^+ $\Delta H = 21.89$; $\Delta G = 33.99$; $K_{eq} = 1.21 \cdot 10^{-25}$

b TPO_2•H^+ + **5.1** ⇌ 2TPO + **5.1**•H^+ $\Delta H = 16.45$; $\Delta G = 5.76$; $K_{eq} = 5.96 \cdot 10^{-5}$

c **5.1**•H^+ + 2PC ⇌ **5.1** + PC_2•H^+ $\Delta H = 5.49$; $\Delta G = 15.06$; $K_{eq} = 9.20 \cdot 10^{-12}$

Scheme 5.1. DFT calculated isodesmic proton transfer reactions: **a**, from **5.2a**·H^+ to 2•TPO; **b**, from 2•TPO·H^+ to **5.1**; **c**, from **5.1**·H^+ to 2•PC. ΔH and ΔG are given in kcal·mol^{-1}.

Electron density surfaces: The electron density surface with electrostatic potentials was extracted from optimized **5.1** and **5.2a** and clearly shows that **5.2a** has a significantly larger negative electron density located at the oxygen atoms of the P=O moieties.

5.5 References

1. Adamantiades, A. & Kessides, I. Nuclear power for sustainable development: Current status and future prospects. *Energ. Policy* **37**, 5149-5166, doi:10.1016/j.enpol.2009.07.052 (2009).

2. Abu-Qare, A. W., Flaherty, M. M., Garofolo, M. C., Rincavage, H. L. & Abou-Donia, M. B. Depleted and Natural Uranium: Chemistry and Toxicological Effects. *J. Toxicol. Env. Heal. B* **7**, 297-317, doi:10.1080/10937400490452714 (2004).

3. Jungseung, K. *et al.* Recovery of Uranium from Seawater: A Review of Current Status and Future Research Needs. *Sep. Sci. Technol.* **48**, 367-387, doi:10.1080/01496395.2012.712599 (2013).

4. Parker, B. F., Zhang, Z., Rao, L. & Arnold, J. An overview and recent progress in the chemistry of uranium extraction from seawater. *Dalton Trans.* **47**, 639-644, doi:10.1039/C7DT04058J (2018).

5. Xiong, L.-p. *et al.* Efficient capture of actinides from strong acidic solution by hafnium phosphonate frameworks with excellent acid resistance and radiolytic stability. *Chem. Eng. J.* **355**, 159-169, doi:10.1016/j.cej.2018.08.118 (2019).

6. Sun, Q. *et al.* Bio-inspired nano-traps for uranium extraction from seawater and recovery from nuclear waste. *Nat. Commun.* **9**, 1644, doi:10.1038/s41467-018-04032-y (2018).

7. Jang, J.-H., Dempsey, B. A. & Burgos, W. D. A Model-Based Evaluation of Sorptive Reactivities of Hydrous Ferric Oxide and Hematite for U(VI). *Environ. Sci. Technol.* **41**, 4305-4310, doi:10.1021/es070068f (2007).

8. Mellah, A., Chegrouche, S. & Barkat, M. The removal of uranium(VI) from aqueous solutions onto activated carbon: Kinetic and thermodynamic investigations. *J. Colloid Interf. Sci.* **296**, 434-441, doi:10.1016/j.jcis.2005.09.045 (2006).

9. Kim, J. H., Lee, H. I., Yeon, J.-W., Jung, Y. & Kim, J. M. Removal of uranium(VI) from aqueous solutions by nanoporous carbon and its chelating polymer composite. *J. Radioanal. Nucl. Ch.* **286**, 129-133, doi:10.1007/s10967-010-0624-3 (2010).

10. Plesek, J. Potential applications of the boron cluster compounds. *Chem. Rev.* **92**, 269-278, doi:10.1021/cr00010a005 (1992).

11. Mehio, N. *et al.* Quantifying the binding strength of salicylaldoxime–uranyl complexes relative to competing salicylaldoxime–transition metal ion complexes in aqueous solution: a combined experimental and computational study. *Dalton Trans.* **45**, 9051-9064, doi:10.1039/C6DT00116E (2016).

12. Paiva, A. P. & Malik, P. Recent advances on the chemistry of solvent extraction applied to the reprocessing of spent nuclear fuels and radioactive wastes. *J. Radioanal. Nucl. Ch.* **261**, 485-496, doi:10.1023/B:JRNC.0000034890.23325.b5 (2004).

13. Kuo, L.-J. *et al.* Investigations into the Reusability of Amidoxime-Based Polymeric Adsorbents for Seawater Uranium Extraction. *Ind. Eng. Chem. Res.* **56**, 11603-11611, doi:10.1021/acs.iecr.7b02893 (2017).

14. Heying, T. L. *et al.* A New Series of Organoboranes. I. Carboranes from the Reaction of Decaborane with Acetylenic Compounds. *Inorg. Chem.* **2**, 1089-1092, doi:10.1021/ic50010a002 (1963).

15. Fisher, S. P. *et al.* Nonclassical Applications of closo-Carborane Anions: From Main Group Chemistry and Catalysis to Energy Storage. *Chem. Rev.*, DOI: 10.1021/acs.chemrev.1028b00551, doi:10.1021/acs.chemrev.8b00551 (2019).

16. Núñez, R., Tarrés, M., Ferrer-Ugalde, A., de Biani, F. F. & Teixidor, F. Electrochemistry and Photoluminescence of Icosahedral Carboranes, Boranes, Metallacarboranes, and Their Derivatives. *Chem. Rev.* **116**, 14307-14378, doi:10.1021/acs.chemrev.6b00198 (2016).

17. Saxena, A. K. & Hosmane, N. S. Recent advances in the chemistry of carborane metal complexes incorporating d- and f-block elements. *Chem. Rev.* **93**, 1081-1124, doi:10.1021/cr00019a011 (1993).

18. Fronczek, F. R., Halstead, G. W. & Raymond, K. N. The synthesis, crystal structure, and reactions of an actinide metallocarborane complex, bis(.eta.5-(3)-1,2-dicarbollyl)dichlorouranium(IV) dianion, [U(C2B9H11)2Cl2]2. *J. Am. Chem. Soc.* **99**, 1769-1775, doi:10.1021/ja00448a015 (1977).

19. Axtell, J. C., Saleh, L. M. A., Qian, E. A., Wixtrom, A. I. & Spokoyny, A. M. Synthesis and Applications of Perfunctionalized Boron Clusters. *Inorg. Chem.* **57**, 2333-2350, doi:10.1021/acs.inorgchem.7b02912 (2018).

20. Barton, J. L., Wixtrom, A. I., Kowalski, J. A., Brushett, F. & Spokoyny, A. M. Perfunctionalized Dodecaborate Clusters as Stable Metal-Free Active Materials for Charge Storage. *ChemRxiv*, doi:10.26434/chemrxiv.7472921.v1 (2018).

21. Fisher, S. P., Tomich, A. W., Guo, J. & Lavallo, V. Teaching an old dog new tricks: new directions in fundamental and applied closo-carborane anion chemistry. *Chem. Commun.* **55**, 1684-1701, doi:10.1039/C8CC09663E (2019).

22. Grimes, R. N. *Carboranes*. 2nd edn, (Elsevier Science & Technology, 2011).

23. Xie, Z. Advances in the chemistry of metallacarboranes of f-block elements. *Coord. Chem. Rev.* **231**, 23-46, doi:10.1016/S0010-8545(02)00112-1 (2002).

24. Weber, L. *et al.* Electrochemical and spectroelectrochemical studies of C-benzodiazaborolyl-ortho-carboranes. *Dalton Trans.* **42**, 2266-2281, doi:10.1039/C2DT32378H (2013).

25. Charmant, J. P. H. *et al.* A simple entry into nido-C2B10clusters: HCl promoted cleavage of the C–C bond in ortho-carboranyl diphosphines. *Dalton Trans.*, 1409-1411, doi:10.1039/B719404H (2008).

26. Deng, L., Cheung, M.-S., Chan, H.-S. & Xie, Z. Reduction of 1,2-(CH2)n-1,2-C2B10H10 by Group 1 Metals. Effects of Bridge Length/Rigidity on the Formation of Carborane Anions. *Organometallics* **24**, 6244-6249, doi:10.1021/om050683x (2005).

27. Wade, K. The structural significance of the number of skeletal bonding electron-pairs in carboranes, the higher boranes and borane anions, and various transition-metal carbonyl cluster compounds. *J. Chem. Soc. D.*, 792-793, doi:10.1039/C29710000792 (1971).

28. Popescu, A.-R. *et al.* Uncommon Coordination Behaviour of P(S) and P(Se) Units when Bonded to Carboranyl Clusters: Experimental and Computational Studies on the Oxidation of Carboranyl Phosphine Ligands. *Chem. Eur. J.* **17**, 4429-4443, doi:10.1002/chem.201003330 (2011).

29. Sundberg, M. R. *et al.* Nature of intramolecular interactions in hypercoordinate C-substituted 1,2-dicarba-closo-dodecaboranes with short P···P distances. *Inorg. Chem. Commun.* **10**, 713-716, doi:10.1016/j.inoche.2007.03.003 (2007).

30. Bombieri, G., Forsellini, E., Day, J. P. & Azeez, W. I. Crystal and molecular structure of dichlorodioxobis(triphenylphosphine oxide)uranium(VI). *J. Chem. Soc. Dalton Trans.*, 677-680, doi:10.1039/DT9780000677 (1978).

31. Brighli, M., Fux, P., Lagrange, J. & Lagrange, P. Discussion on the complexing ability of the uranyl ion with several crown ethers and cryptands in water and in propylene carbonate. *Inorg. Chem.* **24**, 80-84, doi:10.1021/ic00195a016 (1985).

32. Akona, S. B., Fawcett, J., Holloway, J. H., Russell, D. R. & Leban, I. Structures of cis- and trans-dichlorodioxobis(triphenylphosphine oxide)uranium(VI). *Acta Cryatallogr. C* **47**, 45-48, doi:10.1107/S0108270190007181 (1991).

33. Bard, A. J. & Faulkner, L. R. *Electrochemical Methods: Fundamentals and Applications*. 2nd edn, (Wiley, 2000).

34. Liu, C. *et al.* A half-wave rectified alternating current electrochemical method for uranium extraction from seawater. *Nat. Energy* **2**, 17007, doi:10.1038/nenergy.2017.7 (2017).

35. Chi, F., Zhang, S., Wen, J., Xiong, J. & Hu, S. Highly Efficient Recovery of Uranium from Seawater Using an Electrochemical Approach. *Ind. Eng. Chem. Res.* **57**, 8078-8084, doi:10.1021/acs.iecr.8b01063 (2018).

36. Quilès, F., Nguyen-Trung, C., Carteret, C. & Humbert, B. Hydrolysis of Uranyl(VI) in Acidic and Basic Aqueous Solutions Using a Noncomplexing Organic Base: A Multivariate Spectroscopic and Statistical Study. *Inorg. Chem.* **50**, 2811-2823, doi:10.1021/ic101953q (2011).

37. Pant, D. D. & Khandelwal, D. P. The absorption and fluorescence spectra of uranyl nitrate solutions at room temperature. *P. Indian Acad. Sci. A* **50**, 323-335, doi:10.1007/bf03048924 (1959).

38. Görller-Walrand, C. & De Jaegere, S. Correlation between the vibronic spectra of the uranyl ion and the geometry of its coordination. *Spectrochim. Acta A-M* **28**, 257-268, doi:10.1016/0584-8539(72)80250-2 (1972).

39. Hunt, C., Mattejat, M., Anderson, C., Sepunaru, L. & Ménard, G. Symmetric Phthalocyanine Charge Carrier for Dual Redox Flow Battery/Capacitor Applications. *ACS Appl. Energy Mater.*, doi:10.1021/acsaem.9b01317 (2019).

40. The fate of the remaining uranyl remains under investigation. However, we note that given the appearance of some impurities upon discharge, coupled with the initial capture of 0.9 equivalent, we should not expect the recovery of a full equivalent of uranyl.

41. Bombieri, G., Forsellini, E., Day, J. P. & Azeez, W. I. Crystal and molecular structure of dichlorodioxobis(triphenylphosphine oxide)uranium(VI). *J. Chem. Soc. Dalton Trans.*, 677-680, doi:10.1039/DT9780000677 (1978).

42. Wilkerson, M. P., Burns, C. J., Paine, R. T. & Scott, B. L. Synthesis and Crystal Structure of UO2Cl2(THF)3: A Simple Preparation of an Anhydrous Uranyl Reagent. *Inorg. Chem.* **38**, 4156-4158, doi:10.1021/ic990159g (1999).

43. Lalancette, J. M., Rollin, G. & Dumas, P. Metals Intercalated in Graphite. I. Reduction and Oxidation. *Can. J. Chem.* **50**, 3058-3062, doi:10.1139/v72-485 (1972).

44. Liu, Y. *et al.* Mechanistic Understanding of Dinuclear Cobalt(III) Complex Mediated Highly Enantioselective Copolymerization of meso-Epoxides with CO2. *Macromolecules* **47**, 7775-7788, doi:10.1021/ma5019186 (2014).

45. Alexander, R. P. & Schroeder, H. Chemistry of Decaborane-Phosphorus Compounds. IV. Monomeric, Oligomeric, and Cyclic Phosphinocarboranes. *Inorg. Chem.* **2**, 1107-1110, doi:10.1021/ic50010a006 (1963).

46. Popescu, A.-R. *et al.* Uncommon Coordination Behaviour of P(S) and P(Se) Units when Bonded to Carboranyl Clusters: Experimental and Computational Studies on the Oxidation of Carboranyl Phosphine Ligands. *Chem. Eur. J.* **17**, 4429-4443, doi:10.1002/chem.201003330 (2011).

47. Bard, A. J. & Faulkner, L. R. *Electrochemical Methods: Fundamentals and Applications*. 2nd edn, (Wiley, 2000).

48. *Gaussian 09 et al.*, Gaussian, Inc., Wallingford CT, 2010.

49. Lee, C., Yang, W. & Parr, R. G. Development of the Colle-Salvetti correlation-energy formula into a functional of the electron density. *Physical Review B* **37**, 785-789, doi:10.1103/PhysRevB.37.785 (1988).

50. Weigend, F. & Ahlrichs, R. Balanced basis sets of split valence, triple zeta valence and quadruple zeta valence quality for H to Rn: Design and assessment of accuracy. *Phys. Chem. Chem. Phys.* **7**, 3297-3305, doi:10.1039/B508541A (2005).

51. Cossi, M., Rega, N., Scalmani, G. & Barone, V. Energies, structures, and electronic properties of molecules in solution with the C-PCM solvation model. *J. Comput. Chem.* **24**, 669-681, doi:10.1002/jcc.10189 (2003).

52. Barone, V. & Cossi, M. Quantum Calculation of Molecular Energies and Energy Gradients in Solution by a Conductor Solvent Model. *J. Phys. Chem. A* **102**, 1995-2001, doi:10.1021/jp9716997 (1998).

53. Andzelm, J., Kölmel, C. & Klamt, A. Incorporation of solvent effects into density functional calculations of molecular energies and geometries. *J. Chem. Phys.* **103**, 9312-9320, doi:10.1063/1.469990 (1995).